Dissertation zur Erlangung des Doktorgrades
der Fakultät für Chemie und Pharmazie
der Ludwig-Maximilians-Universität München

Density Functional Calculations of Pressure-Induced Phase Transformations of Group II Element Nitrides, Nitridosilicates and Nitridophosphates

Dipl. Chem. Susanne Rebecca Römer

aus

München

2008

Erklärung:

Diese Dissertation wurde im Sinne von § 13 Abs. 3 bzw. 4 der Promotionsordnung vom 31. Mai 2002 von Herrn Prof. Dr. Wolfgang Schnick betreut.

Ehrenwörtliche Versicherung:

Diese Dissertation wurde selbständig, ohne unerlaubte Hilfe erarbeitet.

München, den 28. November 2008

Susanne Rebecca Römer

Dissertation eingereicht am   28.11.2008

1. Gutachter   Prof. Dr. Wolfgang Schnick
2. Gutachter   Prof. Dr. Dirk Johrendt

Mündliche Prüfung am   03.02.2009

In loving memory of my father,
who will never be forgotten.

To my mother

Acknowledgment

„The most exciting phrase to hear in science,
the one that heralds new discoveries,
is not 'Eureka!' (I found it!),
but 'That's funny ...'"
(Isaac Asimov)

Contents

1 Introduction

Material properties of nitrides (e.g. mechanical hardness, stability) often are superior to those of the respective oxides (c.f. boron oxide/boron nitride, silicon oxide/silicon nitride, aluminum oxide/aluminum nitride). This observation is attributed to the higher covalency of the constituting chemical bonds and the higher degree of cross linking in nitride structures in comparison to oxides [1].

Binary silicon nitride Si_3N_4 is the most important non-oxidic ceramic material for high performance applications. Sintered components have been widely used in motor and turbine production (Figure 1.1). Until 1999 only the two polymorphs α- and β-Si_3N_4 have been known, which are both built up by a three-dimensional network of corner sharing SiN_4 tetrahedra comprising 3-bonded $N^{[3]}$ atoms (superscript numbers in square brackets denote the connectivity/coordination of an atom) [2, 3]. Recently, cubic spinel-type γ-Si_3N_4 has been discovered, containing a novel structural motif, SiN_6 octahedra, besides well known SiN_4 tetrahedra [4, 5]. First principle calculations for γ-Si_3N_4 showed an excellent agreement between experimentally observed quantities and calculated results. The transition pressure of γ-Si_3N_4 was computed to 12 to 13 GPa, matching quite well experimentally determined 12 to 15 GPa [4–6]. The bulk modulus of the γ-phase was determined to 290 - 317 GPa [7, 8] and computed to 280 to 310 GPa [4, 6, 9].

Figure 1.1: Workpieces made from Si_3N_4 (©Kyocera Corp.).

The discovery of the spinel-type structure of γ-Si_3N_4 (Figure 1.2) triggered further studies. A first objective was the search for so-called post-spinel phases of silicon

nitride. Scanning a manifold of candidate structures, Kroll et al. [10] identified a $CaTi_2O_4$-type Si_3N_4 appearing above 150 GPa. Sekine [11] has recently proposed a post-spinel phase of Si_3N_4 based on shock-wave data. The formation pressure of this novel modification of silicon nitride, which was not quenchable to ambient conditions, was deduced to be larger than 140 GPa.

β-Si_3N_4 γ-Si_3N_4
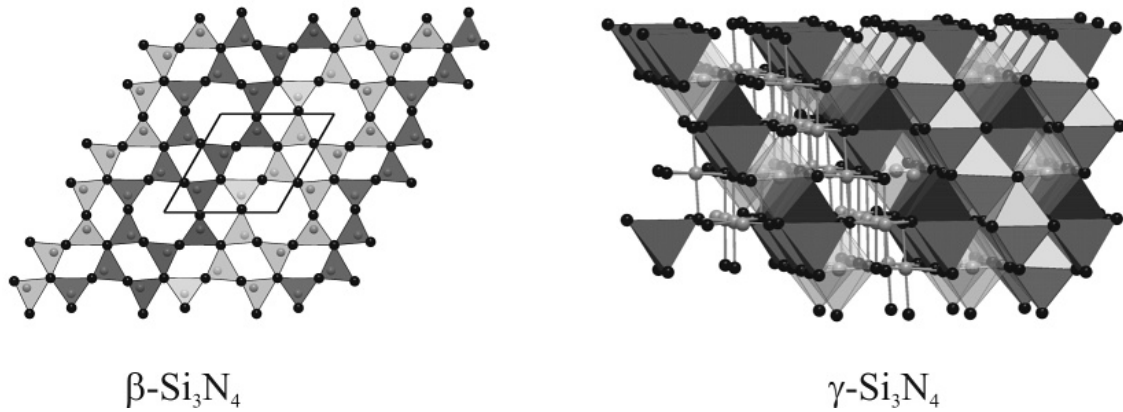
Figure 1.2: Structures of β- and γ-Si_3N_4.

A second direction in the high-pressure chemistry of silicon nitride was devoted to the intermediate and metastable phase of wII-Si_3N_4 [4, 12]. It turned out that this hypothetical modification of silicon nitride (related to a high-pressure modification of the zinc silicate willemite) is structurally related to the spinel-type by a Bain-correspondence. As the anion sublattice in spinel is approximately fcc, the anion packing in the wII-type approximately bcc, a transition from wII-Si_3N_4 to spinel-type Si_3N_4 might be induced kinetically in a similar way that martensitic transitions happen [12] (Figure 1.3).

γ-Si_3N_4 ⟶ wII-Si_3N_4

Figure 1.3: The transformation between the spinel-type γ-Si_3N_4 and wII-Si_3N_4 (ball-and-stick illustration of the distortion of SiN_6 octahedra to SiN_4 tetrahedra) [12].

The synthesis and structural chemistry of ternary and higher nitridosilicates (deriving from the binary nitride Si_3N_4) has only recently been

explored in detail. In contrast to ternary oxosilicates, which are usually synthesizable from binary oxides, ternary nitridosilicates could not yet be synthesized from binary nitrides. Nitridosilicates are usually obtained by high-temperature reaction of the respective alkaline earth and/or rare earth metals with polymeric silicon diimide.

Compared to common oxosilicates, nitridosilicates exhibit significantly extended structural possibilities. As basic building blocks SiN_4, SiN_6, N_3Si-SiN_3 etc. have to be considered (compare for examples [13–17]). Furthermore, while in oxosilicates the possibilities of linking the fundamental building units is limited by the possibilities of oxygen to either connect two polyhedra centers ($O^{[2]}$) or being terminally bound ($O^{[1]}$), nitrogen can either be terminally bound ($N^{[1]}$), bridging ($N^{[2]}$) or connecting three or even four polyhedra centers ($N^{[3]}$, $N^{[4]}$) (Figure 1.4).
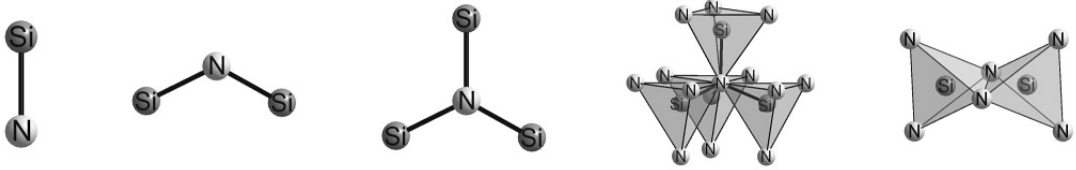
Figure 1.4: Possibilities of linking coordination polyhedra by N.

Additional to the wide variety nitridosilicates show in their structural chemistry, they exhibit interesting material properties. Besides extraordinary mechanical hardness and thermal as well as chemical stability, they exhibit interesting optical properties. The luminescence in Eu^{2+}-doped $Ba_2Si_5N_8$ has been studied giving rise to strong fluorescence, thermoluminescence and upconversion properties [18]. $Sr_2Si_5N_8$:Eu^{2+} and $SrSi_2O_2N_2$:Eu^{2+} as novel powerful red- and green-emitting phosphors have been combined with a blue GaN primary emitter to give the first all-nitride phosphor-converted white LED (2pc-LED) [19]. Furthermore, the nitridosilicates $M_2Si_5N_8$ (M = Ca, Sr, Ba), $CeSi_3N_5$, and $BaYbSi_4N_7$ show rather high nonlinearities up to $0.9\,pm^2/V^2$ for second harmonic generation (SHG) [20]. Nitridosilicates might therefore be specifically useful as a new class of nonlinear optical materials. In addition, the magnetic properties of several lanthanide containing nitridosilicates have been investigated [21].

Phosphorus nitride and the deriving nitridophosphates are structurally related to both oxidic phosphates and silicates but also to silicon nitride and the nitridosilicates. In 2001, a new high-pressure polymorph γ-P_3N_5 was discovered [22, 23]. Similarly to the high-pressure phase transformation of Si_3N_4 a partial increase of the coordination number of P from 4 (tetrahedral) to 5 (quadratic pyramidal) occurs (Figure 1.5) and this structural transformation is accompanied by a significant increase of density and mechanical hardness [22, 23].

Density functional calculations led to the prediction of an even higher condensed kyanite-type δ-P_3N_5 polymorph with PN_6 octahedra and PN_4 tetrahedra, coming into existence at pressures exceeding 40 GPa. On decompression, this phase is likely to undergo a shear-distortion, resulting in the yet unknown structure of δ'-P_3N_5, which consists of PN_6 octahedra, trigonal prisms PN_5, and PN_4 tetrahedra (Figure 1.5). A further significant increase in density and mechanical hardness is predicted [24].

α-P_3N_5 $\qquad$ γ-P_3N_5 $\qquad$ δ'-P_3N_5
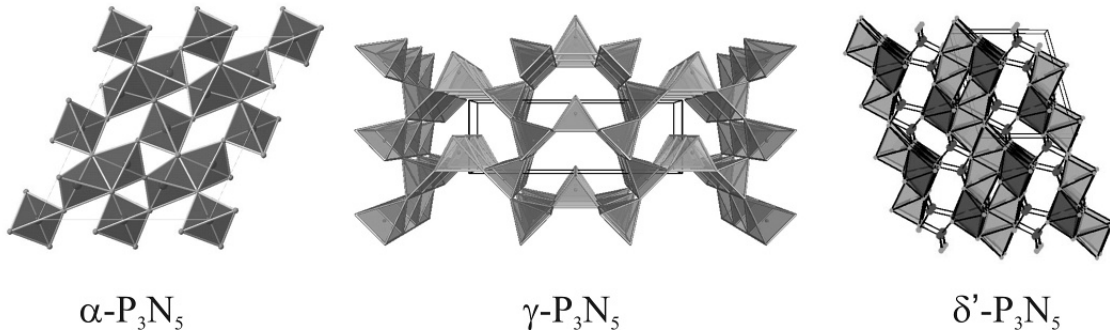
Figure 1.5: Structures of α-P_3N_5 as well as the high-pressure polymorph γ-P_3N_5 and predicted δ'-P_3N_5.

Besides this pressure induced increase of the coordination number of P in γ-P_3N_5, a number of novel highly condensed nitridophosphates consisting of condensed PN_4 tetrahedra were successfully synthesized at higher pressure. Known from experience these highly condensed compounds are not accessible by classical solid-state reactions of the respective binary nitrides. By application of the so called "azide-route" (reaction of the respective metal azide with P_3N_5 at high pressure and high temperature) – among others – the syntheses of MP_2N_4 (M = Be, Mg, Ca, Sr, Ba) was possible. While BeP_2N_4 crystallizes in the phenakite (Be_2SiO_4) structure [25],

MgP$_2$N$_4$, CaP$_2$N$_4$ and SrP$_2$N$_4$ exhibit the megakalsilite (KAlSiO$_4$) structure [25–27] and BaP$_2$N$_4$ is isotypic to CaB$_2$O$_4$-IV [25, 28, 29].

While the crystal structures and the materials properties of normal-pressure nitridosilicates and nitridophosphates have been intensively investigated, nearly nothing is known about any high-pressure phases of these two classes of compounds. However, with respect to the recent endeavors that have been undertaken on the preparation and materials properties of the binary high-pressure phases γ-Si$_3$N$_4$ and γ-P$_3$N$_5$ and the diverse structural chemistry and broad spectrum of properties of ternary nitridosilicates and -phosphates, such high-pressure Si/N and P/N-phases should be accessible and would be specifically promising, both to basic solid-state chemistry and materials research.

The objective of this thesis is to predict new high-pressure phases of nitridosilicates and nitridophosphates within density functional theory (DFT), aiming at identifying promising systems for high-pressure experiments as well as facilitating structural characterization of such (e.g. from powder diffraction data) by offering structural models.

The search for novel high-pressure polymorphs for a given compound is governed by Le Châtelier's Principle ("Lorsque les modifications extérieures apportées à un système physico-chimique en équilibre provoquent une évolution vers un nouvel état d'équilibre, l'évolution s'oppose aux perturbations qui l'ont engendrée et en modère l'effet."), which has been specified by Le Châtelier himself for the parameter pressure (Loi expeérimentale de Le Châtelier). An augmentation in pressure applied to a closed system in equilibrium and maintained at a constant temperature results in a shift of the equilibrium towards a smaller volume. Applied to structural transformations induced by high pressure, this means a pressure-induced phase transition is characterized by a negative volume change ΔV, or – equivalent – a positive density change $\Delta\rho$. A new high-pressure phase therefore can crystallize in a structure either having in average shorter distances between the constituting atoms (giving rise to increased electrostatic repulsion between the constituting atoms) or an increased coordination number resulting in larger interatomic distances to reduce electrostatic repulsion (Pressure Distance Paradoxon). In this thesis special attention was payed to the second possibility, aiming at coordination numbers for both Si and P greater than four.

In the first part of this thesis a short outline of the standard theoretical methods as well as the underlaying theory is given. In the second part an extensive study on the high-pressure behavior of the compounds M_3N_2, $MSiN_2$ and $M_2Si_5N_8$ (M = Be, Mg, Ca, Sr, Ba) concerning the evolution of high-pressure phases as well as pressure-induced decomposition reactions is presented. In Chapter 7 the pressure-induced transformation of phenakite-type BeP_2N_4 into spinel-type and inverse spinel-type BeP_2N_4 is examined. The research presented in this thesis was conducted as part of a research project within the priority project SPP 1236 ("Strukturen und Eigenschaften von Kristallen bei extrem hohen Drücken und Temperaturen" - "Structures and properties of crystals at extreme high pressures and temperatures") of the Deutsche Forschungsgemeinschaft (DFG).

2 Theory and Methods

In principle, all physical and chemical knowledge about a system can be obtained from the quantum mechanical wave function, which is obtained by solving the Schrödinger equation of the complete many particle system. However, in practice analytically solving the Schrödinger equation for a N-particle system proves to be impossible for systems with more than two particles [30]. Therefore approximations have to be introduced, since in solid state compounds the number of electrons N is of the order of magnitude of 10^{23}.

This chapter will give a brief description of the quantum mechanical theroy and methods used in this thesis, followed by a short assessment of the Equations of States (EOS) used to evaluate the calculated energy-volume data.

2.1 The Schrödinger Equation

Schrödingers equation covers most problems in the electronic structure of matter, including time. In the majority of cases, however, atomic structures without time-dependent interactions are examined. The time-independent Schrödinger equation for a system composed of N electrons and M nuclei is given as

$$\boldsymbol{H}\Psi(r_i, R_A) = E\Psi(r_i, R_A) \tag{2.1}$$

where $\boldsymbol{H}$ is the Hamiltonian, E the energy of the system, and $\Psi(r_i, R_A)$ the wave function with r_i and R_i corresponding to the electronic, spin and nuclear coordinates. The non-relativistic Hamiltonian $\boldsymbol{H}$, given in atomic units (see [31]), is

$$\boldsymbol{H} = -\sum_{i=1}^{N}\frac{1}{2}\nabla_i^2 - \sum_{A=1}^{M}\frac{1}{2M_A}\nabla_A^2 - \sum_{i=1}^{N}\sum_{A=1}^{M}\frac{Z_A}{r_{iA}} + \sum_{i=1}^{N}\sum_{j>i}^{N}\frac{1}{r_{ij}} + \sum_{A=1}^{M}\sum_{B>A}^{M}\frac{Z_A Z_B}{R_{AB}}. \tag{2.2}$$

The first term corresponds to the kinetic energy T_e of the electrons i, the second term to the kinetic energy T_n of the nuclei A, where M_A is the mass of nucleus A. The third term represents the Coulomb attraction V_{en} between the nuclei and electrons with Z_A being the atomic number of the nuclei and r_{iA} being the distance between the respective electrons and nuclei. The fourth term describes the Coulomb repulsion V_{nn} between the electrons with r_{ij} being the distances between the electrons i and j. The fifth term gives the repulsion V_{nn} between the nuclei, where Z_A and Z_B are the atomic numbers of the nuclei and the R_{AB} are the distances between the nuclei A and B, respectively.

In a more compact way, the Hamiltonian can be written as

$$\boldsymbol{H} = \boldsymbol{T}_e + \boldsymbol{T}_n + \boldsymbol{V}_{en} + \boldsymbol{V}_{ee} + \boldsymbol{V}_{nn} \tag{2.3}$$

2.2 The Born-Oppenheimer Approximation

In 1923 Born and Oppenheimer [32] stated - since the nuclei are much heavier than electrons and therefore move on a time scale which is approximately three orders of magnitude larger than that of the electrons - that the electrons can be considered to be moving in a field of fixed nuclei and electronic and nuclear motion can be separated. Resulting from this assumption, $\boldsymbol{T}_n$ in Eq. 2.3 can be neglected and the contribution of $\boldsymbol{V}_{nn}$ can be considered as a constant. The electronic Hamiltonian then can be written as

$$\boldsymbol{H}_{elec} = -\sum_{i=1}^{N} \frac{1}{2}\nabla_i^2 - \sum_{i=1}^{N}\sum_{A=1}^{M} \frac{Z_A}{r_{iA}} + \sum_{i=1}^{N}\sum_{j>i}^{N} \frac{1}{r_{ij}} \tag{2.4}$$

or short

$$\boldsymbol{H}_{elec} = \boldsymbol{T}_e + \boldsymbol{V}_{en} + \boldsymbol{V}_{ee}. \tag{2.5}$$

The Schrödinger equation

$$\boldsymbol{H}_{elec}\psi(r_i, R_A) = E_{elec}\psi(r_i, R_A) \tag{2.6}$$

then gives the electronic energy E_{elec} with $\psi(r_i, R_A)$ being the electronic wave function. Both, E_{elec} and $\psi(r_i, R_A)$ depend parametrically on the nuclear coordinates R_A. The energy for a given nuclear arrangement must also contain the nuclear repulsion:

$$E_{tot} = E_{elec} + V_{nn}, \tag{2.7}$$

with V_{nn} being a constant. In the same way as the electronic Hamiltonian, the nuclear Hamiltonian can be formulated as

$$\boldsymbol{H}_{nuc} = -\sum_{A=1}^{M} \frac{1}{2M_A} \nabla_A^2 + E_{tot}(\{R_A\}). \tag{2.8}$$

The energy $E_{tot}(\{R_A\})$ becomes a potential for the nuclear motion.

The corresponding approximation to the total wave function then can be written as a product of the electronic wave function $\psi(r_i, R_A)$ and the nuclear wave function $\Xi(R_A)$:

$$\Psi(r_i, R_A) = \psi(r_i, R_A)\Xi(R_A). \tag{2.9}$$

2.3 The Variational Principle

The variational principle [31] allows to approximate the ground state energy E_0 of a system without solving the Schrödinger equation exactly.

Assume $\tilde{\Psi}$ is a trial wave function for the exact ground state wave function Ψ_0 as defined in 2.6, the variational integral gives an upper boundary for the ground state energy:

$$\frac{\int \tilde{\Psi}^* \boldsymbol{H} \tilde{\Psi} d\tau}{\int \tilde{\Psi}^* \tilde{\Psi} d\tau} \geq E_0. \tag{2.10}$$

If $\tilde{\Psi}$ is normalized, i.e. $\int \tilde{\Psi}^* \tilde{\Psi} d\tau = 1$, 2.10 simplifies to:

$$\int \tilde{\Psi}^* \boldsymbol{H} \tilde{\Psi} d\tau \geq E_0. \tag{2.11}$$

The lower the value of the variational integral the closer is $\tilde{\Psi}$ to Ψ_0. Therefore, by minimizing the variational integral the exact ground state wave function Ψ_0 can be approximated.

2.4 Density Functional Theory

In **D**ensity **F**unctional **T**heory (DFT) the electronic many body wave function is substituted by the ground-state electronic density ρ_0. Thereby the degrees of freedom are drastically reduced, as the electronic wave function of an N electron system depends on $3N$ space-spin coordinates, whereas the ground-state electronic density only depends on 3 space-spin coordinates.

Density functional theory is founded on the works of Thomas and Fermi in the 1920s [33–36]. They approximated the electronic kinetic energy in terms of the electronic density $\rho(\mathbf{r})$. But it required the publication of Hohenberg and Kohns landmark paper [37] in the 1960s to boost density functional theory and finally render it one of the widestly used quantum mechanical methods in solid state science.

2.4.1 The Hohenberg-Kohn Theorems

The first *Hohenberg-Kohn Theorem* states, that the external potential of a system $\upsilon(\mathbf{r})$ is determined – within a trivial additive constant – by the electron density $\rho(\mathbf{r})$. As $\rho(\mathbf{r})$ also gives the number of electrons N via

$$N = N[\rho(\mathbf{r})] = \int \rho(\mathbf{r})d\mathbf{r}, \tag{2.12}$$

it also determines the ground-state wave function, the Hamiltonian and all other electronic properties of the system.

Thus, one can formulate an energy functional $E[\rho(\mathbf{r})]$ in terms of the electron density $\rho(\mathbf{r})$:

$$E[\rho(\mathbf{r})] = T_e[\rho(\mathbf{r})] + V_{ee}[\rho(\mathbf{r})] + V_{ne}[\rho(\mathbf{r})] =$$
$$= F_{HK}[\rho(\mathbf{r})] + \int \rho(\mathbf{r})\upsilon(\mathbf{r})d\mathbf{r}. \tag{2.13}$$

The term $F_{HK}[\rho(\mathbf{r})]$ is the *Hohenberg-Kohn Functional*, which comprises the kinetic energy $T_e[\rho(\mathbf{r})]$ and the potential energy of the electrons $V_{ee}[\rho(\mathbf{r})]$.

The second *Hohenberg-Kohn Theorem* provides the energy variational principle. For

a trial electronic density $\tilde{\rho}(\mathbf{r})$ with

$$\tilde{\rho}(\mathbf{r}) \geq 0 \qquad \text{and} \qquad \int \tilde{\rho}(\mathbf{r}) d\mathbf{r} = N \qquad (2.14)$$

the total energy $\tilde{E}[\rho(\mathbf{r})]$, calculated from 2.13, is always greater or equal to the true ground-state energy E_0:

$$\tilde{E}[\rho(\mathbf{r})] \geq E_0$$
$$\int \tilde{\rho}(\mathbf{r}) \upsilon(\mathbf{r}) d\mathbf{r} + F_{HK}[\tilde{\rho}(\mathbf{r})] \geq E[\rho_0(\mathbf{r})] \qquad (2.15)$$

If the *Hohenberg-Kohn Functional* $F_{HK}[\rho(\mathbf{r})]$ is known, one can easily calculate the ground-state energy E_0 and ground-state electron density $\rho_0(\mathbf{r})$ by minimizing the energy functional $E[\rho_0(\mathbf{r})]$ with respect to the electron density.

2.4.2 The Kohn-Sham Equations

In 1965 density functional theory was further advanced by the publication of the *Kohn-Sham Equations* [38], which introduced an indirect approach to the kinetic energy functional $T[\rho(\mathbf{r})]$ and thereby approached the problem of expressing the electronic kinetic energy in terms of the charge density.

Kohn and Sham used a reference system of N non-interacting, independent electrons, which are moving in an effective potential υ_{eff}. Then the *Hohenberg-Kohn Functional*

$$H_{HK}[\rho] = T_e[\rho] + V_{ee}[\rho] =$$
$$= T_e[\rho] + J[\rho] + V_{ee,non-classical} \qquad (2.16)$$

can be rewritten to

$$H_{HK}[\rho] = T_s[\rho] + J[\rho] + E_{XC}[\rho], \qquad (2.17)$$

with $T_s[\rho]$ being the functional of the kinetic energy of N non-interacting electrons, $J[\rho]$ the functional of the classical part of $V_{ee}[\rho]$ and $E_{XC}[\rho]$ the functional of the exchange-correlation energy of the electrons.

The functional for the exchange-correlation energy is defined as:

$$E_{XC}[\rho] = (T_e[\rho] - T_s[\rho]) + (V_{ee}[\rho] - J[\rho]) \tag{2.18}$$

containing the difference between the exact kinetic energy and the kinetic energy for N non-interacting electrons as well as the non-classical part of $V_{ee}[\rho]$.

The non-negative and continuous electron density of N non-interacting electrons can be represented by

$$\rho(\mathbf{r}) = \sum_i^N \sum_s |\psi_i(\mathbf{r}, s)|^2 \,, \tag{2.19}$$

introducing the orthonormal ($\langle \psi_i | \psi_j \rangle = \delta_{ij}$) Kohn-Sham orbitals ψ_i, which represent the N lowest eigenstates of the one-electron Hamiltonian.

The energy functional of Eq. 2.13 now can be rewritten to (using Eq. 2.17):

$$E[\rho] = \int \rho(\mathbf{r})v(\mathbf{r})d\mathbf{r} + T_s[\rho] + J[\rho] + E_{XC}[\rho] =$$

$$= \int \rho(\mathbf{r})v(\mathbf{r})d\mathbf{r} + \sum_i^N \sum_s \int \psi_i^*(\mathbf{x})(-\frac{1}{2}\bigtriangledown^2)\psi_i(\mathbf{x})d\mathbf{r} + J[\rho] + E_{XC}[\rho]. \tag{2.20}$$

Minimizing $E[\rho]$ leads to the N equations:

$$\left[-\frac{1}{2}\bigtriangledown^2 + v_{eff} \right] \psi_i = \epsilon_i \psi_i. \tag{2.21}$$

The *Kohn-Sham effective potential* v_{eff} is defined by

$$v_{eff}(\mathbf{r}) = v(\mathbf{r}) + \frac{\delta J[\rho]}{\delta \rho(\mathbf{r})} + \frac{\delta E_{XC}[\rho]}{\delta \rho(\mathbf{r})} =$$

$$= v(\mathbf{r}) + \int \frac{\rho(\mathbf{r'})}{|\mathbf{r} - \mathbf{r'}|} + v_{XC}(\mathbf{r}) \tag{2.22}$$

with the *exchange-correlation potential*

$$v_{XC}(\mathbf{r}) = \frac{\delta E_{XC}[\rho]}{\delta \rho(\mathbf{r})} \tag{2.23}$$

and where $\frac{\delta}{\delta\rho(\mathbf{r})}$ denotes function variation.

Eqs. 2.19 and 2.21 to 2.23 are the famous *Kohn-Sham Equations*. They need to be solved self-consistently because of the dependency of v_{eff} on the electron density $\rho(\mathbf{r})$ as expressed in Eq. 2.22. Starting from a guess for $\rho(\mathbf{r})$ the effective potential v_{eff} is constructed via Eq. 2.22. Subsequently the *Kohn-Sham orbitals* ψ_i are derived from Eq. 2.21 and a new electron density is calculated from Eq. 2.19. These steps are repeated until $\rho(\mathbf{r})$ does not change any further.

2.4.3 The Exchange-Correlation Potential E_{XC}

In principle, the *Kohn-Sham Theory* is exact, fully incorporating the exchange-correlation effects of the electrons. It would yield the exact ground-state electron density and energy, if the exchange-correlation functional $E_{XC}[\rho]$ was known precisely. Unfortunately, the exact form of $E_{XC}[\rho]$ is not known. Therefore a number of models have been developed in order to approximate the exchange-correlation functional $E_{XC}[\rho]$ and the corresponding operator.

2.4.3.1 The Local Density Approximation LDA

In the **L**ocal **D**ensity **A**pproximation (LDA) it is assumed, that the exchange-correlation energy of a non-uniform system can be obtained by applying uniform electron gas results to infinitesimal portions of the non-uniform electron distribution. Here, the electron density $\rho(\mathbf{r})$ of the uniform electron gas [39] and the non-uniform electron gas at point $\mathbf{r}$ in space are the same.

In LDA the exchange-correlation energy E_{XC} is given by

$$E_{XC}^{LDA}[\rho] = \int \rho(\mathbf{r})\epsilon_{XC}[\rho]d\mathbf{r}, \qquad (2.24)$$

where ϵ_{XC} is the exchange-correlation energy of one electron of an uniform electron gas of the electron density $\rho(\mathbf{r})$. The exchange-correlation potential v_{XC}^{LDA} then can

be written as:

$$v_{XC}^{LDA}(\mathbf{r}) = \frac{\delta E_{XC}^{LDA}}{\delta \rho(\mathbf{r})} =$$
$$= \epsilon_{XC}(\rho) + \rho(\mathbf{r}) \frac{\partial \epsilon_{XC}(\rho)}{\partial \rho(\mathbf{r})}. \tag{2.25}$$

The exchange-correlation energy E_{XC} can be split into an exchange and a correlation energy part:

$$E_{XC}[\rho] = E_X[\rho] + E_C[\rho]. \tag{2.26}$$

The exchange energy part E_X is given by the Dirac exchange-energy functional [39]:

$$E_X[\rho] = -C_x \int \rho(\mathbf{r})^{\frac{4}{3}} d\mathbf{r}, \tag{2.27}$$

where $C_x = \frac{3}{4}(\frac{3}{\pi})^{\frac{1}{3}}$.

For the correlation energy part E_C accurate values have been calculated via quantum Monte Carlo simulations and the results have been interpolated to give an analytical form for ϵ_C by Vosko, Wilk and Nusair [40, 41].

Despite of its simplicity the *Local Density Approximation* has been successful in describing the electronic structure, the formation enthalpy and the elastic and vibrational properties of many systems. The disadvantages of the *Local Density Approximation* are its applicability only to systems with slowly varying electron densities, the general underestimation of the exchange energy by 10% and the overestimation of the correlation energy – which is a magnitude smaller than the exchange energy – by a factor close to 2. Therfore, LDA tends to overestimate bonding interactions and to underestimate lattice constants [39, 42].

2.4.3.2 The Local Spin Density Approximation LSDA

Within LSDA, additionally open-shell molecules and molecular geometries near dissociation as well as many-electron systems in the presence of a magnetic field acting on the spin of the electrons can be described in a better way [39].

In *Spin-Density Functional Theory* the electron density is separated into the α-spin electron density $\rho^\alpha(\mathbf{r})$ and the β-spin electron density $\rho^\beta(\mathbf{r})$. All functionals of

DFT, which depend on $\rho(\mathbf{r})$ become functionals of $\rho^\alpha(\mathbf{r})$ and $\rho^\beta(\mathbf{r})$. The exchange-correlation energy E_{XC} is then written as

$$E_{XC}[\rho^\alpha, \rho^\beta] = E_X[\rho^\alpha, \rho^\beta] + E_C[\rho^\alpha, \rho^\beta], \tag{2.28}$$

with the exchange energy E_X being [43]

$$E_X^{LSDA}[\rho^\alpha, \rho^\beta] = -2^{\frac{1}{3}} C_x \int \left[(\rho^\alpha)^{\frac{4}{3}} + (\rho^\beta)^{\frac{4}{3}} \right] d\mathbf{r}. \tag{2.29}$$

The correlation energy E_C as a function of r_s (radius of a sphere whose volume is the effective volume of an electron) and the spin polarization ζ has been cast into a analytic interpolation formula of Monte Carlo simulation results by Vosko, Wilk and Nusair [40, 41]. The spin polarization ζ is given by:

$$\zeta = \frac{\rho^\alpha - \rho^\beta}{\rho^\alpha + \rho^\beta}, \tag{2.30}$$

and $\zeta = 0$ gives the non-polarized and $\zeta = 1$ the fully polarized case. r_s is given by

$$r_s = \left(\frac{4\pi\rho}{3} \right)^{\frac{1}{3}}. \tag{2.31}$$

2.4.3.3 The Generalized Gradient Approximation GGA

By including the gradient of the electron density $\bigtriangledown\rho(\mathbf{r})$ into the exchange-correlation energy functional E_{XC}, corrections are made for non-uniform densities, which undergo rapid changes. The exchange-correlation energy is now not only a functional of the electron density but also of its gradient

$$E_{XC} = E_{XC}^{GGA}\left[\rho(\mathbf{r}), \bigtriangledown\rho(\mathbf{r})\right], \tag{2.32}$$

and again is usually split into an exchange and a correlation part [30, 42]. Several approximations have been proposed for the exchange and the correlation energy functionals. The more important are listed in Table 2.1.

Where LDA tends to overestimate bonding interactions and underestimates lattice constants, the various GGA functionals give more accurate binding energies but

Table 2.1: Examples for frequently used exchange and correlation functionals in GGA.

Exchange energy ε_X	Correlation energy ε_C
PW86 (Perdew, Wang)[a] [44]	LYP (Lee, Yang, Parr)[b] [45]
P88 (Becke)[a] [46]	P86 (Perdew)[a] [47, 48]
BR (Becke, Roussel)[b] [49]	PW91 (Perdew, Wang)[a] [50]
PW91 (Perdew, Wang)[a] [50]	B95 (Becke)[b] [51]

[a] correction to LSDA functional

[b] independent functional form

overestimate lattice constants. The cohesive energy (the difference in energy between atoms in a crystalline state and a system of free atoms at rest far apart from each other) for solids is significantly improved in GGA calculations over results of LDA calculations (see [52, 53] and references therein).

2.5 The Plane Wave Method

Kohn-Sham Theory reduces the many body problem of the N-particle wave function to N single particle problems. Nevertheless, for every bulk material there does still remain an infinite number of non-interacting electrons moving in a potential caused by an infinite number of nuclei (always bearing in mind that an infinite crystal is always an approximation of a finite real crystal).

For crystalline materials the spatial periodicity of the electrostatic potential of the nuclei imposes a periodic boundary condition on the wave functions which are solutions of the Schrödinger equation. This concept was first expressed by Bloch, known as *Bloch's Theorem* [54].

2.5.1 Bloch's Theorem

In an ideal crystal with the translation vector $\mathbf{R}$ the electrostatic potential $V(\mathbf{r})$ obeys translational invariance, i.e. it is a periodic function with the periodicity of the crystal lattice:

$$V(\mathbf{r}) = V(\mathbf{r} + \mathbf{R}). \tag{2.33}$$

This is also valid for the effective potential $V_{eff}(\mathbf{r})$ of the Kohn-Sham equations:

$$V_{eff}(\mathbf{r}) = V_{eff}(\mathbf{r} + \mathbf{R}). \tag{2.34}$$

Every eigenfunction $\psi_k(\mathbf{r})$, that is a solution to the single particle Schrödinger equation – as given by the Kohn-Sham equations –

$$\left[-\frac{1}{2} \, \triangledown^2 + V_{eff}(\mathbf{r}) \right] \psi_k(\mathbf{r}) = E_{\mathbf{k}} \psi_k(\mathbf{r}) \tag{2.35}$$

can be expressed as a product of a plane wave $\exp[i\mathbf{kr}]$ ($\mathbf{k}$ denoting a reciprocal space vector) and a function $u_k(\mathbf{r})$ with the same periodicity as the real space lattice ($u_k(\mathbf{r}) = u_k(\mathbf{r} + \mathbf{R})$):

$$\psi_k(\mathbf{r}) = u_k(\mathbf{r}) e^{i\mathbf{kr}}. \tag{2.36}$$

Both, the periodic electrostatic potential $V_{eff}(\mathbf{r})$ and the Bloch waves $\psi_k(\mathbf{r})$, can be expanded as a Fourier series in terms of reciprocal lattice vectors $\mathbf{G}$

$$V_{eff}(\mathbf{r}) = \frac{1}{\Omega} \sum_G V_{eff}(\mathbf{G}) e^{i\mathbf{Gr}} \tag{2.37}$$

$$\psi_k(\mathbf{r}) = \frac{1}{\sqrt{\Omega}} \sum_G u_k(\mathbf{G}) e^{i(\mathbf{k}+\mathbf{G})\mathbf{r}} \tag{2.38}$$

with Ω being the volume of the unit cell of the system ($\Omega = \mathbf{a}_1 \cdot (\mathbf{a}_2 \times \mathbf{a}_3)$).
The reciprocal lattice vectors $\mathbf{G}$ are defined as

$$\mathbf{G} = u\mathbf{b}_1 + v\mathbf{b}_2 + w\mathbf{b}_3. \tag{2.39}$$

Here, $\mathbf{b}_i$ is the reciprocal lattice basis and $u, v, w \in \mathbb{Z}$, with the primitive reciprocal lattice basis $\mathbf{b}_i$ satisfying the condition

$$\mathbf{b}_i \mathbf{a}_j = 2\pi \delta_{ij} \tag{2.40}$$

with respect to the real-space lattice basis $\mathbf{a}_j$ [55–57].

2.5.2 Expansion into Plane Waves

Since the functions $u_k(\mathbf{r})$ of the bloch waves $\psi_k(\mathbf{r})$ (2.36) are periodic, they can be expanded into a set of plane waves:

$$u_k(\mathbf{r}) = \sum_{\mathbf{G}} c_{\mathbf{G}}^{\mathbf{k}} e^{i\mathbf{G}\mathbf{r}}. \tag{2.41}$$

This gives for $\psi_k(\mathbf{r})$:

$$\psi_k(\mathbf{r}) = u_k(\mathbf{r})e^{i\mathbf{k}\mathbf{r}} = \sum_{\mathbf{G}} c_{\mathbf{G}}^{\mathbf{k}} e^{i(\mathbf{k}+\mathbf{G})\mathbf{r}}. \tag{2.42}$$

Using this form for $\psi_k(\mathbf{r})$, inserting it into the Schrödinger equation (2.35), multiplying from the left with $\exp[-i(\mathbf{k} + \mathbf{G}')\mathbf{r}]$ and integrating over $\mathbf{r}$, gives:

$$\sum_{\mathbf{G}} \left[\frac{1}{2}|\mathbf{k} + \mathbf{G}|^2 \delta_{\mathbf{G},\mathbf{G}'} + V_{eff}(\mathbf{G}' - \mathbf{G}) \right] c_{\mathbf{G}}^{\mathbf{k}} = \epsilon_{\mathbf{k}} c_{\mathbf{G}}^{\mathbf{k}}. \tag{2.43}$$

The Kronecker delta $\delta_{\mathbf{G},\mathbf{G}'}$ denotes the orthonormality of the plane waves with respect to the reciprocal lattice vectors $\mathbf{G}$:

$$\delta_{\mathbf{G},\mathbf{G}'} = \int \psi_{\mathbf{G}}(\mathbf{r}) * \psi_{\mathbf{G}'}(\mathbf{r})d\mathbf{r} = \begin{cases} 1 & \text{if } \mathbf{G} = \mathbf{G}' \\ 0 & \text{if } \mathbf{G} \neq \mathbf{G}'. \end{cases} \tag{2.44}$$

For practical use, only such plane wave vectors $(\mathbf{k} + \mathbf{G})$ are kept, that give kinetic energies ϵ_{kin}, that are lower than a chosen cut-off energy E_{cut}:

$$\frac{1}{2}|\mathbf{k} + \mathbf{G}|^2 = \epsilon_{kin} \leq E_{cut}. \tag{2.45}$$

The cut-off energy has to be carefully chosen to be large enough to achieve convergence for the intended calculations [56, 57].

2.5.3 K-point Sampling

By employing Bloch's Theorem, the problem of calculating the eigenstates of an infinite number of electrons extended infinitely in space is reduced to calculating

eigenstates of a finite number of electrons at an infinite number of k-points in a single unit cell in k-space ($\hat{=}$ reciprocal space).

This problem is solved by assuming, that the electronic wave functions are almost identical at k-points, which are very close to each other. Therefore, the wave function of a region in k-space can be represented by the wave function of one single k-point of this region. The 1st Brillouin zone (unit cell in k-space) now can be sampled by a regular mesh of k-points.

This simplifies the calculation of the electronic density $\rho(\mathbf{r})$ by approximating the integration over the 1st Brillouin zone by a sum over the N_{kpt} k-points:

$$
\rho(\mathbf{r}) = 2\frac{\Omega}{(2\pi)^3}\sum_j \int_{BZ} |\psi_{\mathbf{k}j}(\mathbf{r})|^2 \Theta(\epsilon_F - \epsilon_{\mathbf{k}j}) d^3\mathbf{k} =
$$
$$
= 2\frac{1}{N_{kpt}}\sum_j \sum_k f_{\mathbf{k}j}|\psi_{\mathbf{k}j}(\mathbf{r})|^2. \tag{2.46}
$$

Here $\Theta(\epsilon_F - \epsilon_{\mathbf{k}j})$ is a step-function which is either 1 for $\epsilon_{\mathbf{k}j} \leq \epsilon_F$ and zero for $\epsilon_{\mathbf{k}j} > \epsilon_F$ and $f_{\mathbf{k}j}$ are occupation numbers (which are either 1 ore zero for insulators or semiconductors). ϵ_F is the *Fermi energy*, which gives the energy of the highest occupied state in a quantum mechanical system at absolute zero point temperature [57].

In the present work, the Monkhorst-Pack Scheme [58] as implemented in the *Vienna ab-initio Simulation Package* (VASP) [59–63], was used to create equally spaced k-point meshes in the Brillouin zone:

$$
\mathbf{k} = \mathbf{b}_1\frac{n_1 + 0.5}{N_1} + \mathbf{b}_2\frac{n_2 + 0.5}{N_2} + \mathbf{b}_3\frac{n_3 + 0.5}{N_3}, \tag{2.47}
$$

with

$$
n_1 = 0, ..., (N_1 - 1)
$$
$$
n_2 = 0, ..., (N_2 - 1)
$$
$$
n_3 = 0, ..., (N_3 - 1)
$$

and the N_i being the numbers of subdivisions along each reciprocal lattice vector $\mathbf{b}_i$. Symmetry is used to map equivalent k-points onto each other, thereby reducing the

total number of k-points. k-point grids with an even number of subdivisions N_n are shifted of the Γ-point (center of the Brillouin zone with the reciprocal coordinates (000)).

For hexagonal lattices Gamma centered Monkhorst-Pack grids were preferred, as standard Monkhorst-Pack grids do not represent the full hexagonal symmetry:

$$\mathbf{k} = \mathbf{b}_1 \frac{n_1}{N_1} + \mathbf{b}_2 \frac{n_2}{N_2} + \mathbf{b}_3 \frac{n_3}{N_3}. \tag{2.48}$$

2.6 The Projector Augmented-Wave Method

For pure plane wave methods two major problems occur:

(1) Convergence is slow, as a large number of plane waves is needed in order to accurately describe the rapidly oscillating wave function close to the nuclei, whereas the fairly smooth part of the wave function in the bonding regions is easier to describe.

(2) Core and valence electrons are treated equally as nearly free electrons, which is not true for core electrons. The plane wave basis only yields good results for nearly free electrons (i.e. valence electrons) and results in wrong energies for the core electrons.

Different approaches have been developed to solve this problem (i.e. the pseudopotential method, the LAPW method or the PAW method). They all make use of the *Frozen-Core Approximation*. In this work, the *Projector Augmented-Wave Method*, developed by Blöchl [64], as implemented in the *Vienna ab-initio Simulation Package* (VASP) [65] has been used.

2.6.1 The Frozen-Core Approximation

The core electrons are considered as non-essential for the description of chemical bonding in a crystal. They are strongly localized at the nuclei and are less sensitive to their environment than the valence electrons. The chemical bonding is mainly described by the valence electrons. Thus, the core electron distribution basically is the same for atoms when placed in different chemical environments. Therefore, the

core electrons can be considered inert ("frozen") and the core electron distribution of the isolated atom can be kept for the atoms in a crystal [56, 57].

2.6.2 The Valence States and the Transformation Operator

In the PAW method pseudo (PS) wave functions $|\tilde{\psi}\rangle$ (The *bra-ket* or *Dirac notation* used here is explained in detail for example in Ref. [31]) are defined, which give the real all electron (AE) wave function $|\psi\rangle$ by a transformation $\boldsymbol{T}$ (nota bene: $|\psi\rangle$ meaning a full one-electron Kohn-Sham wave function, NOT a many-electron wave function.):

$$|\psi\rangle = \boldsymbol{T}|\tilde{\psi}\rangle. \tag{2.49}$$

This transformation operator $\boldsymbol{T}$ differs from identity by a sum over local, atom-centered contributions $\boldsymbol{T}_{\mathbf{R}}$:

$$\boldsymbol{T} = 1 + \sum_{\mathbf{R}} \boldsymbol{T}_{\mathbf{R}}, \tag{2.50}$$

with $\mathbf{R}$ indicating a specific atom center.

The operators $\boldsymbol{T}_{\mathbf{R}}$ act only within a specific spherical augmentation region – denoted $\Omega_{\mathbf{R}}$ – enclosing the atomic centers at $\mathbf{R}$. Therefore $|\tilde{\psi}\rangle$ is identical to $|\psi\rangle$ outside the augmentation region $\Omega_{\mathbf{R}}$:

$$|\psi\rangle = \boldsymbol{T}|\tilde{\psi}\rangle = \begin{cases} |\psi\rangle & \text{outside } \Omega_{\mathbf{R}} \\ \left(1 + \sum_{\mathbf{R}} \boldsymbol{T}_{\mathbf{R}}\right)|\tilde{\psi}\rangle & \text{within } \Omega_{\mathbf{R}}. \end{cases} \tag{2.51}$$

Both, the AE wave function $|\psi\rangle$ and the PS wave function $|\tilde{\psi}\rangle$ can be expanded into a set of partial waves, $|\phi_i\rangle$ and $|\tilde{\phi}_i\rangle$:

$$|\psi\rangle = \sum_i |\phi_i\rangle c_i \tag{2.52}$$

$$|\tilde{\psi}\rangle = \sum_i |\tilde{\phi}_i\rangle c_i, \tag{2.53}$$

where the c_i are identical and are given by:

$$c_i = \langle \tilde{p}_i | \tilde{\psi} \rangle. \tag{2.54}$$

The $\langle \tilde{p}_i |$ are projector functions localized within the augmentation region $\Omega_{\mathbf{R}}$ of the atom centers. There exists exactly one projector function $\langle \tilde{p}_i |$ for every $|\tilde{\phi}_i\rangle$, which are orthogonal:

$$\langle \tilde{p}_i | \tilde{\phi}_j \rangle = \delta_{ij}. \tag{2.55}$$

The AE wave function can now be expressed as follows:

$$|\psi\rangle = |\tilde{\psi}\rangle - \sum_i |\tilde{\phi}_i\rangle c_i + \sum_i |\phi_i\rangle c_i. \tag{2.56}$$

Comparing this expression with 2.50 and using 2.54 we get for the transformation operator $\boldsymbol{T}$:

$$\boldsymbol{T} = 1 + \sum_i \left(|\phi_i\rangle - |\tilde{\phi}_i\rangle \right) \langle \tilde{p}_i |. \tag{2.57}$$

2.6.3 The Core States

The core states are treated within the *Frozen-Core Approximation*. The values for density and energy of the core electrons are imported from all-electron calculations of the corresponding isolated atoms. The core states are expressed by:

$$|\psi^c\rangle = |\tilde{\psi}^c\rangle - |\tilde{\phi}^c\rangle + |\phi^c\rangle \tag{2.58}$$

similarly to the AE valence wave functions. $|\tilde{\psi}^c\rangle$ is a PS core wave function, $|\tilde{\phi}^c\rangle$ a "PS core partial wave" and $|\phi^c\rangle$ is an "AE core partial wave".

2.6.4 Expectation Values

Two ways are conceivable to obtain expectation values $\langle A \rangle$:

(1) Retransforming the PS wave functions to the AE wave functions via the relation $|\psi\rangle = \boldsymbol{T}|\tilde{\psi}\rangle$ and using the well known relation

$$\langle A \rangle = \sum_n f_n \langle \psi_n | \boldsymbol{A} | \psi_n \rangle. \tag{2.59}$$

(2) Using the PS wave functions directly to obtain the desired expectation value via

$$\langle A \rangle = \sum_n f_n \langle \tilde{\psi}_n | \boldsymbol{T}^\dagger \boldsymbol{A} \, \boldsymbol{T} | \tilde{\psi}_n \rangle, \tag{2.60}$$

resulting in a PS operator $\tilde{\boldsymbol{A}}$:

$$\tilde{\boldsymbol{A}} = \boldsymbol{T}^\dagger \boldsymbol{A} \boldsymbol{T} \tag{2.61}$$

A detailed description of how to calculate expectation values within the PAW method is given in Blöchls original work [64] and – for the implementation into VASP – in the article of Kresse and Joubert [65].

2.7 Equations of State

A thermodynamic **E**quation **of S**tate (EOS) is a function that maps certain state variables (variables that describe the current condition of a system, i.e. pressure p, temperature T, volume V, energy E) onto each other. In high-pressure chemistry the relation between volume V and pressure p is the most widely-used used, as these data are easily obtained from experiments. In computational chemistry the relation between energy E and volume V is preferred, as it can be easily calculated by using ab-initio electronic structure techniques.

Pressure-volume and energy-volume data can be interconverted by integration over volume and – respectively – differentiation with respect to volume:

$$E(V) = E_0 - \int p(V) dV \tag{2.62}$$

$$p(V) = \frac{\partial E(V)}{\partial V}. \tag{2.63}$$

Several forms of EOSs for solids have been proposed. One of the oldest EOSs is the Murnaghan EOS, developed in 1944 [66], which is still widely used. Many other EOSs have been developed over the years, among them the Birch EOS [67] and Vinet EOS [68, 69], which – together with the Murnaghan EOS – have been used in this thesis to map energy-volume data.

All EOS for solids are parameterized fits of $E(V)$ and $p(V)$, respectively, in terms of the ground state bulk modulus B_0 and its pressure derivative B_0'. The Bulk Modulus is the reciprocal of the compressibility and is defined as the pressure increase that is required to cause a given relative decrease in volume.

$$B = -V\frac{\partial p}{\partial V} \tag{2.64}$$

$$B' = \frac{\partial B}{\partial p} \tag{2.65}$$

From here on the following quantities are used: (1) the zero-pressure volume V_0, (2) the zero-pressure energy E_0, (3) the zero-pressure bulk modulus B_0 and (4) the pressure derivative of the zero-pressure bulk modulus B_0'. It should be kept in mind, that these quantities in principle are temperature dependent, but they are further on used as isothermal parameters.

2.7.1 Murnaghan Equation of State

The Murnaghan EOS is based on the assumption that the bulk modulus B varies linearly with the pressure p. It is derived by representing the bulk modulus B as a power series in pressure p and omitting all terms but the first two. The pressure dependency of the bulk modulus is then given by:

$$B(p) = B_0 + B_0'p + B_0''p^2 + Cp^3 + Dp^4 + ...$$
$$B(p) = B_0 + B_0'p. \tag{2.66}$$

By integration, employing the relations given in Eq. 2.62 and Eq. 2.64, one gets the term for $E(V)$:

$$E(V) = \left(\frac{B_0 V}{B_0'}\right)\left[\frac{\left(\frac{V_0}{V}\right)^{B_0'}}{B_0' - 1} + 1\right] - \frac{B_0 V_0}{(B_0' - 1)} + E_0. \tag{2.67}$$

2.7.2 Birch Equation of State

The Birch EOS was developed by postulating that at high pressures strain can not be assumed as infinitesimal and therefore be neglected. Therefore the strain energy is expanded in a Taylor series of the finite Eulerian strain f_E:

$$f_E = \frac{\left[\left(\frac{V_0}{V}\right)^{(2/3)} - 1\right]}{2}.$$ (2.68)

$E(V)$ is then given by:

$$E(V) = \left(\frac{9V_0 B_0}{16}\right) \left\{ (2f_E)^3 B_0' + (2f_E)^2 \left[6 - 4\left(\frac{V_0}{V}\right)^{\left(\frac{2}{3}\right)}\right]\right\} + E_0,$$ (2.69)

and the pressure dependency of the Bulk Modulus by:

$$B(p) = B_0(1 + f_E)^{\left(\frac{1}{2}\right)}[1 + (7 + 2a)f_E + 9af_E^2]$$ (2.70)

$$\text{with } a = \frac{3}{2}(B_0' - 4).$$

2.7.3 Vinet Equation of State

The Vinet EOS is a semiempiric relation of pressure p and volume V, which is determined from the measured isotherms for a wide variety of different kinds of solids, i.e. metallic, covalent, ionic and van der Waals solids. Its development stems from the discovery, that the isothermal EOS of metals has a simple universal form [70, 71] and is based on the assumption, that the compressional EOS of all classes of solids can be described by a universal function, which is scaled with the zero-pressure volume V_0, the isothermal bulk modulus B_0 and the pressure derivative of

the isothermal bulk modulus B_0'. The term for $E(V)$ for the Vinet EOS is given by:

$$E(V) = \left(\frac{9B_0V_0}{\eta}\right)\left\{1 - [1 - \eta(1-x)]\,e^{[\eta(1-x)]}\right\} + E_0 \qquad (2.71)$$

$$\text{with } x = \left(\frac{V}{V_0}\right)^{(1/3)} \text{ and } \eta = \left(\frac{3}{2}\right)(B_0' - 1).$$

The pressure dependency of the Bulk Modulus is:

$$B(p) = x^{-2}\left[1 + (\eta x + 1)(1 - x)\right]e^{[\eta(1+x)]}. \qquad (2.72)$$

2.7.4 Validity of the Murnaghan, Birch and Vinet Equation of State

The above given EOS are based on different assumptions and models. Therefore, the chosen EOS influences the results obtained from fitting E-V data. Generally, for small compressions, all three EOS, the Murnaghan, the Birch, and the Vinet EOS, give the same results. For larger compressions, the Vinet EOS is superior to the Birch EOS which in turn is superior to the Murnaghan EOS ([69, 72] and references therein). E_0 and V_0 are given quite accurately by all three EOS over a wide volume or pressure range, respectively. However, the values for B_0 and B_0' depend quite sensitively on the EOS employed and on the range of pressure or volume for which data points are available. B_0' has been reported to be subjected to uncertainties of 10% from fitting [73].

Vinet et al. [69] related, that the Vinet EOS predicts experimental p-V data quite accurately for NaCl and H_2, whereas the Murnaghan EOS fails for values of $\frac{V}{V_0}$ larger than 0.8. For NaCl a comparison of the Birch EOS is also presented. The Birch EOS gives reasonable values throughout the experimental data (up to $\frac{V}{V_0} = 0.7$), but still the results for the Vinet EOS are superior. *Hama* and *Suito* [72] conducted an encompassing study on the validity of various EOS by comparing them to theoretical results calculated by the APW method [74] and the quantum-statistical model proposed by *Kalitkin* and *Kuz'mina* [75]. As reference systems they used different solids with one or two atoms in the unit cell (Ne, Ar, Al, Cu, LiH

and MgO). They found, that *p-V* data were best represented by the Vinet EOS (for values of $\frac{V}{V_0}$ up to 0.3), followed by the Birch EOS ($\frac{V}{V_0}$ up to 0.4) and the Murnaghan EOS ($\frac{V}{V_0}$ up to 0.75). With regard to fits of *E-V* and *B-p* data the results are similar. The Vinet EOS gives the most accurate results up to large compressions, whereas the Birch and Murnaghan EOS are less successful.

2.7.5 Energy-Volume Data Evaluation

To obtain the ground state bulk modulus B_0 the volume was varied around the zero pressure volume V_0 and the calculated energies were fitted to the Murnaghan, Birch and Vinet EOS. The range used for this evaluations encompasses values for the lattice parameters a, b and c of $95\,\%$ to $102.5\,\%$ from the equilibrium values a_0, b_0 and c_0.

The complete *E-V* diagrams (no compressions larger than a reduction of the lattice parameters than $20\,\%$ was calculated) can be transformed easily to give enthalpy *H* versus pressure *p* diagrams. To obtain the pressure *p* from the *E-V* graph a simple numerical differentiation of a spline fit and the Murnaghan, Birch and Vinet EOS was employed: $p = -\frac{\partial E}{\partial V}$.

In equilibrium a system will adopt the structure with the lowest Gibbs free energy *G*. A phase transformation is therefore governed by the difference of Gibbs free energy:

$$\Delta G = \Delta E + p\Delta V - T\Delta S. \tag{2.73}$$

The contribution of the entropy is usually neglected, due to the small difference in entropy between solid-state crystal structures and the comparably larger changes of ΔH within $1\,\mathrm{GPa}$ of pressure change. Therefore,

$$\Delta H = \Delta E + p\Delta V \tag{2.74}$$

is a good measure to compare the relative thermodynamic stability of solid-state structures under pressure. The enthalpy *H* as a function of pressure *p* for every compound/modification was calculated via:

$$H = E + pV, \tag{2.75}$$

using the values of E and p, obtained from the respective fitting procedures of the E-V data. The reaction enthalpy ΔH_R was calculated according to the formalism:

$$nA + mB \rightarrow kC + lD$$
$$\Delta H_R = [kH_{(C)} + lH_{(D)}] - [nH_{(A)} + mH_{(B)}]. \qquad (2.76)$$

Here, n, m, k, and l denote stoichiometric factors and A, B, C, and D the educts and products of a reaction. Resulting from this formalism, exothermic reactions are characterized by $\Delta H_R \leq 0$ and endothermic reactions by $\Delta H_R \geq 0$.

2.8 Practical Calculations

Structural optimizations, total energies, and properties are calculated within *Density Functional Theory* (DFT) [37] (chapter 2.4, page 10), for which the *Vienna ab-initio Simulation Package* (VASP) was used. It combines the total energy pseudopotential method with a plane-wave basis set [59–62, 76]. The electron exchange and correlation energy is treated within the *Local Density Approximation* (LDA) [77] (chapter 2.4.3.1, page 13) and *Generalized Gradient Approximation* (GGA) [50, 78, 79] (chapter 2.4.3.3, page 15). The *Projector-Augmented-Wave* (PAW) method was employed [64, 65] (chapter 2.6, page 20). The cut-off energy for the expansion of the wave function into the plane wave basis is $500\,\text{eV}$. Residual forces are converged below $5 * 10^{-3}\,\text{eV}/\text{Å}$. The Brillouin-Zone integration is done via the Monkhorst-Pack scheme [58].

Structure optimizations are obtained through relaxation of all structural parameters, atomic positions as well as cell parameters. Details on the used k-point mesh as well as the calculated cell of the relevant structures of this thesis are listed in Table B1 in Appendix B. However, it has to be noted, that a wide selection of structures with composition M_3N_2 and $MSiN_2$ (M = Be, Mg, Ca, Sr, Ba) was computed and only the data for the structures ultimately discussed in this thesis are given in B1. In most cases, only transition pressures derived from GGA calculations are given. The choice of the GGA functional is based on the experience that it significantly better describes the relative energies of structures, especially when structures with different environments for the constituting atoms are concerned. As the calcu-

lated transition pressure p_t strongly depends on the calculated energy difference ΔE ($p_t = \frac{\partial E}{\partial V} \approx \frac{\Delta E}{\Delta V}$), p_t derived from GGA calculations give more accurate results than those derived from LDA calculations.

Demuth et al. [80] and Zupan et al. [81] found for α-quartz and stishovite, that L(S)DA calculations seriously underestimate ΔE (exp.: 0.51 - 0.54 eV (references in [80]); L(S)DA: 0.1044 eV [80]; -0.09 eV [81]; GGA: 0.6367 eV, 0.691 eV [80], 0.51 eV [81]). Zupan et al. even found in LSDA calculations an energetic preference of stishovite over α-quartz.

The transition pressure of α-quartz to stishovite has been experimentally determined to 7.2 to 7.5 GPa (references in [80, 81]). The calculated transition pressure from LDA calculations amounts to 1.3 GPa [80], whereas it amounts to 8.0 GPa [80] and 6.2 GPa [81], respectively, for GGA calculations. Similar results were obtained for the diamond to β-tin structure type transition in Si, which can be observed at 10.5 to 12.5 GPa (references in [81]). Zupan et al. [81] calculated p_t to 6.7 GPa within L(S)DA and to 9.2 GPa (PBE) and 10.6 GPa (PW91) within GGA.

Since target of this thesis is to study structures and structural transformations at high pressures, the GGA is the better choice in comparison to the LDA. Therefore, while all calculations were controlled within the LDA as well, all enthalpy differences and transition pressures given in this thesis are based on GGA calculations, if not noted otherwise.

3 Silicon Nitride Si$_3$N$_4$

Silicon nitride Si$_3$N$_4$, due to its extraordinary physical and chemical properties, is a very important ceramic material. Its combined hardness, exceptional chemical inertness, low density and high wear resistance render it a high-performance ceramic, which is used in many fields of technology. Its main applications are as a construction material for engine and turbine building, as it withstands temperatures up to 1400°C. This is attributed to the fact, that Si$_3$N$_4$ ceramics are encoated with a thin SiO$_2$ layer upon heating in air. Processing occurs mainly by injection or extrusion molding, slip casting or pressing combined with sintering (hot-press sintering, gas pressure sintering or pressure-less sintering) [82].

Three modifications of Si$_3$N$_4$ are known, two at ambient pressure, α-Si$_3$N$_4$ and β-Si$_3$N$_4$ [2, 3], and a high-pressure modification, γ-Si$_3$N$_4$ [4, 5]. α-Si$_3$N$_4$ and β-Si$_3$N$_4$ are three-dimensional networks of corner-sharing SiN$_4$ tetrahedra, whereas γ-Si$_3$N$_4$ exhibits the cubic spinel structure with tetrahedrally as well as octahedrally coordinated Si in a molar ratio 1 to 2. δ-Si$_3$N$_4$, appearing at 160 GPa and possessing a CaTi$_2$O$_4$-type structure, has been theoretically predicted [10].

To synthesize pure Si$_3$N$_4$ three processes are of major importance: (1) direct nitridation of silicon powder, carbothermic reduction of SiO$_2$ under N$_2$ or NH$_3$ atmosphere and (3) ammonolysis of SiCl$_4$ or SiH$_4$. Ammonolysis of reactive silicon compounds does not directly result in Si$_3$N$_4$ but intermediate silicon diimide "Si(NH)$_2$" is formed, which gives amorphous Si$_3$N$_4$ upon heating [82].

Regarding stability, below 1500°C the α-phase is favored, while above the β-phase is formed. α-Si$_3$N$_4$ transforms into β-Si$_3$N$_4$ at temperatures exceeding 1650°Ċ [2, 83]. A retransformation of β-Si$_3$N$_4$ into α-Si$_3$N$_4$ could not be observed, which is attributed to kinetic inhibition [82]. Due to the unobserved retransformation and frequent oxygen-impurity in α-Si$_3$N$_4$, it has been discussed, that α-Si$_3$N$_4$ does not constitute a true polymorph of Si$_3$N$_4$. However, today α-Si$_3$N$_4$ is generally accepted

as an independent Si$_3$N$_4$ modification [82]. γ-Si$_3$N$_4$ is synthesized from α-Si$_3$N$_4$, β-Si$_3$N$_4$ or amorphous Si$_3$N$_4$ at pressures between 10 to 13 GPa and at temperatures of 1600 to 1800° C [4, 5].

For the purpose of high-pressure studies on nitridosilicates the two phases of Si$_3$N$_4$ to be considered are β-Si$_3$N$_4$ and γ-Si$_3$N$_4$, since α-Si$_3$N$_4$ differs only within the error of the method used in this thesis in energy from β-Si$_3$N$_4$ [6] and solely either β-Si$_3$N$_4$ or γ-Si$_3$N$_4$ are obtained from high-pressure experiments.

3.1 Structure Optimization of β-Si$_3$N$_4$ and γ-Si$_3$N$_4$

The structures of β-Si$_3$N$_4$ (Figure 3.1) and γ-Si$_3$N$_4$ (Figure 3.2) were optimized within LDA and GGA.

β-Si$_3$N$_4$ crystallizes in the hexagonal space group $P6_3/m$ (no. 176) and is isotypic to phenakite Be$_2$SiO$_4$ [3]. Along [001] *sechser* and *vierer* ring channels penetrate the three-dimensional network of corner-sharing SiN$_4$ tetrahedra. Every N atom is connecting three Si atoms. Therefore, every SiN$_4$ tetrahedra is connected to eight other SiN$_4$ tetrahedra.

γ-Si$_3$N$_4$ crystallizes in $Fd\bar{3}m$ (no. 227) in the spinel structure [4, 5]. Si occupies half of the octahedral voids and $^1/_8{}^{\mathrm{th}}$ of the tetrahedral voids in the cubic close packing of N atoms, forming a dense network of SiN$_4$ tetrahedra and SiN$_6$ octahedra. Every SiN$_4$ tetrahedron is connected to 12 SiN$_6$ octahedra via common corners and every SiN$_6$ octahedron shares a common corner with six SiN$_4$ tetrahedra and a common edge with six SiN$_6$ octahedra.

Data on calculated bond lengths compared to the experimental data are given in Table 3.2. The calculated crystallographic data compared to experimental results are given in Appendix A. The results of the zero-pressure optimization of the crystal structures for both β- and γ-Si$_3$N$_4$ are in agreement with experimental values and previous calculations [4, 6]. For β-Si$_3$N$_4$ the calculated volume per formula unit Si$_3$N$_4$ differs by 1.5 % (LDA) and 1.7 % (GGA) from the experimentally found volume and are in good accordance with previously calculated data (Table 3.1).
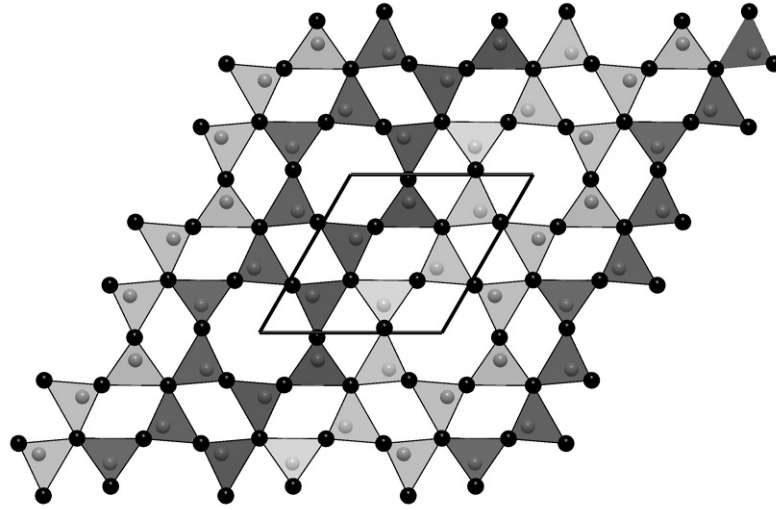
Figure 3.1: Crystal Structure of β-Si$_3$N$_4$, view along [001] (Si atoms are depicted dark gray, N atoms are depicted black, SiN$_4$ tetrahedra are drawn).
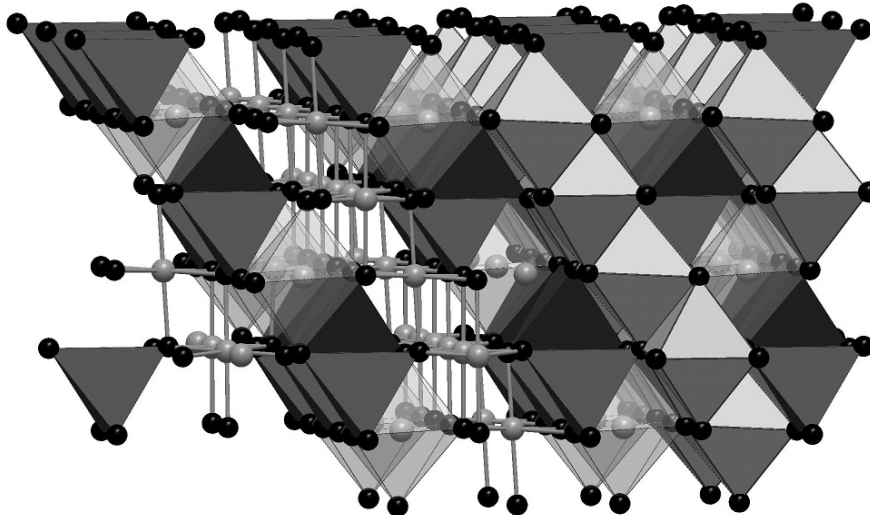
Figure 3.2: Crystal Structure of γ-Si$_3$N$_4$ (Si atoms are depicted gray, N atoms black, SiN$_4$ tetrahedra are drawn black, SiN$_6$ octahedra light gray).

Regarding γ-Si$_3$N$_4$, the calculated volumes are 1.7 % smaller (LDA) and 1.9 % larger (GGA) than the experimantal volume. An overview of calculated lattice parameters in comparison to the experimetal data as well as previously calculated data is given in Table 3.1.

Table 3.1: Comparrison of calculated and experimental lattice parameter of β-Si$_3$N$_4$ and γSi$_3$N$_4$.

β-Si$_3$N$_4$, $P6_3/m$, Z = 2			
V / 10^6 pm^3	c / pm	a / pm	Ref.
145.90	291.07	760.80	exp. [3]
146.42	291.02	762.20	[9]
146	291	761	[84]
142.70	288.52	755.75	[85]
142.68	/	/	[6]
147.76	/	/	[6]
143.74	289.14	757.65	this thesis (LDA)
148.43	292.38	765.63	this thesis (GGA)
γ-Si$_3$N$_4$, $Fd\bar{3}m$, Z = 8			
V / 10^6 pm^3	a / pm		Ref.
463.81	773.81		exp. [5]
481.34	783.7		[9]
467	776		[4]
452.64	767.8		[6]
469.52	777.2		[6]
468.8	776.8		[10]
455.64	769.50		this thesis (LDA)
472.02	778.62		this thesis (GGA)

The calculated Si-N bonds in β-Si$_3$N$_4$ are almost identical, as can be expected for solely Si[4]-N[3] bonds. They are in good agreement with the experimental values (see Table 3.2). For γ-Si$_3$N$_4$, the Si[6]-N bonds are longer than the Si[4]-N bonds, as is to be expected for an increased coordination number of Si. This corresponds well to the experimental findings (see Table 3.2).

Comparing the calculated densities of the two considered Si$_3$N$_4$ modifications to the experimental values, reveals that LDA overestimates the experimental density and GGA underestimates it, as can be expected from the corresponding volume under- and overestimation. Nevertheless, the density trend of γ-Si$_3$N$_4$ being denser than β-Si$_3$N$_4$ is correctly reproduced (β-Si$_3$N$_4$: 3.24 (LDA), 3.14 (GGA); γ-Si$_3$N$_4$: 4.09

Table 3.2: Bond lengths (in pm) in β-Si$_3$N$_4$ [3] and γ-Si$_3$N$_4$ [4, 5] compared to values for the optimized structures.

β-Si$_3$N$_4$	experimental	LDA	GGA
N1[3]-Si	175.12, 175.18	172.23	174.11
N2[3]-Si	171.95, 175.34	172.87, 172.98	174.63, 174.70
γ-Si$_3$N$_4$	experimental	LDA	GGA
Si[4]-N	180.51	176.49	178.61
Si[6]-N	186.26	186.84	189.04

(LDA), 3.95 (GGA) g cm$^{3\text{-}}$). Within both LDA and GGA, β-Si$_3$N$_4$ is lower in energy (-63.291 eV (LDA), -57.577 eV (GGA)) than γ-Si$_3$N$_4$ (-62.802 eV (LDA), -56.497 eV (GGA)) by 0.489 eV (LDA) and 1.080 eV (GGA), respectively.

The zero-pressure bulk moduli B_0 were calculated to 235 GPa and 293 GPa (GGA) for β-Si$_3$N$_4$ and γ-Si$_3$N$_4$, respectively, agreeing with experimental values (β-Si$_3$N$_4$: 256-273 GPa [86–89]; γ-Si$_3$N$_4$: 290-317 GPa [7, 8]) and being almost identical to the calculated bulk moduli reported by Kroll and Milko [6] (β-Si$_3$N$_4$: 234 GPa; γ-Si$_3$N$_4$: 292 GPa) and Zerr et al. [4] (γ-Si$_3$N$_4$: 300 GPa). Further calculated values for the bulk modulus for β-Si$_3$N$_4$ range from 263-297 GPa [9, 84, 90]. For γ-Si$_3$N$_4$ the bulk modulus was calculated to 280 GPa by Chiang et al. [9].

3.2 Energy-volume calculations of β-Si$_3$N$_4$ and γ-Si$_3$N$_4$

The energy-volume curves of β-Si$_3$N$_4$ and γ-Si$_3$N$_4$ are depicted in Figure 3.3, from which the enthalpy was extracted as a function of pressure as illustrated in Figure 3.4. Accordingly, the transition pressure p_t of β-Si$_3$N$_4$ into γ-Si$_3$N$_4$ was calculated to 11.5 GPa. This value of p_t agrees excellently with the experimentally observed transition pressures (10 - 13 GPa) [4, 5]. The results obtained for p_t from the different evaluations of the energy-volume data are virtually the same. The maximum difference in transition pressure amounts to 0.5 GPa.
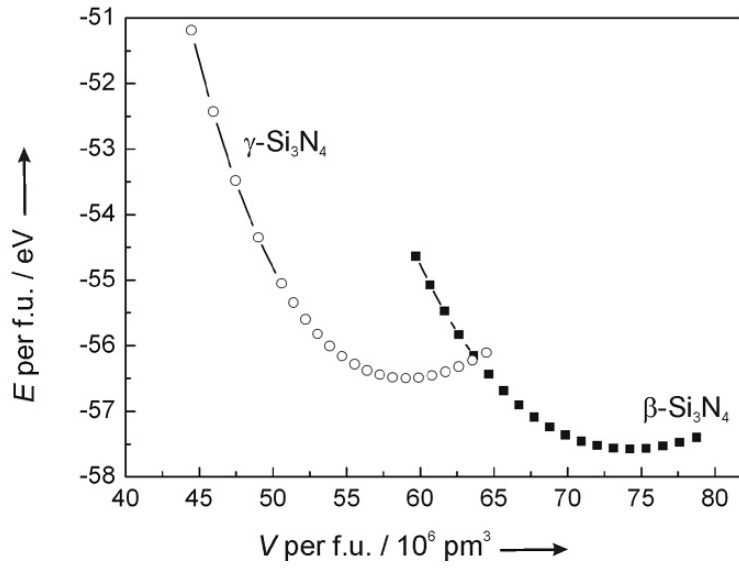
Figure 3.3: Energy-volume (E-V) phase diagram of β-Si$_3$N$_4$ and γ-Si$_3$N$_4$, calculated within the GGA. Each symbol represents a calculation.
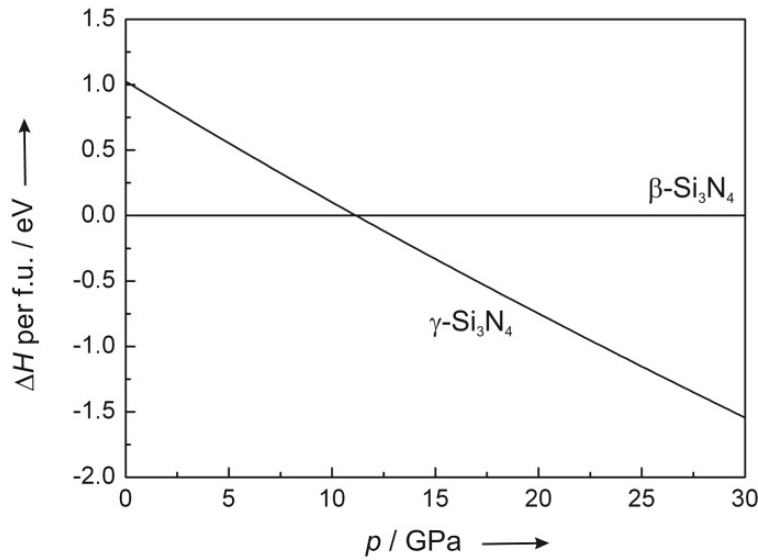
Figure 3.4: Enthalpy-pressure (H-p) diagram for the transition of β-Si$_3$N$_4$ into γ-Si$_3$N$_4$ (p$_t$ = 11.5 GPa) (derived from the evaluation of the E-V data by the Murnaghan EOS).

The data for Si$_3$N$_4$ are needed for examining the decomposition behavior under high pressure of different nitridosilicates. The phase transition of β-Si$_3$N$_4$ into γ-Si$_3$N$_4$ is taken into account for these decomposition reactions. Therefore, bellow the calculated transition pressure, the enthalpy H for β-Si$_3$N$_4$ is used; at higher pressures H for γ-Si$_3$N$_4$ is employed. Ignoring the phase transition of Si$_3$N$_4$ would lead to inaccurate results and wrong decomposition or formation pressures.

4 Nitrides M$_3$N$_2$ of group II elements

The binary nitrides of the group II elements M$_3$N$_2$ (M = Be, Mg, Ca, Sr, Ba) are known for over 100 years [91–94] and are applied in different areas of science and industry. They are widely used as starting materials for the synthesis of multinary nitrides or as flux in chemical syntheses [95–111]. In industry they find various applications, among others, as additives in the refinement process of steel [112–116], as sintering additives for AlN and Si$_3$N$_4$ [117–123] and as catalysts for the transformation of hexagonal into cubic BN [124–131]. Be$_3$N$_2$ and Mg$_3$N$_2$ are also discussed as materials used in combination with lithium-nitrogen compounds (e.g. LiN$_3$ and Li$_2$NH) for hydrogen storage [132–137]. An effective hydrogen storage system is strongly needed for the development of new hydrogen-based energy technologies, to render hydrogen a viable alternative to the increasingly scarce fossil fuels.

Two modifications of Be$_3$N$_2$ with established crystal structures are known. α-Be$_3$N$_2$ has been identified (together with α-Mg$_3$N$_2$ and α-Ca$_3$N$_2$) to crystallize in the cubic anti-bixbyite structure (corner- and edge-sharing BeN$_4$ tetrahedra) in 1933 [138]. The high-temperature modification β-Be$_3$N$_2$ exhibits a hexagonal structure consisting of BeN$_4$ tetrahedra and BeN$_3$ units and is obtained from α-Be$_3$N$_2$ at temperatures above 1400°C [139].

For Mg$_3$N$_2$ only the cubic anti-bixbyite modification has been unequivocally confirmed. Gladkaya et al. [140] investigated the temperature-pressure phase diagram of Mg$_3$N$_2$ in a range up to 1900 K and 1.5 to 9.0 GPa by *in situ* differential thermal analysis. They proposed six phases, of which two should be attainable from α-Mg$_3$N$_2$ upon heating at ambient pressure and three were obtained at temperatures exceeding 1000 K at high pressure. All phase transitions where reported as reversible and the HP- and/or HT-phases as not quenchable to ambient conditions.

No crystal structures where presented.

Three different structural modifications of Ca_3N_2 have been discussed in the literature: (1) α-Ca_3N_2 (maroon or yellow, cubic, synthesized at T $>$ 700 °C), (2) "β-Ca_3N_2" (black, hexagonal or tetragonal, synthesized at T $<$ 700 °C) and (3) HP/HT-Ca_3N_2 (orthorhombic, synthesized at 1800 °C and 46 kbar) [138, 141–143]. The true nature of "β-Ca_3N_2" has recently been questioned. It apparently is a Na-Ca-N compound, possibly a Na-Ca subnitride [144]. The description of the HP/HT-phase of Ca_3N_2 by Bradley et al. [143] is, unfortunately, the only reference addressing synthesis and characterization of this structure in the literature. The continuing interest in Ca-N compounds then is manifested in the recent synthesis of a new modification of Ca_3N_2 at 200 and 420 °C from the elements or from Ca_2N and N_2 by Höhn [145]. Careful structural characterization revealed a hexagonal (anti-corundum) structure. As a second phase of Ca_3N_2 established beyond doubts, this modification was termed β-Ca_3N_2.

The structures and true nature of Sr_3N_2 and Ba_3N_2 are yet unknown, even though these compounds have been first mentioned in 1892 by Maquenne [94]. In 1980 Künzel [146] proposed a defect NaCl-type structure for Ba_3N_2 but no further mentioning of this structure can be found in the literature. Even the existence of Sr_3N_2 and Ba_3N_2 has been questioned, as a multitude of binary Sr-N (Sr_2N [147], SrN [148], Sr_4N_3 [149], SrN_2 [148], $Sr(N_3)_2$ [150]) and Ba-N (Ba_3N [151], Ba_2N [152], Ba_3N_4 [153], BaN_2 [154], $Ba(N_3)_2$ [155]) compounds have been synthesized and characterized but still the binary nitrides M_3N_2 elude endeavors for characterization beyond any doubts.

The relation of α-M_3N_2 (M = Be, Mg, Ca) and β-Ca_3N_2 to the anti-structures of some sesquioxides motivates the search of potential high-pressure phases of M_3N_2 among the (anti-)HP-phases of M_2O_3-oxides which exhibit a very rich high-pressure chemistry. Recent advances in instrumentation and characterization have shown a tremendous amount of new discoveries. For example, Mn_2O_3, bixbyite, transforms into the post-perovskite structure ($CaIrO_3$-type) at 27 to 38 GPa [156]. Besides the post-perovskite structure type, the Rh_2O_3-II and the perovskite structure are also widely discussed high pressure candidates for several sesquioxides. Many binary oxides with a corundum structure at ambient pressure have been found to undergo phase transformations first into a Rh_2O_3-II structure, then further at even higher

pressures into a perovskite or post-perovskite modification [157–171]. Corundum (α-Al_2O_3) itself transforms into the Rh_2O_3-II-type structure at 80 to 100 GPa and is predicted to undergo a second phase transformation into the $CaIrO_3$-type structure at 131 to 156 GPa, which has been recently observed at 130 GPa. [157–167]. The higher homologue In_2O_3 has been predicted to exhibit a transformation from the bixbyite-type to Rh_2O_3-II-type structure at 10 GPa and further to post-perovskite at about 45 GPa [166, 172]. Most recent experiments confirm the prediction of the Rh_2O_3-II phase for both Ga_2O_3 and In_2O_3 [173]. Hematite (Fe_2O_3) exhibits both phase transformations, into a Rh_2O_3-II-type structure at 50 to 56 GPa and into a post-perovskite phase at 65 GPa [169–171].

4.1 Optimized Structures and Energy-Volume Calculations for M_3N_2 (M = Be, Mg, Ca, Sr, Ba)

About 20 structure types where considered as potential high-pressure phases for M_3N_2 (M = Be, Mg, Ca, Sr, Ba). Only those that proved to be of relevance for the enthalpy-pressure phase diagram are described here. For all optimized structures the coordination numbers of the M^{2+} ions were determined by calculating effective coordination numbers (ECoN) [174] with MAPLE [175–178] in order to compare them to the data for the experimentally determined structures (if available).

4.1.1 Be_3N_2

For Be_3N_2 three polymorphs were considered: (1) α-Be_3N_2 (cubic anti-bixbyite structure, space group $Ia\bar{3}$, no. 206) [179], (2) hexagonal β-Be_3N_2 (space group $P6_3/mmc$, no. 194) [139] and (3) γ-Be_3N_2, crystallizing in the anti-A-sesquioxide structure (space group $P\bar{3}m1$, no. 164) [180, 181] (Figure 4.1). In α-Be_3N_2 the Be atoms are tetrahedrally coordinated by N, whereas the N-atoms are octahedrally coordinated by Be. The structure is built up by a three-dimensional network of corner- and edge-sharing BeN_4-tetrahedra. For β-Be_3N_2 there exist two structural models, which differ in the position of one Be atom. Eckerlin and Rabenau [139] ascribe

this Be-atom to a fully occupied 2b position, whereas Hall et al. [182] refer to it as occupying a split-position on 4e. Thereby, the Be atom is deferred from the central position of a trigonal bipyramid (three N atoms at 164.03 pm and two at 242.32 pm) to a distorted tetrahedral environment (three N at 169.75 pm, one at 198.71 pm and one at 285.94 pm). For calculational convenience the structure originally proposed by Eckerlin and Rabenau was used. The anti-A-sesquioxide structure comprises layers of edge-sharing BeN_6 octahedra and BeN_4 tetrahedra double layers, which are stacked along [001] (Figure 4.1)

The average coordination number for Be in β-Be_3N_2 is 3.7 for Be and 5.5 for N, resulting in a coordination description of $Be_1^{[3]}Be_2^{[4]}N_1^{[5]}N_1^{[6]}$. The coordination numbers are increased for α-Be_3N_2 to CN(Be) = 4 and CN(N) = 6. A further increase is achieved for γ-Be_3N_2, where Be is averagely coordinated by 4.7 N atoms and N by seven Be ($Be_2^{[4]}Be_1^{[6]}N_2^{[7]}$).

The calculated bond lengths Be-N for α-Be_3N_2 and β-Be_3N_2 reproduce well the experimental data (see Table 4.1). In γ-Be_3N_2 the Be-N distances for four-fold coordinated Be are in the range of those in α- and β-Be_3N_2, whereas the distances for six-fold coordinated Be are about 20 pm longer, which can be explained by the increased coordination number (Table 4.1).

Referring to GGA calculations, α-Be_3N_2 exhibits the lowest energy of the three considered polymorphs (E = -33.483 eV per formula unit) and is 0.140 eV lower in energy than β-Be_3N_2 and 1.064 eV than γ-Be_3N_2. β-Be_3N_2 has still a 0.924 eV lower energy

Table 4.1: Bond lengths (in pm) in α-, β- and γ-Be_3N_2 compared to experimental values.

Structure	Bond type	LDA	GGA	exp.
α-Be_3N_2	$Be^{[4]}$-N	$168.51 - 176.95$	$170.05 - 179.53$	$172.45 - 181.55$ [179]
β-Be_3N_2	$Be^{[3]}$-N	162.68	164.43	164.03 [139]
	$Be^{[4]}$-N	$165.69 - 179.21$	$167.60 - 181.34$	$169.63 - 179.42$ [139]
γ-Be_3N_2	$Be^{[4]}$-N	$167.18 - 181.91$	$168.86 - 185.35$	/
	$Be^{[6]}$-N	198.33	201.08	/
Ionic Radii	bond type	Shannon [183]	Baur [184]	
	$Be^{[4]}$-$N^{[4]}$	173	/	
	$Be^{[4]}$-$N^{[6]}$	/	181	
	$Be^{[6]}$-$N^{[4]}$	191	/	

anti-bixbyite   β-Be₃N₂

anti-B-sesquioxid   anti-A-sesquioxid

β-Ca₃N₂ (anti-Al₂O₃)   anti-Rh₂O₃-II

hexagonal *P*6₃/*mmc*   anti-CaIrO₃
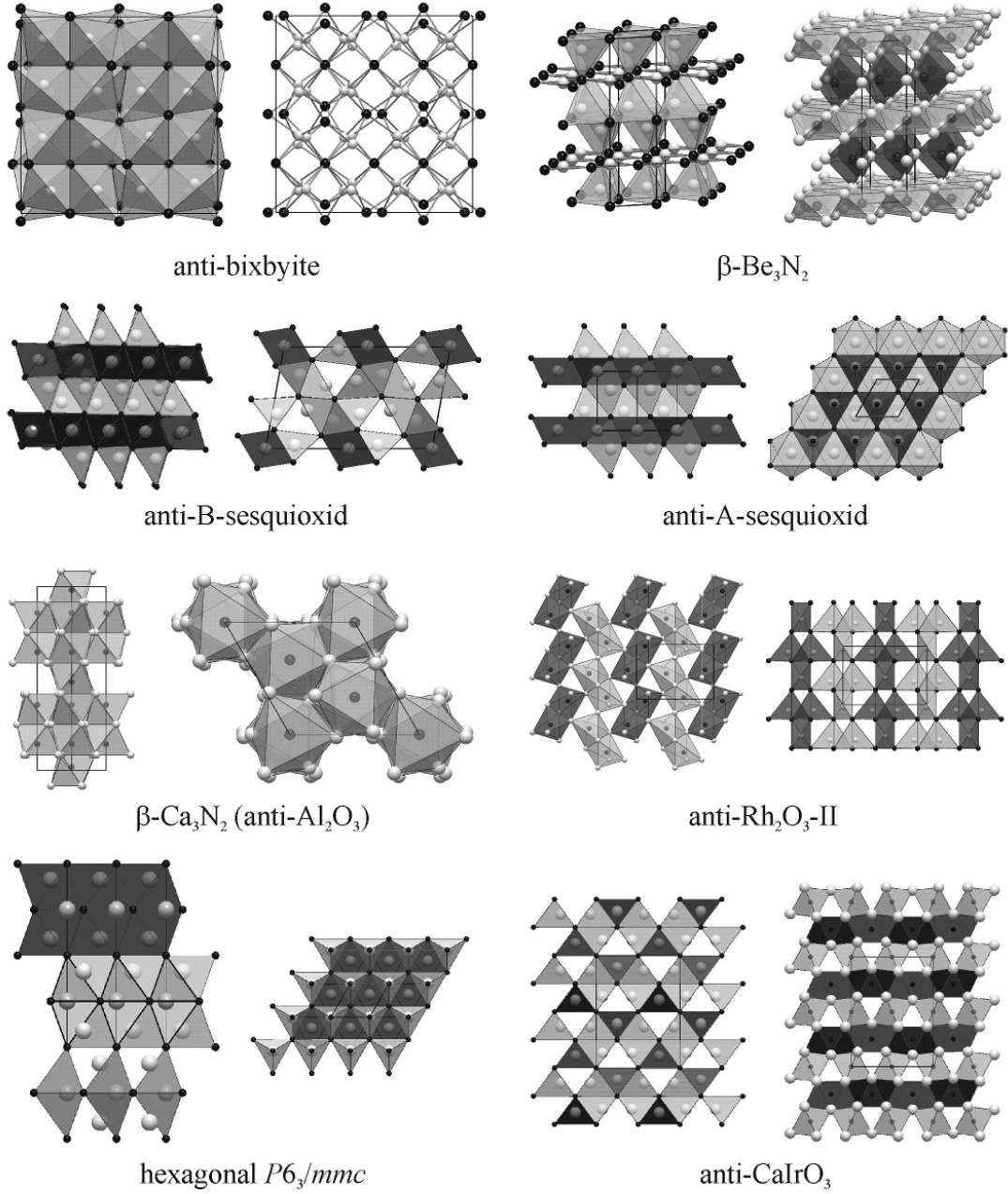
Figure 4.1: Crystal Structures of the different M_3N_2 structures: (1) anti-bixbyite (left: MN_4 tetrahedra drawn, right: ball-stick), (2) β-Be₃N₂ (left: BeN$_x$ polyhedra, right: NBe$_x$ polyhedra), (3) anti-B-sesquioxide (left: view along [$^1/_3$ 1 $^2/_3$], right: view along [010]), (4) anti-A-sesquioxide (left: view along [$^1/_2$ $^1/_2$ 0], right: view along [001]), (5) β-Ca₃N₂ (anti-Al₂O₃) (NCa₆ octahedra are drawn; left: view along [001], right: view along [-$^1/_2$ $^1/_2$ 0]), (6) anti-Rh₂O₃-II (right: NM₆ octahedra layer viewed along [001], right: MN_4 tetrahedra viewed along [010]), (7) hexagonal $P6_3/mmc$ (left: view along [$^1/_2$ $^1/_2$ 0], interpenetrating networks of corner-sharing MN₅ trigonal bipyramids and double-layers of face-sharing MN₆ octahedra, right: view along [001], MN₆ octahedra are depicted black, MN₅ trigonal bipyramids light gray), (8) anti-CaIrO₃ (view along [100], left: MN$_x$ polyhedra, right: NM$_x$ polyhedra) (M atoms are depicted light gray, N atoms black).

per formula unit than γ-Be_3N_2. This order is partly reversed with regard to density, as β-Be_3N_2 exhibits the lowest density ($\rho = 2.67\,\mathrm{g\,cm^{-3}}$, matching the experimental density of $2.70\,\mathrm{g\,cm^{-3}}$ [139]), with α-Be_3N_2 being $1.5\,\%$ and γ-Be_3N_2 $6.74\,\%$ denser (α-Be_3N_2: calculated density: $2.71\,\mathrm{g\,cm^{-3}}$, experimental density: $2.71\,\mathrm{g\,cm^{-3}}$ [179]; γ-Be_3N_2: calculated density: $2.85\,\mathrm{g\,cm^{-3}}$).

Calculations of α-Be_3N_2 and β-Be_3N_2 regarding their properties can be found in the literature [185–190], but no studies in their high-pressure behavior have been done yet. Data on the cell parameters as well as the calculated bulk moduli in comparison to the data calculated in this work and experimental data are listed in Table 4.2. In general, the data obtained in this work are in good agreement with previously published values.

Table 4.2: Comparison of previousliy calculated data for α- and β-Be_3N_2 compared to results of this thesis and experimental values.

α-Be_3N_2, $Ia\bar{3}$, Z = 16

V / 10^6 pm^3	a / pm		B$_0$ / GPa	Reference
542.34	815.5		257	[188]
540.15	814.4		254	[185]
542.54	815.6		217	[190]
529.48	809		/	[189]
540.39(1)	814.52		/	Exp. [179]
521.98	805.16		233	this thesis (LDA)
540.46	814.56		215	this thesis (GGA)

β-Be_3N_2, $P6_3/mmc$, Z = 2

V / 10^6 pm^3	a / pm	c / pm	B$_0$ / GPa	Reference
68.2	284.7	972.0	236	[188]
68.8	285.5	974.0	220	[190]
68.2	284.7	971.4	261	[186]
67.8	284.2	969.5	259	[186]
62.1	272.7	963.7	244	[187]
63.3	276.3	942.5	235	[187]
62.4	273.2	965.4	228	[187]
62.6	276.7	943.9	232	[187]
68.5	285.1	972.6	216	[187]
67.75	284.1	969.3	/	Exp. [139]
66.24	281.77	963.41	/	this thesis (LDA)
68.58	284.80	976.26	210	this thesis (GGA)

The complete computed crystallographic data of all Be_3N_2 polymorphs (as well as those for all further on presented crystal structures) together with the experimental data, if available, can be found in Appendix A.

The energy-volume data of α-, β- and γ-Be_3N_2 are depicted in Figure 4.3. Transformation into H-p data (Figure 4.4) shows, that only one high-pressure phase for Be_3N_2 comes into existence up to very high pressures. γ-Be_3N_2 is a high-pressure phase of α-Be_3N_2 and becomes lower in enthalpy at pressures exceeding 125 GPa. β-Be_3N_2 is no high-pressure phase of α-Be_3N_2. Neither is α-Be_3N_2 a high-pressure polymorph of β-Be_3N_2, but the transformation pressure of β- into γ-Be_3N_2 is calculated to 82 GPa. However, if γ-Be_3N_2, synthesized from β-Be_3N_2 at pressures between 82 and 125 GPa, can be observed, strongly depends on the kinetics of the retransformation of γ-Be_3N_2 into α-Be_3N_2, since α-Be_3N_2 is thermodynamically favored over γ-Be_3N_2 in this pressure range. All three phases and their interrelations are illustrated in Figure 4.2.
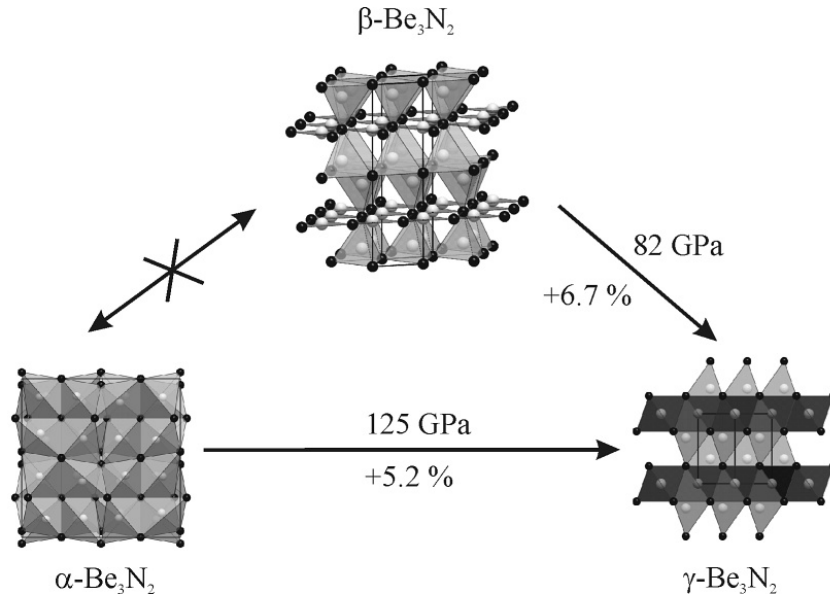
Figure 4.2: Sequence of structures of Be_3N_2 together with transition pressures and changes in density.
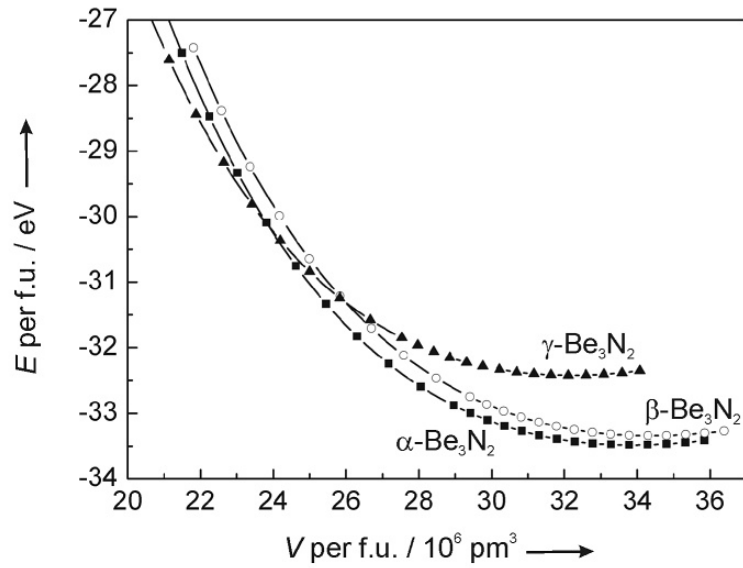
Figure 4.3: Energy-volume (E-V) phase diagram of α-, β- and γ-Be$_3$N$_2$, calculated within the GGA. Each symbol represents a calculation.
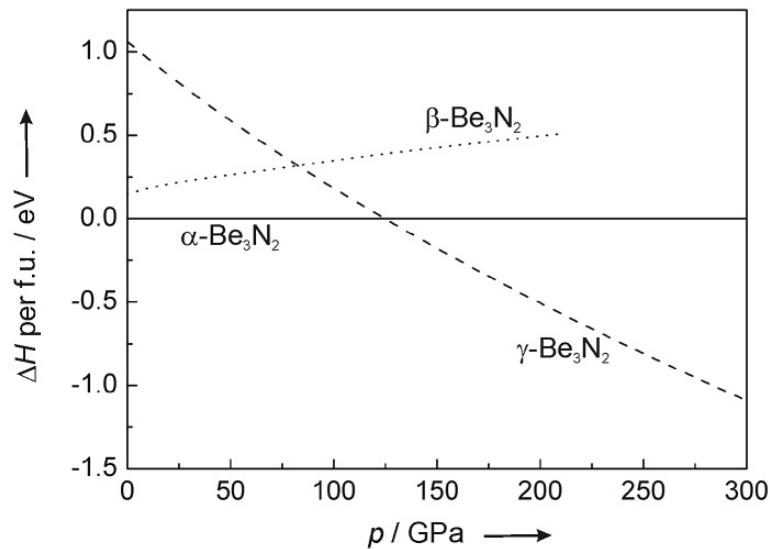
Figure 4.4: Enthalpy-pressure (H-p) diagram for the transition of α-Be$_3$N$_2$ into γ-Be$_3$N$_2$ (p$_t$ = 125 GPa) and for the transition of β-Be$_3$N$_2$ into γ-Be$_3$N$_2$ (p$_t$ = 82 GPa) (derived from the evaluation of the E-V data by the Murnaghan EOS).

4.1.2 Mg$_3$N$_2$

Besides α-Mg$_3$N$_2$ (cubic anti-bixbyite [144], see Figure 4.1) two more structure types proved to be of importance for the high-pressure behavior of Mg$_3$N$_2$. The first structure type, assigned to β-Mg$_3$N$_2$, is the monoclinic anti-B-sesquioxide structure (space group $C2/m$, no. 12) [191] (Figure 4.1). γ-Mg$_3$N$_2$ adopts an anti-A-sesquioxide-type structure (space group $P\bar{3}m1$, no. 164) [180, 181] (Figure 4.1). Both, the anti-bixbyite and the anti-A-sesquioxide structure have been described above (see chapter 4.1.1, page 41). The anti-B-sesquioxide structure exhibits three different coordinations for Mg: tetrahedral (67 %), quadratic pyramidal (22 %) and octahedral (11 %). The N atoms are either six- or seven-fold coordinated in a molar ratio of 1 to 2, resulting in a coordination representation of $Mg^{[4]}_{2/3}Mg^{[5]}_{2/9}Mg^{[6]}_{1/9}N^{[6]}_{1/3}N^{[7]}_{2/3}$. Average coordination numbers for Mg are increased in the row α-, β- to γ-Mg$_3$N$_2$ from 4 to 4.4 to 4.7. The coordination of N changes from octahedral (6) to an avarage 6.7 and further to 7.

The calculated distances Mg-N for α-Mg$_3$N$_2$ are in good accordance with those in experimental α-Mg$_3$N$_2$ [144] (compare Table 4.3). The distances for Mg$^{[4]}$-N in β-Mg$_3$N$_2$ and γ-Mg$_3$N$_2$ still match satisfactorily. Those for increased coordinations of Mg are longer, as can be expected (Table 4.3).

Table 4.3: Bond lengths (in pm) in α-, β- and γ-Mg$_3$N$_2$ compared to experimental values.

Structure	Bond type	LDA	GGA	exp.
α-Mg$_3$N$_2$	Mg$^{[4]}$-N	206.42 − 215.48	209.76 − 219.35	209.76 − 219.34 [144]
β-Mg$_3$N$_2$	Mg$^{[4]}$-N	200.47 − 234.66	204.36 − 240.83	/
	Mg$^{[5]}$-N	204.83 − 229.36	208.30 − 233.85	/
	Mg$^{[6]}$-N	226.84, 253.07	230.78, 258.94	/
γ-Mg$_3$N$_2$	Mg$^{[4]}$-N	203.39, 230.95	206.52, 237.36	/
	Mg$^{[6]}$-N	238.25	243.03	/
Ionic Radii	bond type	Shannon [183]	Baur [184]	
	Mg$^{[4]}$-N$^{[4]}$	203	/	
	Mg$^{[4]}$-N$^{[6]}$	/	214	
	Mg$^{[6]}$-N$^{[4]}$	218	/	
	Mg$^{[6]}$-N$^{[6]}$	/	220	

Within GGA, α-Mg_3N_2 exhibits the lowest energy per formula unit (-25.217 eV), with β-Mg_3N_2 having a higher energy by 0.443 eV per formula unit. γ-Mg_3N_2 is 0.661 eV higher in energy than α-Mg_3N_2 and 0.218 eV than β-Mg_3N_2. The order is preserved regarding density increasement. The lowest density is attributed to α-Mg_3N_2. The calculated density of 2.67 g cm^{-3} corresponds well to the experimental density of 2.71 g cm^{-3} [144]. β-Mg_3N_2 ($\rho = 2.83$ g cm^{-3}) comes out 6.0 % denser than α-Mg_3N_2 and for γ-Mg_3N_2 the density ($\rho = 2.85$ g cm^{-3}) is even augmented by 6.7 % with respect to α-Mg_3N_2 and by 0.7 % with respect to β-Mg_3N_2.

Comparing the calculated data for α-Mg_3N_2 of this thesis with previously published results for anti-bixbyite Mg_3N_2 reveals a good agreement (see Table 4.4).

Table 4.4: Comparison of previousliy calculated data for α-Mg_3N_2 compared to results of this thesis and experimental values.

α-Mg_3N_2, $Ia\bar{3}$, Z = 16			
V / 10^6 pm^3	a / pm	B_0 / GPa	Reference
958.0	985.8	165	[188]
1011.1	1003.7	111	[190]
985	995	/	[189]
990.31(7)	996.76(4)	/	Exp. [144]
952.86	984.03	122	this thesis (LDA)
1004.50	1001.50	109	this thesis (GGA)
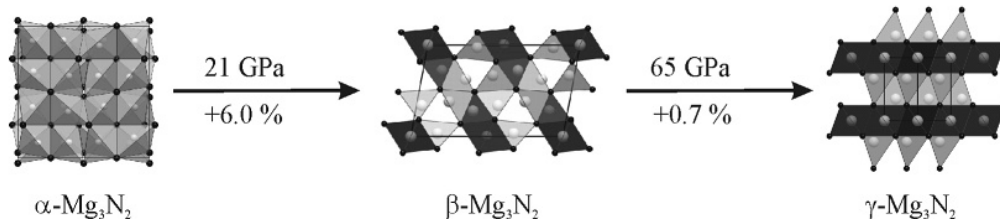
Figure 4.5: Sequence of structures of Mg_3N_2 together with transition pressures and changes in density.

Two high-pressure phases could be identified for Mg_3N_2. By converting the *E-V* data of Figure 4.6 into an *H-p* diagram (Figure 4.7) the transition pressure of α-Mg_3N_2 into β-Mg_3N_2 was calculated to 21 GPa. At pressures exceeding 65 GPa γ-Mg_3N_2 is
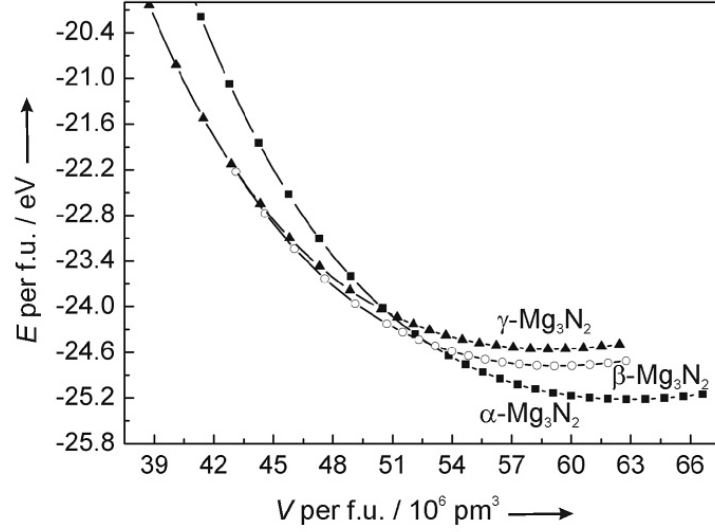
Figure 4.6: Energy-volume (E-V) phase diagram of α-, β- and γ-Mg_3N_2, calculated within the GGA. Each symbol represents a calculation.
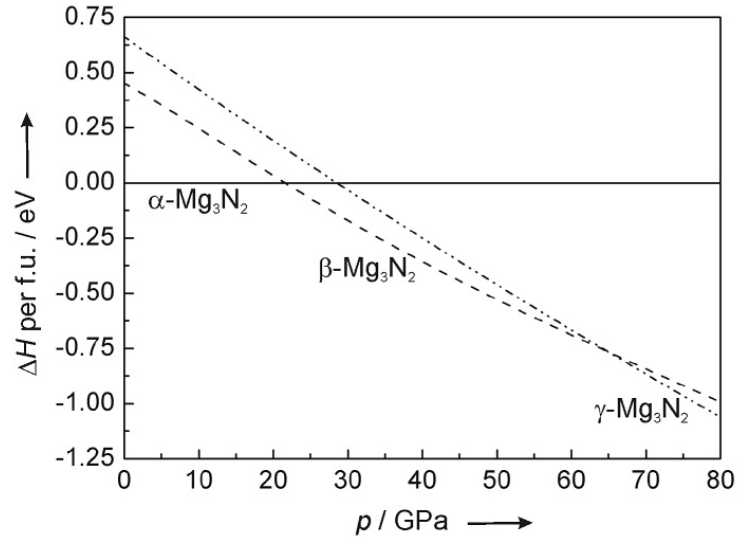
Figure 4.7: Enthalpy-pressure (H-p) diagram for the transition of α-Mg_3N_2 into β-Mg_3N_2 (p_t = 21 GPa) and into γ-Mg_3N_2 (p_t = 65 GPa) (derived from the evaluation of the E-V data by the Murnaghan EOS).

lower in enthalpy than β-Mg_3N_2 and will consequently form. Due to the gentle slope of the relative enthalpy curves, the transition pressure of β-Mg_3N_2 into γ-Mg_3N_2 has an uncertainty of about $2\,GPa$, as small deviations resulting from fitting with different EOSs lead to comparatively large changes in transition pressure. The three phases of Mg_3N_2 and their pressure relation are depicted in Figure 4.5.

4.1.3 Ca$_3$N$_2$

Six polymorphs prove to be relevant for being considered in the phase diagram of Ca_3N_2. α-Ca_3N_2 adopts an anti-bixbyite structure, space group $Ia\bar{3}$ (no. 206) [192] (Figure 4.1). β-Ca_3N_2 crystallizes in the trigonal space group $R\bar{3}c$ (no. 167) in the anti-Al_2O_3 structure [145] (Figure 4.1). The third candidate structure adopts an orthorhombic anti-Rh_2O_3-II structure, space group $Pbna$ (no. 60) [168] (Figure 4.1). Anticipating the results and the discussion, this polymorph was denoted as γ-Ca_3N_2. All these three structures comprise Ca atoms tetrahedrally coordinated by N, and N atoms in octahedral coordination by Ca. The fourth structure – denoted δ-Ca_3N_2 – exhibits the monoclinic anti-B-sesquioxide structure (space group $C2/m$, no. 12) [191] and the fifths structure – denoted ϵ-Ca_3N_2 – the trigonal anti-A-sesquioxide structure (space group $P\bar{3}m1$, no. 164) [180, 181] (Figure 4.1). In δ-Ca_3N_2 the coordination numbers of Ca and N are partially increased. Whereas in α-, β- and γ-Ca_3N_2 Ca is always tetrahedrally and N octahedrally coordinated ($Ca_3^{[4]}N_2^{[6]}$), in δ-Ca_3N_2 Ca exhibits a four-, five and six-fold coordination (tetrahedral, quadratic prismatical, octahedral) and N a six- and seven-fold coordination (octahedral and seven-fold), the coordination description being $Ca_{2/3}^{[4]}Ca_{2/9}^{[5]}Ca_{1/9}^{[6]}N_{1/3}^{[6]}N_{2/3}^{[7]}$. For ϵ-Ca_3N_2 coordination numbers are further increased to five (trigonal bipyramids) and six (octahedra) for Ca and eight for N (cubes) ($Ca_2^{[5]}Ca_1^{[6]}N_2^{[8]}$). Given the sequence of the anti-structures of bixbyite, corundum, and Rh_2O_3-II, yet another high-pressure phase with an anti-post-perovskite structure would be rational. But when compressing Ca_3N_2 in the anti-post-perovskite structure (space group $Cmcm$, no. 63) [193], a distortion towards a higher hexagonal symmetry was found. This fourth candidate structure, termed λ-Ca_3N_2, has been identified with space group $P6_3/mmc$ (no. 194) (Figure 4.1). It exhibits a hitherto undetected structure of Ca_3N_2 which is related to that of β-Be_3N_2 [139] (the Wyck-

off positions for M1, M2 and N1 are the same, but N2 occupies the 2d position in λ-Ca_3N_2 and the 2c position in β-Be_3N_2). λ-Ca_3N_2 exhibits partially increased coordination numbers for Ca and N compared to ϵ-Ca_3N_2. Whereas the coordination polyhedra of Ca remain unchanged, the molar ratio of CN = 5 to CN = 6 shifts from 2:1 to 1:2. N is now eight- and nine-fold coordinated.

For α-Ca_3N_2 the calculated crystallographic data were also compared to those of previous calculations [189, 190], which are in good accordance with the results of this thesis (compare Table 4.5).

Table 4.5: Comparison of previousliy calculated data for α-Ca_3N_2 compared to results of this thesis and experimental values.

α-Ca_3N_2, $Ia\bar{3}$, Z = 16			
V / 10^6 pm^3	a / pm	B_0 / GPa	Reference
1510.2	1147.3	170	[190]
1489	1142	/	[189]
1510.19(23)	1147.3(1)	/	Exp. [192]
1404.44	1119.87	79	this thesis (LDA)
1502.54	1154.36	68	this thesis (GGA)

The calculated bond lengths Ca-N of α-, β- and γ-Ca_3N_2 are all in the range of those in the experimentally determined structures for α-Ca_3N_2 [192] and β-Ca_3N_2 [145] and correspond well to the sum of the ionic radii (Table 4.6). For δ-Ca_3N_2, ϵ-Ca_3N_2 and λ-Ca_3N_2 the spread of bond lengths is larger with the longest Ca-N distances in λ-Ca_3N_2 being found for the two vertices of the CaN_5 trigonal bipyramids, which are substantially reduced under pressure.

Referring to our GGA-calculations at ambient pressure, α-Ca_3N_2 has the lowest energy of the four polymorphs (-26.728 eV per formula unit) and also the lowest density, $\rho = 2.62\,g\,cm^{-3}$ (exp. value $2.61\,g\,cm^{-3}$ [192]). β-Ca_3N_2 is only about 0.072 eV per formula unit higher in energy, but also about 2.3 % denser (computed $2.68\,g\,cm^{-3}$, matching exp. $2.68\,g\,cm^{-3}$ [145]). The density of γ-Ca_3N_2 ($\rho = 2.79\,g\,cm^{-3}$) is higher than that of both α- and β-Ca_3N_2, about 6.4 % and 4.0 %, respectively. The energy of γ-Ca_3N_2 in its ground state comes out 0.163 eV per formula unit higher with respect to α-Ca_3N_2. δ-Ca_3N_2 ($\rho = 2.79\,g\,cm^{-3}$) is 7.6 % denser than α-Ca_3N_2 and 1.1 % denser than γ-Ca_3N_2. Its ground-state energy lays 0.239 eV higher than that

Table 4.6: Bond lengths (in pm) in α-, β-, γ-,δ-,ϵ- and λ-Ca$_3$N$_2$ compared to experimental values.

Structure	Bond type	LDA	GGA	exp.
α-Ca$_3$N$_2$	Ca$^{[4]}$-N	240.53 − 241.37	245.38 − 246.86	245.16 − 248.38 [192]
β-Ca$_3$N$_2$	Ca$^{[4]}$-N	236.21 − 247.04	241.26 − 253.04	236.44 − 255.14 [145]
γ-Ca$_3$N$_2$	Ca$^{[4]}$-N	235.65 − 255.14	240.37 − 258.49	/
δ-Ca$_3$N$_2$	Ca$^{[4]}$-N	228.01 − 260.10	233.46 − 271.60	/
	Ca$^{[5]}$-N	230.58 − 263.67	234.95 − 270.90	/
	Ca$^{[6]}$-N	261.77, 271.28	267.73, 279.45	/
ϵ-Ca$_3$N$_2$	Ca$^{[4+1]}$-N	240.18 − 284.00	244.32 − 295.51	/
	Ca$^{[6]}$-N	264.45	272.40	/
ϵ'-Ca$_3$N$_2$	Ca$^{[4+1]}$-N	230.39 − 368.88	233.93 − 388.02	/
	Ca$^{[6]}$-N	267.14	273.16	/
λ-Ca$_3$N$_2$	Ca$^{[3+2]}$-N	221.07, 307.52	224.65, 329.66	/
	Ca$^{[6]}$-N	246.42, 297.20	251.77, 311.64	/
Ionic Radii	bond type	Shannon [183]	Baur [184]	
	Ca$^{[4]}$-N$^{[4]}$	/	242	
	Ca$^{[4]}$-N$^{[6]}$	/	246	
	Ca$^{[6]}$-N$^{[4]}$	246	251	
	Ca$^{[6]}$-N$^{[6]}$	/	255	

of α-Ca$_3$N$_2$ and 0.077 eV than that of γ-Ca$_3$N$_2$. ϵ-Ca$_3$N$_2$ then is the polymorph with the highest density we found. With $\rho = 2.99\,\mathrm{g\,cm^{-3}}$ it is about 14.1 % denser than α-Ca$_3$N$_2$, 7.2 % denser than γ-Ca$_3$N$_2$ and 5.7 % denser than δ-Ca$_3$N$_2$. Its energy lays 0.850 eV above that of α-Ca$_3$N$_2$ and 0.611 eV above that of δ-Ca$_3$N$_2$. Finally, λ-Ca$_3$N$_2$ is lower in density than ϵ-Ca$_3$N$_2$ by 4.7 %, but it is 8.6 % denser than α-Ca$_3$N$_2$ and still 2.1 % denser than γ-Ca$_3$N$_2$ and 1.1 % than δ-Ca$_3$N$_2$. The energy of λ-Ca$_3$N$_2$ is 0.980 eV per formula units higher than that of α-Ca$_3$N$_2$, and 0.130 eV per formula units higher than that of ϵ-Ca$_3$N$_2$. The zero-pressure bulk moduli at ambient pressure of the first three phases increase with increasing density from 68 GPa over 72 GPa to 73 GPa in the sequence of α-, β- and γ-Ca$_3$N$_2$. δ-Ca$_3$N$_2$ exhibits an equilibrium bulk modulus B$_0$ of 67 GPa, ϵ-Ca$_3$N$_2$ of 76 GPa and λ-Ca$_3$N$_2$ of 45 GPa. In Figure 4.9 the energy-volume curves of the six considered structures of Ca$_3$N$_2$ are shown. The E-V data were converted into the enthalpy-pressure phase diagram shown in Figure 4.10 by standard methods (see chapter 2.7.5).

With respect to enthalpy, it turns out that α-Ca$_3$N$_2$ is the most stable polymorph

of Ca_3N_2 for pressures up to 5 GPa, at which it will transform to γ-Ca_3N_2. β-Ca_3N_2 on the other hand does not appear as a valid high-pressure phase from these calculations, which refer to zero Kelvin temperature. Its appearance is likely due to entropy effects that impact the free enthalpy G at higher temperatures. Once γ-Ca_3N_2 is formed, it will remain stable up to about 10 GPa. At this pressure the monoclinic structure of δ-Ca_3N_2 becomes the most stable polymorph of Ca_3N_2. Reaching pressures exceeding 27 GPa, hexagonal ϵ-Ca_3N_2 is lower in enthalpy and will consequently form. Above 38 GPa, λ-Ca_3N_2 becomes lower in enthalpy.

In total, four new high-pressure phases of Ca_3N_2 are thus proposed. The sequence of structures together with transition pressures and density increases are illustrated in Figure 4.8.
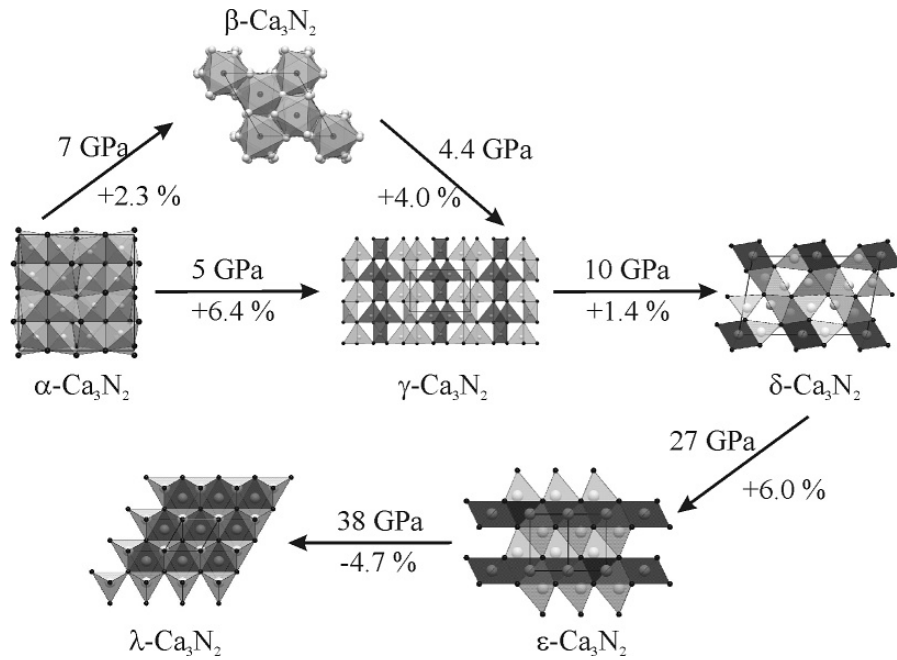
Figure 4.8: Sequence of structures of Ca_3N_2 together with transition pressures and changes in density.

4.1.4 Sr_3N_2

Four auspicious structures for the high-pressure phase diagram of Sr_3N_2 could be identified. The structure with the lowest energy, as for Be_3N_2, Mg_3N_2 and Ca_3N_2,
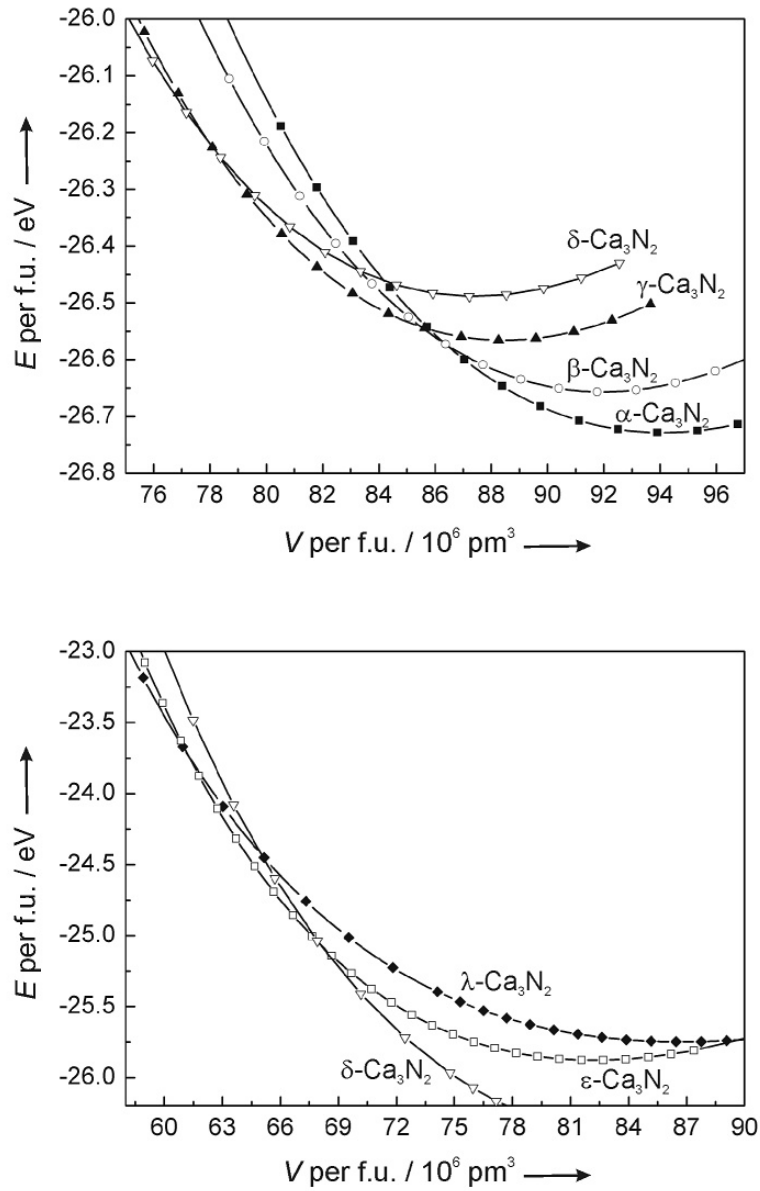
Figure 4.9: Energy-volume (E-V) phase diagrams of α-, β-, γ-, δ-, ϵ- and λ-Ca_3N_2, calculated within the GGA. Each symbol represents a calculation.
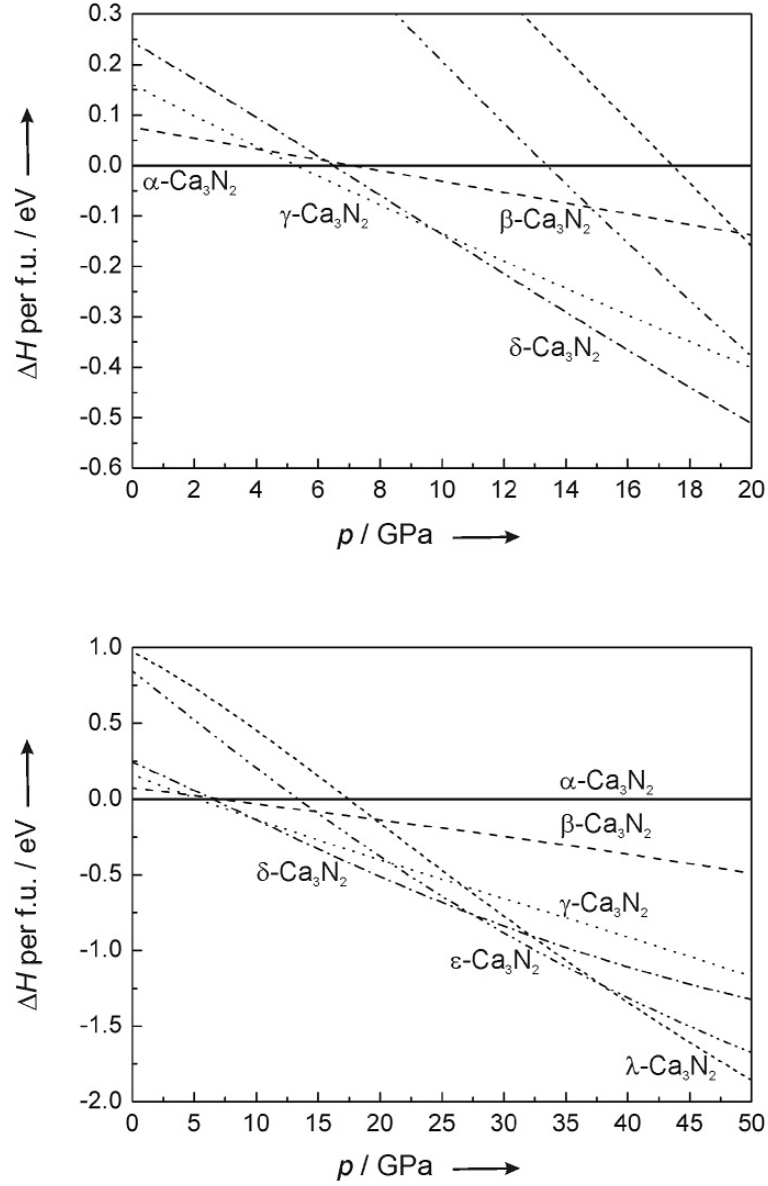
Figure 4.10: Enthalpy-pressure (H-p) diagrams for the transition of α-Ca_3N_2 into γ-Ca_3N_2 (p_t = 5 GPa), into δ-Ca_3N_2 (p_t = 10 GPa), into ϵ-Ca_3N_2 (p_t = 27 GPa) and into λ-Ca_3N_2 (p_t = 38 GPa) as well as for the transformation of β-Ca_3N_2 into γ-Ca_3N_2 (p_t = 4.5 GPa)(derived from the evaluation of the E-V data by the Murnaghan EOS).

was the cubic anti-bixbyite structure (Figure 4.1). Hence, this theoretical modification of Sr_3N_2 was termed α-Sr_3N_2. For β-Sr_3N_2 an anti-Rh_2O_3-II-type structure (space group *Pbna*, no. 60, see Figure 4.1) [168] was discerned. Both α-Sr_3N_2 and β-Sr_3N_2 are built up by SrN_4 tetrahedra, both corner- and edge-sharing. Nitrogen exhibits an octahedral coordination. As a third phase, denoted γ-Sr_3N_2, an anti-B-sesquioxide structure [191] was identified (Figure 4.1), with tetrahedral, quadratic pyramidal and octahedral coordination for Sr and six- and seven-fold coordination for N, resulting in a coordination description of $Sr_{2/3}^{[4]}Sr_{2/9}^{[5]}Sr_{1/9}^{[6]}N_{1/3}^{[6]}N_{2/3}^{[7]}$. Finally, the above described hexagonal $P6_3/mmc$ structure (see chapter 4.1.3, page 50 and Figure 4.1) was found to be promising under high-pressure and was therefore termed δ-Sr_3N_2. From α-, β- to γ- and δ-Sr_3N_2 coordination numbers are continuously increased for both Sr and N. In the order given above, Sr changes its coordination number from 4 to an average 4.4 and finally 5.7, while N goes from CN = 6 over 6.7 to 8.5.

The calculated distances Sr-N for all four Sr_3N_2 are listed in Table 4.7. They resemble quite well the Sr-N distances found in strontium nitridosilicates (examples given in Table 4.7).

For α-Sr_3N_2 the energy per formula unit was calculated to -24.422 eV and the density to 4.13 g cm^{-3}, referring to GGA calculations. β-Sr_3N_2 comes out 0.126 eV higher in energy and 6.7 % denser ($\rho = 4.41$ g cm^{-3}). γ-Sr_3N_2 exhibits a still 0.107 eV higher energy than β-Sr_3N_2 and 0.233 eV higher than α-Sr_3N_2. The density increase amounts to 0.8 % relative to β-Sr_3N_2 and to 7.6 % respecting α-Sr_3N_2, resulting in a density of 4.447 g cm^{-3}. δ-Sr_3N_2 then is the polymorph with the highest energy (0.956 eV higher than α-Sr_3N_2 and 0.723 eV higher than γ-Sr_3N_2) and density (4.454 g cm^{-3}). This renders it 7.8 % denser than α-Sr_3N_2 and at least 0.2 % denser than γ-Sr_3N_2. Orhan et al. [189] also calculated Sr_3N_2 (and Ba_3N_2) in the anti-bixbyite-type structure. Their results agree well with those of this work (c.f. Table 4.8). The energy-volume curves (Figure 4.12) and the enthalpy-pressure phase diagram derived thereof (Figure 4.13) revealed four phases of interest for the high-pressure behavior of Sr_3N_2. Three high-pressure phases of anti-bixbyite α-Sr_3N_2 were found. β-Sr_3N_2, which is lower in enthalpy than α-Sr_3N_2 at pressures exceeding 3 GPa, will remain the stable polymorph up to 12 GPa, when γ-Sr_3N_2 becomes lower in enthalpy. The transition pressure of β-Sr_3N_2 into γ-Sr_3N_2 has an uncertainty of

Table 4.7: Bond lengths (in pm) in α-, β-, γ- and δ-Sr_3N_2 compared to experimental values.

Structure	Bond type	LDA	GGA	exp.
α-Sr_3N_2	$Sr^{[4]}$-N	$256.56 - 260.81$	$262.76 - 266.76$	/
β-Sr_3N_2	$Sr^{[4]}$-N	$253.19 - 270.01$	$258.63 - 278.28$	/
γ-Sr_3N_2	$Sr^{[4]}$-N	$244.36 - 277.92$	$250.79 - 290.44$	/
	$Sr^{[5]}$-N	$245.93 - 285.49$	$250.90 - 294.91$	/
	$Sr^{[6]}$-N	$282.04 - 286.30$	$288.91 - 294.93$	/
γ'-Sr_3N_2	$Sr^{[3]}$-N	$243.37 - 248.99$	$248.79 - 254.74$	/
	$Sr^{[4]}$-N	$253.13 - 260.01$	$258.93 - 267.55$	/
	$Sr^{[5]}$-N	$254.85 - 284.32$	$262.27 - 293.18$	/
	$Sr^{[6]}$-N	$272.49 - 277.87$	$280.59 - 285.01$	/
δ-Sr_3N_2	$Sr^{[3+2]}$-N	$237.59, 331.12$	$241.54, 357.70$	/
	$Sr^{[6]}$-N	$265.16, 319.35$	$271.39, 336.27$	/
Nitridosilicates				
$SrSiN_2$ [14]	$Sr^{[9]}$-N	/	/	$256.29 - 340.65$
$Sr_2Si_5N_8$ [16]	$Sr^{[10]}$-N	/	/	$254.22 - 338.06$
Ionic Radii	bond type	Shannon [183]	Baur [184]	
	$Sr^{[6]}$-$N^{[4]}$	264	/	
	$Sr^{[7]}$-$N^{[6]}$	/	273	
	$Sr^{[7]}$-$N^{[8]}$	/	277	

Table 4.8: Comparison of previously calculated data for α-Sr_3N_2 and Ba_3N_2 in the anti-bixbyite structure compared to results of this thesis.

α-Sr_3N_2, $Ia\bar{3}$, Z = 16			
V / 10^6 pm^3	a / pm	B_0 / GPa	Reference
1834	1224	/	[189]
1737.08	1202.10	61	this thesis (LDA)
1869.73	1231.95	51	this thesis (GGA)
Ba_3N_2 bixbyite-type, $Ia\bar{3}$, Z = 16			
V / 10^6 pm^3	a / pm	B_0 / GPa	Reference
2331	1326	/	[189]
2086.70	1277.87	40	this thesis (LDA)
2279.23	1316.02	35	this thesis (GGA)

about 2 GPa, as the relative enthalpy curves exhibit similar slopes which effect a flat crossing. Therefore, the difference in enthalpy resulting from the use of different equations of state gives rise to a comparatively large divergence in transition pressure. Above 26 GPa δ-Sr_3N_2 becomes lower in enthalpy than γ-Sr_3N_2. The complete sequence of structures for anti-bixbyite-type Sr_3N_2 is shown in Figure 4.11.
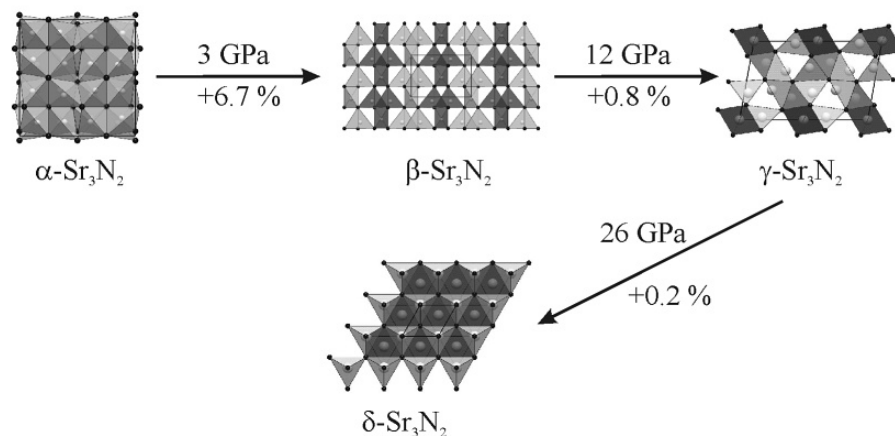
Figure 4.11: Sequence of structures of Sr_3N_2 together with transition pressures and changes in density.
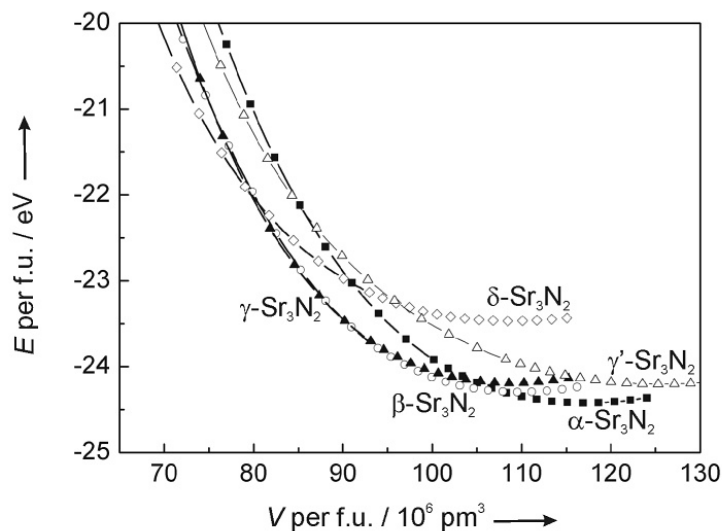
Figure 4.12: Energy-volume (E-V) phase diagram of α-, β-, γ-, γ'- and δ-Sr_3N_2, calculated within the GGA. Each symbol represents a calculation.
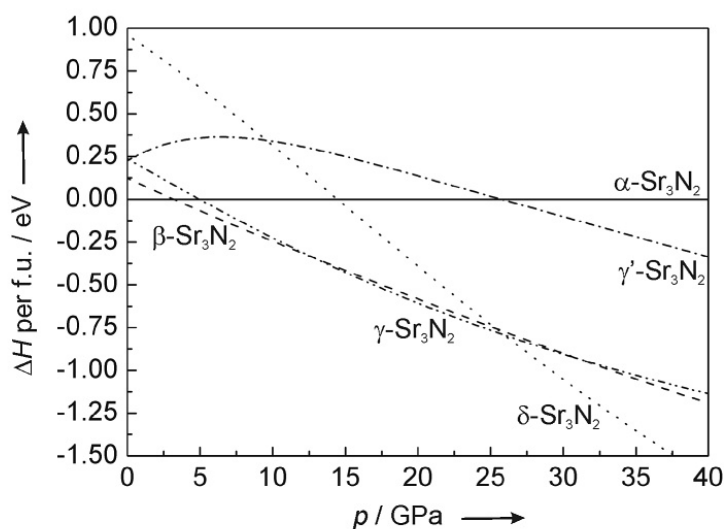
Figure 4.13: Enthalpy-pressure (H-p) diagram for the transition of α-Sr_3N_2 into β-Sr_3N_2 (p_t = 3 GPa), into γ-Sr_3N_2 (p_t = 12 GPa) and into δ-Sr_3N_2 (p_t = 26 GPa) (derived from the evaluation of the E-V data by the Murnaghan EOS).

4.1.5 Ba_3N_2

Four structure types were found to be of importance for the pressure enthalpy phase diagram of Ba_3N_2. Interestingly, Ba_3N_2 is the only alkaline earth nitride which has not the anti-bixbyite-type structure as its ground-state energy form. The anti-A-sesquioxide structure (Figure 4.1) [180, 181] comes out lower in energy (-24.422 eV compared to -24.272 eV within GGA). Therefore, the anti-A-sesquioxide-type Ba_3N_2 was termed α-Ba_3N_2. Noticeably, the c/a-ratio in this anti-A-sesquioxide-type structure is increased to 2.7 from the known 1.7 for rare earth oxides [180] and 1.2 for intermetallic compounds of the Ni_2Al_3-type [181]. Calculating Ba_3N_2 with fixed c/a-ratios of 1.7 and 1.2 leads to structures exhibiting internal pressure and with higher energies than the structure with c/a = 2.7 (c/a = 1.2: -23.204 eV; c/a = 1.7: -23.813 eV). The elongation of the c-axis with respect to the a-axis results in a change of coordination for the Ba atom occupying the originally tetrahedrally co-ordinated site to three. The structure thereby becomes a layered structure with BaN_6 octahedra layers, which are flanked on both sides by Ba atoms, coordinating solely to N atoms within the central layer. The coordination description of this

anti-"A-sesquioxide"-type structure is $Ba_2^{[3]}Ba_1^{[6]}N_2^{[6]}$.

β-Ba_3N_2 was identified to have an anti-Rh_2O_3-II structure [168] with tetrahedrally coordinated Ba and octahedrally coordinated N (Figure 4.1). The third structure found – termed γ-Ba_3N_2 – exhibits the anti-$CaIrO_3$ post-perovskite structure (Figure 4.1) [193]. Ba is either tetrahedrally or quadratically pyramidally coordinated by N, whereas N is octahedrally and eight-fold coordinated by Ba. The structure is built up by a three-dimensional network of edge-sharing BaN_5 quadratic pyramids which is interpenetrated by an equally three-dimensional network of corner-sharing BaN_4 tetrahedra. BaN_5 quadratic pyramids and BaN_4 tetrahedra share common edges ($Ba_1^{[4]}Ba_2^{[5]}N_1^{[6]}N_1^{[8]}$). The fourth relevant structure type is the above described hexagonal $P6_3/mmc$ structure (see chapter 4.1.3, page 50 and Figure 4.1), denoted δ-Ba_3N_2, which is related to the post-perovskite structure by a group-subgroup relation.

The calculated Ba-N distances are listed in Table 4.9 and are in the same range as those found in barium nitridosilicates.

Table 4.9: Bond lengths (in pm) in α-, β-, γ- and δ-Ba_3N_2 compared to experimental values.

Structure	Bond type	LDA	GGA	exp.
α-Ba_3N_2	$Ba^{[3]}$-N	259.22	265.11	/
	$Ba^{[6]}$-N	290.77	298.68	/
β-Ba_3N_2	$Ba^{[4]}$-N	$265.23 - 290.43$	$267.08 - 300.56$	/
γ-Ba_3N_2	$Ba^{[4]}$-N	$263.39 - 278.79$	$267.09 - 293.82$	/
	$Ba^{[5]}$-N	$268.92 - 342.14$	$273.54 - 363.44$	/
δ-Ba_3N_2	$Ba^{[3+2]}$-N	253.34, 341.35	257.27, 359.11	/
	$Ba^{[6]}$-N	284.07, 341.35	290.80, 359.11	/
Nitridosilicates				
$BaSiN_2$ [14]	$Ba^{[10]}$-N	/	/	$277.71 - 357.49$
$Ba_2Si_5N_8$ [16]	$Ba^{[10]}$-N	/	/	$267.70 - 341.79$
Ionic Radii	bond type	Shannon [183]	Baur [184]	
	$Ba^{[6]}$-$N^{[4]}$	281	/	
	$Ba^{[6]}$-$N^{[6]}$	/	290	
	$Ba^{[6]}$-$N^{[8]}$	/	294	

As aforementioned, α-Ba_3N_2 has the lowest energy, with β-Ba_3N_2 laying 0.189 eV higher in energy and being 18.6 % denser (α-Ba_3N_2: $\rho = 4.68\,\mathrm{g\,cm^{-3}}$; β-Ba_3N_2: $\rho =$

$5.55\,\mathrm{g\,cm^{-3}}$). γ-Ba_3N_2 is the densest polymorph ($\rho = 5.60\,\mathrm{g\,cm^{-3}}$). It is $19.7\,\%$ denser than α-Ba_3N_2 and $0.9\,\%$ denser than β-Ba_3N_2. Its energy is higher than that of α-Ba_3N_2 by $0.593\,\mathrm{eV}$ and by $0.404\,\mathrm{eV}$ than that of β-Ba_3N_2. δ-Ba_3N_2 has the highest energy of the four polymorphs, $1.074\,\mathrm{eV}$ higher than α-Ba_3N_2 and $0.481\,\mathrm{eV}$ higher than β-Ba_3N_2. However, with its density of $5.50\,\mathrm{g\,cm^{-3}}$ it is less dense than both β-Ba_3N_2 ($-0.9\,\%$) and γ-Ba_3N_2 ($-1.8\,\%$) but still denser than α-Ba_3N_2 by $17.5\,\%$.

For Ba_3N_2 the structure type with the lowest energy (α-Ba_3N_2) is the anti-"A-sesquioxide"-type structure, however exhibiting a significantly increased c/a-ratio of 2.7 (compare above page 59). Under pressure the c/a-ratio is gradually reduced. Up to $7\,\mathrm{GPa}$ c/a $= 2.7$ is favored, above c/a $= 1.7$ (similar to those of the rare earth oxides M_2O_3 [180]) becomes more favorable. At pressures exceeding $36\,\mathrm{GPa}$ the c/a-ratio is further reduced to 1.2 (similar to the intermetallic compounds, e.g. Ni_2Al_3 [181]) (compare Figure 4.15). However, the anti-"A-sesquioxide"-type structure is only stable up to $2\,\mathrm{GPa}$, when β-Ba_3N_2 will form, followed at about $32\,\mathrm{GPa}$ by γ-Ba_3N_2. At pressures above $52\,\mathrm{GPa}$ δ-Ba_3N_2 is lower in enthalpy than γ-Ba_3N_2. For both transitions β-Ba_3N_2 into γ-Ba_3N_2 and γ-Ba_3N_2 into δ-Ba_3N_2 the error resulting from employing different equations of state (EOS) amounts to about $2\,\mathrm{GPa}$ and $3\,\mathrm{GPa}$, respectively. In contrast to the two cases discussed above (see chapter 4.1.2, page 48 and 4.1.4, page 56), this error does not result from similar slopes of the enthalpy-pressure curves but is founded on the difficulties arising when fitting the calculated data points with the EOSs. Since the energy-volume curves are quite flat around V_0 an accurate fit of V_0 and E_0 taking all calculated data points into consideration was not feasible. Therefore, V_0 and E_0 were determined by only using the data points in a small range around V_0 and subsequently all data points where fitted with fixed V_0 and E_0. However, more or less large deviations from the calculated data occurred at larger compressions, depending on the EOS employed (a detailed example of these deviations is given in Appendix D).

All high-pressure phases of anti-"A-sesquioxide"-type Ba_3N_2 together with transition pressures are illustrated in Figure 4.14. The energy-volume curves and the enthalpy-pressure phase diagram are shown in Figure 4.16 and Figure 4.17.
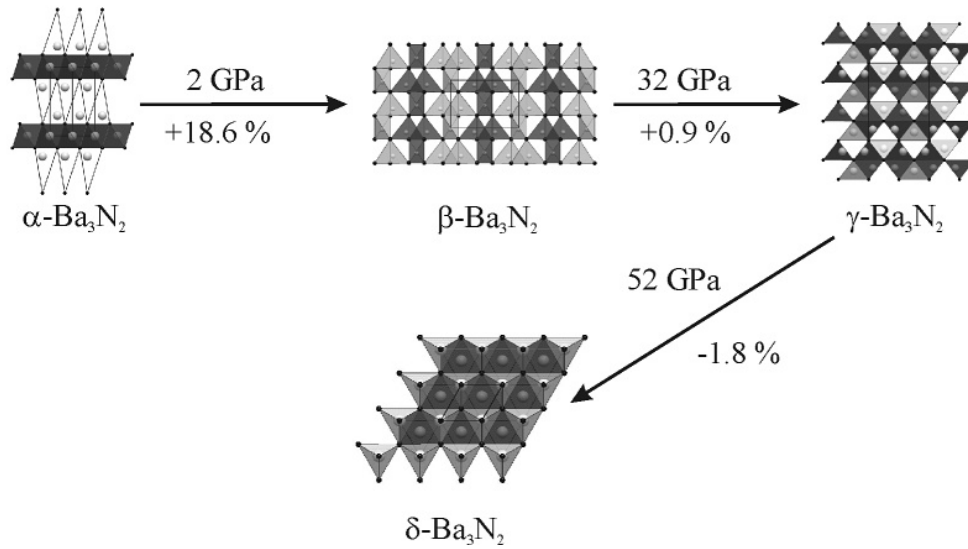
Figure 4.14: Sequence of structures of Ba_3N_2 together with transition pressures and changes in density.
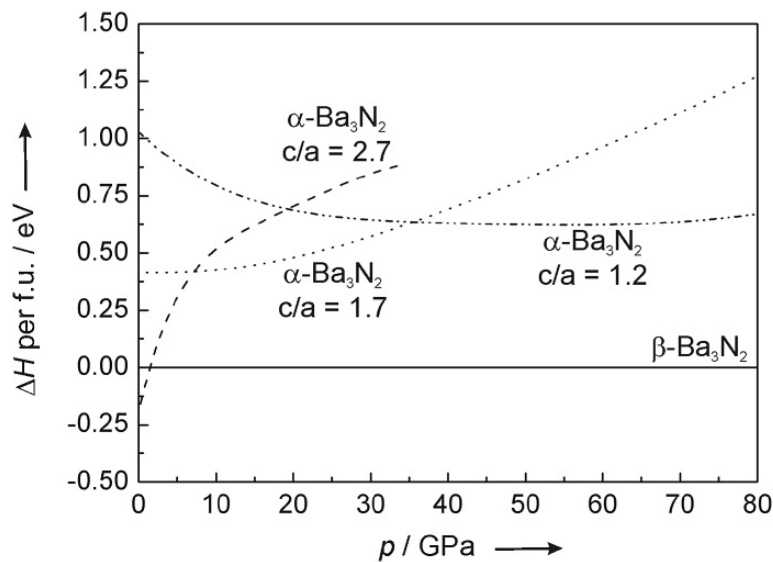
Figure 4.15: Enthalpy-pressure (H-p) diagram for α-Ba_3N_2 with different c/a-ratios (derived from the evaluation of the E-V data by the Murnaghan EOS).
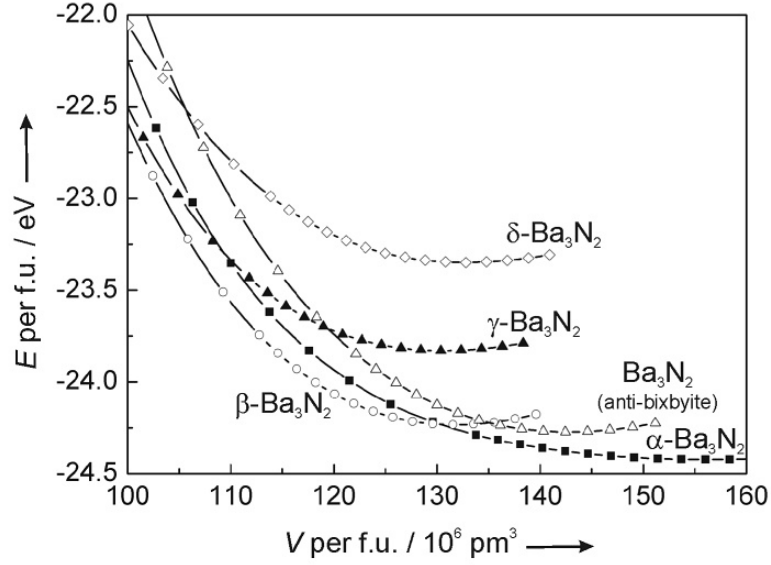
Figure 4.16: Energy-volume (*E-V*) phase diagram of α-, β-, γ- and δ-Ba$_3$N$_2$ as well as anti-bixbyite-type Ba$_3$N$_2$, calculated within the GGA. Each symbol represents a calculation.
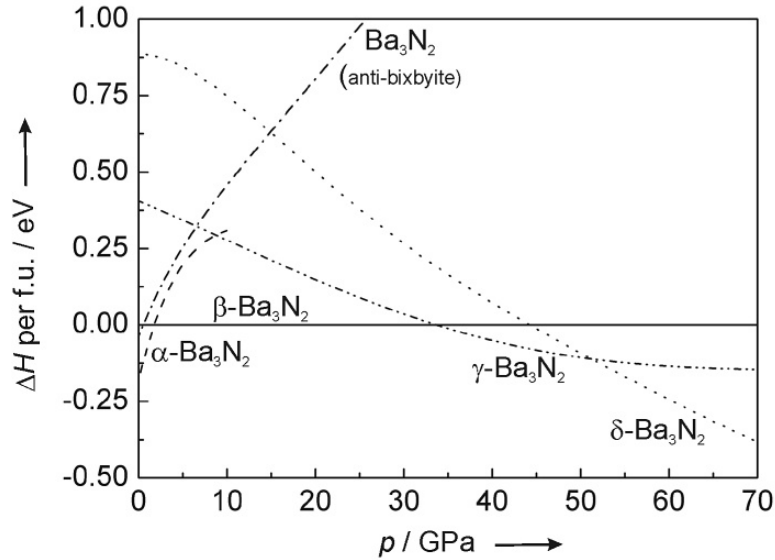
Figure 4.17: Enthalpy-pressure (*H-p*) diagram for the transition of α-Ba$_3$N$_2$ into β-Ba$_3$N$_2$ (p$_t$ = 2 GPa), into γ-Ba$_3$N$_2$ (p$_t$ = 32 GPa) and into δ-Ba$_3$N$_2$ (p$_t$ = 56 GPa) (derived from the evaluation of the *E-V* data by the Murnaghan EOS).

Table 4.10: E_0, V_0, B_0 and ρ_0 of α-, β- and γ-Be_3N_2 (E_0, V_0, B_0 given per formula unit).

	E_0 / eV	V_0 / 10^6 pm^3	B_0 / GPa	ρ_0 / g cm^{-1}
α-Be_3N_2	-33.483	33.78	215	2.71
β-Be_3N_2	-33.343	34.29	210	2.67
γ-Be_3N_2	-32.419	32.11	213	2.85

Table 4.11: E_0, V_0, B_0 and ρ_0 of α-, β- and γ-Mg_3N_2 (E_0 and V_0 given per formula unit).

	E_0 / eV	V_0 / 10^6 pm^3	B_0 / GPa	ρ_0 / g cm^{-1}
α-Mg_3N_2	-25.217	62.78	109	2.67
β-Mg_3N_2	-24.774	59.15	109	2.83
γ-Mg_3N_2	-24.556	58.83	104	2.85

Table 4.12: E_0, V_0, B_0 and ρ_0 of α-, β-, γ-, δ-, ϵ-, ϵ'- and λ-Ca_3N_2 (E_0 and V_0 given per formula unit).

	E_0 / eV	V_0 / 10^6 pm^3	B_0 / GPa	ρ_0 / g cm^{-1}
α-Ca_3N_2	-26.728	93.91	68	2.62
β-Ca_3N_2	-26.657	91.77	72	2.68
γ-Ca_3N_2	-26.566	88.26	73	2.79
δ-Ca_3N_2	-26.489	87.22	67	2.82
ϵ-Ca_3N_2	-25.878	82.35	76	2.99
ϵ'-Ca_3N_2	-26.261	88.29	67	2.79
λ-Ca_3N_2	-25.748	86.46	45	2.85

Table 4.13: E_0, V_0, B_0 and ρ_0 of α-, β-, γ-,γ'- and δ-Sr_3N_2 (E_0 and V_0 given per formula unit).

	E_0 / eV	V_0 / 10^6 pm^3	B_0 / GPa	ρ_0 / g cm^{-1}
α-Sr_3N_2	-24.422	116.86	51	4.13
β-Sr_3N_2	-24.296	109.52	55	4.41
γ-Sr_3N_2	-24.189	108.61	52	4.447
γ'-Sr_3N_2	-24.202	125.30	32	3.85
δ-Sr_3N_2	-23.466	108.44	34	4.454

Table 4.14: E_0, V_0, B_0 and ρ_0 of α-, β-, γ- and δ–Ba_3N_2 (E_0 and V_0 given per formula unit).

	E_0 / eV	V_0 / 10^6 pm^3	B_0 / GPa	ρ_0 / g cm^{-1}
α-Ba_3N_2	-24.422	156.03	10	4.68
β-Ba_3N_2	-24.233	131.55	44	5.55
γ-Ba_3N_2	-23.829	130.38	33	5.60
δ-Ba_3N_2	-23.348	132.79	31	5.50

4.2 Discussion

For Be_3N_2, Mg_3N_2 and Ca_3N_2 promising candidates for high-pressure phases have been identified and for Sr_3N_2 and Ba_3N_2, whose ambient condition crystal structures are yet unknown, zero-pressure ground state structures as well as high-pressure phases are proposed. For all compounds, except Be_3N_2, several high-pressure polymorphs appearing below 100 GPa were found. Be_3N_2, for which two ambient-pressure phases (α-Be_3N_2 (anti-C-sesquioxid $\hateq$ anti-bixbyite) and high-temperature β-Be_3N_2) are known, exhibits only one high-pressure phase, γ-Be_3N_2 (anti-A-sesqui-oxide), which is attainable from α-Be_3N_2 at 125 GPa and from β-Be_3N_2 at 82 GPa, if the retransformation of γ-Be_3N_2 into α-Be_3N_2 is sufficiently kinetically hindered. However, for rare earth sesquioxides, it has been frequently reported, that C→A (as well as the C→B) phase transformations are not easily reversible, as they are of first order (reconstructive phase transition) [194–198]. Therefore it may be assumed that γ-Be_3N_2 can be obtained from β-Be_3N_2 and quenched to ambient conditions. No pressure induced transformation of α-Be_3N_2 into β-Be_3N_2 and *vice versa* will take place according to the calculations.

Mg_3N_2 exhibits two phase transformations up to 100 GPa, the first occurring at 21 GPa (β-Mg_3N_2) and the second at 65 GPa (γ-Mg_3N_2). Both terminal units of the high-pressure phase sequences of Be_3N_2 and Mg_3N_2 exhibit the anti-A-sesquioxide-type structure with a c/a-ratio of about 1.7 (equivalent to the A-sesquioxide-type structure of the rare earth metal oxides [180]). Mg_3N_2 exhibits an intermediate anti-B-sesquioxide structure, which is related to the anti-A-sesquioxide structure by group-subgroup relation (compare Figure 4.18). The B→A phase transition has been classified as second order phase transformation (displacive phase transforma-

Table 4.15: Atom coordinates of β-Mg$_3$N$_2$ (B-sesquioxide structure [191]) and of γ-Mg$_3$N$_2$ (A-sesquioxide structure [180, 181]) in $C2/m$ setting (GGA and LDA calculation). Decimal numbers marked with [a] have fixed values for space group $P\bar{3}m1$ (e.g. 0.25 $\hat{=}$ 1/4), but could deviate from this value in space group $C2/m$.

atom	structure	Wyckoff-Position	x	y	z
Mg1	β-Mg$_3$N$_2$ LDA	4i	0.12317	0	0.28107
	β-Mg$_3$N$_2$ GGA		0.12250	0	0.28111
	γ-Mg$_3$N$_2$ LDA		0.16667[a]	0	0.33333[a]
	γ-Mg$_3$N$_2$ GGA		0.16667[a]	0	0.33333[a]
Mg2	β-Mg$_3$N$_2$ LDA	4i	0.32770	1/2	0.03116
	β-Mg$_3$N$_2$ GGA		0.32776	1/2	0.03094
	γ-Mg$_3$N$_2$ LDA		0.33031	1/2	0.00302
	γ-Mg$_3$N$_2$ GGA		0.33048	1/2	0.00286
Mg3	β-Mg$_3$N$_2$ LDA	4i	0.29010	0	0.37810
	β-Mg$_3$N$_2$ GGA		0.28967	0	0.37809
	γ-Mg$_3$N$_2$ LDA		0.33636	0	0.33031
	γ-Mg$_3$N$_2$ GGA		0.33619	0	0.33048
Mg4	β-Mg$_3$N$_2$ LDA	4i	0.46478	1/2	0.33560
	β-Mg$_3$N$_2$ GGA		0.46368	1/2	0.33487
	γ-Mg$_3$N$_2$ LDA		0.49698	1/2	0.33636
	γ-Mg$_3$N$_2$ GGA		0.49714	1/2	0.33619
Mg5	β-Mg$_3$N$_2$ LDA	2b	0	1/2	0
	β-Mg$_3$N$_2$ GGA		0	1/2	0
	γ-Mg$_3$N$_2$ LDA		0	1/2	0
	γ-Mg$_3$N$_2$ GGA		0	1/2	0
N1	β-Mg$_3$N$_2$ LDA	4i	0.13562	1/2	0.48614
	β-Mg$_3$N$_2$ GGA		0.13562	1/2	0.48725
	γ-Mg$_3$N$_2$ LDA		0.14106	1/2	0.52561
	γ-Mg$_3$N$_2$ GGA		0.14089	1/2	0.52578
N2	β-Mg$_3$N$_2$ LDA	4i	0.18964	1/2	0.13759
	β-Mg$_3$N$_2$ GGA		0.19012	1/2	0.13765
	γ-Mg$_3$N$_2$ LDA		0.19228	1/2	0.14106
	γ-Mg$_3$N$_2$ GGA		0.19244	1/2	0.14089
N3	β-Mg$_3$N$_2$ LDA	4i	0.46790	1/2	0.18128
	β-Mg$_3$N$_2$ GGA		0.49790	1/2	0.18104
	γ-Mg$_3$N$_2$ LDA		0.47439	1/2	0.19228
	γ-Mg$_3$N$_2$ GGA		0.47422	1/2	0.19244

tion) and for rare earth oxides it has been observed, that frequently the B→A transformation is reverted after the physical force (i.e. pressure or temperature) ceases to act on the sample [194, 195, 198, 199]. Therefore, for Mg$_3$N$_2$ probably only anti-B-sesquioxide-type Mg$_3$N$_2$ can be quenched to ambient conditions, whereas anti-A-sesquioxide-type Mg$_3$N$_2$ may be only observed *in situ*. In Table 4.15 the

atom coordinates of β- and γ-Mg$_3$N$_2$, both set in $C2/m$, are compared to further illustrate the relation between the two structures.
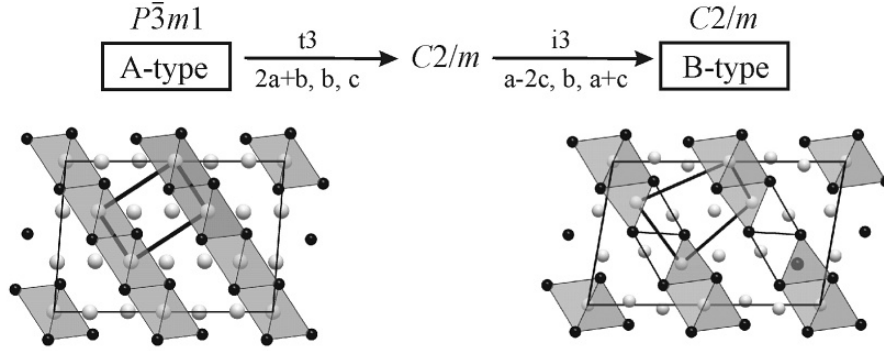
Figure 4.18: Group-subgroup relation of the A- and B-sesquioxide structure (The structure pictures feature the monoclinic unit cell of B-sesquioxide (thin black line) and of A-sesquioxide (thick black line).

Compared to Mg$_3$N$_2$, Ca$_3$N$_2$ exhibits two more high-pressure phases. An anti-Rh$_2$O$_3$-II phase (γ-Ca$_3$N$_2$) intermittently appears ere the anti-B-sesquioxide and the anti-A-sesquioxide-type structures come into existence. In contrast to Be$_3$N$_2$ and Mg$_3$N$_2$ the last high-pressure phase found for Ca$_3$N$_2$ is not the anti-A-sesquioxide structure but a novel hexagonal structure type (λ-Ca$_3$N$_2$) (for a description see chapter 4.1.3, page 50). A comparison of the atomic positions of anti-B-sesquioxide and anti-A-sesquioxide-type Ca$_3$N$_2$ (δ- and ϵ-Ca$_3$N$_2$) in $C2/m$ setting, elucidating the relationship of the two structure types as above for β/γ-Mg$_3$N$_2$, is given in Table 4.16.

According to the calculations, α-Ca$_3$N$_2$ will be stable up to 5 GPa. γ-Ca$_3$N$_2$ will come into existence between 5 and 10 GPa. Above 10 GPa, another high-pressure phase, δ-Ca$_3$N$_2$, becomes lower in enthalpy than γ-Ca$_3$N$_2$, easily accessible in today's high-pressure experimental set-ups. δ-Ca$_3$N$_2$ remains stable up to 27 GPa, when ϵ-Ca$_3$N$_2$ comes into existence, followed by λ-Ca$_3$N$_2$ above 38 GPa. This pressure range is still attainable in diamond anvil cell (DAC) experiments.

About 50 years ago, a high-pressure phase of Ca$_3$N$_2$ with orthorhombic structure has been mentioned by Bradley et al. [143]. It was synthesized at 4.6 GPa (and 1800 °C),

Table 4.16: Atom coordinates of δ-Ca_3N_2 (B-sesquioxide structure [191]) and of ϵ-Ca_3N_2 (A-sesquioxide structure [180, 181]) in $C2/m$ setting (GGA and LDA calculation). Decimal numbers marked with ^{a} have fixed values for space group $P\bar{3}m1$ (e.g. $0.16667 \,\hat{=}\, 1/6$), but could deviate from this value in space group $C2/m$.

atom	structure	Wyckoff-Position	x	y	z
Ca1	δ-Ca_3N_2 LDA	4i	0.12762	0	0.27897
	δ-Ca_3N_2 GGA		0.12567	0	0.27775
	ϵ-Ca_3N_2 LDA		0.16667^a	0	0.33333^a
	ϵ-Ca_3N_2 GGA		0.16667^a	0	0.33333^a
Ca2	δ-Ca_3N_2 LDA	4i	0.32764	1/2	0.03494
	δ-Ca_3N_2 GGA		0.32800	1/2	0.03518
	ϵ-Ca_3N_2 LDA		0.34008	1/2	-0.00674
	ϵ-Ca_3N_2 GGA		0.33881	1/2	-0.00548
Ca3	δ-Ca_3N_2 LDA	4i	0.29041	0	0.37822
	δ-Ca_3N_2 GGA		0.28073	0	0.37949
	ϵ-Ca_3N_2 LDA		0.32659	0	0.34008
	ϵ-Ca_3N_2 GGA		0.32768	0	0.33881
Ca4	δ-Ca_3N_2 LDA	4i	0.47058	1/2	0.34129
	δ-Ca_3N_2 GGA		0.46826	1/2	0.33945
	ϵ-Ca_3N_2 LDA		0.50674	1/2	0.32659
	ϵ-Ca_3N_2 GGA		0.50548	1/2	0.32786
Ca5	δ-Ca_3N_2 LDA	2b	0	1/2	0
	δ-Ca_3N_2 GGA		0	1/2	0
	ϵ-Ca_3N_2 LDA		0	1/2	0
	ϵ-Ca_3N_2 GGA		0	1/2	0
N1	δ-Ca_3N_2 LDA	4i	0.14105	1/2	0.48721
	δ-Ca_3N_2 GGA		0.14539	1/2	0.48828
	ϵ-Ca_3N_2 LDA		0.14646	1/2	0.52021
	ϵ-Ca_3N_2 GGA		0.14539	1/2	0.52128
N2	δ-Ca_3N_2 LDA	4i	0.18231	1/2	0.13116
	δ-Ca_3N_2 GGA		0.18256	1/2	0.13023
	ϵ-Ca_3N_2 LDA		0.18688	1/2	0.14646
	ϵ-Ca_3N_2 GGA		0.18794	1/2	0.14539
N3	δ-Ca_3N_2 LDA	4i	0.46954	1/2	0.18805
	δ-Ca_3N_2 GGA		0.46936	1/2	0.18775
	ϵ-Ca_3N_2 LDA		0.47979	1/2	0.18688
	ϵ-Ca_3N_2 GGA		0.47872	1/2	0.18794

which matches the transition pressure we computed for α-Ca_3N_2 into γ-Ca_3N_2 very closely. The cell parameters reported at that time, however, do not agree with the data propose for γ-Ca_3N_2. Nevertheless, this concurrence strongly motivates experiments designated to elucidate the high-pressure behavior of Ca_3N_2.

A constant increase in density is attained by each phase transition up to ϵ-Ca_3N_2,

but remarkably, at ambient pressure, λ-Ca_3N_2 is lower in density than ϵ-Ca_3N_2, although λ-Ca_3N_2 will be attained at higher pressure than ϵ-Ca_3N_2. At first sight, this finding is counterintuitive for a high-pressure phase, as one expects high-pressure phases to be denser then the corresponding low pressure phase. But when examining the density development under pressure, one finds, that λ-Ca_3N_2 becomes denser than ϵ-Ca_3N_2 above 11 GPa (Figure 4.19).
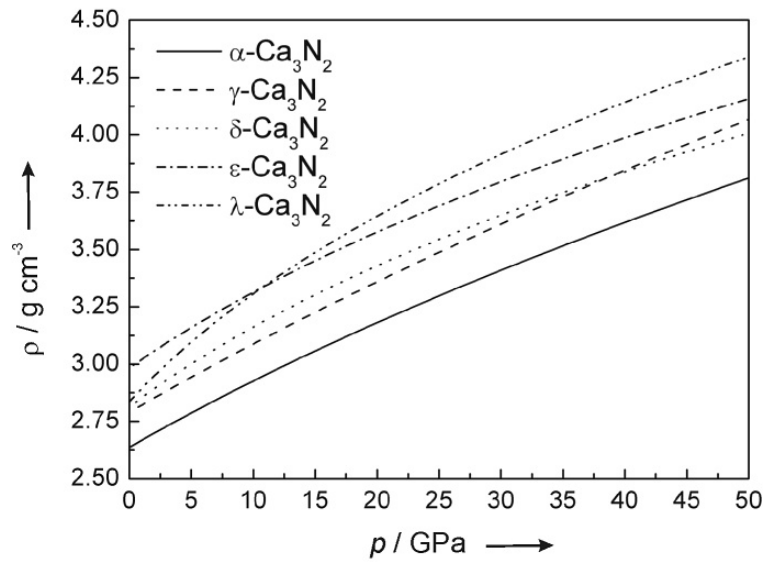
Figure 4.19: Pressure dependency of the density ρ of the high-pressure phases of Ca_3N_2 (Murnaghan EOS).

These results are somewhat complicated by a strong response of the c/a-ratio in ϵ-Ca_3N_2 to the applied pressure. Note that above 12 GPa ϵ-Ca_3N_2 with a c/a-ratio of 1.29 is more favorable (corresponding to a anti-Ni_2Al_3-type structure [181]), while below 12 GPa the structure suddenly expands to a c/a-ratio of 1.78 (denoted ϵ' and corresponding to a anti-La_2O_3-type structure [180]) (see Tables A14 and A15 in Appendix A). Computations with fixed c/a-ratio clearly indicated the crossover within this anti-A-sesquioxide structure type (Figure 4.20).
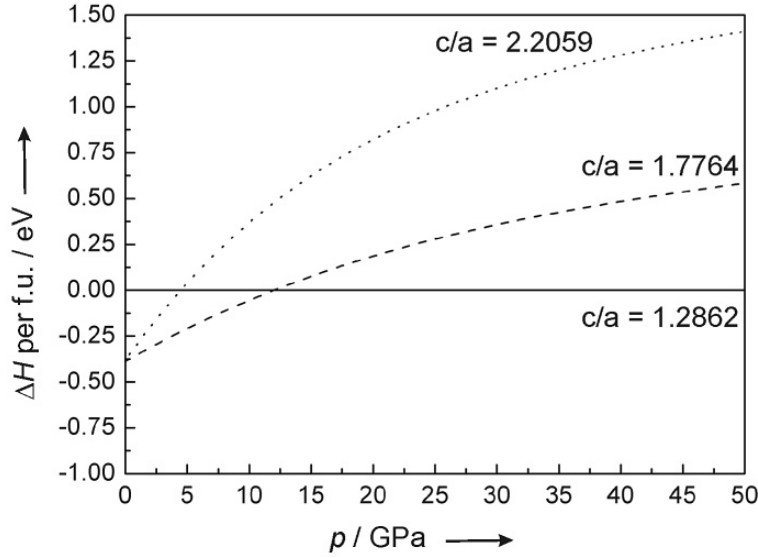
Figure 4.20: Enthalpy-pressure (H-p) diagram for different c/a-ratios of ϵ-Ca$_3$N$_2$ (Murnaghan EOS evaluation).

In our calculations, β-Ca$_3$N$_2$ does not appear as a valid high-pressure phase of Ca$_3$N$_2$, since it is always found to be higher in energy than either α-, γ-, δ-, ϵ- or λ-Ca$_3$N$_2$. The transition pressure of α-Ca$_3$N$_2$ into β-Ca$_3$N$_2$ is calculated to 7 GPa and lays higher than the transition pressure of α-Ca$_3$N$_2$ into γ-Ca$_3$N$_2$ (5 GPa) as well as the transition pressure of β-Ca$_3$N$_2$ into γ-Ca$_3$N$_2$ (4.4 GPa). This finding may well be attributed to temperature effects and the influence of defects occurring in β-Ca$_3$N$_2$ on the Gibbs free energy. For crystals containing point defects, the equation for the Gibbs free energy $G = H - TS$ has to be rewritten to $G = H_0 - TS_0 + n_D(H_D^f - TS_D^f) - kT(lnW_D)$, where $H_0 - TS_0$ denotes the Gibbs free energy of the perfect crystal, n_D the number of defects, H_D^f the enthalpy of defect formation, S_D^f the thermal entropy and $kT(lnW_D)$ the configurational entropy. These additional terms to the Gibbs free energy are not negligible for solids containing a significant defect concentration. Given the small enthalpy difference between α- and β-Ca$_3$N$_2$ they may have substantial influence on the Gibbs free energy and, thus, on the phase development.

Hypothetic anti-bixbyite Sr$_3$N$_2$ exhibits a quite similar high-pressure phase sequence as Ca$_3$N$_2$, with the exception that the anti-A-sesquioxide structure is skipped. Con-

sequently anti-bixbyite-type Sr_3N_2 exhibits three high-pressure phases. β-Sr_3N_2 comes into existence at pressures between 3 and 12 GPa, followed by γ-Sr_3N_2, which remains stable up to 26 GPa, when δ-Sr_3N_2 becomes more favorable. The pressure sensitivity of the c/a-ratio of ϵ-Ca_3N_2 (anti-A-sesquioxide-type structure) is here reflected in a similar behavior of γ-Sr_3N_2 (anti-B-sesquioxide-type structure). Two structure variants of the anti-B-sesquioxide structure turn out to have very similar ground state energies. When converting the monoclinic cell to a pseudo-hexagonal cell, these two structures correspond to c/a-ratios of 1.7 (called γ-Sr_3N_2) and 2.0 (called γ'-Sr_3N_2). As in ϵ-Ca_3N_2 this pseudo-c/a-ratio is very sensitive to pressure and computations with fixed pseudo-c/a-ratio clearly show that under pressure the γ-Sr_3N_2 anti-B-sesquioxide-type structure is preferred (Figure 4.21).
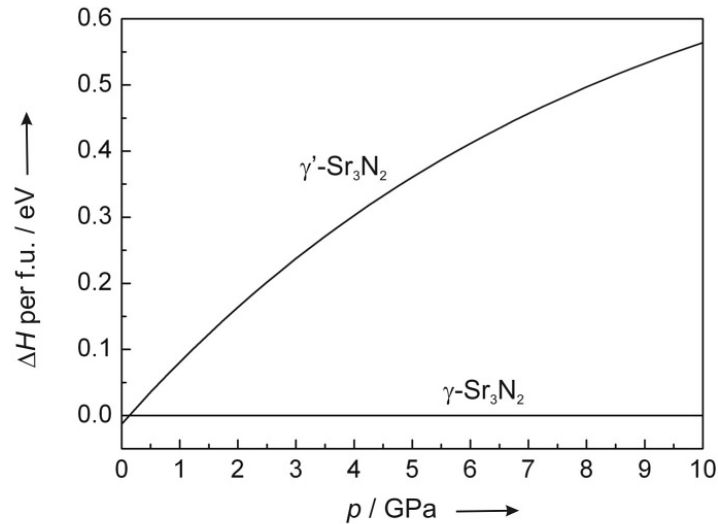
Figure 4.21: Enthalpy-pressure (*H*-*p*) diagram for the different pseudo-c/a-ratios of γ-Sr_3N_2 (c/a = 1.7) and γ'-Sr_3N_2 (c/a = 2.0) (Murnaghan EOS evaluation).

Ba_3N_2 is the only compound in the row of the binary nitrides of the group II elements exhibiting a different ground state structure type. Hypothetic α-Ba_3N_2 exhibits an anti-A-Sesquioxide-type structure with an enlarged c/a-ratio (compare chapter 4.1.5, page 59). The phase sequence of Ba_3N_2 is different from that of the other nitrides of the group II elements. It is the only compound for which an anti-post-perovskite

high-pressure phase is found (γ-Ba$_3$N$_2$). However the final high-pressure phase found for Ba$_3$N$_2$ is the same as for Ca$_3$N$_2$ and Sr$_3$N$_2$. They all adopt the hexagonal phase (space group $P6_3/mmc$) derived from the post-perovskite structure. The group-subgroup relation of the post-perovskite and the $P6_3/mmc$ structure are depicted in Figure 4.22. Due to this relation, the phase transformation from γ- to δ-Ba$_3$N$_2$ is a displacive one. The movements of the atoms are indicated in Figure 4.22 and the atomic positions for γ- to δ-Ba$_3$N$_2$ in *Cmca* setting are compared in Table 4.17.
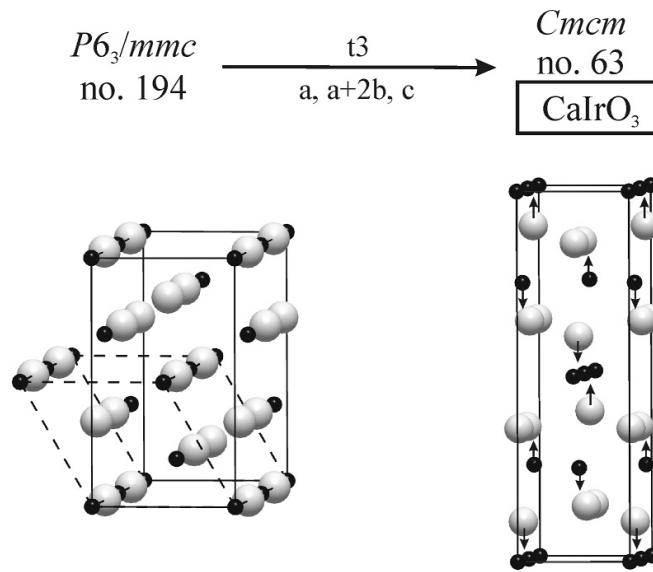
Figure 4.22: Group-subgroup relation of the $P6_3/mmc$ and the post-perovskite structure (The structure pictures feature the orthorhombic unit cell of post-perovskite (solid line) and of $P6_3/mmc$ in the left picture (dashed line); Atom movements for the transformation are indicated in the right picture by small arrows).

However, for Ba$_3$N$_2$ δ-Ba$_3$N$_2$ exhibits a lower density than both high-pressure phases appearing before it comes into existence. But when examining the density development under pressure, δ-Ba$_3$N$_2$ evinces an higher density increase per 1 GPa, in accordance with its lower bulk modulus compared to the other two phases. Hence, δ-Ba$_3$N$_2$ exhibits a higher density than β-Ba$_3$N$_2$ above 1 GPa and a higher density than γ-Ba$_3$N$_2$ above 3.5 GPa (Figure 4.23).

Table 4.17: Atom coordinates of γ-Ba$_3$N$_2$ (post-perovskite CaIrO$_3$ structure (*Cmcm*) [193]) and of δ-Ba$_3$N$_2$ (*P6$_3$/mmc* structure) (GGA and LDA calculation). Decimal numbers marked with [a] have fixed values for space group $P\bar{3}m1$ (e.g. $0.5 \,\hat{=}\, 1/2$), but could deviate from this value in space group $C2/m$.

atom	structure	Wyckoff-Position	x	y	z
Ba1	γ-Ba$_3$N$_2$ LDA	4c	1/2	0.39532	1/4
	γ-Ba$_3$N$_2$ GGA		1/2	0.39154	1/4
	δ-Ba$_3$N$_2$ LDA		1/2	0.5[a]	1/4
	δ-Ba$_3$N$_2$ GGA		1/2	0.5[a]	1/4
Ba2	γ-Ba$_3$N$_2$ LDA	8f	1/2	0.14124	0.06922
	γ-Ba$_3$N$_2$ GGA		1/2	0.13641	0.07233
	δ-Ba$_3$N$_2$ LDA		1/2	0.16667[a]	0.08990
	δ-Ba$_3$N$_2$ GGA		1/2	0.16667[a]	0.08780
N1	γ-Ba$_3$N$_2$ LDA	4c	0	0.25037	1/4
	γ-Ba$_3$N$_2$ GGA		0	0.25067	1/4
	δ-Ba$_3$N$_2$ LDA		0	0.33333[a]	1/4
	δ-Ba$_3$N$_2$ GGA		0	0.33333[a]	1/4
N2	γ-Ba$_3$N$_2$ LDA	4a	0	0	0
	γ-Ba$_3$N$_2$ GGA		0	0	0
	δ-Ba$_3$N$_2$ LDA		0	0	0
	δ-Ba$_3$N$_2$ GGA		0	0	0
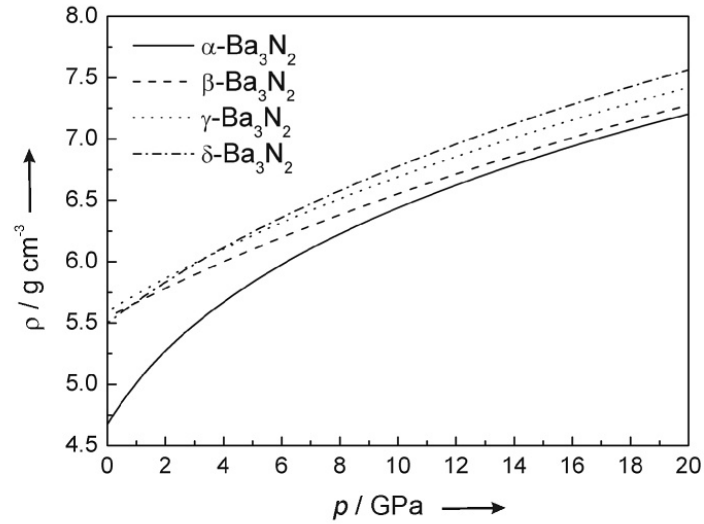
Figure 4.23: Pressure dependency of the density ρ of the high-pressure phases of Ba$_3$N$_2$ (Murnaghan EOS).

Still, the structure and true nature of Sr_3N_2 and Ba_3N_2 are yet unknown. Even their existence has been questioned, since they elude all endeavors for characterization beyond any doubt. But, even if these compounds are not synthesizeable at ambient-pressure, they may be obtained in high-pressure experiments. However, as a wide variety of binary Sr-N and Ba-N compounds with compositions different from M_3N_2 are known (Sr_2N [147], SrN [148], Sr_4N_3 [149], SrN_2 [148], $Sr(N_3)_2$ [150], Ba_3N [151], Ba_2N [152], Ba_3N_4 [153], BaN_2 [154], $Ba(N_3)_2$ [155]), the thermodynamic stability under pressure of the proposed Sr_3N_2 and Ba_3N_2 polymorphs against phase agglomerates of other binary compounds and N_2 or Sr and Ba, respectively, needs to be examined. It is still unknown, if this multitude of known other binary strontium-nitrogen and barium-nitrogen compounds constitutes a thermodynamic and kinetic sink, which prevents the formation of the binary nitrides Sr_3N_2 and Ba_3N_2.

An overview of all high-pressure phases for the row of the nitrides M_3N_2 of the group II elements is shown in Figure 4.24. This figure clearly illustrates the above described similarities and differences in the high-pressure phases sequences and the development of these sequences going down in group II of the periodic table.

The overall average values for the calculated zero-pressure bulk moduli decreases in the row Be_3N_2, Mg_3N_2, Ca_3N_2, Sr_3N_2, Ba_3N_2. The values for B_0 for Be_3N_2 range from 210 to 215 GPa, placing them in bulk modulus among compounds as α-Si_3N_4 [200, 201], β-Si_3N_4 [201, 202], B_4C [203] and SiC [203]. β-Be_3N_2 exhibits the lowest ambient-pressure bulk modulus of 210 GPa, followed by γ-Be_3N_2 with a bulk modulus of 213 GPa. α-Be_3N_2 has the highest bulk modulus, evincing a value of 215 GPa. The zero-pressure bulk moduli for the examined Mg_3N_2 polymorphs are about 100 GPa lower than those of the Be_3N_2 phases. α-Mg_3N_2 and β-Mg_3N_2 exhibit the same B_0 of 109 GPa, whereas the bulk modulus of γ-Mg_3N_2 is slightly smaller (104 GPa).

Comparing the bulk moduli at zero pressure for the considered Ca_3N_2 polymorphs, which are on average 35 GPa lower than those of the Mg_3N_2 phases, it appears that B_0 increases from 68 GPa to 73 GPa for α-, β- and γ-Ca_3N_2, then goes down to 67 GPa for δ-Ca_3N_2, increases to 76 GPa for ϵ-Ca_3N_2 and finally drops to 45 GPa for λ-Ca_3N_2, even lower than that of α-Ca_3N_2 (68 GPa). This finding implies that λ-Ca_3N_2 should be the most compressible and ϵ-Ca_3N_2 the least compressible of all discussed modifications of Ca_3N_2. This can be also drawn on to explain why

λ-Ca$_3$N$_2$ becomes denser under pressure than ϵ-Ca$_3$N$_2$, since it is more compressible and therefore the same change in pressure Δp results in a larger volume change ΔV in λ-Ca$_3$N$_2$ than in ϵ-Ca$_3$N$_2$.
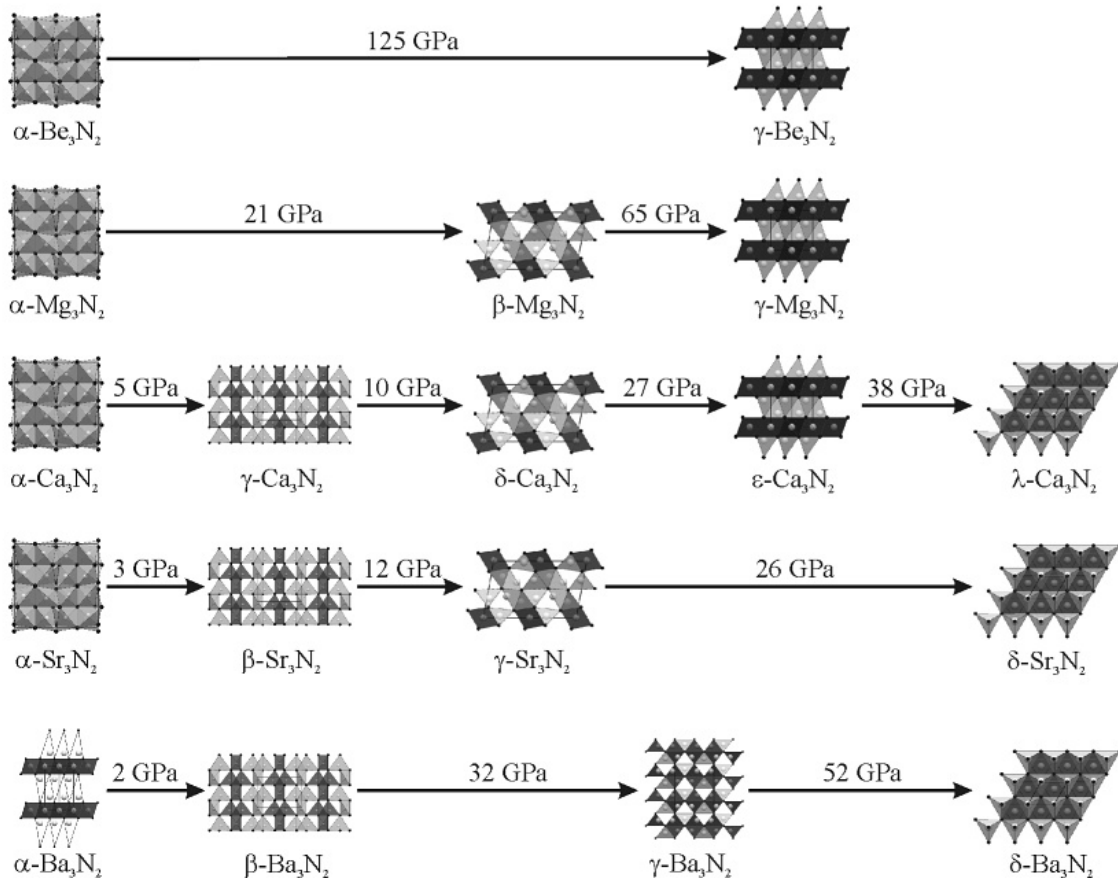
Figure 4.24: Phase sequences of M$_3$N$_2$ (M = Be, Mg, Ca, Sr, Ba) under pressure.

The zero-pressure bulk modulus for Sr$_3$N$_2$ starts at 51 GPa for α-Sr$_3$N$_2$, increases to 55 GPa for β-Sr$_3$N$_2$, then goes down to 52 GPa for γ-Sr$_3$N$_2$ and 32 GPa for γ'-Sr$_3$N$_2$, respectively, and finally adopts a value of 34 GPa for δ-Sr$_3$N$_2$. These values are on average 20 GPa lower than those found for Ca$_3$N$_2$.

The average B_0 for the considered Ba$_3$N$_2$ compounds is about 15 GPa lower than that for Sr$_3$N$_2$. The highest ambient-pressure bulk modulus found is adopted by β-Ba$_3$N$_2$ (44 GPa), the lowest by α-Ba$_3$N$_2$ (10 GPa), thereby being the overall most compressible compound in the row of the binary alkaline earth nitrides. γ-Ba$_3$N$_2$

and δ-Ba$_3$N$_2$ exhibit bulk moduli of 33 and 31 GPa, respectively.

All high-pressure transition of M$_3$N$_2$ (M = Be, Mg, Ca, Sr ,Ba) should be easily detectable via X-ray diffraction experiments (*ex situ* and *in situ*), as the powder patterns of all phases are quite different. Simulated powder patterns for all compounds at the respective transition pressures can be found in Appendix C.

5 Nitridosilicates MSiN$_2$ of group II elements

The MSiN$_2$ compounds (M = Be, Mg, Ca, Sr, Ba), which are the only nitridosilicates known for all group II elements, excepting radioactive Ra, are not only widely used in industry, but are also of great importance for the high-pressure chemistry of the prominent Eu^{2+}-doped LED phosphors M$_2$Si$_5$N$_8$ (M = Ca, Sr, Ba)([204], c.f. chapter 6.4.3). BeSiN$_2$ and MgSiN$_2$ are both used as sintering additives for Si$_3$N$_4$ ceramics [205–213]. Even BaSiN$_2$ has been discussed as a sintering agent [214]. Especially the influence of MgSiN$_2$ on the properties of Si$_3$N$_4$ ceramics, either as a direct sintering agent or as a product or intermediate product when using Mg containing additives, are widely discussed [208, 209, 215–218]. MgSiN$_2$ itself is a prominent ceramic [219–223] (thermally stable up to 1400°C [205] and studied particularly with regard to thermal conductivity [222, 224–226]) and discussed to substitute for AlN [227]. CaSiN$_2$, besides possessing promising properties for ceramics applications [228], is an auspicious phosphor host lattice. Doped with Eu^{2+} or Ce^{3+} it is considered for use in LEDs [229, 230]. CaSiN$_2$:Ce^{3+} is one of the rare phosphor materials that can be excited by yellow-green light [230]. MgSiN$_2$, SrSiN$_2$ and BaSiN$_2$ were also shown to exhibit luminescence when doped with luminescence centers (Eu^{2+}, Ce^{3+}) [231–233], rendering them interesting for possible industrial applications.

For both, BeSiN$_2$ and MgSiN$_2$, there is only one polymorph known. They have been identified to crystallize in an ordered wurtzite-type structure (NaFeO$_2$-type structure), space group $Pna2_1$ (no. 33) [13, 234, 235]. The structure is built up of all-side corner sharing SiN$_4$ and MgN$_4$ tetrahedra. The MN$_4$ tetrahedra built honeycomb layers of 3er rings perpendicular to [001] with all apices jutting out of the layers in one direction. These layers follow an ABAB ordering and the SiN$_4$ and MgN$_4$ tetrahedra are arranged in alternating 1-1 zigzag rows.

$CaSiN_2$ crystallizes in the orthorhombic space group *Pbca* (no. 61), in the $KGaO_2$-type structure. The structure is built up by all side corner sharing SiN_4 tetrahedra, forming a three-dimensional network. The Ca^{2+} ions are 6- and 8-fold coordinated by nitrogen [14]. A second, cubic modification has also been described in the literature, but no detailed crystallographic data have been presented until now [230, 236]. Apparently, the luminescence properties described above are attributed to this cubic modification [230]. Furthermore, Cheetham et al. have pointed out, that the cubic and the orthorhombic $CaSiN_2$ unit cells are related by the following relation: $a_c = 2\sqrt{2}a_o$, $a_c = \sqrt{2}b_o$, $a_c = c_o$, $V_c = 4V_o$ [230].

It has to be noted, that both the wurtzite-type structure of $BeSiN_2$ and $MgSiN_2$ as well as the $CaSiN_2$ structure can be derived from the filled β-cristobalite structure (also termed filled C9 structure). By rotating the SiN_4 tetrahedra of the idealized filled C9 structure in a certain way, one arrives either at the $NaFeO_2$-type (C1-type distortion) or the $KGaO_2$-type structure (D1-type distortion) [237, 238].

$SrSiN_2$ and $BaSiN_2$ structures are quite different from those of the other three $MSiN_2$ compounds. They do not exhibit a three-dimensional network structure of corner-sharing SiN_4 tetrahedra, but layers $[Si^{[4]}N_2^{[2]}]_\infty^{2-}$ containing "bowtie" units Si_2N_6 (pairs of edge-sharing tetrahedra) further connected through common corners. Between these layers, the M^{2+} cations are situated. $BaSiN_2$ crystallizes in the orthorhombic space group *Cmca* (no. 64), whereas $SrSiN_2$ exhibits a monoclinic distorted variation of the same structure with space group $P2_1/c$ (no. 14) [14].

The different structural behavior at ambient pressure of the $MSiN_2$ compounds can easily be attributed to the larger size of the group II element cations. As it emerges, the interesting question is how such structures may behave if substantial pressure is applied.

5.1 Optimized Structures and Energy-Volume Calculations for MSiN₂ (M = Be, Mg, Ca, Sr, Ba)

About 15 structure types where tested as potential high-pressure phases for $MSiN_2$ (M = Be, Mg, Ca, Sr, Ba). Only those that proved to be of relevance for the

enthalpy-pressure phase diagram are described here. For all optimized structures the coordination numbers of the M^{2+} and Si^{4+} ions were determined by calculating effective coordination numbers (ECoN) [174] with MAPLE [175–178] in order to compare them to the data for the experimentally determined structures (if available).

5.1.1 BeSiN$_2$

α-BeSiN$_2$ crystallizes in an ordered wurtzite-type structure (space group $Pna2_1$, no. 33) [13] which can also be described as related to the β-cristobalite structure, as a C1-type distortion of the idealized filled C9 structure of β-cristobalite [237] (Figure 5.1). Two high-pressure candidate structures were identified. β-BeSiN$_2$ exhibits a chalcopyrite-like structure with tetrahedrally coordinated Be and Si (space group $I\bar{4}2d$, no. 122) [239]. This is another structure which is related to β-cristobalite by a B1-type distortion [237] (Figure 5.1). Both α- and β-BeSiN$_2$ are three-dimensional MN$_4$ tetrahedra networks, built up of all-side corner sharing tetrahedra. γ-BeSiN$_2$ adopts a LiFeO$_2$ structure (further on called s-LiFeO$_2$ as it corresponds to the stable low-temperature modification of LiFeO$_2$) with the tetragonal space group $I4_1/amd$ (no. 141) [240]. It is a rock salt superstructure (doubled unit cell), where O^{2-} forms a cubic close packing and Fe^{3+} and Li^+ occupy the octahedral holes, forming zigzag rows of edge-sharing octahedra along [-0.5 -0.5 0], filled with the same cations (Figure 5.1).

The Be-N distances and Si-N bond lengths of the optimized structures have been examined and compared to distances in experimental BeSiN$_2$ (Table 5.1). The calculated values for four-fold coordinated Si and Be correspond with the experimental values very well. Bond lengths for the octahedrally coordinated cations are longer, as can be expected for increased coordination spheres.

Referring to ambient-pressure GGA-calculations, α-BeSiN$_2$ has the lowest energy of the four polymorphs (-30.902 eV per formula unit) and also the lowest density, $\rho = 3.19\,\mathrm{g\,cm^{-3}}$ (exp. value 3.24 g cm^{-3} [13]). β-BeSiN$_2$ is only about 0.005 eV per formula unit higher in energy and about 0.3 % denser (computed 3.20 g cm^{-3}). This result is not surprising given the close resemblance of the two modifications. γ-BeSiN$_2$ then exhibits the highest density. With $\rho = 3.82\,\mathrm{g\,cm^{-3}}$ this octahedra structure is 19.7 % denser than α-BeSiN$_2$ and 19.4 % denser than β-BeSiN$_2$, but also 2.146 eV

per formula units higher in energy than α-BeSiN$_2$, and 2.141 eV than β-BeSiN$_2$. The zero-pressure bulk moduli of the three polymorphs are 220 GPa for α-BeSiN$_2$, 222 GPa for β-BeSiN$_2$ and 244 GPa for γ-BeSiN$_2$. Shaposhnikov et al. [241] and Petukhov et al. [242] reported bulk moduli of 243 GPa and 240 GPa for α-BeSiN$_2$ and
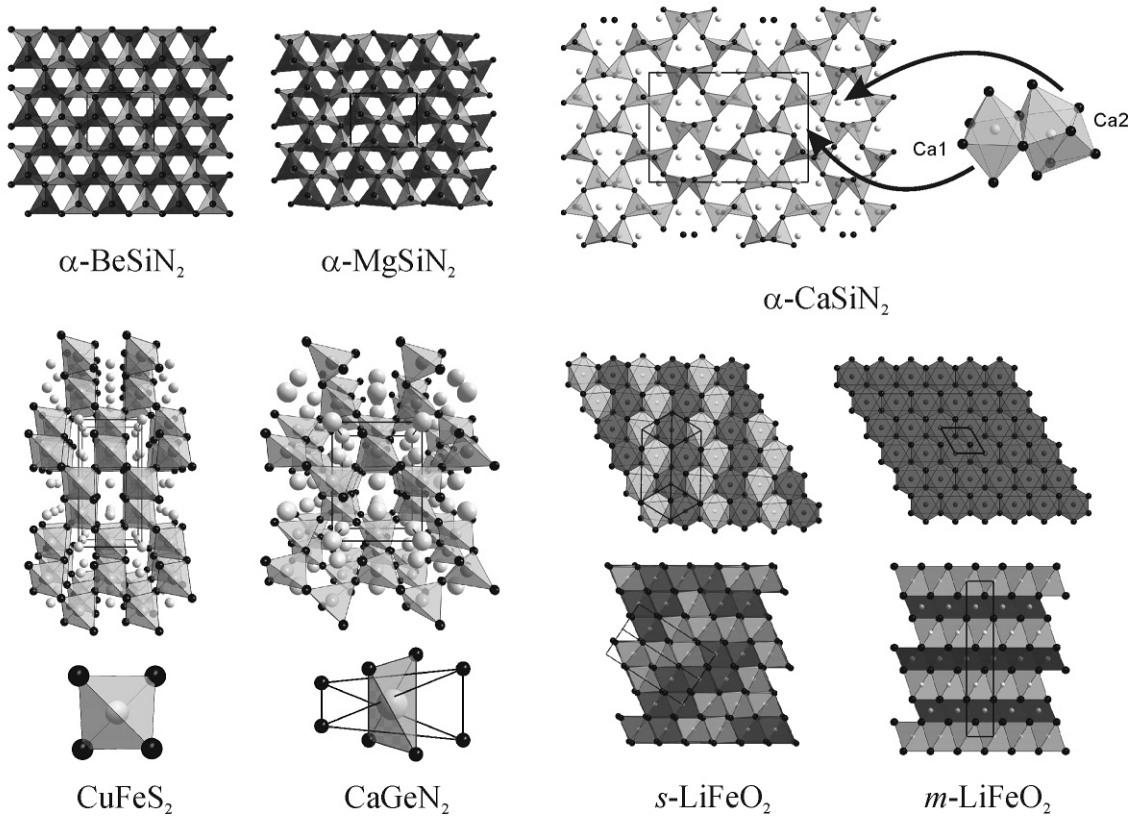
Figure 5.1: Crystal Structures of MSiN$_2$: (1) α-BeSiN$_2$ and α-MgSiN$_2$, view along [001] (SiN$_4$ tetrahedra drawn light gray, BeN$_4$ and MgN$_4$ tetrahedra black), (2) α-CaSiN$_2$, view along [100] (SiN$_4$ tetrahedra drawn light gray), (3) Chalcopyrite (CuFeS$_2$) and CaGeN$_2$ (top: view along [010], bottom: CuS$_4$ tetrahedron and CaN$_8$ bisdisphenoide), (4) s-LiFeO$_2$ and m-LiFeO$_2$ (top: octahedral layer (s-LiFeO$_2$: view along [-0.5 -0.5 0] rotated, m-LiFeO$_2$: view along [001]), bottom: stacking of octahedral layers (s-LiFeO$_2$: view along [0.5 -0.5 0.25] rotated, m-LiFeO$_2$: view along [010])).

and of 242 GPa β-BeSiN$_2$, respectively, but did not consider a γ-BeSiN$_2$ or any high-pressure phase transitions. Their values match our LDA results for the bulk modulus (241 GPa for both structures). With respect to the bulk moduli, both β-BeSiN$_2$ and γ-BeSiN$_2$ are likely to be hard materials, ranking between B$_4$C (200 GPa) [203],

α-Si_3N_4 (229 GPa) [200] and SiC (248 GPa) [203].

The ground state structures of α- as well as β-BeSiN$_2$ have been presented in two contributions [241, 242]. The values from these contributions in comparison to the values of this thesis are presented in Table 5.2. For both structures of BeSiN$_2$ the data from this thesis agree well with those found in the literature.

Table 5.1: Bond lengths (in pm) in α-, β- and γ-BeSiN$_2$ compared to experimental values.

Structure	Bond type	LDA	GGA	exp.
α-BeSiN$_2$	Be$^{[4]}$-N$^{[6]}$	174.47–176.23	176.77–178.66	175.58–176.05 [13]
	Si$^{[4]}$-N$^{[6]}$	172.84–174.45	174.65–176.22	175.58–176.05 [13]
β-BeSiN$_2$	Be$^{[4]}$-N$^{[6]}$	175.11	177.52	/
	Si$^{[4]}$-N$^{[6]}$	173.53	175.33	/
γ-BeSiN$_2$	Be$^{[6]}$-N$^{[6]}$	186.86, 204.29	188.93, 210.54	/
	Si$^{[6]}$-N$^{[6]}$	184.85, 186.86	187.20, 188.93	/
γ-Si$_3$N$_4$	Si$^{[6]}$-N	186.84 [6]	189.04 [6]	186.26 [5]
Ce$_{16}$Si$_{15}$O$_6$N$_{32}$	Si$^{[6]}$-N	/	/	210.44 [243]
Ionic Radii	bond type	Shannon [183]	Baur [184]	
	Be$^{[4]}$-N	173	181	
	Be$^{[6]}$-N	191	/	
	Si$^{[4]}$-N	172	179	
	Si$^{[6]}$-N	182	/	

Table 5.2: Comparison of previousliy calculated data for α- and β-BeSiN$_2$ compared to results of this thesis and experimental values.

α-BeSiN$_2$, $Pna2_1$, Z = 4					
V / 10^6 pm^3	a / pm	b / pm	c / pm	B$_0$ / GPa	Reference
130.5	493.9	569.7	463.9	264	[241]
135.6	499.9	577.2	469.9	243	[241]
133.7(3)	497.7(5)	574.7(6)	467.4(3)	/	exp. [13]
130.68	494.03	569.89	464.15	239	this thesis
135.49	499.73	577.02	469.89	220	this thesis

β-BeSiN$_2$, $I\bar{4}2d$, Z = 4				
V / 10^6 pm^3	a / pm	c / pm	B$_0$ / GPa	Reference
135.4	407.3	816.4	242	[241]
141	410	836	240	[242]
130.48	401.91	807.66	241	this thesis
135.26	407.06	816.31	222	this thesis

In Figure 5.3 the *E-V* curves of the three structures of BeSiN$_2$ are displayed. The *E-V* data were transformed into enthalpy-pressure data (Figure 5.4) by standard methods as described in chapter 2.7.5, page 27. With respect to enthalpy, it turns out that α-BeSiN$_2$ is the most stable polymorph of BeSiN$_2$ for pressures up to 20 GPa, at which it will transform to β-BeSiN$_2$. Given the small enthalpy differences between α- and β-BeSiN$_2$, the calculated value of the transition pressure has to be taken with care. However, once β-BeSiN$_2$ is formed, a tetrahedra structure will remain stable up to about 76 GPa. At this pressure the structure of γ-BeSiN$_2$ with octahedral coordination for both Si and Be becomes the most stable polymorph of BeSiN$_2$. The sequence of structures together with transition pressures and density changes is illustrated in Figure 5.2.
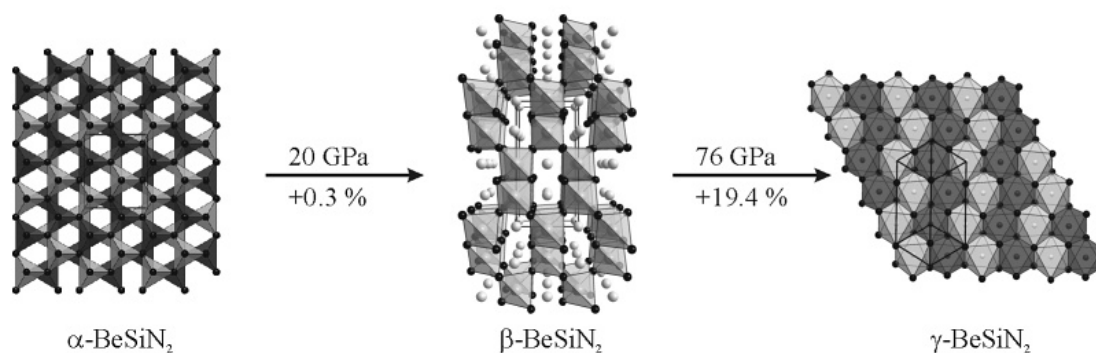
Figure 5.2: Sequence of structures of BeSiN$_2$ together with transition pressures and changes in density.

5.1.2 MgSiN$_2$

α-MgSiN$_2$ crystallizes in the orthorhombic space group $Pna2_1$ (no. 33) and exhibits the same wurtzite-like structure as α-BeSiN$_2$ [234, 235] (Figure 5.1). The search for high-pressure polymorphs revealed only β-MgSiN$_2$ (Figure 3) exhibiting yet another LiFeO$_2$-type structure (space group $R\bar{3}m$, no. 166, denoted m-LiFeO$_2$, as it corresponds to the **m**eta-stable low-temperature modification of LiFeO$_2$) [244]. The m-LiFeO$_2$ structure can be derived from the CdCl$_2$ structure (also $R\bar{3}m$), if all unoccupied octahedral sites are occupied by a second sort of cation (Figure 5.1). Hence, both s- and m-LiFeO$_2$ are superstructures of the rocksalt structure, differing only in
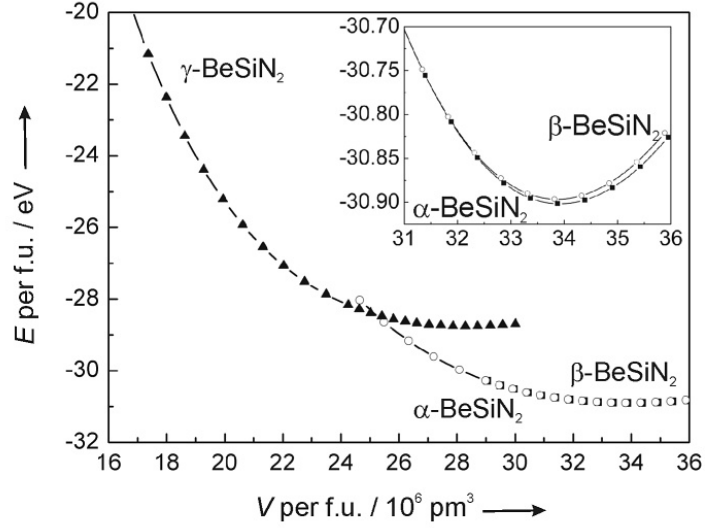
Figure 5.3: Energy-volume (E-V) phase diagram of α-, β- and γ-BeSiN$_2$, calculated within the GGA. Each symbol represents a calculation.
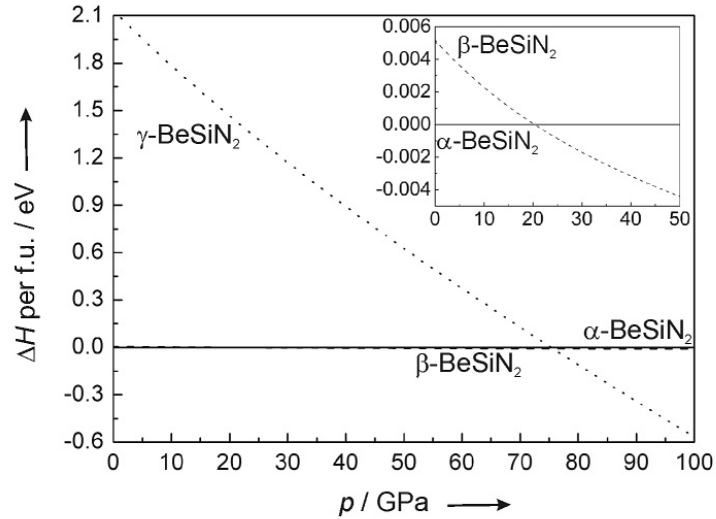
Figure 5.4: Enthalpy-pressure (H-p) diagram for the transition of α-BeSiN$_2$ into β-BeSiN$_2$ (p$_t$ = 20 GPa) and into γ-BeSiN$_2$ (p$_t$ = 76 GPa)(derived from the evaluation of the E-V data by the Murnaghan EOS).

the ordering of the two cations.

The calculated Mg-N and Si-N distances of α-MgSiN$_2$ are well within the range of the experimental values (Table 5.3). The obtained values for β-MgSiN$_2$ are larger, reflecting the increased coordination. The Si-N bonds are a little bit longer than those of octahedrally coordinated Si in γ-Si$_3$N$_4$ (186.26 pm [5]), in average about 5 pm. However, the Si-N bond lengths in Ce$_{16}$Si$_{15}$O$_6$N$_{32}$ amount to 210.44 pm [243], which is about 15 to 20 pm longer than the values calculated for β-MgSiN$_2$.

Table 5.3: Bond lengths (in pm) in α- and β-MgSiN$_2$ compared to experimental values.

Structure	Bond type	LDA	GGA	exp.
α-MgSiN$_2$	Mg$^{[4]}$-N$^{[6]}$	205.33–210.27	208.33–213.77	205.92–211.50 [235]
	Si$^{[4]}$-N$^{[6]}$	172.60–174.95	174.41–176.99	173.81–179.65 [235]
β-MgSiN$_2$	Mg$^{[6]}$-N$^{[6]}$	213.84	217.35	/
	Si$^{[6]}$-N$^{[6]}$	191.33	193.95	/
γ-Si$_3$N$_4$	Si$^{[6]}$-N	186.84 [6]	189.04 [6]	186.26 [5]
Ce$_{16}$Si$_{15}$O$_6$N$_{32}$	Si$^{[6]}$-N	/	/	210.44 [243]
Ionic Radii	bond type	Shannon [183]	Baur [184]	
	Mg$^{[4]}$-N	191	214	
	Mg$^{[6]}$-N	218	220	
	Si$^{[4]}$-N	172	179	
	Si$^{[6]}$-N	182	/	

Within the ambient-pressure GGA calculations, the ground state of α-MgSiN$_2$ has an energy per formula unit of -28.495 eV and a density of 3.08 g cm^{-3} (exp. value: 3.13 g cm^{-3} [234, 235]). β-MgSiN$_2$ is 1.166 eV higher in energy than α-MgSiN$_2$ and approximately 26 % denser (3.88 g cm^{-3}). The zero-pressure bulk modulus is 172 GPa for α-MgSiN$_2$, well within the range of previously calculated (182 GPa [245], 174 GPa [246]) and measured values (146 GPa [247], 184 GPa [248]). For β-MgSiN$_2$ a zero-pressure bulk modulus of 223 GPa was calculated, which is comparable to the experimental bulk modulus of α-Si$_3$N$_4$ (220 GPa) [200], which is a widely used ceramic.

Comparing the calculated crystallographic data of α-MgSiN$_2$ with those found in the literature (both published by Fang et al. [245, 249]) reveals a good agreement (compare Table 5.4).

According to the enthalpy-pressure phase diagram (Figure 5.7), derived from the energy-volume data depicted in Figure 5.6, α-MgSiN$_2$ will transform into β-MgSiN$_2$

Table 5.4: Comparison of previousliy calculated data for α-MgSiN$_2$ compared to results of this thesis and experimental values.

α-MgSiN$_2$, *Pna*2$_1$, Z = 4

V / 10^6 pm^3	a / pm	b / pm	c / pm	B$_0$ / GPa	Reference
164.62	522.61	637.65	493.99	182	[245]
169.94	527.08	646.92	498.40	/	[249]
170.66	527.9	647.6	499.2	/	exp. [235]
166.57	523.77	641.75	499.55	201	this thesis
173.39	530.69	649.89	502.75	172	this thesis

at 24 GPa, increasing the coordination for both Mg and Si from a tetrahedral to an octahedral one (Figure 5.5).

Fang et al. [245] reported a high-pressure transition of α-MgSiN$_2$ into a CsICl$_2$-type structure ($R\bar{3}m$, no. 166) and proposed a transition pressure of 16.5 GPa using LDA calculations. The lower transition pressure they received is explained by the choice of the different functional that artificially favors higher coordination. The structure type of CsICl$_2$ is, however, misleading. Both CsICl$_2$ and m-LiFeO$_2$ (our choice) exhibit the same space group, but very different c/a-ratios (CsICl$_2$: c/a = 1.9269; m-LiFeO$_2$: c/a = 4.9899). Moreover, the coordination environments are different, eightfold in CsICl$_2$ and six-fold in m-LiFeO$_2$. Since Fang et al. report their optimized structure of β-MgSiN$_2$ having octahedral coordination, it is more precisely described by the m-LiFeO$_2$-type.
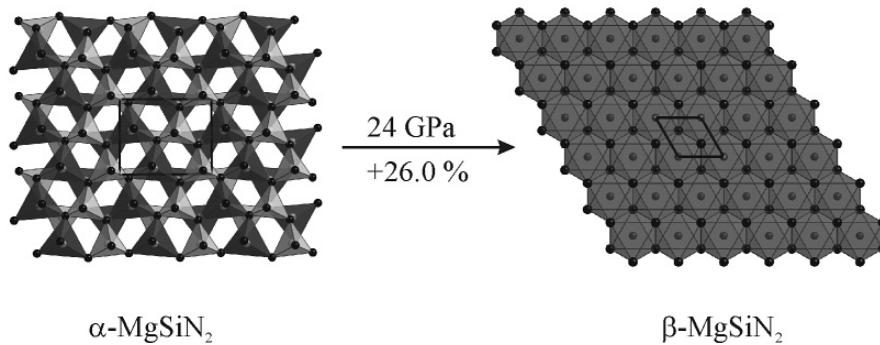
Figure 5.5: Sequence of structures of MgSiN$_2$ together with transition pressures and changes in density.
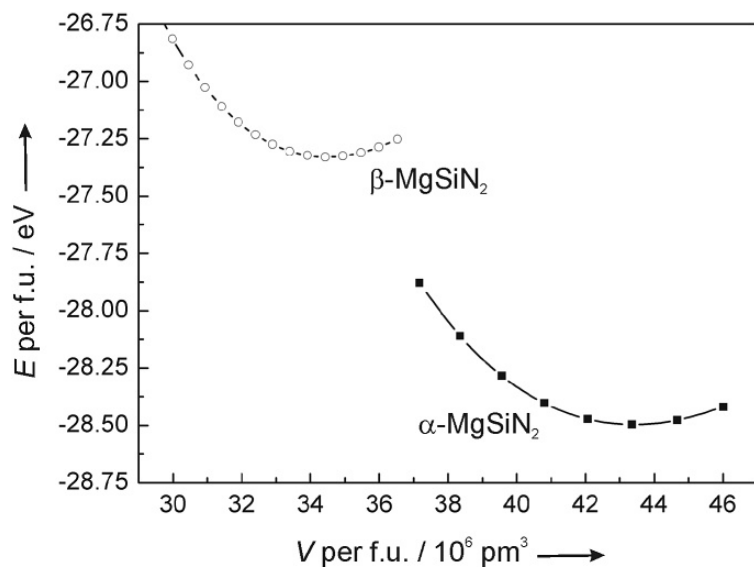
Figure 5.6: Energy-volume (*E-V*) phase diagram of α- and β-MgSiN$_2$, calculated within the GGA. Each symbol represents a calculation.
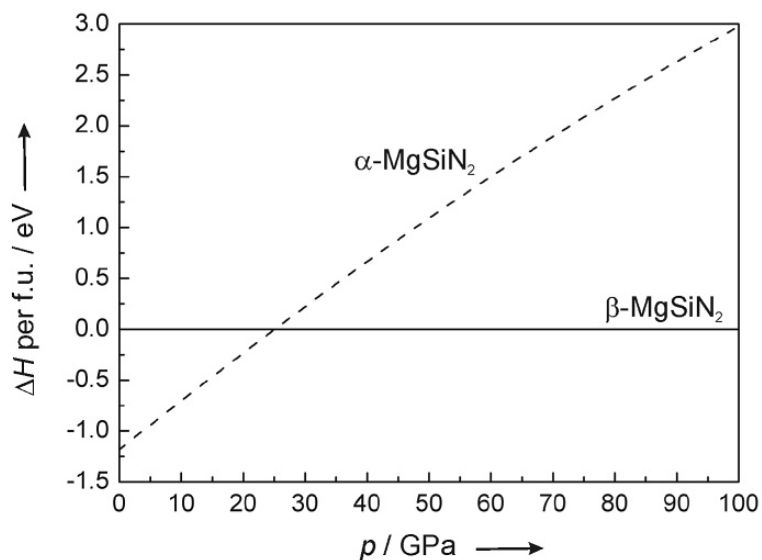
Figure 5.7: Enthalpy-pressure (*H-p*) diagram for the transition of α-MgSiN$_2$ into β-MgSiN$_2$ ($p_t = 24$ GPa) (derived from the evaluation of the *E-V* data by the Murnaghan EOS).

5.1.3 CaSiN$_2$

Ambient-pressure α-CaSiN$_2$ crystallizes in the orthorhombic space group *Pbca* (no. 61) [14]. The structure is built up by all side corner sharing SiN$_4$ tetrahedra, forming a three-dimensional network, related to the β-cristobalite structure (D1-type distortion of idealized C9 structure of β-cristobalite) [237]. Ca is 6- and 8-fold coordinated to nitrogen (Figure 5.1). A first high-pressure polymorph found, β-CaSiN$_2$, may be isostructural to CaGeN$_2$ [250] (B1-type distortion of the idealized filled C9 structure of β-cristobalite), which is closely related to the chalcopyrite structure [239]. It crystallizes in the tetragonal space group $I\bar{4}2d$ (no. 122). The Si atoms are tetrahedrally coordinated by N, but Ca^{2+} exhibits a 4+4 bisdisphenoidal coordination. The main difference between chalcopyrite-type and CaGeN$_2$-type structures is founded on a different c/a-ratio, which results in an elongation or compression, respectively, of the same basic structure. In chalcopyrite-type structures, both cations are tetrahedrally coordinated, whereas in CaGeN$_2$-like structures one cation exhibits a bisdisphenoidal coordination (Figure 5.1). The third candidate structure, γ-CaSiN$_2$, again adopts a m-LiFeO$_2$-type structure (Figure 5.1) [244].

For α- and β-CaSiN$_2$, which both comprise four-fold coordinated Si and Ca in six- and eight-fold coordination, the calculated bond lengths reflect very well those found in experimental α-CaSiN$_2$ (Table 5.5). So do the Ca-N distances in γ-CaSiN$_2$. The Si-N bond lengths for the SiN$_6$ octahedra are about 20 pm longer than those found for SiN$_4$ tetrahedra in α- and β-CaSiN$_2$ and about 10 pm than those found for SiN$_6$ octahedra in γ-Si$_3$N$_4$ (186.26 pm [5]), but also about 10 pm shorter than those for SiN$_6$ octahedra in Ce$_{16}$Si$_{15}$O$_6$N$_{32}$ (210.44 pm [243]).

The energy of α-CaSiN$_2$ is computed to -29.140 eV per formula unit, its density to 3.24 g cm^{-3} (exp. value 3.30 g cm^{-3} [14]) within GGA. β-CaSiN$_2$ is marginally higher in energy, some 0.006 eV per formula unit, and about 0.6 % denser (computed density 3.26 g cm^{-3}) than α-CaSiN$_2$. γ-CaSiN$_2$, with octahedral coordination of all atoms exhibits the highest density. With $\rho = 3.87$ g cm^{-3} it is about 19.3 % denser than α-CaSiN$_2$ and 18.5 % denser than β-CaSiN$_2$. The energy of γ-CaSiN$_2$ is 1.830 eV per formula units higher than that of α-CaSiN$_2$, and 1.825 eV per formula units higher than that of β-CaSiN$_2$. The zero-pressure bulk moduli of the three phases are 131 GPa, 126 GPa and 189 GPa for α-, β- and γ-CaSiN$_2$, respectively. This

Table 5.5: Bond lengths (in pm) in α-, β- and γ-CaSiN$_2$ compared to experimental values.

Structure	Bond type	LDA	GGA	exp.
α-CaSiN$_2$	Ca$^{[6,8]}$-N$^{[6]}$	236.98–304.81	241.00–314.27	240.60–309.83 [14]
	Si$^{[4]}$-N$^{[6]}$	172.30–175.65	174.33–177.77	172.90–176.47 [14]
β-CaSiN$_2$	Ca$^{[4+4]}$-N$^{[6]}$	239.17, 298.56	243.66, 307.22	/
	Si$^{[4]}$-N$^{[6]}$	174.28	176.28	/
γ-CaSiN$_2$	Ca$^{[6]}$-N$^{[6]}$	235.42	239.59	/
	Si$^{[6]}$-N$^{[6]}$	196.58	199.78	/
γ-Si$_3$N$_4$	Si$^{[6]}$-N	186.84 [6]	189.04 [6]	186.26 [5]
Ce$_{16}$Si$_{15}$O$_6$N$_{32}$	Si$^{[6]}$-N	/	/	210.44 [243]
Ionic Radii	bond type	Shannon [183]	Baur [184]	
	Ca$^{[4]}$-N	/	246	
	Ca$^{[6]}$-N	246	255	
	Si$^{[4]}$-N	172	179	
	Si$^{[6]}$-N	182	/	

places them among compounds as Zr$_2$InC (127 GPa) [251], Al$_4$C$_3$ (130 GPa) [252] and CaIrO$_3$ (180 GPa) [253]. Along the sequence BeSiN$_2$, MgSiN$_2$, and CaSiN$_2$, therefore, CaSiN$_2$ phases show the lowest bulk moduli.

Interestingly, when calculating CaSiN$_2$ in the MgSiN$_2$-type structure [234, 235] an even lower energy than that computed for α-CaSiN$_2$ was obtained (-29.141 eV per formula unit), when using the GGA. The energy-difference (only 0.001 eV), however, is very small, and well within a systematic error range of DFT calculations. When calculating an enthalpy-pressure phase diagram including CaSiN$_2$ in the MgSiN$_2$-type structure, one arrives at a transition pressure of CaSiN$_2$ in the MgSiN$_2$-type structure into α-CaSiN$_2$ of 0.2 GPa. Employing LDA calculations, on the other hand, places the α-CaSiN$_2$ 0.032 eV below the MgSiN$_2$-type.

The energy-volume curves (Figure 5.9) and the thereof derived enthalpy-pressure diagram (Figure 5.10) disclose two high-pressure phases of CaSiN$_2$. Accordingly, a first transition of α-CaSiN$_2$ into β-CaSiN$_2$ is found already at 1.6 GPa. β-CaSiN$_2$ will be the most stable polymorph up to 60 GPa, when the octahedrally coordinated structure of γ-CaSiN$_2$ is adopted. The coordination of Si is only increased during the second phase transformation (from four to six), whereas the coordination of Ca does not fully obey the empiric pressure-coordination rule [254]. First an increase from an average coordination number of seven to eight takes place during transition from α- to β-CaSiN$_2$, but when transforming into γ-CaSiN$_2$, the coordination number is

reduced to six. However, the increase in density gained by six-fold coordinated Si in combination with a higher condensation degree of the SiN$_x$ polyhedra (coordination representation for the Si-N framework: α/β-CaSiN$_2$: $[\text{Si}^{[4]}\text{N}_2^{[2]}]^{2-}$; γ-CaSiN$_2$: $[\text{Si}^{[6]}\text{N}_2^{[3]}]^{2-}$) is overcompensating the reduction of the coordination number of Ca. The succeeding polymorphs together with transition pressures and density changes are illustrated in Figure 5.8.
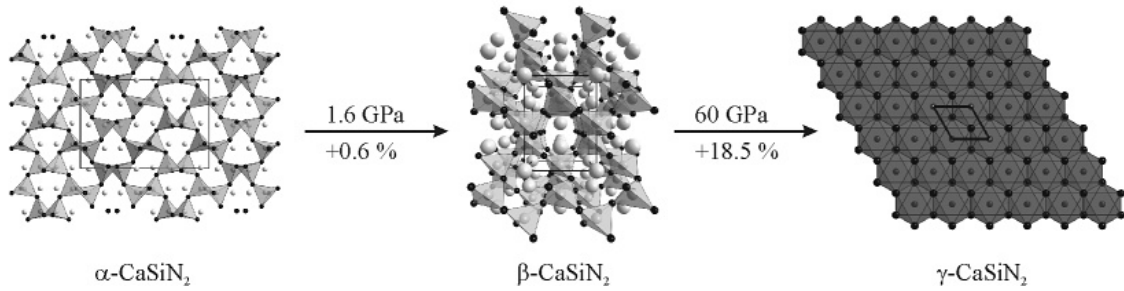
Figure 5.8: Sequence of structures of CaSiN$_2$ together with transition pressures and changes in density.
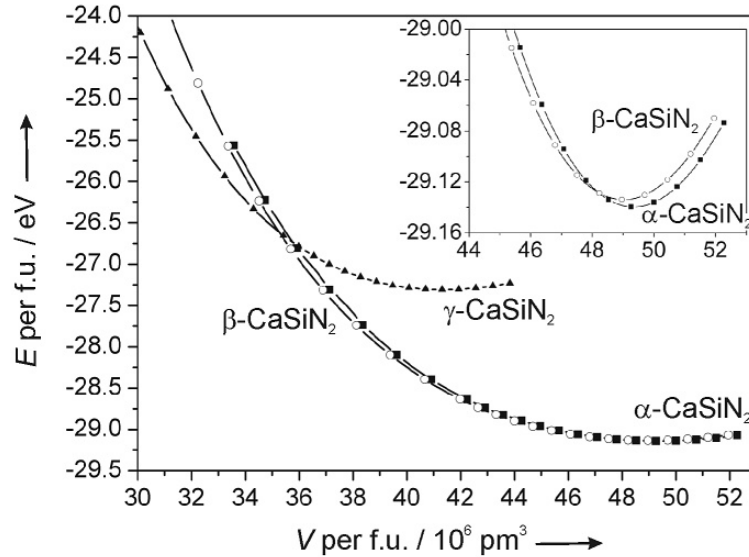
Figure 5.9: Energy-volume (E-V) phase diagram of α-, β- and γ-CaSiN$_2$, calculated within the GGA. Each symbol represents a calculation.
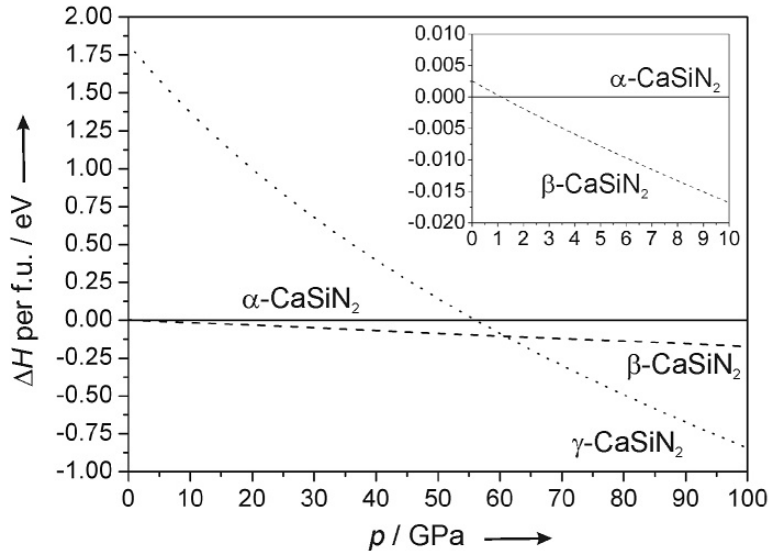
Figure 5.10: Enthalpy-pressure (*H-p*) diagram for the transition of α-CaSiN$_2$ into β-CaSiN$_2$ (p$_t$ = 1.6 GPa) and into γ-CaSiN$_2$ (p$_t$ = 60 GPa) (derived from the evaluation of the *E-V* data by the Murnaghan EOS).

5.1.4 SrSiN$_2$

α-SrSiN$_2$ crystallizes in the monoclinic space group $P2_1/c$ (no. 14) in a layered structure [14] (Figure 5.11). The basic structure motives are pairs of edge-sharing SiN$_4$ tetrahedra, which are connected through the remaining four corners to other tetrahedra pairs, thereby forming non-corrugated layers in the [011] plane. The Sr^{2+} ions are situated between these layers in two layers, being eight-fold coordinated by N. β-SrSiN$_2$, the first high-pressure polymorph found, exhibits the BaSiN$_2$ structure (space group *Cmca*, no. 64) [14] (Figure 5.11), which is closely related to the α-SrSiN$_2$ structure insofar as they are connected by a group-subgroup relation. The further search for high-pressure polymorphs revealed three more structures besides β-SrSiN$_2$. γ-SrSiN$_2$ was identified with the CaSiN$_2$-type structure [14] (Figure 5.1). δ-SrSiN$_2$ adopts a hitherto undetected structure in space group *Pbcm* (no. 57) (Figure 5.11), which is related to the CaSiN$_2$-type structure by a group-subgroup relation. However, in this structure Si is no longer tetrahedrally coordinated, but in a trigonal bipyramidal way, whereas Sr is still eight-fold coordinated as in α-, β-

and γ-SrSiN$_2$. Finally, ϵ-SrSiN$_2$ was found to exhibit the m-LiFeO$_2$ structure (space group $R\bar{3}m$, no. 166) [244]. Here, the coordination of Si atoms is increased to six (SiN$_6$ octahedra), whereas the coordination of Sr decreases to six (SrN$_6$ octahedra) (Figure 5.1).

α-SrSiN$_2$ α-BaSiN$_2$

Si1   Si2   Si1   Si1

Si1   Si2   Si1   Si1

Pbcm structure type   *Imma* structure type
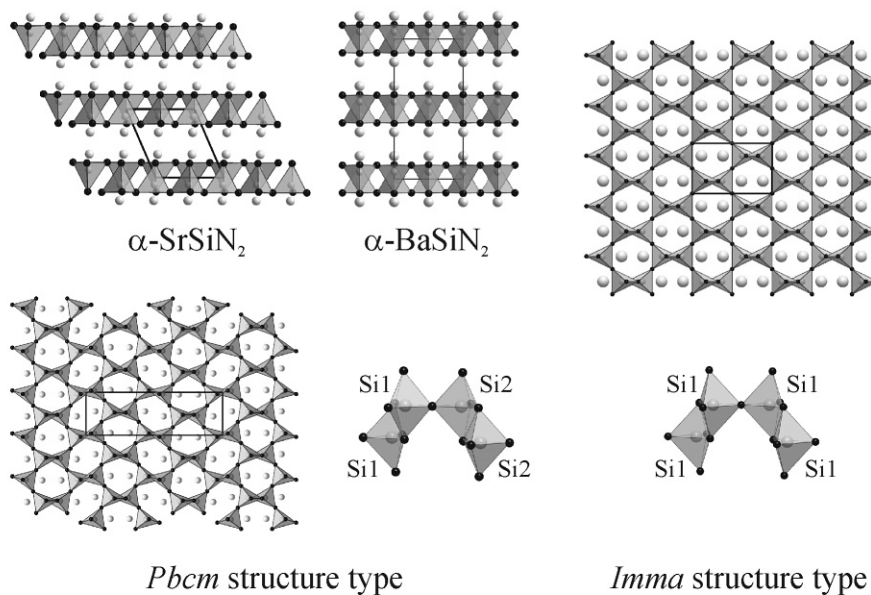
Figure 5.11: Crystal Structures of further MSiN$_2$ structures: (1) α-SrSiN$_2$, view along [010] (SiN$_4$ tetrahedra drawn light gray, Sr atoms between the SiN$_4$ tetrahedra layers), (2) α-BaSiN$_2$, view along [001] (SiN$_4$ tetrahedra drawn light gray, Ba atoms between the SiN$_4$ tetrahedra layers), (3) *Pbcm* structure, left: view along [001], right: edge- and corner-sharing SiN$_5$ trigonal bipyramids (SiN$_5$ trigonal bipyramids light gray, metal atoms in channels), (4) *Imma* structure, top: view along [001], bottom: edge- and corner-sharing SiN$_5$ trigonal bipyramids (SiN$_5$ trigonal bipyramids light gray, metal atoms in channels).

The calculated bond lengths (Table 5.6) in α-, β- and γ-SrSiN$_2$, which all three contain tetrahedrally coordinated Si and eight-fold coordinated Sr, correspond well with those found in experimental α-SrSiN$_2$. Sr-N distances in δ-SrSiN$_2$ also fit in this category. The Sr-N distances calculated for ϵ-SrSiN$_2$ are on average shorter and are close to the lower limit of the Sr-N distances for eight-fold coordinated Sr. Si-N bonds for octahedrally coordinated Si in ϵ-SrSiN$_2$ are about 20 pm longer than those in α-, β- and γ-SrSiN$_2$ and some 10 pm longer than those found in γ-Si$_3$N$_4$ [4], but still about 10 pm shorter than those for SiN$_6$ in Ca$_{16}$Si$_{15}$O$_6$N$_{32}$ [243]. δ-SrSiN$_2$ shows a noticeable large difference for axial Si-N distances of the SiN$_5$ trigonal bipyramids

between LDA and GGA calculations (this finding is likely to result from an over-estimation of the cohesive energy in LDA), whereas the three equatorial bonds are similar. The calculated Si-N$_{ax}$ distances within GGA are about 30 pm longer than within LDA and correspond to an individual bond valence ν_{ij} [1] [256–258] of 0.15. ν_{ij} for Si-N$_{ax}$ within LDA amounts to 0.43. The valence sums for Si are 3.6 (GGA) and 4.0 (LDA), respectively. The Si-N$_{ax}$ distances are approximately parallel to [001]. The development of the unit cell parameters under pressure shows, that the only unit cell parameter, that is constantly decreasing in lengths is the c-axis, whereas the a-axis remains fairly constant before it starts to decrease and the b-axis even increases at first (Figure 5.12). The equatorial Si-N bonds of the SiN$_5$ trigonal bipyramids
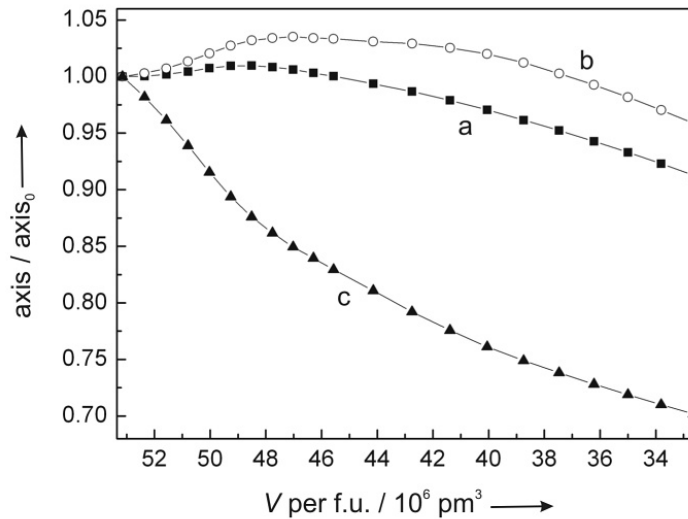
Figure 5.12: Development of the unit cell parameters of δ-SrSiN$_2$ upon compression.

---

[1] The individual bond valence according to the bond-length-bond-strength concept for a bond between two atoms i and j is calculated via

$$\nu_{ij} = \exp\left\{\frac{R_{ij} - d_{ij}}{b}\right\}.$$

Here, R_{ij} is the bond valence parameter, b a constant (34 pm) and d_{ij} the distance between atoms i and j. The valence sum is the sum of the individual bond valences:

$$V_i = \sum_j \nu_{ij}.$$

The bond-length-bond-strength concept has been developed from Pauling's concept of bond strength [255] and is an empiric approach to bonding.

remain almost constant during compression, whereas the axial Si-N bond lengths are decreased constantly, arriving at reasonable values after 20 % volume reduction (Figure 5.13), well before δ-SrSiN$_2$ is adopted as a high-pressure phase.
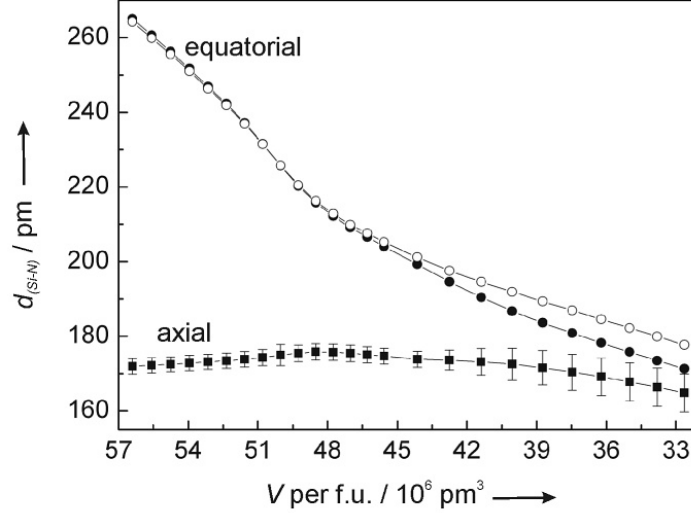
Figure 5.13: Si-N bond lengths in δ-SrSiN$_2$. The error bars for the axial bonds give the dispersion of the axial bonds. Black circles give the Si1-N distances, white circles the Si2-N distances.

The zero-pressure bulk modulus of α-SrSiN$_2$ amounts to 102 GPa and increases from 104 GPa for β-SrSiN$_2$ to 125 GPa for γ-SrSiN$_2$ (Table 5.12). δ-SrSiN$_2$ has the lowest bulk modulus (33 GPa), which renders it the most compressible of all SrSiN$_2$ polymorphs. This finding is attributed to the exceptionally large compressibility of the Si-N$_{ax}$ bonds parallel to the c-axis, compared to those situated in the ab-plane (Figure 5.13). Furthermore, while the a- and b-axis are only reduced by 9 and 3 %, respectively, upon a volume reduction of 45 %, the c-axis is reduced by 35 % (Figure 5.12). The zero-pressure ϵ-SrSiN$_2$ evinces the highest bulk modulus, exhibiting 163 GPa, which is similar to the bulk moduli of MgO (160 GPa [259]) and CaIrO$_3$ (189 GPa [253]).

α-SrSiN$_2$ exhibits both the lowest energy (-28.633 eV per formula unit) and density ($\rho = 4.24$ g cm^{-3}, matching experimental 4.35 g cm^{-3} [14]), referring to GGA calculations. β-SrSiN$_2$ is 0.010 eV higher in energy and 0.47 % denser ($\rho = 4.26$ g cm^{-3})

Table 5.6: Bond lengths (in pm) in α-, β-, γ-, δ- and ϵ-SrSiN$_2$ compared to experimental values.

Structure	Bond type	LDA	GGA	exp.
α-SrSiN$_2$	Sr$^{[8]}$-N	253.11–307.64	260.10–322.87	256.29–314.52 [14]
	Si$^{[4]}$-N	170.21–176.77	172.20–178.75	170.88–178.80 [14]
β-SrSiN$_2$	Sr$^{[8]}$-N	251.90–296.99	256.87–308.01	/
	Si$^{[4]}$-N	170.09–176.60	172.06–178.34	/
γ-SrSiN$_2$	Sr$^{[8]}$-N	252.25–319.43	256.85–325.04	/
	Si$^{[4]}$-N	173.49–175.39	175.69–177.62	/
δ-SrSiN$_2$	Sr$^{[8]}$-N	242.43–338.90	240.21–330.66	/
	Si$^{[3+2]}$-N$_{eq}$	173.54-178.12	171.01–175.18	/
	Si$^{[3+2]}$-N$_{ax}$	208.10, 208.67	246.36, 246.89	/
ϵ-SrSiN$_2$	Sr$^{[6]}$-N	250.71	254.87	/
	Si$^{[6]}$-N	199.74	203.53	/
γ-Si$_3$N$_4$	Si$^{[6]}$-N	186.84 [6]	189.04 [6]	186.26 [5]
Ce$_{16}$Si$_{15}$O$_6$N$_{32}$	Si$^{[6]}$-N	/	/	210.44 [243]

Ionic Radii	bond type	Shannon [183]	Baur [184]	
	Sr$^{[6]}$-N	264	/	
	Sr$^{[8]}$-N	272	273	
	Si$^{[4]}$-N	172	179	
	Si$^{[6]}$-N	182	/	

than α-SrSiN$_2$, followed by γ-SrSiN$_2$. γ-SrSiN$_2$ exhibits a 0.181 eV higher energy than α-SrSiN$_2$ and 0.171 eV higher energy than β-SrSiN$_2$ and is about 4.93 % denser than β-SrSiN$_2$ and 5.42 % denser than α-SrSiN$_2$ ($\rho = 4.47$ g cm^{-3}). The energy of δ-SrSiN$_2$ in its ground state comes out 1.523 eV higher than that of α-SrSiN$_2$ and 1.342 eV higher than that of γ-SrSiN$_2$. The density is increased by 0.46 % with respect to γ-SrSiN$_2$ and 5.90 % with respect to α-SrSiN$_2$. ϵ-SrSiN$_2$ is the polymorph with the highest density and energy. With $\rho = 5.16$ g cm^{-3} it is 21.70 % denser than α-SrSiN$_2$ and still 14.9 % denser than δ-SrSiN$_2$. Its energy lays 2.975 eV above that of α-SrSiN$_2$ and 1.452 eV above that of δ-SrSiN$_2$. For an overview of the data given here, see Table 5.12.

In Figure 5.14 the energy-volume curves of all considered SrSiN$_2$ polymorphs are depicted. From these the enthalpy-pressure phase diagram as given in Figure 5.15 was derived. α-SrSiN$_2$ (symmetry fixed to $P2_1/c$) is only stable up to approximately 2 GPa. The calculated transition pressure into β-SrSiN$_2$ has a rather large error margin of 1 GPa because of the similar slopes of the enthalpy-pressure curves, which results in minimal differences in the evaluation by different equations of state having
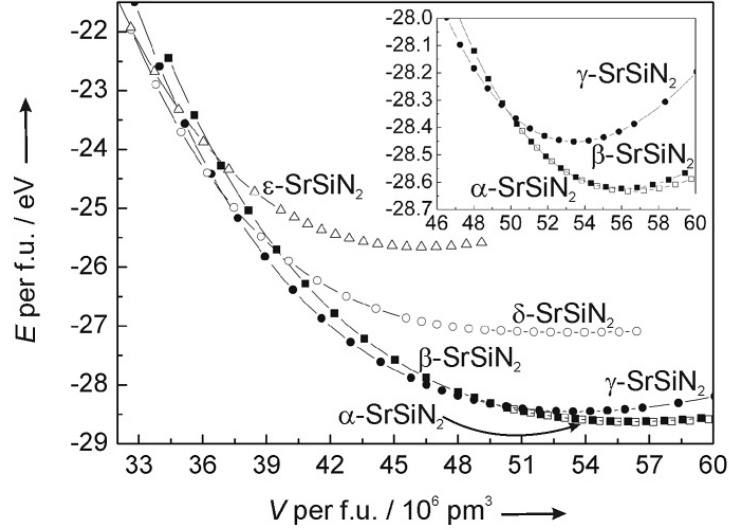
Figure 5.14: Energy-volume (E-V) phase diagram of α-, β-, γ-, δ- and ϵ-SrSiN$_2$, calculated within the GGA. Each symbol represents a calculation.
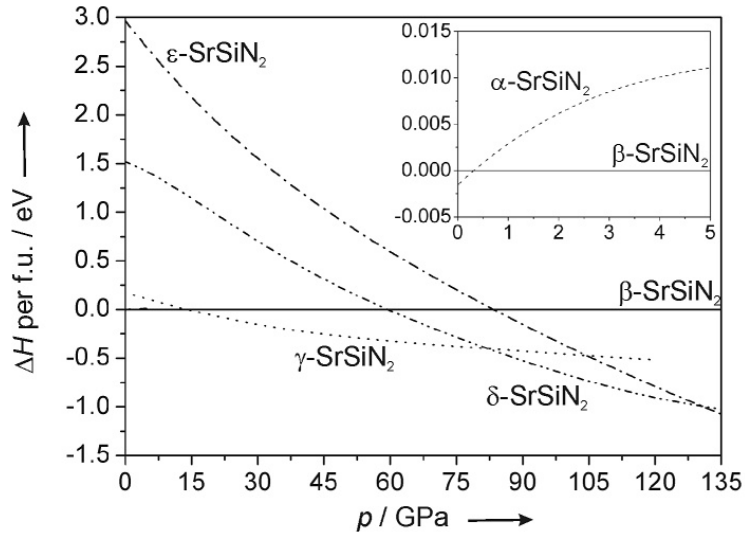
Figure 5.15: Enthalpy-pressure (H-p) diagram for the transition of α-SrSiN$_2$ into β-SrSiN$_2$ (p$_t$ = 2 GPa), into γ-SrSiN$_2$ (p$_t$ = 14 GPa), into δ-SrSiN$_2$ (p$_t$ = 84 GPa) and into ϵ-SrSiN$_2$ (p$_t$ = 130 GPa) (derived from the evaluation of the E-V data by the Murnaghan EOS).

significant influences on the resultant transition pressure. β-SrSiN$_2$ remains the stable polymorph up to 14 GPa, when γ-SrSiN$_2$ becomes lower in enthalpy. The calculated transition pressure of γ-SrSiN$_2$ into δ-SrSiN$_2$ amounts to 84 GPa. At pressures exceeding 130 GPa the enthalpy of ϵ-SrSiN$_2$ is lower than that of δ-SrSiN$_2$. The coordination of Sr (CN = 8) remains constant up to the transition into ϵ-SrSiN$_2$, when it decreases to six. In α-, β- and γ-SrSiN$_2$ Si is tetrahedrally coordinated and increases to five in δ-SrSiN$_2$ and further to six in ϵ-SrSiN$_2$. As in CaSiN$_2$ (c.f. chapter 5.1.3, page 88) the density gained by octahedrally coordinated Si combined with a higher condensation degree of the SiN$_x$ polyhedra (coordination representation for the Si-N framework: $\alpha/\beta/\gamma$-SrSiN$_2$: $[\text{Si}^{[4]}\text{N}_2^{[2]}]^{2-}$; δ-SrSiN$_2$: $[\text{Si}^{[5]}\text{N}^{[2]}\text{N}^{[3]}]^{2-}$; ϵ-SrSiN$_2$: $[\text{Si}^{[6]}\text{N}_2^{[3]}]^{2-}$) is overcompensating the reduction of the coordination number of Sr. An overview of SrSiN$_2$ and its predicted high-pressure phases is given in Figure 5.16.
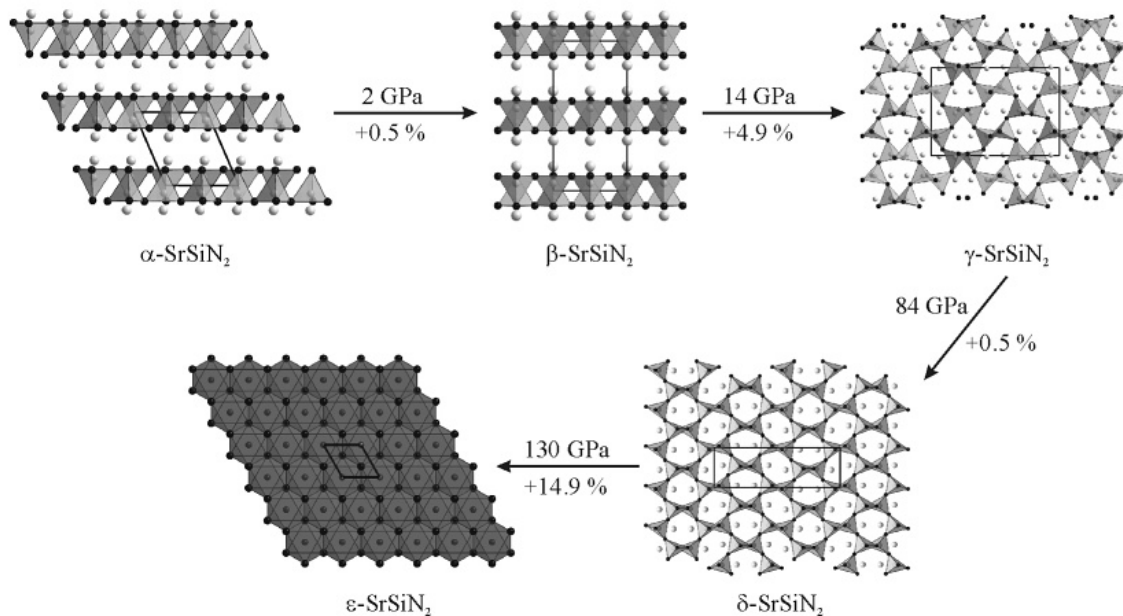
Figure 5.16: Sequence of structures of SrSiN$_2$ together with transition pressures and changes in density.

5.1.5 BaSiN$_2$

α-BaSiN$_2$ is a layered nitridosilicate, crystallizing in the orthorhombic space group *Cmca* (no. 64) [14]. The layers are built up by so-called "bowtie" units, consisting of a pair of edge-sharing SiN$_4$ tetrahedra. These units are further interconnected via common corners, forming layers perpendicular to [010] (Figure 5.11). As a second structure of interest, the CaSiN$_2$ structure, a three-dimensional corner-sharing SiN$_4$ tetrahedra network structure [14] was identified (Figure 5.1) and subsequently denoted β-BaSiN$_2$. A third structure, termed γ-BaSiN$_2$ exhibits the aforementioned *Pbcm* structure of δ-SrSiN$_2$, consisting of edge-sharing trigonal bipyramids (Figure 5.11), already found for δ-SrSiN$_2$ (compare chapter 5.1.4, page 90). The coordination for Ba is 10 in α-BaSiN$_2$, 10+1 in β-BaSiN$_2$ and 9 in the *Pbcm* structure.

With an energy per formula unit of -28.711 eV α-BaSiN$_2$ is the polymorph with the lowest energy. The calculated density of 5.14 g cm^{-3} (matching experimental 5.34 g cm^{-3} [14]) is also the lowest of all considered polymorphs. β-BaSiN$_2$ is 0.414 eV higher in energy and 5.64 % denser than α-BaSiN$_2$. γ-BaSiN$_2$ is the densest polymorph found. With its density of 5.80 g cm^{-3} it is 12.8 % denser than α-BaSiN$_2$ and 6.8 % denser than β-BaSiN$_2$. Its energy is 2.012 eV higher than that of α-BaSiN$_2$ and 1.599 eV than that of β-BaSiN$_2$.

The energy-volume curves calculated for the different BaSiN$_2$ polymorphs are depicted in Figure 5.17, the corresponding enthalpy-pressure diagram in Figure 5.18. Accordingly, layered α-BaSiN$_2$ remains lowest in enthalpy up to 43 GPa. From here on up to 102 GPa the three-dimensional tetrahedra network structure of β-BaSiN$_2$ is the most stable polymorph. At pressures exceeding 102 GPa γ-BaSiN$_2$ will be adopted. An uncertainty of about 5 GPa in this transition pressure, resulting solely from the use of different equations of state (EOS) to fit the calculated *E-V* data, was observed. This uncertainty is attributed to the different aptitude of the EOSs to fit data at (very) large compressions (c.f. chapter 2.7.4, page 26). Furthermore, since the transition of β-BaSiN$_2$ into γ-BaSiN$_2$ is a displacive one, mainly affected by a rotation of the SiN$_4$ tetrahedra (see below Figure 5.19 and chapter 5.2, page 108), the transformation should occur gradually, leaving some leeway for the actual transition pressure.
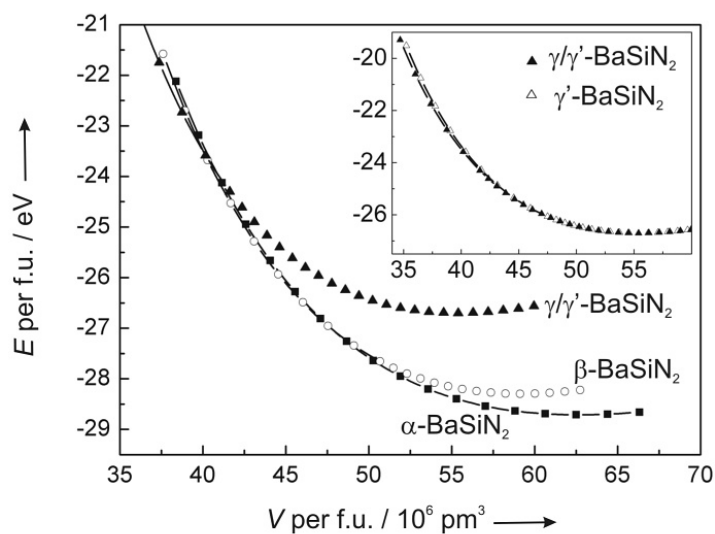
Figure 5.17: Energy-volume (E-V) phase diagram of α-, β-, γ- and γ'-BaSiN$_2$, calculated within the GGA. Each symbol represents a calculation. Inset shows the E-V of γ/γ'-BaSiN$_2$ and of γ'-BaSiN$_2$ (symmetry fixed to *Imma*).
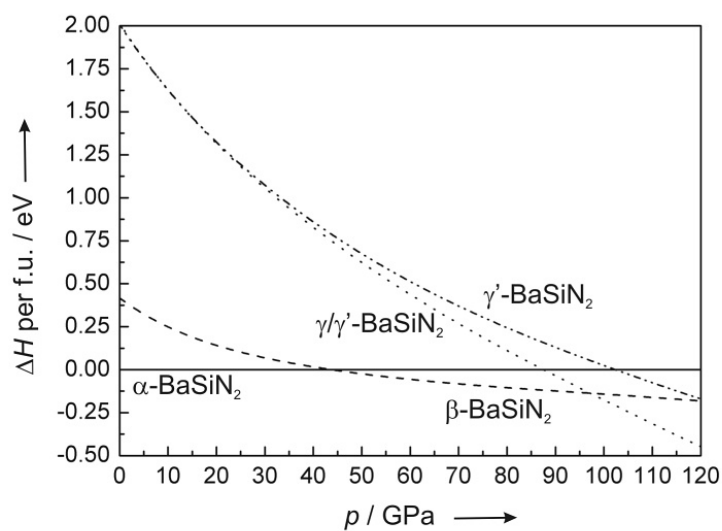
Figure 5.18: Enthalpy-pressure (H-p) diagram for the transition of α-BaSiN$_2$ into β-BaSiN$_2$ ($p_t = 43$ GPa) and into γ-BaSiN$_2$ ($p_t = 102$ GPa) as well as of γ'-BaSiN$_2$ (*Imma*) into γ-BaSiN$_2$ (*Pbcm*) ($p_t = 32$-35 GPa) (derived from the evaluation of the E-V data by the Murnaghan EOS).

The *Pbcm* structure of γ-BaSiN$_2$, however, is not stable at lower pressure. It is not quenchable to zero pressure when optimizing all structural parameters (unit cell as well as atomic parameters). Upon fixing the unit cell axes ratios, the structure could be quenched to zero pressure. However, a gradual distortion of the structure was detected, resulting in a more symmetric structure with space group *Imma*, denoted γ'-BaSiN$_2$. The two structures, *Imma* and *Pbcm*, are once more related by a group subgroup relation (Figure 5.19). The *Imma* structure exhibits the same topology as the *Pbcm* structure and is built up by edge- and corner-sharing trigonal bipyramids (Figure 5.11). Interestingly, this structure transformation upon compression/relaxation is not reflected in the energy-volume calculations and the symmetrization could not be suppressed in calculations using the *Pbcm* primitive unit cell. Differentiation of the *E-V* curve ($\partial E/\partial V$) reveals no fluctuations for the derivation (Figure 5.20), which would be characteristic for structural transformations. However, upon fixing the symmetry to *Imma*, using the smaller *Imma* unit cell ($V_{(Imma)} = {}^1/_2 \, V_{(Pbcm)}$), the obtained *E-V* curve and the thereof derived enthalpy-pressure curve diverge from the *Imma/Pbcm* curve from the point of the *Imma-Pbcm* transformation on (32 to 35 GPa) (Figure 5.17 and 5.18). The distortion from *Imma* to *Pbcm* is clearly energetically favored above 35 GPa (Figure 5.18). A comparison of the atomic coordinates of γ'-BaSiN$_2$ at zero pressure, of γ'-BaSiN$_2$ at 32 GPa, of γ-BaSiN$_2$ at 35 GPa and of γ-BaSiN$_2$ at 105 GPa in *Pbcm* setting to illustrate the gradual distortion is given in Table 5.7. Full crystallographic data for γ'-BaSiN$_2$ at zero pressure and of γ-BaSiN$_2$ at 105 GPa are given in Appendix A.
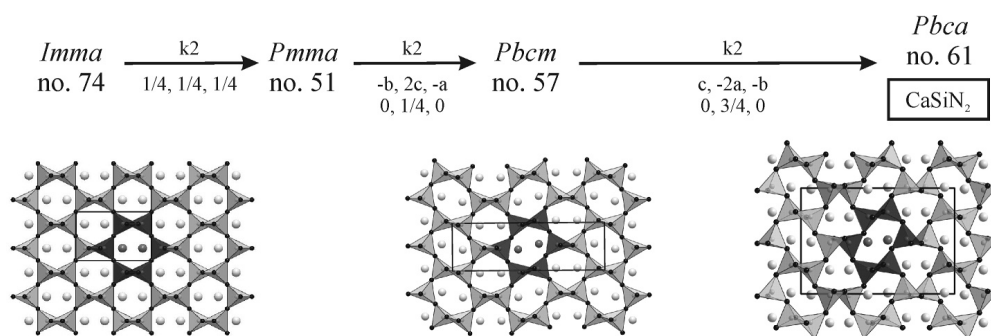
Figure 5.19: Group-subgroup relation of the CaSiN$_2$, the *Pbcm* and the *Imma* structure (Compare Figure 5.23 for relation to β-cristobalite).
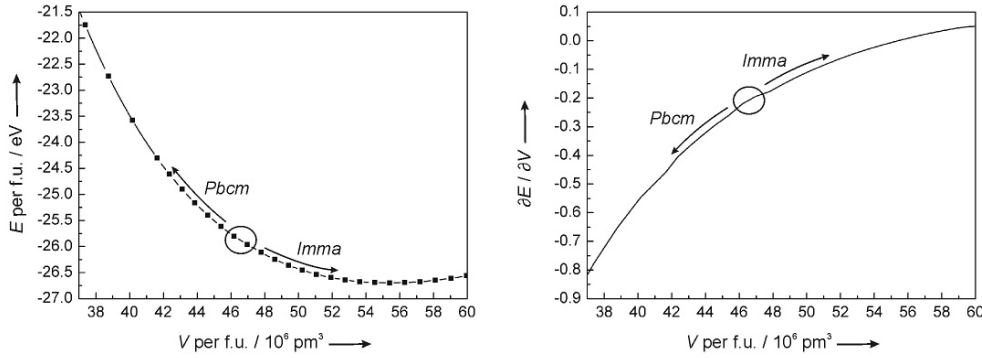
Figure 5.20: Energy-volume (*E-V*) of γ/γ'-BaSiN$_2$ (left) and differentiation $\partial E/\partial V$ thereof (right); the *Imma/Pbcm* transformation is marked by a circle in both graphs.

Upon further pressure reduction, the *Imma* structure of γ'-BaSiN$_2$ further distorts below 10 GPa within space group *Imma* (Figure 5.21), with the final structure at zero pressure (γ'-BaSiN$_2$ III) possessing a very low density, even lower than that of α-BaSiN$_2$ by 21 %. At zero pressure the enthalpy difference between γ'-BaSiN$_2$ and γ'-BaSiN$_2$ III amounts to 0.158 eV, with γ'-BaSiN$_2$ III being still 1.854 eV higher in enthalpy than α-BaSiN$_2$.
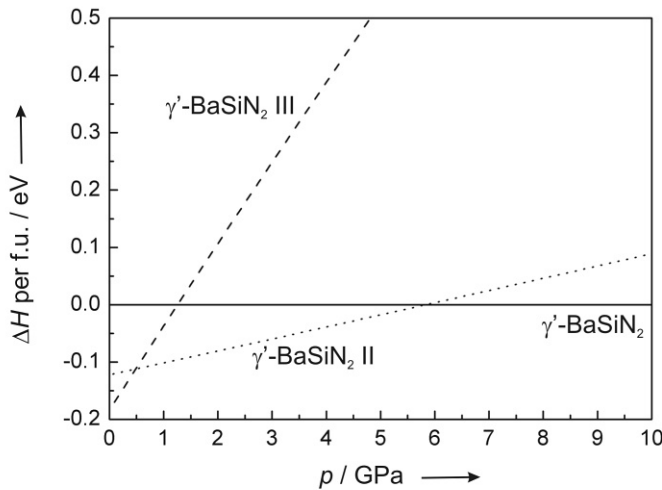
Figure 5.21: Enthalpy-pressure (*H-p*) diagram for the transition of γ'-BaSiN$_2$ III into γ'-BaSiN$_2$ II ($p_t = 0.5$ GPa) and into γ'-BaSiN$_2$ ($p_t = 6$ GPa) (derived from the evaluation of the *E-V* data by the Murnaghan EOS).

Table 5.7: Atom coordinates of γ'-BaSiN$_2$ (*Pbcm* structure) at 0 GPa and 32 GPa and of γ-BaSiN$_2$ (*Imma* structure) at 35 GPa and 105 GPa (GGA calculation) in *Pbcm*. Decimal numbers marked with [a] have fixed values for space group *Imma* (e.g. 0.5 $\hat{=}$ 1/2), but could deviate from this value in space group *Pbcm*.

atom	structure	Wyckoff-Position	x	y	z
Ba1	γ'-BaSiN$_2$ 0 GPa	4d	0.5[a]	0.06750	3/4
	γ'-BaSiN$_2$ 32 GPa		0.5[a]	0.06451	3/4
	γ-BaSiN$_2$ 35 GPa		0.44775	0.06329	3/4
	γ-BaSiN$_2$ 105 GPa		0.41827	0.06061	3/4
Ba2	γ'-BaSiN$_2$ 0 GPa	4d	1[a]	0.18250	3/4
	γ'-BaSiN$_2$ 32 GPa		1[a]	0.18549	3/4
	γ-BaSiN$_2$ 35 GPa		0.95929	0.18555	3/4
	γ-BaSiN$_2$ 105 GPa		0.93317	0.18658	3/4
Si1	γ'-BaSiN$_2$ 0 GPa	4d	0.5[a]	0.18860	1/4
	γ'-BaSiN$_2$ 32 GPa		0.5[a]	0.18927	1/4
	γ-BaSiN$_2$ 35 GPa		0.46649	0.18945	1/4
	γ-BaSiN$_2$ 105 GPa		0.44409	0.19073	1/4
Si2	γ'-BaSiN$_2$ 0 GPa	4d	1[a]	0.06140	1/4
	γ'-BaSiN$_2$ 32 GPa		1[a]	0.06073	1/4
	γ-BaSiN$_2$ 35 GPa		0.97284	0.06097	1/4
	γ-BaSiN$_2$ 105 GPa		0.95136	0.05981	1/4
N1	γ'-BaSiN$_2$ 0 GPa	4d	0.5[a]	0.28699	1/4
	γ'-BaSiN$_2$ 32 GPa		0.5[a]	0.28979	1/4
	γ-BaSiN$_2$ 35 GPa		0.46851	0.29022	1/4
	γ-BaSiN$_2$ 105 GPa		0.44379	0.29327	1/4
N2	γ'-BaSiN$_2$ 0 GPa	4d	0.75[a]	0.125[a]	1/4
	γ'-BaSiN$_2$ 32 GPa		0.75[a]	0.125[a]	1/4
	γ-BaSiN$_2$ 35 GPa		0.70654	0.11975	1/4
	γ-BaSiN$_2$ 105 GPa		0.67902	0.11816	1/4
N3	γ'-BaSiN$_2$ 0 GPa	4d	0.25[a]	0.125[a]	1/4
	γ'-BaSiN$_2$ 32 GPa		0.25[a]	0.125[a]	1/4
	γ-BaSiN$_2$ 35 GPa		0.20410	0.13123	1/4
	γ-BaSiN$_2$ 105 GPa		0.17285	0.13458	1/4
N4	γ'-BaSiN$_2$ 0 GPa	4d	1[a]	0.03699	3/4
	γ'-BaSiN$_2$ 32 GPa		1[a]	0.03979	3/4
	γ-BaSiN$_2$ 35 GPa		0.94855	0.03741	3/4
	γ-BaSiN$_2$ 105 GPa		0.90961	0.03497	3/4

The high-pressure phases of BaSiN$_2$ together with their transition pressures and density changes are illustrated in Figure 5.22.

The calculated Ba-N distances and Si-N bond lengths for α-BaSiN$_2$ agree well with those in experimental α-BaSiN$_2$ (Table 5.8). β-BaSiN$_2$, which, like α-BaSiN$_2$, contains tetrahedrally coordinated Si, shows similar bond distances (Table 5.8). γ- and
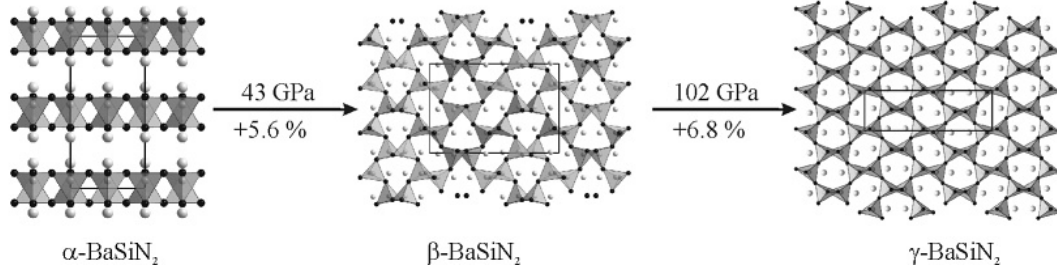
Figure 5.22: Sequence of structures of BaSiN₂ together with transition pressures and changes in density.

γ'-BaSiN₂ exhibits SiN₅ trigonal bipyramids for which axial and equatorial bonds differ in length. The equatorial bonds are in their lengths between those in α-BaSiN₂ and γ-Si₃N₄, whereas the axial bonds are longer, in average about 10 pm longer than those found in Ce₁₆Si₁₅O₆N₃₂ for SiN₆ octahedra bonds (Table 5.8). Individual bond valence ν_{ij} calculations (c.f. footnote on page 92 and [256–258]) result in values for Si-N$_{ax}$ of 0.33 (LDA) and 0.29 (GGA), respectively, which is about $^3/_4$rd of the value for Si$^{[6]}$-N in Ce₁₆Si₁₅O₆N₃₂ ($\nu_{ij} = 0.41$). The valence sum for Si in γ- and γ'-BaSiN₂ amounts to 3.7 (LDA) and 3.4 (GGA). For γ'-BaSiN₂ II and γ'-BaSiN₂ III the equatorial bonds become shorter and the axial bonds longer (Table 5.8), resulting in a trigonal coordination for Si and a five-fold coordination for Ba in γ'-BaSiN₂ III according to MAPLE [175–178] calculations. The resultant structures are built up by chains of planar SiN₃ units, which are interconnected by Ba-N coordinative bonds. This makeup of these two structures renders them most unlikely candidates for nitridosilicates as all nitridosilicates are built up by at least SiN₄ tetrahedra as fundamental building blocks.

The zero-pressure bulk moduli for α-, β- and γ/γ'-BaSiN₂ were calculated to 89, 129 and 135 GPa, increasing from the ambient-pressure to the second high-pressure phase. These bulk moduli are comparable to those of rocksalt-type SrO (82 to 108 GPa) and CaO (96 to 129 GPa) ([260, 261] and references therein). As expected, the zero-pressure bulk moduli for γ'-BaSiN₂ II and γ'-BaSiN₂ III are lower, 118 GPa and 80 GPa respectively, than that of γ/γ'-BaSiN₂, since the elongation of the axial Si-N distances in the SiN₅ trigonal bipyramids results in a higher compressibility of the structure, at least along [001].

Table 5.8: Bond lengths (in pm) in α-, β-, γ- and γ'-BaSiN$_2$ compared to experimental values.

Structure	Bond type	LDA	GGA	exp.
α-BaSiN$_2$	Ba[10]-N	$275.73 - 356.83$	$281.42 - 361.94$	$277.72 - 357.49$ [14]
	Si[4]-N	$170.99 - 177.17$	$173.13 - 179.06$	$172.04 - 177.70$ [14]
β-BaSiN$_2$	Ba[10+1]-N	$273.34 - 384.66$	$280.45 - 390.60$	/
	Si[4]-N	$172.79 - 174.60$	$175.14 - 177.11$	/
γ/γ'-BaSiN$_2$	Ba[9]-N	$256.25 - 365.36$	$261.36 - 373.46$	/
	Si[3+2]-N$_{eq}$	$174.72 - 178.23$	$176.75 - 181.55$	/
	Si[3+2]-N$_{ax}$	218.45	222.92	/
γ'-BaSiN$_2$ II	Ba[9]-N	$246.55 - 342.57$	$251.44 - 349.89$	/
	Si[3]-N$_{eq}$	$168.33 - 170.61$	$170.23 - 173.22$	/
	Si[3]-N$_{ax}$	251.11	256.05	/
γ'-BaSiN$_2$ III	Ba[5]-N	$253.87 - 295.81$	$258.31 - 301.79$	/
	Si[3]-N$_{eq}$	$163.54 - 166.17$	$164.92 - 168.09$	/
	Si[3]-N$_{ax}$	355.36	361.16	/
γ-Si$_3$N$_4$	Si[6]-N	186.84 [6]	189.04 [6]	186.26 [5]
Ce$_{16}$Si$_{15}$O$_6$N$_{32}$	Si[6]-N	/	/	210.44 [243]
Ionic Radii	bond type	Shannon [183]	Baur [184]	
	Ba[6]-N	281	290	
	Ba[8]-N	288	304	
	Ba[9]-N	293	/	
	Ba[10]-N	298	/	
	Si[4]-N	172	179	
	Si[6]-N	182	/	

Table 5.9: E$_0$, V$_0$, B$_0$ and ρ_0 of α-, β- and γ-BeSiN$_2$ (E$_0$ and V$_0$ given per formula unit).

	E$_0$ / eV	V$_0$ / 10^6 pm^3	B$_0$ / GPa	ρ_0 / g cm^{-1}
α-BeSiN$_2$	-30.902	33.87	220	3.19
β-BeSiN$_2$	-30.897	33.82	222	3.20
γ-BeSiN$_2$	-28.756	28.29	244	3.82

Table 5.10: E$_0$, V$_0$, B$_0$ and ρ_0 of α- and β-MgSiN$_2$ (E$_0$ and V$_0$ given per formula unit).

	E$_0$ / eV	V$_0$ / 10^6 pm^3	B$_0$ / GPa	ρ_0 / g cm^{-1}
α-MgSiN$_2$	-28.495	43.35	172	3.08
β-MgSiN$_2$	-27.330	34.42	223	3.88

Table 5.11: E$_0$, V$_0$, B$_0$ and ρ_0 of α-, β- and γ-CaSiN$_2$ (E$_0$ and V$_0$ given per formula unit).

	E$_0$ / eV	V$_0$ / 10^6 pm^3	B$_0$ / GPa	ρ_0 / g cm^{-1}
α-CaSiN$_2$	-29.140	49.26	131	3.24
β-CaSiN$_2$	-29.134	48.96	126	3.26
γ-CaSiN$_2$	-27.309	41.31	189	3.87
"MgSiN$_2$"	-29.141	50.64	121	3.15

Table 5.12: E$_0$, V$_0$, B$_0$ and ρ_0 of α-, β-, γ-, δ- and ϵ-SrSiN$_2$ (E$_0$ and V$_0$ given per formula unit).

	E$_0$ / eV	V$_0$ / 10^6 pm^3	B$_0$ / GPa	ρ_0 / g cm^{-1}
α-SrSiN$_2$	-28.633	56.34	102	3.24
β-SrSiN$_2$	-28.623	56.00	104	4.26
γ-SrSiN$_2$	-28.452	53.41	125	4.47
δ-SrSiN$_2$	-27.110	53.15	33	4.49
ϵ-SrSiN$_2$	-25.658	46.28	163	5.16

Table 5.13: E$_0$, V$_0$, B$_0$ and ρ_0 of α-, β-, γ- and γ'-BaSiN$_2$ (E$_0$ and V$_0$ given per formula unit).

	E$_0$ / eV	V$_0$ / 10^6 pm^3	B$_0$ / GPa	ρ_0 / g cm^{-1}
α-BaSiN$_2$	-28.711	62.50	89	5.14
β-BaSiN$_2$	-28.298	59.12	129	5.43
γ/γ'-BaSiN$_2$	-26.699	55.40	135	5.80
γ'-BaSiN$_2$ II	-26.814	59.39	118	5.41
γ'-BaSiN$_2$ III	-26.857	79.06	80	4.06

5.2 Discussion

The ground state structures of α-MSiN$_2$ (M = Be, Mg, Ca) as well as β-BeSiN$_2$ and β-CaSiN$_2$ are related to the filled β-cristobalite structure (filled C9 structure) by group-subgroup relations (Figure 5.23). They derive from the parent filled C9 structure (space group $Fd\bar{3}m$, no. 227) by concerted rotation of tetrahedra (for a detailed discussion on these rotation patterns see Appendix E). Hence, displacive phase transition pathways are conceivable for α-BeSiN$_2$ ($Pna2_1$) into β-BeSiN$_2$ ($I\bar{4}2d$) and for α-CaSiN$_2$ ($Pnma$) into β-CaSiN$_2$ ($I\bar{4}2d$). This might well result in quite low activation energy barriers for these two phase transitions.

The structures of γ-BeSiN$_2$ ($I4_1/amd$, s-LiFeO$_2$), β-MgSiN$_2$ ($R\bar{3}m$, m-LiFeO$_2$), γ-CaSiN$_2$ ($R\bar{3}m$, m-LiFeO$_2$) and ϵ-SrSiN$_2$ ($R\bar{3}m$, m-LiFeO$_2$) are all related to the rocksalt structure. The difference between the s- and m-LiFeO$_2$-type structures is a different ordering of the two types of cations on octahedral sites. In m-LiFeO$_2$ layers of condensed LiO$_6$ octahedra alternate with layers of condensed FeO$_6$ octahedra. In s-LiFeO$_2$ each layer is occupied half by Li and half by Fe cations. The s-LiFeO$_2$-type structure seems to be preferred for compounds with both cations having approximately the same size as in BeSiN$_2$ (r(Be) = 59 [183], 31 pm [184]; r(Si) = 54 [183], 29 pm [184]). If the two cations differ substantially in size as in MgSiN$_2$, CaSiN$_2$ and SrSiN$_2$ (r(Mg) = 86 [183], 70 pm [184]; r(Ca) = 114 [183], 105 pm [184]; r(Sr) = 132 [183], 123 pm [184]), the m-LiFeO$_2$-type structure is favored, as the height of the octahedral layers can be adjusted to the size of the cation occupying it.

The s-LiFeO$_2$ structure adopted by BeSiN$_2$ (γ-phase) is related to the α-BeSiN$_2$ (and α-MgSiN$_2$) structure by a group-subgroup relation (Figure 5.24). By compressing α-BeSiN$_2$ along two unit cell axes and simultaneously elongating the third (corresponding to the c-axis in tetragonal s-LiFeO$_2$), the distorted hexagonal close packing (hcp) of the anions in α-BeSiN$_2$ is transformed into a cubic close packing (ccp, distorted as well). The cations are thereby transferred from the tetrahedral sites in hcp to the octahedral sites in ccp by only a small movement (Figure 5.24). This transformation is analogous to the well known wurtzite-rocksalt transition [262–270], since α-BeSiN$_2$ exhibits an ordered wurtzite structure and s-LiFeO$_2$ the corresponding ordered rocksalt structure (compare Figure 5.25). The ordering of the cations
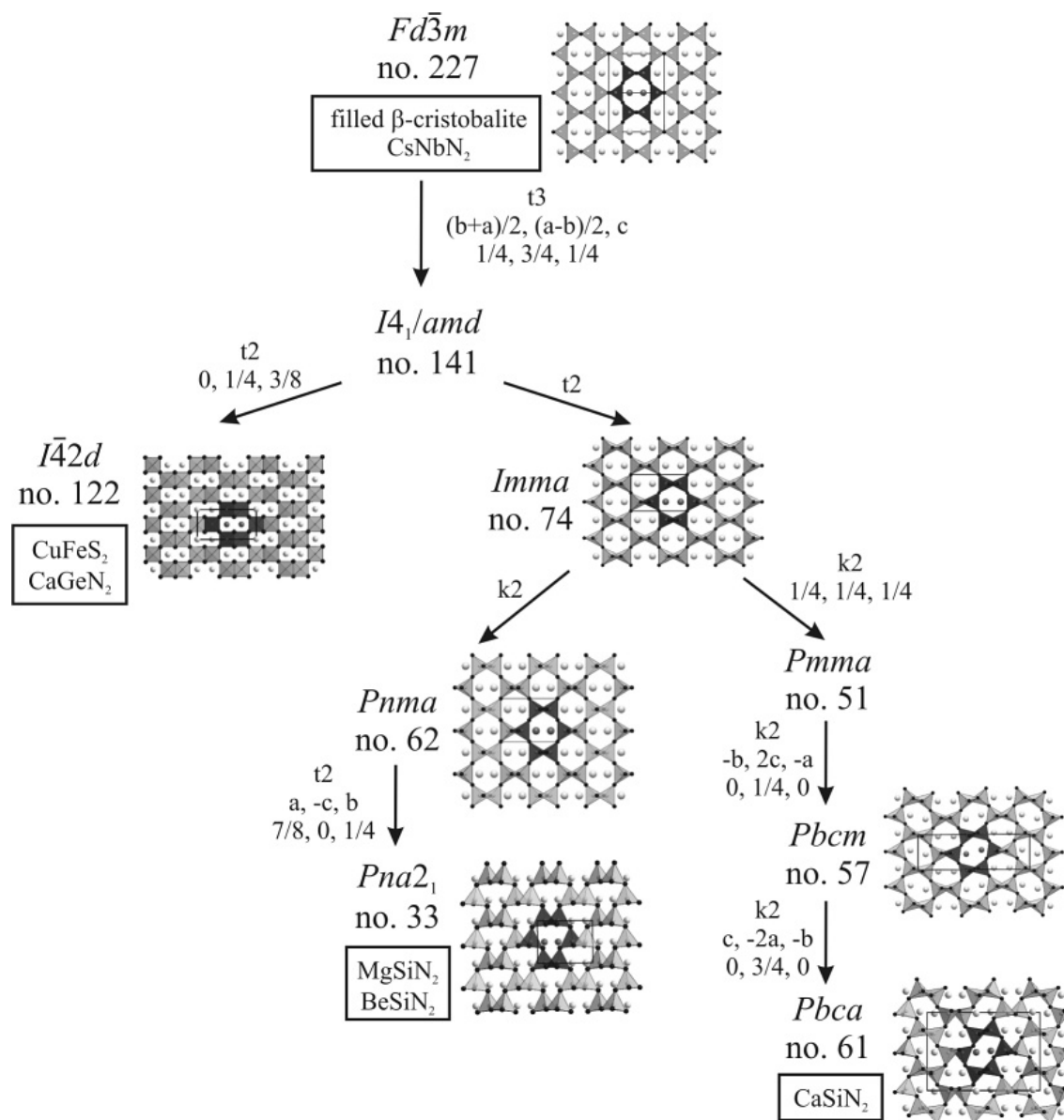
Figure 5.23: Group-subgroup scheme for filled β-cristobalite, chalcopyrite, CaGeN$_2$, BeSiN$_2$, MgSiN$_2$ and CaSiN$_2$. Structure pictures of equivalent views of intermediate phases are given if crystallographic data were available.

results in a doubled unit cell for s-LiFeO$_2$ and α-BeSiN$_2$ with regard to the rocksalt and wurtzite structure, respectively. However, as wurtzite-type BeSiN$_2$ transforms first into a CuFeS$_2$-type structure according to the enthalpy-pressure phase diagram (Figure 5.4), which is not related to the s-LiFeO$_2$-type structure, no displacive phase
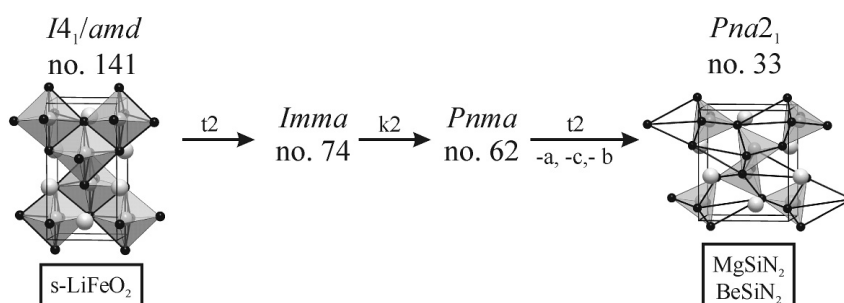
Figure 5.24: Group-subgroup scheme for s-LiFeO$_2$ and BeSiN$_2$/MgSiN$_2$. Both structures are presented in equivalent details and the polyhedra of the partner structure are enhanced by thick black lines, respectively.
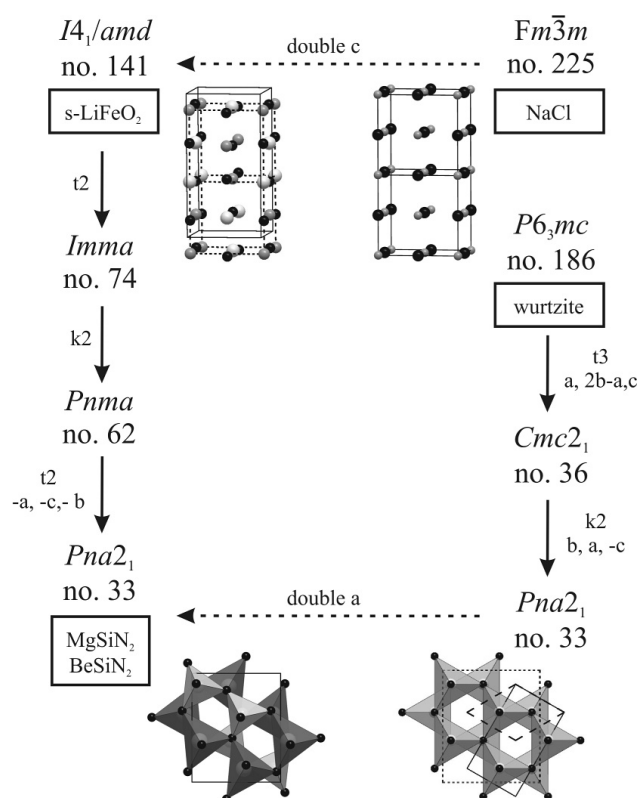
Figure 5.25: Relation of the NaCl structure to the s-LiFeO$_2$ structure and of the wurtzite (ZnS) structure to the BeSiN$_2$ and MgSiN$_2$ structure (pictures: s-LiFeO$_2$: unit cell of s-LiFeO$_2$ (solid line), double unit cell of NaCl (dotted line); BeSiN$_2$ and MgSiN$_2$: SiN$_4$ tetrahedra depicted light gray, MN$_4$ tetrahedra dark gray; wurtzite: unit cell of wutzite (dashed line), of wurtzite reduced to *Pna*2$_1$ (solid line), of BeSiN$_2$ and MgSiN$_2$ (dotted line)).

transition along the wurtzite-rocksalt transformation pathway will take place. The m-LiFeO$_2$-type structure, while also exhibiting an ordered rocksalt superstructure, is not related to either of the discussed structures.

It has to be noted, that the s-LiFeO$_2$ structure ($I4_1/amd$) is not related to the filled β-cristobalite structure, even though the space group sequence $I4_1/amd$ to $Pna2_1$ is identical to that of filled β-cristobalite $I4_1/amd$ to $Pna2_1$. In filled β-cristobalite, reduced to $I4_1/amd$, the X atoms of ABX$_2$ occupy the 8c positions whereas in s-LiFeO$_2$ they occupy the 8e positions.

Four high-pressure phases are proposed for SrSiN$_2$. The first, at bout 2 GPa occurs from the monoclinic α-SrSiN$_2$ structure ($P2_1/c$, no. 14) to the orthorhombic BaSiN$_2$ structure (*Cmca*, no. 64). This transformation, therefore, follows the pressure-homologues rule [254], according to which high pressure conditions favor the formation of phases with the structure of heavier homologues. These two structures are related by a *translationengleiche* (*t*2) group-subgroup relation and only small displacements of the atoms (Table 5.14) suffice to transform from $P2_1/c$ to *Cmca* (Figure 5.26). Presumably, this displacive phase transformation will have a rather low activation energy barrier. Consequently, the transformation may be reversed upon quenching, which makes synthesis of β-SrSiN$_2$ a true challenge. Nevertheless, in-situ, for example in the DAC, the orthorhombic β-phase of SrSiN$_2$ should be detectable.
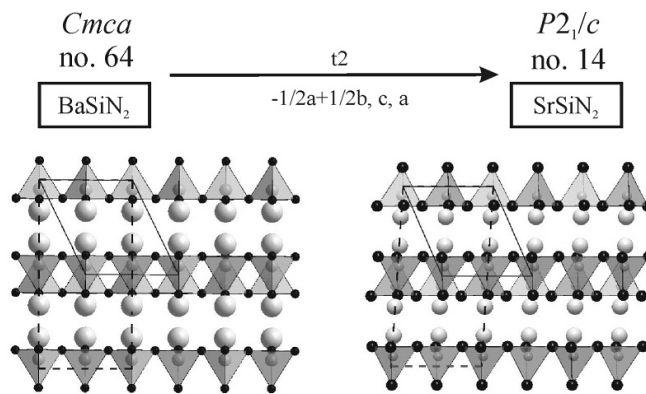
Figure 5.26: Group-Subgroup relation of the BaSiN$_2$ and the SrSiN$_2$ structure. Unit cell drawn: (1) solid line $P2_1/c$, (2) dashed line: *Cmca*.

Table 5.14: Atom coordinates of α-SrSiN$_2$ [14], β-SrSiN$_2$ (LDA and GGA calculation) and BaSiN$_2$ [14] in $P2_1/c$ (at 0 GPa). Decimal numbers marked with ^{a} have fixed values for space group *Cmca* (e.g. 0.25 ≙ 1/4), but could deviate from this value in space group $P2_1/c$.

atom	structure	Wyckoff-Position	x	y	z
Sr1	α-SrSiN$_2$	4e	0.3393(1)	0.5724(1)	0.1756(1)
	β-SrSiN$_2$ LDA		0.34308	0.56799	0.17150
	β-SrSiN$_2$ GGA		0.33911	0.56848	0.16960
Ba1	BaSiN$_2$		0.32860	0.56520	0.16430
Si1	α-SrSiN$_2$	4e	0.1078(4)	0.1419(3)	0.0671(4)
	β-SrSiN$_2$ LDA		0.11212	0.14191	0.05610
	β-SrSiN$_2$ GGA		0.11047	0.14142	0.05520
	BaSiN$_2$		0.09900	0.13990	0.04950
N1	α-SrSiN$_2$	4e	0.2096(11)	0.5905(8)	0.5847(12)
	β-SrSiN$_2$ LDA		0.20502	0.59521	0.60250
	β-SrSiN$_2$ GGA		0.20300	0.59363	0.60150
	BaSiN$_2$		0.20400	0.58070	0.60200
N2	α-SrSiN$_2$	4e	0.2192(11)	0.2252(8)	0.3845(11)
	β-SrSiN$_2$ LDA		0.23468	0.25^a	0.36740
	β-SrSiN$_2$ GGA		0.22772	0.25^a	0.36380
	BaSiN$_2$		0.19580	0.25^a	0.34790

The calculations then revealed a CaSiN$_2$-type structure as a second high-pressure phase of SrSiN$_2$. Interestingly, this transformation disregards the aforementioned empiric "rule". In this structural transformation the layered β-SrSiN$_2$ structure is converted into a three-dimensional network structure. The connection pattern of the SiN$_4$ tetrahedra changes fundamentally from mixed edge- and corner-sharing tetrahedra forming SiN$_2$ layers to edge-sharing tetrahedra forming a three-dimensional network structure. Note further, that the total coordination of neither Si nor N is changed in this process. However, this phase transformation is unambiguously reconstructive.

Transforming γ- into δ-SrSiN$_2$ again is a displacive process. It follows a *klassenglei-che* ($k2$) group-subgroup relation pathway from orthorhombic *Pbca* (γ-SrSiN$_2$) to *Pbcm* (δ-SrSiN$_2$) (Figure 5.19). Like the first transformation from α- to β-SrSiN$_2$ this phase transformation can be expected to take place gradually. However, as a difference to the α/β-transformation, an increase in the coordination number for Si will be observed. Changes in the atom positions occur mainly for the x-coordinates, becoming obvious from comparing both structures in *Pbca* setting (Table 5.15). A

similar behavior is found for the B-sesquioxide to A-sesquioxide phase transitions frequently found for rare earth oxides M$_2$O$_3$. A small displacement of the atoms during the transition results in increased coordination numbers for the constituting atoms. These phase transformations are often only observable in-situ, as the A-sesquioxide structure usually reverts to the B-sesquioxide structure upon pressure release [194, 195, 198, 199].

Table 5.15: Atom coordinates of γ-SrSiN$_2$ (CaSiN$_2$-type structure [14]) and δ-SrSiN2 (*Pbcm* structure) in *Pbca* (at 0 GPa, LDA and GGA). Decimal numbers marked with [a] have fixed values for space group *Pbcm* (e.g. 0.25 $\hat{=}$ 1/4), but could deviate from this value in space group *Pbca*.

atom	structure	Wyckoff-Position	x	y	z
Sr1	γ-SrSiN$_2$ LDA	8c	0.25574	0.02069	0.06517
	γ-SrSiN$_2$ GGA		0.25391	0.01776	0.06476
	δ-SrSiN$_2$ LDA		0.25[a]	0.02869	0.06842
	δ-SrSiN$_2$ GGA		0.25[a]	0.00928	0.06488
Sr2	γ-SrSiN$_2$ LDA	8c	0.33234	0.26880	0.18461
	γ-SrSiN$_2$ GGA		0.33032	0.26868	0.18502
	δ-SrSiN$_2$ LDA		0.25[a]	0.27502	0.18030
	δ-SrSiN$_2$ GGA		0.25[a]	0.25751	0.18512
Si1	γ-SrSiN$_2$ LDA	8c	0.25543	0.00989	0.31166
	γ-SrSiN$_2$ GGA		0.25366	0.01031	0.31164
	δ-SrSiN$_2$ LDA		0.25[a]	0.01892	0.31091
	δ-SrSiN$_2$ GGA		0.25[a]	0.01862	0.31427
Si2	γ-SrSiN$_2$ LDA	8c	0.30310	0.26477	0.43640
	γ-SrSiN$_2$ GGA		0.29974	0.26465	0.43649
	δ-SrSiN$_2$ LDA		0.25[a]	0.26581	0.43903
	δ-SrSiN$_2$ GGA		0.25[a]	0.26758	0.43597
N1	γ-SrSiN$_2$ LDA	8c	0.06281	0.47638	0.21831
	γ-SrSiN$_2$ GGA		0.06207	0.47809	0.21898
	δ-SrSiN$_2$ LDA		0.25[a]	0.51061	0.20941
	δ-SrSiN$_2$ GGA		0.25[a]	0.50061	0.21088
N2	γ-SrSiN$_2$ LDA	8c	0.11090	0.29309	0.02194
	γ-SrSiN$_2$ GGA		0.10577	0.29095	0.02177
	δ-SrSiN$_2$ LDA		0.25[a]	0.27063	0.03851
	δ-SrSiN$_2$ GGA		0.25[a]	0.26392	0.03809
N3	γ-SrSiN$_2$ LDA	8c	0.17218	0.41296	0.40228
	γ-SrSiN$_2$ GGA		0.17456	0.41235	0.40145
	δ-SrSiN$_2$ LDA		0.25[a]	0.40601	0.38690
	δ-SrSiN$_2$ GGA		0.25[a]	0.42181	0.40039
N4	γ-SrSiN$_2$ LDA	8c	0.31842	0.16840	0.34290
	γ-SrSiN$_2$ GGA		0.31232	0.16760	0.34371
	δ-SrSiN$_2$ LDA		0.25[a]	0.15680	0.36340
	δ-SrSiN$_2$ GGA		0.25[a]	0.17230	0.24967

The fourth phase transition occurs at very high pressures (130 to 140 GPa), achieving a further increase of the coordination of Si from five to six. By adopting the m-LiFeO$_2$-type structure, which is a superstructure of the rocksalt structure, ϵ-SrSiN$_2$ finally follows the trend already found for BeSiN$_2$, MgSiN$_2$ and CaSiN$_2$, for which also rocksalt-derived high-pressure phases were found.

BaSiN$_2$ adheres to the same high-pressure structure sequence as SrSiN$_2$. From orthorhombic *Cmca* BaSiN$_2$ it transforms into a CaSiN$_2$-type structure, followed by the displacive phase transformation into the *Pbcm*-type structure (Figure 5.19, Table 5.16). No transformation into the m-LiFeO$_2$-type structure was found up to 120 GPa.

Table 5.16: Atom coordinates of β-BaSiN$_2$ (CaSiN$_2$ structure [14]) at 91 GPa and of γ-BaSiN$_2$ (*Pbcm* structure) at 105 GPa (GGA calculation) in *Pbca*. Decimal numbers marked with ^{a} have fixed values for space group *Pbcm* (e.g. $0.25 \,\hat{=}\, 1/4$), but could deviate from this value in space group *Pbca*.

atom	structure	Wyckoff-Position	x	y	z
Ba1	β-BaSiN$_2$ 91 GPa	8c	0.26678	0.03027	0.06353
	γ-BaSiN$_2$ 105 GPa		0.25^a	0.04089	0.06061
Ba2	β-BaSiN$_2$ 91 GPa	8c	0.33215	0.25867	0.18942
	γ-BaSiN$_2$ 105 GPa		0.25^a	0.28339	0.18658
Si1	β-BaSiN$_2$ 91 GPa	8c	0.25647	0.00336	0.31274
	γ-BaSiN$_2$ 105 GPa		0.25^a	0.02789	0.30933
Si2	β-BaSiN$_2$ 91 GPa	8c	0.32080	0.25916	0.43786
	γ-BaSiN$_2$ 105 GPa		0.25^a	0.27429	0.44019
N1	β-BaSiN$_2$ 91 GPa	8c	0.08063	0.48010	0.21604
	γ-BaSiN$_2$ 105 GPa		0.25^a	0.52808	0.20673
N2	β-BaSiN$_2$ 91 GPa	8c	0.15033	0.29413	0.02711
	γ-BaSiN$_2$ 105 GPa		0.25^a	0.29523	0.03497
N3	β-BaSiN$_2$ 91 GPa	8c	0.18048	0.40253	0.39851
	γ-BaSiN$_2$ 105 GPa		0.25^a	0.41052	0.38177
N4	β-BaSiN$_2$ 91 GPa	8c	0.33508	0.15576	0.35171
	γ-BaSiN$_2$ 105 GPa		0.25^a	0.16357	0.36542

As has been already noted, the *Pbcm* structure of γ-BaSiN$_2$ distorts through a cascade of higher-symmetry *Imma* structures (γ'-BaSiN$_2$, γ'-BaSiN$_2$ II, compare chapter 5.1.5, page 98) into a very open structure (γ'-BaSiN$_2$ III) with lower density, but also higher energy than α-BaSiN$_2$. Since the nature of the β/γ-phase transformation is also displacive, we expect that γ-BaSiN$_2$ right away re-transforms into β-BaSiN$_2$ upon pressure release. γ-BaSiN$_2$ may well be only observable in-situ.

Formation of MSiN$_2$ from Si$_3$N$_4$ and M$_3$N$_2$

With regard to the thermodynamic stability of MSiN$_2$ versus M$_3$N$_2$ and Si$_3$N$_4$, BeSiN$_2$ is thermodynamically stable against decomposition only up to 66 GPa, at which pressure a phase agglomerate of Be$_3$N$_2$ and Si$_3$N$_4$ is more favorable (Figure 5.27). However, above 83 GPa BeSiN$_2$ should reappear adopting the γ-BeSiN$_2$ structure. Consequently, γ-BeSiN$_2$ will be attainable above 83 GPa from the binary nitrides . However, slow interdiffusion in solid-state reactions as well as a presumably high activation energy resulting from strong bonds in Si$_3$N$_4$ and Be$_3$N$_2$ has to be overcome to achieve this goal. Therefore high temperatures should accompany the high-pressure experiment as to overcome high activation barriers.
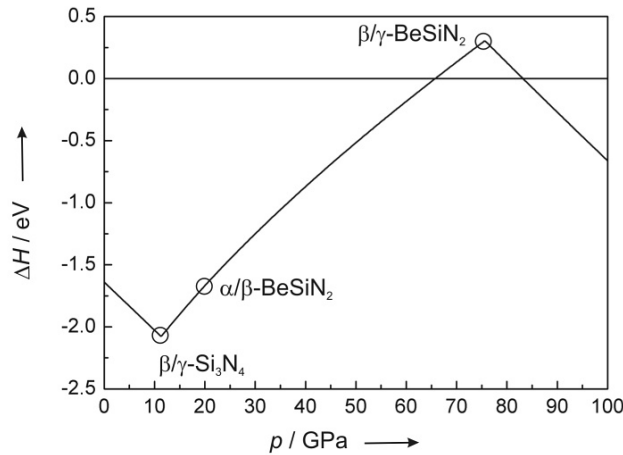
Figure 5.27: Enthalpy-pressure diagram for the formation of BeSiN$_2$ (α-, β- and γ-BeSiN$_2$) from Be$_3$N$_2$ and Si$_3$N$_4$. The phase transition of β- into γ-Si$_3$N$_4$ has been taken into account (No phase transformations of Be$_3$N$_2$ found up to 100 GPa).

For CaSiN$_2$ and MgSiN$_2$ it is found, that MSiN$_2$ (M = Ca, Mg) always is lower in enthalpy than a phase agglomerate of M$_3$N$_2$ (M = Ca, Mg) and Si$_3$N$_4$, taking all predicted high-pressure phases of Ca$_3$N$_2$ (compare chapter 4.1.3, page 52), Mg$_3$N$_2$ (compare chapter 4.1.2, page 48) as well as the β- to γ-phase transition for Si$_3$N$_4$ [4, 5] into account (Figure 5.28 and Figure 5.29). This opens up another possible synthesis route for CaSiN$_2$ and MgSiN$_2$ and its high-pressure phases, as they should

be synthesizeable under high pressure from Si_3N_4 and Ca_3N_2 or Mg_3N_2, respectively (allowing for the same limitations as for $BeSiN_2$).
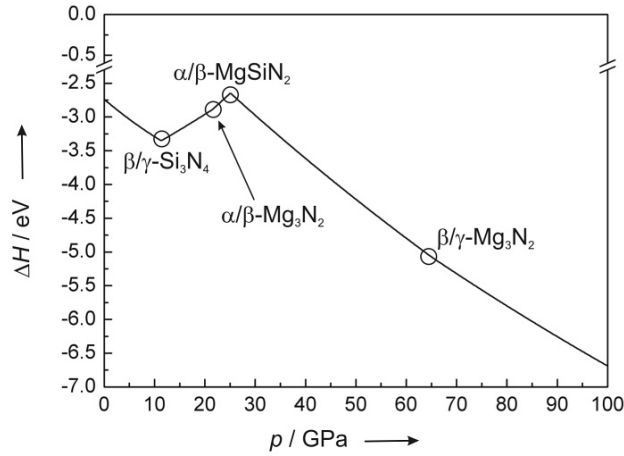
Figure 5.28: Enthalpy-pressure diagram for the formation of $MgSiN_2$ (α- and β-$MgSiN_2$) from Mg_3N_2 and Si_3N_4. The phase transition of β- into γ-Si_3N_4 as well as the proposed phase transformations of Mg_3N_2 (α-, β- and γ-Mg_3N_2) have been taken into account.
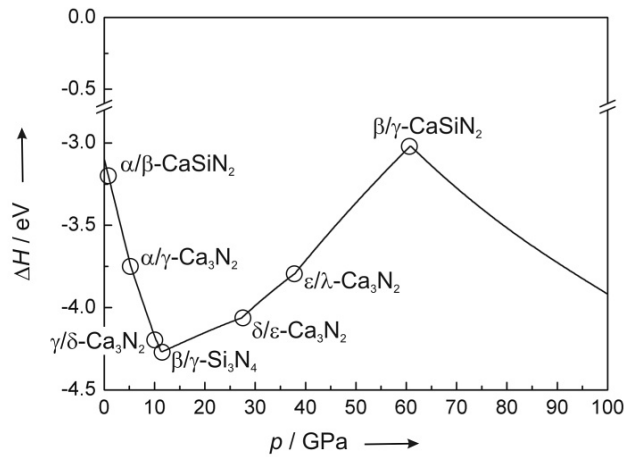
Figure 5.29: Enthalpy-pressure diagram for the formation of $CaSiN_2$ (α-, β- and γ-$CaSiN_2$) from Ca_3N_2 and Si_3N_4. The phase transition of β- into γ-Si_3N_4 as well as the proposed phase transformations of Ca_3N_2 (α-, γ-, δ-, ϵ- and λ-Ca_3N_2) have been taken into account.

The enthalpy of $SrSiN_2$ and $BaSiN_2$ is – like that of $MgSiN_2$ and $CaSiN_2$ – always lower in enthalpy than that of a phase agglomerate of Si_3N_4 and Sr_3N_2 and Ba_3N_2, respectively (Figure 5.30 and Figure 5.31). However, one has to bear in mind, that
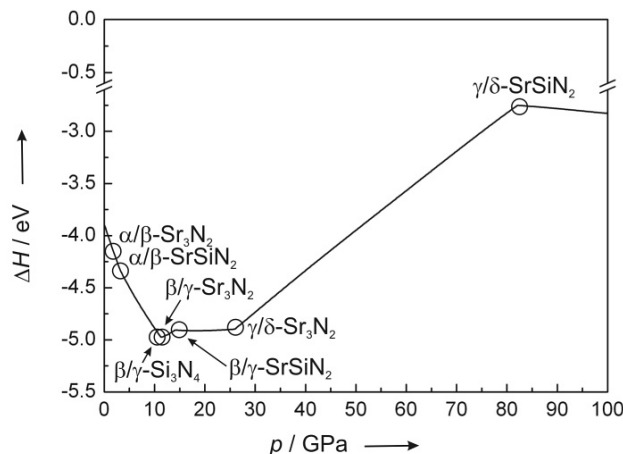
Figure 5.30: Enthalpy-pressure diagram for the formation of $SrSiN_2$ (α-, β-, γ- and δ-$SrSiN_2$) from hypothetic Sr_3N_2 and Si_3N_4. The phase transition of β- into γ-Si_3N_4 as well as the proposed phase transformations of Sr_3N_2 (α-, β-, γ- and δ-Sr_3N_2) have been taken into account.
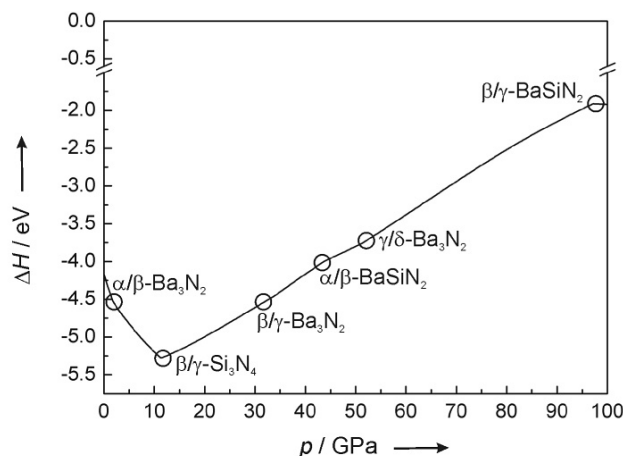
Figure 5.31: Enthalpy-pressure diagram for the formation of $BaSiN_2$ (α-, β- and γ-$BaSiN_2$) from hypothetic Ba_3N_2 and Si_3N_4. The phase transition of β- into γ-Si_3N_4 as well as the proposed phase transformations of Ba_3N_2 (α-, β- and γ-Ba_3N_2) have been taken into account.

neither Sr_3N_2 nor Ba_3N_2 could be unambiguously synthesized and characterized, wherefore hypothetic Sr_3N_2 and Ba_3N_2 and their high-pressure polymorphs as presented in chapter 4.1.4 and 4.1.5 were employed.

6 Nitridosilicates $M_2Si_5N_8$ of group II elements

Three nitridosilicates of composition $M_2Si_5N_8$ are known so far for the elements of group II: $Ca_2Si_5N_8$ [15], $Sr_2Si_5N_8$ and $Ba_2Si_5N_8$ [16]. Since their discovery in 1995, these compounds have become prominent phosphor host lattices for LED (*light emitting diodes*) applications [19, 271–274]. Their high-temperature stability and great chemical inertness as well as their not possessing environmental hazards in service, production, handling and disposal, render them ideal materials for large-scale production and operation. Doped with Eu^{2+}, especially $Sr_2Si_5N_8$ and orthorhombic solid solutions in the system $(Ba_{1-x-y}Sr_xCa_y)_2Si_5N_8$, but also $Ca_2Si_5N_8$ and $Ba_2Si_5N_8$ have already found application in phosphor converted LEDs (pc-LEDs) using (In,Ga)N-GaN short wavelength LEDs as primary blue emitters [18, 19, 275]. Such 2-pc-LEDs (using for example $MSi_2O_2N_2$:Eu^{2+} (M = Ca, Sr, Ba), α-sialon:Yb^{2+} or β-sialon:Eu^{2+} as a second green to yellow emitting converter material [19, 272]) exhibit excellent "warm-white"-light properties with the *General Color Rendering Index* (CRI) and the *Correlated Color Temperature* (CCT) being very stable against operating temperature changes and drive currents [19], as well as significantly improved luminescence in the red region [275].

$M_2Si_5N_8$ (M = Ca, Sr, Ba) is synthesized from silicon diimide and the alkaline earth metal (plus an optional addition of the dopant Eu) in a radio frequency furnace under N_2 atmosphere at temperatures between 800 and 1700 °C [15, 16, 18]. All three compounds exhibit a three-dimensional SiN_4 tetrahedra network with corrugated tetrahedra layers interconnected by further SiN_4 tetrahedra. The cations are situated between these layers. $Ca_2Si_5N_8$ crystallizes in the monoclinic space group *Cc* (no. 9), whereas isotypic $Sr_2Si_5N_8$ and $Ba_2Si_5N_8$ crystallize in $Pnm2_1$ (no. 31, orthorhombic).

6.1 Ca$_2$Si$_5$N$_8$

As possible high-pressure phases for Ca$_2$Si$_5$N$_8$ two structures were considered: (1) the structure of the experimentally found HP-Ca$_2$Si$_5$N$_8$ and (2) that of hypothetic o-Ca$_2$Si$_5$N$_8$, which is isostructural to the ambient pressure modifications of Sr$_2$Si$_5$N$_8$ and Ba$_2$Si$_5$N$_8$. For all optimized structures the coordination numbers of the M^{2+} and Si^{4+} ions were determined by calculating effective coordination numbers (ECoN) [174] with MAPLE [175–178] in order to compare them to the data for the experimentally determined structures (if available).

6.1.1 Structure Optimization for Ca$_2$Si$_5$N$_8$

Ca$_2$Si$_5$N$_8$, HP-Ca$_2$Si$_5$N$_8$ and M$_2$Si$_5$N$_8$ (M = Sr, Ba) (o-Ca$_2$Si$_5$N$_8$) exhibits rather similar structural features (Figure 6.1). The ambient pressure phase of Ca$_2$Si$_5$N$_8$ [15] crystallizes in the monoclinic non-centrosymmetric space group *Cc* (no. 9) and HP-Ca$_2$Si$_5$N$_8$ in the orthorhombic centrosymmetric space group *Pbca* (no. 61). Sr$_2$Si$_5$N$_8$ and likewise isotypic Ba$_2$Si$_5$N$_8$ crystallize in the orthorhombic non-centrosymmetric space group *Pmn*2$_1$ (no. 31) [16]. The three structures share common basic structural motifs. They are built up by layers of corner-sharing SiN$_4$ tetrahedra comprising *dreier* rings. These layers are interconnected by further SiN$_4$ units, forming a three-dimensional network. Between these layers, the M^{2+} ions are situated and predominantly coordinated by N$^{[2]}$.

The SiN$_4$ tetrahedra in the layers of all three structures have three N$^{[3]}$ and one N$^{[2]}$, where the N$^{[3]}$ exclusively form the intra-layer bonds, while the N$^{[2]}$ are situated on the vertices pointing either up or down. The molar fraction of tetrahedra pointing up and down is equal according to the formula $^3_\infty[\text{Si}_5^{[4]}\text{N}_4^{[2]}\text{N}_4^{[3]}]^{4-}$ of the nitridosilicate network. The layers in the three M$_2$Si$_5$N$_8$ structures differ in their degree of corrugation and the pattern of tetrahedra pointing up and down. While the layers are strongly corrugated in M$_2$Si$_5$N$_8$ (M = Sr, Ba) and HP-Ca$_2$Si$_5$N$_8$, they are significantly less corrugated in monoclinic Ca$_2$Si$_5$N$_8$ (Figure 6.1).
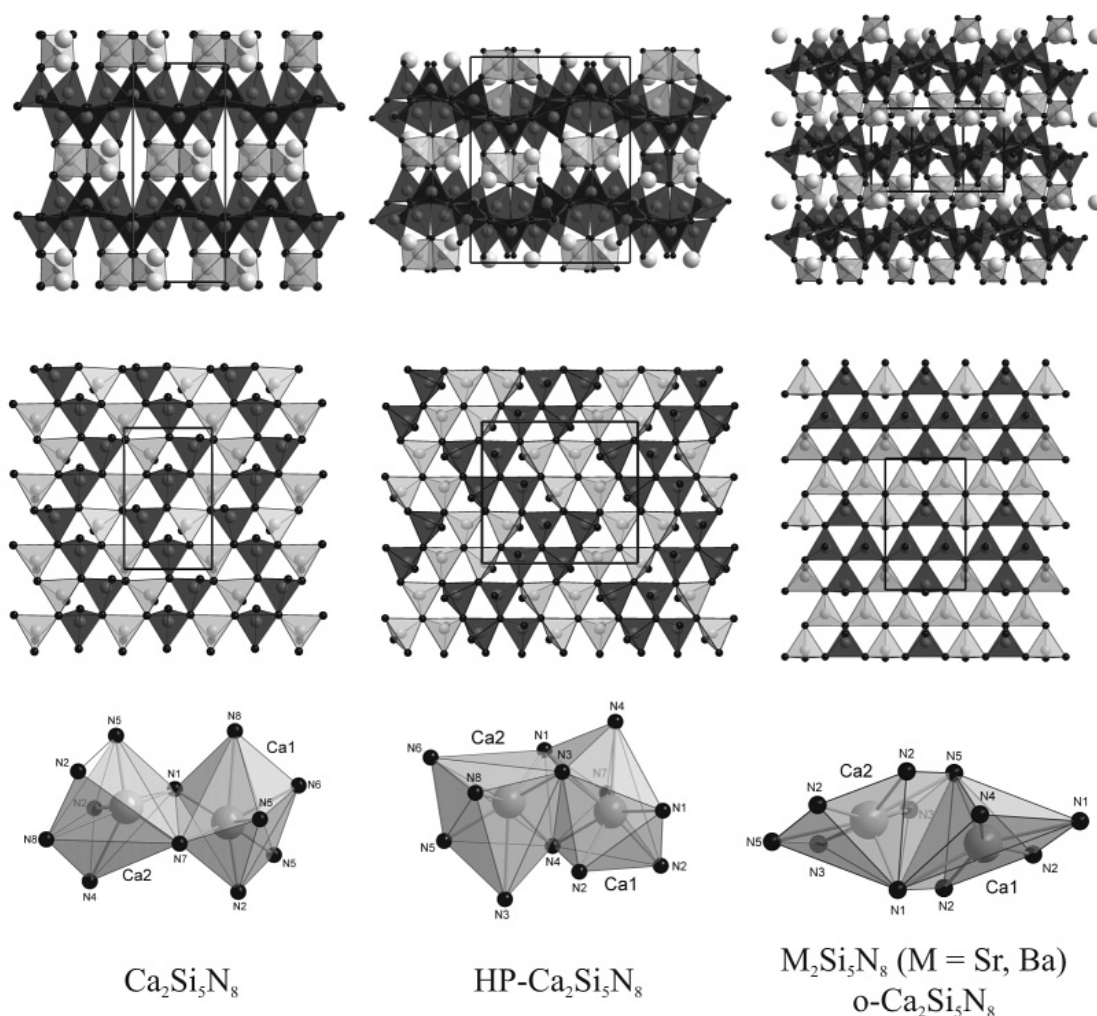
Figure 6.1: Structures of Ca$_2$Si$_5$N$_8$, HP-Ca$_2$Si$_5$N$_8$ and o-Ca$_2$Si$_5$N$_8$/M$_2$Si$_5$N$_8$ (M = Sr, Ba) (top: views of the unit cells; middle: up-down pattern of the SiN$_4$ tetrahedra in the layers; bottom: coordination of the Ca atoms).

The known M$_2$Si$_5$N$_8$ structures are related to that of the mineral sinoite, Si$_2$N$_2$O [276, 277]. Sinoite contains the same honeycomb layers, even though none of the M$_2$Si$_5$N$_8$ layers exhibit the same up-down pattern as the layers in sinoite. The vertices of tetrahedra pointing up and down in Si$_2$N$_2$O are occupied by O atoms, which connect two layers. For M$_2$Si$_5$N$_8$ the bridging O atoms are substituted by SiN$_4$ tetrahedra, resulting in a three-dimensional charged network: $^3_\infty[[\text{Si}^{[4]}\text{N}^{[3]}]_4[\text{Si}^{[4]}\text{N}_4^{[2]}]]^{4-}$. The layers in monoclinic Ca$_2$Si$_5$N$_8$ exhibit a rather simple pattern of alternating

zigzag lines of tetrahedra (along [001]) with their vertices pointing either up or down, whereas the pattern becomes more complex for HP-$Ca_2Si_5N_8$. The up and down pattern in $M_2Si_5N_8$ (M = Sr, Ba) is not related to the pattern of either $Ca_2Si_5N_8$ structure, but exhibits groups of four tetrahedra with their vertices pointing in the same direction. These groups are arranged in "corner-sharing" rows along [100] (Figure 6.1).

HP-$Ca_2Si_5N_8$ can be described as a centrosymmetric variant of the non-centrosymmetric ambient pressure modification. From Figure 6.1 (top) it is evident that high pressure formally shifts two single unit cells of $Ca_2Si_5N_8$ towards each other. This introduces a center of inversion which doubles the unit cell of HP-$Ca_2Si_5N_8$ compared to its ambient pressure phase and still allows for the extreme corrugation of the SiN_4 tetrahedra layers. Despite the similarity between monoclinic $Ca_2Si_5N_8$ and HP-$Ca_2Si_5N_8$, the phase transformation is reconstructive, as required for transforming the differently patterned layers. Therefore, the activation energy for the re-transformation into the ambient pressure phase is high enough to render HP-$Ca_2Si_5N_8$ metastable. Monoclinic non-centrosymmetric $Ca_2Si_5N_8$ exhibits NLO behavior [20], whereas HP-$Ca_2Si_5N_8$ unequivocally crystallizes with a center of inversion.

For $Ca_2Si_5N_8$ coordination number 7 for both crystallographic independent Ca^{2+} ions was derived, whereas in HP-$Ca_2Si_5N_8$ one Ca^{2+} is 6+1 coordinated and the other exhibits 7+1 coordination. This results in an increased coordination number for half of the Ca atoms. For both $Sr_2Si_5N_8$ and $Ba_2Si_5N_8$ a coordination number of 10 was derived for both M^{2+} ions, whereas in o-$Ca_2Si_5N_8$ coordinations of six and seven have been determined for the two crystallographically independent Ca atoms (Figure 6.1).

The calculated Si-N and Ca-N distances are listed in Table 6.1. They are all in the range found in experimental $Ca_2Si_5N_8$ and HP-$Ca_2Si_5N_8$. As expected, Si-N[2] bonds are shorter than Si-N[3] bonds.

Fang et al. [278] calculated the electronic structure of $Ca_2Si_5N_8$ and $Sr_2Si_5N_8$, but they did not give any calculated crystallographic data.

Comparing the density of the three considered $Ca_2Si_5N_8$ structures shows that the ambient pressure phase $Ca_2Si_5N_8$ has the lowest value (ρ = 3.06 g cm^{-3} (experimental); 3.01 g cm^{-3} (calculated within GGA)). The next denser structure is the

Table 6.1: Bond lengths (in pm) in $Ca_2Si_5N_8$, HP-$Ca_2Si_5N_8$ and o-$Ca_2Si_5N_8$ compared to experimental values.

Structure	Bond type	LDA	GGA	exp.
$Ca_2Si_5N_8$	$Ca1^{[7]}$-N	228.80–307.51	232.12–310.33	231.45–305.85 [15]
	$Ca2^{[7]}$-N	235.60–314.22	238.97–319.62	239.71–312.82 [15]
	$Si^{[4]}$-$N^{[2]}$	166.58–173.22	168.22–175.03	167.12–173.90 [15]
	$Si^{[4]}$-$N^{[3]}$	171.76–177.99	174.12–180.52	172.74–179.59 [15]
HP-$Ca_2Si_5N_8$	$Ca1^{[8]}$-N	237.33–330.09	240.68–336.21	241.88–330.14 [204]
	$Ca2^{[7]}$-N	236.81–329.48	240.33–330.55	244.34–326.16 [204]
	$Si^{[4]}$-$N^{[2]}$	164.95–174.82	166.46–176.68	166.41–175.71 [204]
	$Si^{[4]}$-$N^{[3]}$	173.57–176.81	175.67–179.43	173.38–180.35 [204]
o-$Ca_2Si_5N_8$	$Ca1^{[6]}$-N	235.31–287.22	238.61–295.06	/
	$Ca2^{[7]}$-N	235.25–307.49	238.57–313.36	/
	$Si^{[4]}$-$N^{[2]}$	166.39–171.65	168.05–173.34	/
	$Si^{[4]}$-$N^{[3]}$	173.06–174.95	174.98–177.28	/
Ionic Radii	bond type	Shannon [183]	Baur [184]	
	$Ca^{[6]}$-N	246	247–249	
	$Ca^{[7]}$-N	252	/	
	$Ca^{[8]}$-N	258	/	
	$Si^{[4]}$-$N^{[2]}$	/	171	
	$Si^{[4]}$-$N^{[3]}$	/	173	
	$Si^{[4]}$-$N^{[4]}$	172	/	

o-$Ca_2Si_5N_8$ structure ($\rho = 3.06\,\mathrm{g\,cm^{-3}}$ (calculated within GGA)), with HP-$Ca_2Si_5N_8$ being the densest phase ($\rho = 3.17\,\mathrm{g\,cm^{-3}}$ (experimental); $3.12\,\mathrm{g\,cm^{-3}}$ (calculated within GGA)). Within the GGA, $Ca_2Si_5N_8$ has the lowest energy (-116.605 eV per formula unit), followed by HP-$Ca_2Si_5N_8$ (-116.536 eV per formula unit) and o-$Ca_2Si_5N_8$ (-116.093 eV per formula unit).

6.1.2 Energy-Volume Calculations for $Ca_2Si_5N_8$

In Figure 6.2 the energy-volume curves of the three structures of $Ca_2Si_5N_8$ are depicted from which the enthalpy was extracted as a function of pressure as illustrated in Figure 6.3. Accordingly, the transition pressure of monoclinic $Ca_2Si_5N_8$ to HP-$Ca_2Si_5N_8$ was calculated with 1.7 GPa, which reasonably agrees with the experimental value. The phase transformation of $Ca_2Si_5N_8$ into HP-$Ca_2Si_5N_8$ was observed at 6 GPa and 900°C. The difference between calculated and experimental transition pressure is attributed to kinetic effects of the phase transformation.
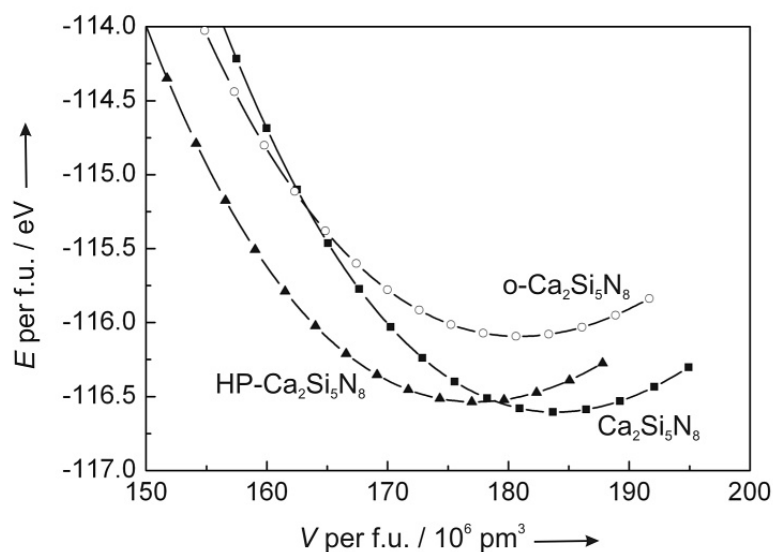
Figure 6.2: Energy-volume (E-V) phase diagram of $Ca_2Si_5N_8$, HP-$Ca_2Si_5N_8$ and o-$Ca_2Si_5N_8$, calculated within the GGA. Each symbol represents a calculation.
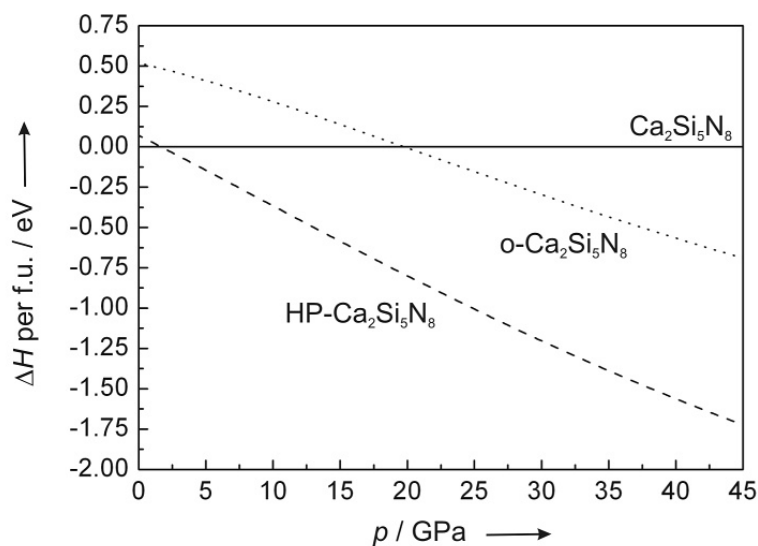
Figure 6.3: Enthalpy-pressure (H-p) diagram for the transition of $Ca_2Si_5N_8$ into HP-$Ca_2Si_5N_8$ ($p_t = 1.7\,GPa$) and of $Ca_2Si_5N_8$ into o-$Ca_2Si_5N_8$ ($p_t = 20\,GPa$) (derived from the evaluation of the E-V data by the Murnaghan EOS).

At 20 GPa the enthalpy of o-$Ca_2Si_5N_8$ becomes more favorable than that of monoclinic $Ca_2Si_5N_8$. However, HP-$Ca_2Si_5N_8$ remains the energetically most stable phase, which is in accordance with the experiment (Figure 6.3).

Calculations of the phonon band structure, furthermore, indicate that o-$Ca_2Si_5N_8$ comprises imaginary vibrational modes within the Brillouin zone already at ambient pressure, amplified at higher pressures. Hence, this particular structure is dynamically instable already at ambient pressure. Monoclinic and HP-$Ca_2Si_5N_8$ were proven to be free of such imaginary vibrational modes [204, 279].

6.1.3 Decomposition Under Pressure

In addition to pressure induced phase transformations, two possible decomposition pathways under pressure were examined: (1) the decomposition of $Ca_2Si_5N_8$ into the binary nitrides Ca_3N_2 and Si_3N_4 (Eq. 6.1) and (2) the decomposition into $CaSiN_2$ and Si_3N_4 (Eq. 6.2).

$$3\ Ca_2Si_5N_8 \rightarrow 2\ Ca_3N_2 + 5\ Si_3N_4 \tag{6.1}$$

$$Ca_2Si_5N_8 \rightarrow 2\ CaSiN_2 + Si_3N_4 \tag{6.2}$$
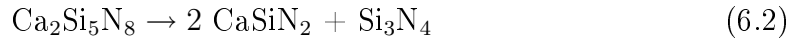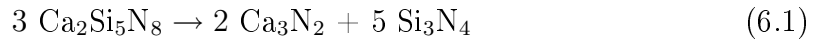
The phase transition of β-Si_3N_4 into γ-Si_3N_4 (compare chapter 3.2) as well as the phase transitions of $CaSiN_2$ (compare chapter 5.2) and Ca_3N_2 (compare chapter 4.2) were taken into account for all decomposition reactions.

It is found that the enthalpy of a phase agglomerate of Si_3N_4 and 2 $CaSiN_2$ is always lower than the enthalpy of a system consisting of (2/3 Ca_3N_2 + 5/3 Si_3N_4). Consequently, a decomposition of $Ca_2Si_5N_8$ will result in the formation of $CaSiN_2$ and Si_3N_4 rather than Ca_3N_2 together with Si_3N_4 (compare Figure 6.4).

In Figure 6.4 the reaction enthalpy of the decomposition of $Ca_2Si_5N_8$ into Si_3N_4 and $CaSiN_2$ is displayed. Accordingly, above 15 GPa $Ca_2Si_5N_8$ will decompose into Si_3N_4 and $CaSiN_2$. This process is mainly driven by the favorable enthalpy of γ-Si_3N_4 at higher pressures. γ-Si_3N_4 is the only structure in this pressure range for which partially octahedral coordination of Si, resulting in a higher density, is achieved. The possibility to further densify the matter at high pressure, hence causes the decom-

position of the ternary compound $Ca_2Si_5N_8$ into binary Si_3N_4 and ternary $CaSiN_2$.
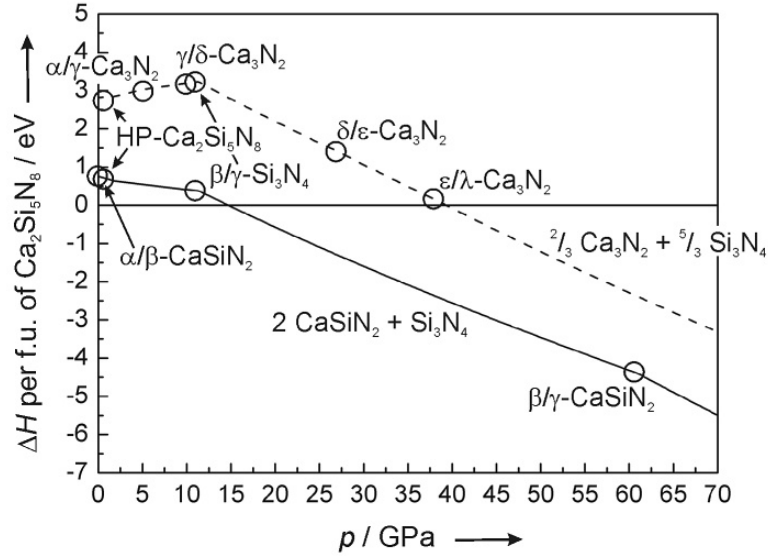
Figure 6.4: Enthalpy-pressure diagram for the decomposition reactions of $Ca_2Si_5N_8$ into $CaSiN_2$ and Si_3N_4 and into Ca_3N_2 and Si_3N_4 (Murnaghan EOS evaluation).

6.2 $Sr_2Si_5N_8$

For $Sr_2Si_5N_8$, besides the experimentally found orthorhombic ambient-pressure structure (space group $Pmn2_1$, no. 31) [16], the structure of the high-pressure phase of $Ca_2Si_5N_8$ (space group $Pbca$, no. 61) [204] was considered (further on denoted HP-$Sr_2Si_5N_8$). For all optimized structures the coordination numbers of the M^{2+} and Si^{4+} ions were determined by calculating effective coordination numbers (ECoN) [174] with MAPLE [175–178] in order to compare them to the data for the experimentally determined structures (if available). For a detailed description of the considered structures and a comparison thereof see chapter 6.1.

6.2.1 Structure Optimization for Sr$_2$Si$_5$N$_8$

Structure optimization of $Sr_2Si_5N_8$ resulted in the exact experimental structure. HP-$Sr_2Si_5N_8$ presents a reasonable structure, retaining the characteristic structural motives of the HP-$Ca_2Si_5N_8$ structure. The Sr^{2+} ions are ten-fold coordinated by N in $Sr_2Si_5N_8$, whereas they are 8+2- and 7+3-fold coordinated in hypothetic HP-$Sr_2Si_5N_8$. A comparison of the SrN_x coordination polyhedra and their connection is given in Figure 6.5.
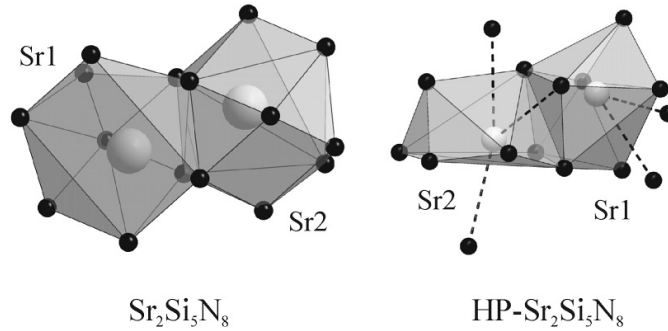
Figure 6.5: SrN_x coordination polyhedra in $Sr_2Si_5N_8$ and hypothetic HP-$Sr_2Si_5N_8$.

The Sr-N and Si-N distances obtained from the optimized structures in comparison to the experimental values from $Sr_2Si_5N_8$ are given in Table 6.2. In general, the Si-N$^{[2]}$ bonds are longer than the Si-N$^{[3]}$ bonds. The calculated Si-N bonds in HP-$Sr_2Si_5N_8$ turn out slightly longer than those in $Sr_2Si_5N_8$. However, the overall agreement of the calculated distances with those in experimental $Sr_2Si_5N_8$ is good. $Sr_2Si_5N_8$ exhibits the lower energy (-115.596 eV per formula unit) and the lower density ($\rho = 3.90\,\mathrm{g\,cm^{-3}}$ (experimental); $3.83\,\mathrm{g\,cm^{-3}}$ (calculated within GGA)) of the two considered structures. The energy per formula unit of HP-$Sr_2Si_5N_8$ amounts to -115.402 eV and the density $3.85\,\mathrm{g\,cm^{-3}}$ within GGA. The zero-pressure bulk moduli for both structures were calculated to 155 GPa.

Table 6.2: Bond lengths (in pm) in $Sr_2Si_5N_8$ and HP-$Sr_2Si_5N_8$ compared to experimental values.

Structure	Bond type	LDA	GGA	exp.
$Sr_2Si_5N_8$	$Sr^{[10]}$-N	$251.21 - 337.18$	$255.13 - 340.91$	$254.22 - 338.06$ [16]
	$Si^{[4]}$-$N^{[2]}$	$165.88 - 171.59$	$167.49 - 173.36$	$165.31 - 173.30$ [16]
	$Si^{[4]}$-$N^{[3]}$	$173.25 - 176.34$	$175.28 - 178.83$	$174.81 - 178.60$ [16]
HP-$Sr_2Si_5N_8$	$Sr1^{[8+2]}$-N	$249.60 - 358.31$	$252.63 - 362.31$	
	$Sr2^{[7+3]}$-N	$251.35 - 367.23$	$255.00 - 369.45$	
	$Si^{[4]}$-$N^{[2]}$	$165.63 - 175.28$	$167.03 - 177.18$	
	$Si^{[4]}$-$N^{[3]}$	$173.78 - 178.29$	$176.10 - 180.99$	
Ionic Radii	bond type	Shannon [183]	Baur [184]	
	$Sr^{[8]}$-N	272	$265 - 273$	
	$Sr^{[10]}$-N	282	/	
	$Si^{[4]}$-$N^{[2]}$	/	171	
	$Si^{[4]}$-$N^{[3]}$	/	173	
	$Si^{[4]}$-$N^{[4]}$	172	/	

6.2.2 Decomposition Under Pressure

The same two decomposition pathways as for $Ca_2Si_5N_8$ were also considered for $Sr_2Si_5N_8$ and HP-$Sr_2Si_5N_8$:

$$3 \, Sr_2Si_5N_8 \rightarrow 2 \, Sr_3N_2 + 5 \, Si_3N_4 \tag{6.3}$$

$$Sr_2Si_5N_8 \rightarrow 2 \, SrSiN_2 + Si_3N_4 \tag{6.4}$$
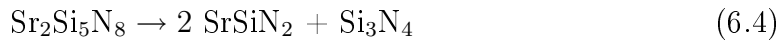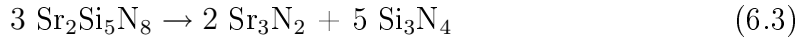
For the phase transformations of $SrSiN_2$ compare chapter 5.2. For the assumed ground state structure of Sr_3N_2 as well as its high-pressure phases see chapter 4.2. As for $Ca_2Si_5N_8$, the enthalpy of a phase agglomerate of Si_3N_4 and 2 $SrSiN_2$ is always lower in enthalpy than that of a system consisting of $(2/3 \, Sr_3N_2 + 5/3 \, Si_3N_4)$. Therefore, a decomposition of $Sr_2Si_5N_8$ will result in the formation of $SrSiN_2$ and Si_3N_4 rather than Sr_3N_2 together with Si_3N_4 (compare Figure 6.6 and Figure 6.7). According to the reaction enthalpy of the decomposition into Si_3N_4 and 2 $SrSiN_2$, $Sr_2Si_5N_8$ will decompose at 19 GPa. HP-$Sr_2Si_5N_8$ decomposes at a slightly lower pressure, at 18 GPa. Here, as in the case of $Ca_2Si_5N_8$, the driving force for the decomposition is the transformation occurring in Si_3N_4 from the phenakite structure with purely tetrahedral Si environment to the spinel structure with partially

octahedrally coordinated Si, which results in a significant densification of matter.
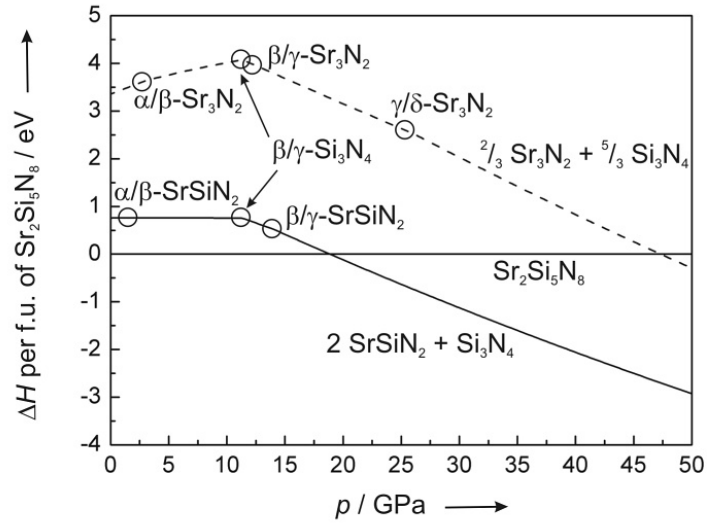
Figure 6.6: Enthalpy-pressure diagram for the decomposition reactions of $Sr_2Si_5N_8$ into $SrSiN_2$ and Si_3N_4 and into Sr_3N_2 and Si_3N_4 (Murnaghan EOS evaluation).
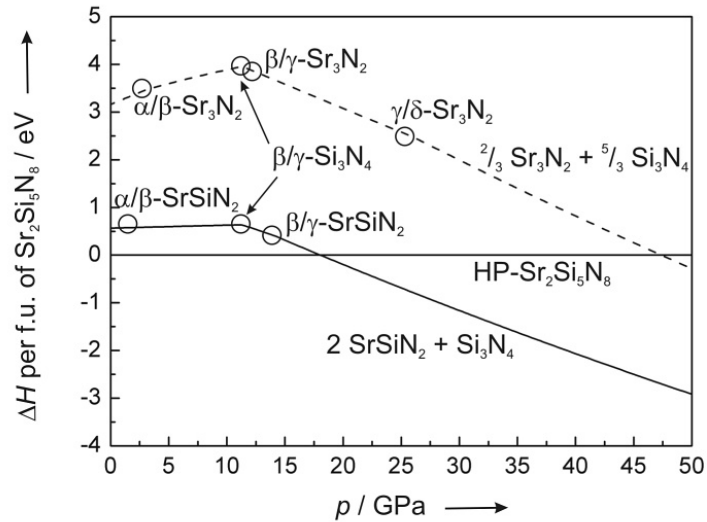
Figure 6.7: Enthalpy-pressure diagram for the decomposition reactions of HP-$Sr_2Si_5N_8$ into $SrSiN_2$ and Si_3N_4 and into Sr_3N_2 and Si_3N_4 (Murnaghan EOS evaluation).

6.2.3 Energy-Volume Calculations for Sr$_2$Si$_5$N$_8$

As both $Sr_2Si_5N_8$ and HP-$Sr_2Si_5N_8$ decompose above approximately 20 GPa, a phase transformation, if taking place at all, has to occur bellow 20 GPa to be detectable. In Figure 6.8 the energy-volume curves of the two considered structures are displayed, in Figure 6.9 the thereof derived enthalpy-pressure phase diagram. It becomes obvious, that no phase transformation from $Sr_2Si_5N_8$ into the HP-$Sr_2Si_5N_8$ structure will take place bellow 30 GPa as $Sr_2Si_5N_8$ is always lower in enthalpy than HP-$Sr_2Si_5N_8$. Therefore, the HP-$Ca_2Si_5N_8$ structure can be ruled out as a high-pressure modification of $Sr_2Si_5N_8$.

6.3 Ba$_2$Si$_5$N$_8$

Besides the experimentally found ambient-pressure structure of $Ba_2Si_5N_8$ (orthorhombic *Pmn2$_1$*, no. 31, isotypic to $Sr_2Si_5N_8$) [16], the HP-$Ca_2Si_5N_8$ structure was considered for a high-pressure phase of $Ba_2Si_5N_8$ (space group *Pbca*, no. 61, further on denoted HP-$Ba_2Si_5N_8$). For the two optimized structures of $Ba_2Si_5N_8$ the coordination numbers of the M^{2+} and Si^{4+} ions were determined by calculating effective coordination numbers (ECoN) [174] with MAPLE [175–178] in order to compare them to the data for the experimentally determined structures (if available). For an in-depth description of the $Ba_2Si_5N_8$ and the HP-$Ca_2Si_5N_8$ structure and a comparison thereof see chapter 6.1.

6.3.1 Structure Optimization for Ba$_2$Si$_5$N$_8$

Structure optimization for both $Ba_2Si_5N_8$ and HP-$Ba_2Si_5N_8$ resulted in reasonable structures, in the case of $Ba_2Si_5N_8$ reproducing very well the experimentally found data. In $Ba_2Si_5N_8$ the two crystallographic independent Ba atoms are both 10-fold coordinated by N, whereas they are 8+3 and 8+4 fold coordinated in hypothetic HP-$Ba_2Si_5N_8$ (Figure 6.10).
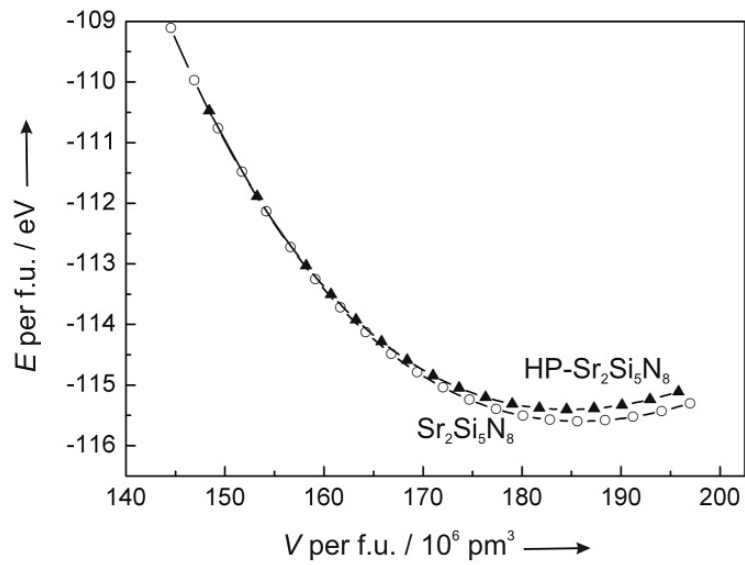
Figure 6.8: Energy-volume (E-V) phase diagram of $Sr_2Si_5N_8$ and HP-$Sr_2Si_5N_8$, calculated within the GGA. Each symbol represents a calculation.
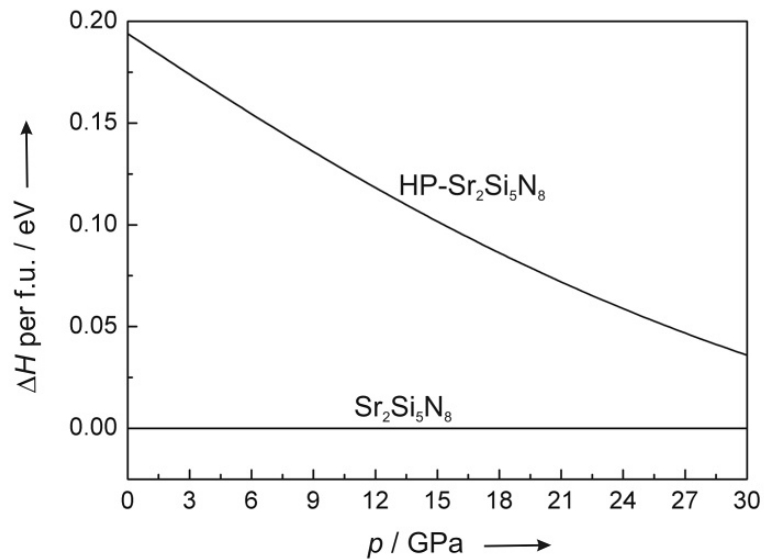
Figure 6.9: Enthalpy-pressure (H-p) diagram for the transition of $Sr_2Si_5N_8$ into HP-$Sr_2Si_5N_8$ (derived from the evaluation of the E-V data by the Murnaghan EOS).
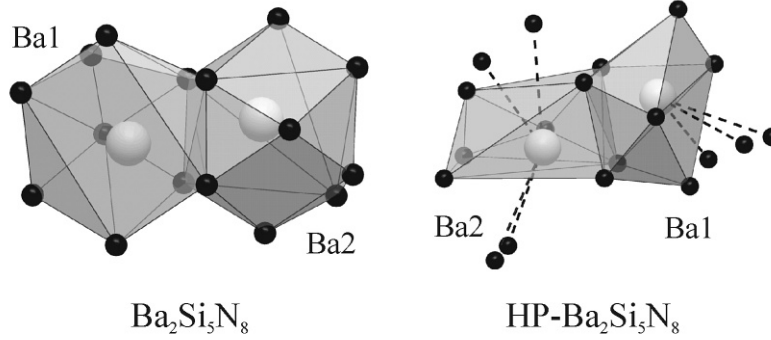
Figure 6.10: BaN_x coordination polyhedra in $Ba_2Si_5N_8$ and hypothetic HP-$Ba_2Si_5N_8$.

Considering the calculated Ba-N and Si-N distances for $Ba_2Si_5N_8$, they are in good agreement with the experimental values (Table 6.3). The values obtained for HP-$Ba_2Si_5N_8$ however reveal certain deficiencies with regard to the Si-N bond lengths, as they are quite long for $Si^{[4]}$-$N^{[3]}$ bonds, more in the range for $Si^{[6]}$ (186.26 pm in γ-Si_3N_4 [4, 5]) than for $Si^{[4]}$ (compare Table 6.3). This may well result from an expansion of the SiN_4 tetrahedra network resulting from the larger cation size of Ba^{2+} compared to Ca^{2+} in the original structure.

Table 6.3: Bond lengths (in pm) in $Ba_2Si_5N_8$ and HP-$Ba_2Si_5N_8$ compared to experimental values.

Structure	Bond type	LDA	GGA	exp.
$Ba_2Si_5N_8$	$Ba^{[10]}$-N	$266.92 - 340.16$	$270.98 - 343.32$	$267.70 - 341.79$ [16]
	$Si^{[4]}$-$N^{[2]}$	$166.00 - 171.65$	$167.64 - 173.67$	$166.55 - 172.56$ [16]
	$Si^{[4]}$-$N^{[3]}$	$173.75 - 177.88$	$175.82 - 180.57$	$174.07 - 179.66$ [16]
HP-$Ba_2Si_5N_8$	$Ba1^{[8+3]}$-N	$259.94 - 360.25$	$262.91 - 366.58$	
	$Ba2^{[8+4]}$-N	$264.30 - 380.32$	$267.75 - 385.92$	
	$Si^{[4]}$-$N^{[2]}$	$166.77 - 175.73$	$168.11 - 177.63$	
	$Si^{[4]}$-$N^{[3]}$	$174.54 - 181.68$	$177.06 - 184.73$	
Ionic Radii	bond type	Shannon [183]	Baur [184]	
	$Ba^{[8]}$-N	288	$296 - 304$	
	$Ba^{[10]}$-N	298	/	
	$Ba^{[12]}$-N	307	/	
	$Si^{[4]}$-$N^{[2]}$	/	171	
	$Si^{[4]}$-$N^{[3]}$	/	173	
	$Si^{[4]}$-$N^{[4]}$	172	/	

Ba$_2$Si$_5$N$_8$ turned out to have the lower energy (-115.586 eV per formula unit) of the two polymorphs, with HP-Ba$_2$Si$_5$N$_8$ being 0.994 eV higher in energy. However, Ba$_2$Si$_5$N$_8$ (ρ = 4.53 g cm^{-3}, matching experimental 4.63 g cm^{-3}) is denser than HP-Ba$_2$Si$_5$N$_8$ (ρ = 4.51 g cm^{-3}) by 0.04 %, which renders HP-Ba$_2$Si$_5$N$_8$ an unlikely candidate for a high-pressure phase of Ba$_2$Si$_5$N$_8$.
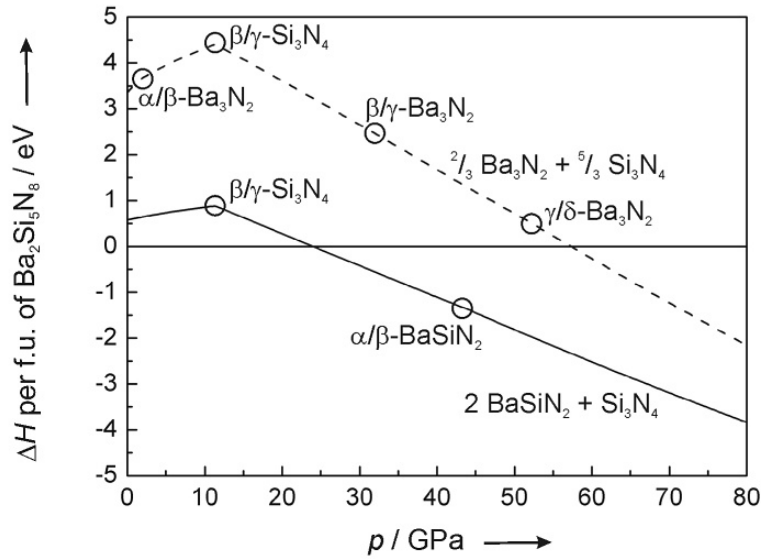
Figure 6.11: Enthalpy-pressure diagram for the decomposition reactions of Ba$_2$Si$_5$N$_8$ into BaSiN$_2$ and Si$_3$N$_4$ and into Ba$_3$N$_2$ and Si$_3$N$_4$ (Murnaghan EOS evaluation).

6.3.2 Decomposition Under Pressure

Analogous to the decomposition of Ca$_2$Si$_5$N$_8$ and Sr$_2$Si$_5$N$_8$ under pressure, the two aforementioned decomposition reactions into (2 BaSiN$_2$ + Si$_3$N$_4$) and into (2/3 Ba$_3$N$_2$ + 5/3 Si$_3$N$_4$) were examined. A decomposition pressure of 58 GPa into 2/3 Ba$_3$N$_2$ and 5/3 Si$_3$N$_4$ and of 24 GPa into 2 BaSiN$_2$ and Si$_3$N$_4$ was calculated and a phase agglomerate of 2 BaSiN$_2$ and Si$_3$N$_4$ is found to be always lower in enthalpy than a phase agglomerate of 2/3 Ba$_3$N$_2$ and 5/3 Si$_3$N$_4$ at ambient and under high pressure (Figure 6.11). Therefor, Ba$_2$Si$_5$N$_8$ is predicted to decompose into BaSiN$_2$ and Si$_3$N$_4$ under pressure. All known high-pressure phases of Si$_3$N$_4$ (compare chapter 3.2) and the potential high-pressure phases of BaSiN$_2$ (compare

chapter 5.2) were taken into account as well as the postulated ambient- and high-pressure phases of hypothetic Ba_3N_2 (compare chapter 4.2).

6.4 Hypothetic $Mg_2Si_5N_8$

Even though the compounds of composition $M_2Si_5N_8$ are known for Ca, Sr and Ba, $Mg_2Si_5N_8$ has until now eluded all synthetical endeavors. For this reason, hypothetic $Mg_2Si_5N_8$ has been calculated in the two experimentally known polymorphs of $Ca_2Si_5N_8$, monoclinic $Ca_2Si_5N_8$ [15] and HP-$Ca_2Si_5N_8$, as well as the structure of $Sr_2Si_5N_8$ and $Ba_2Si_5N_8$ [16]. Their relation under pressure as well as their decomposition behavior towards stoichiometric phase agglomerates of $MgSiN_2/Si_3N_4$ and Mg_3N_2/Si_3N_4 have been studied.

6.4.1 Structure Optimization for $Mg_2Si_5N_8$

Structure optimization for $Mg_2Si_5N_8$ in all three considered structure types was possible and resulted in reasonable structures. Monoclinic $Mg_2Si_5N_8$ (equivalent to monoclinic $Ca_2Si_5N_8$, space group *Cc*, no. 9 [15]) turned out with the lowest energy (-113.832 eV per formula unit) and a density of 2.91 g cm^{-3}. HP-$Mg_2Si_5N_8$ (equivalent to HP-$Ca_2Si_5N_8$, space group *Pbca*, no. 61) is 0.581 eV higher in energy and 2.1 % denser than monoclinic $Mg_2Si_5N_8$. Orthorhombic o-$Mg_2Si_5N_8$ (equivalent to $Sr_2Si_5N_8$ and $Ba_2Si_5N_8$, space group *Pmn2*$_1$, no. 31 [16]) comes out 1.273 eV higher in energy than monoclinic $Mg_2Si_5N_8$ and 0.692 eV higher than HP-$Mg_2Si_5N_8$. However, with a density of 2.71 g cm^{-3} it is less dense than monoclinic $Mg_2Si_5N_8$ and HP-$Mg_2Si_5N_8$. The calculated zero-pressure bulk moduli amount to 154 GPa for monoclinic $Mg_2Si_5N_8$, 109 GPa for HP-$Mg_2Si_5N_8$ and 122 GPa for o-$Mg_2Si_5N_8$. For monoclinic $Mg_2Si_5N_8$ a trigonal pyramidal coordination by N for both crystallographic independent Mg^{2+} ions was derived. The coordination number of half of the Mg atoms is increased to five (quadratic pyramid) in HP-$Mg_2Si_5N_8$, whereas the other half retains CN = 4 (distorted tetrahedron). In o-$Mg_2Si_5N_8$ the Mg^{2+} ions are only three-fold coordinated by N, as they "hover" above a trigonal plane spanned by thee N atoms (Figure 6.12).

The calculated Mg-N and Si-N distances are given in Table 6.4. They are all in the range of such in $MgSiN_2$. However, in contrast to all other $M_2Si_5N_8$ compounds discussed so far, the difference for $Si^{[4]}$-$N^{[2]}$ and $Si^{[4]}$-$N^{[3]}$ distances is not as pronounced in monoclinic $Mg_2Si_5N_8$. The upper boundary for both is virtually identical.
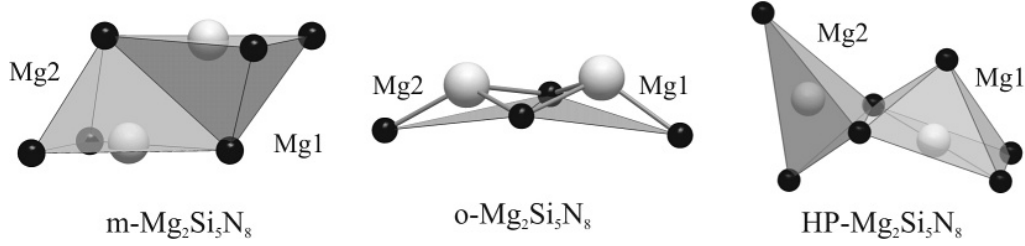
Figure 6.12: MgN_x coordination polyhedra in hypothetic m-$Mg_2Si_5N_8$, HP-$Mg_2Si_5N_8$ and o-$Mg_2Si_5N_8$.

Table 6.4: Bond lengths (in pm) in monoclinic $Mg_2Si_5N_8$, HP-$Mg_2Si_5N_8$ and o-$Mg_2Si_5N_8$ compared to values in $MgSiN_2$ (compare section 5.2).

Structure	Bond type	LDA	GGA	exp.
m-$Mg_2Si_5N_8$	$Mg^{[4]}$-N	$206.34 - 231.55$	$209.25 - 234.27$	/
	$Si^{[4]}$-$N^{[2]}$	$168.65 - 176.47$	$170.37 - 178.33$	/
	$Si^{[4]}$-$N^{[3]}$	$170.10 - 176.65$	$171.94 - 178.63$	/
HP-$Mg_2Si_5N_8$	$Mg1^{[5]}$-N	$216.65 - 229.58$	$219.00 - 234.24$	/
	$Mg2^{[4]}$-N	$209.30 - 240.68$	$211.31 - 253.67$	/
	$Si^{[4]}$-$N^{[2]}$	$166.60 - 174.28$	$168.06 - 176.03$	/
	$Si^{[4]}$-$N^{[3]}$	$171.52 - 177.58$	$173.61 - 179.38$	/
o-$Mg_2Si_5N_8$	$Mg^{[3]}$-N	$202.12 - 207.27$	$203.47 - 209.84$	/
	$Si^{[4]}$-$N^{[2]}$	$169.39 - 172.92$	$170.97 - 174.72$	/
	$Si^{[4]}$-$N^{[3]}$	$171.52 - 174.82$	$173.34 - 176.98$	/
$MgSiN_2$	$Mg^{[4]}$-$N^{[6]}$	$205.33 - 210.27$	$208.33 - 213.77$	$205.92 - 211.50$ [235]
	$Si^{[4]}$-$N^{[6]}$	$172.60 - 174.95$	$174.41 - 176.99$	$173.81 - 179.65$ [235]

Ionic Radii	bond type	Shannon [183]	Baur [184]	
	$Mg^{[4]}$-N	203	$206 - 214$	
	$Mg^{[6]}$-N	218	$212 - 220$	
	$Si^{[4]}$-$N^{[2]}$	/	171	
	$Si^{[4]}$-$N^{[3]}$	/	173	
	$Si^{[4]}$-$N^{[4]}$	172	/	

6.4.2 Energy-Volume Calculations for Mg$_2$Si$_5$N$_8$

In Figure 6.13 the energy-volume curves of the three hypothetic $Mg_2Si_5N_8$ phases are depicted. The enthalpy as a function of pressure, as derived of these energy-volume curves, is shown in Figure 6.14. According to this enthalpy-pressure phase diagram, monoclinic $Mg_2Si_5N_8$ should be the stable polymorph up to 20 GPa, when HP-$Mg_2Si_5N_8$ becomes lower in enthalpy. o-$Mg_2Si_5N_8$ remains higher in enthalpy than both other polymorphs up to pressures of at least 40 GPa.
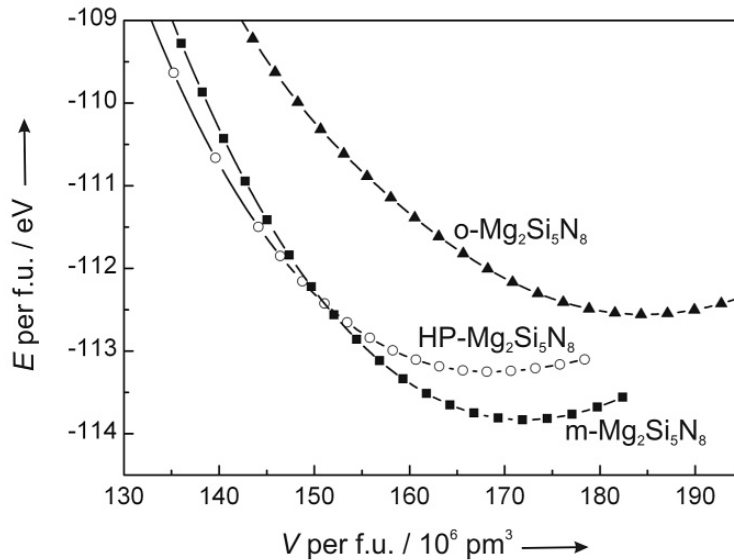
Figure 6.13: Energy-volume (E-V) phase diagram of m-$Mg_2Si_5N_8$, HP-$Mg_2Si_5N_8$ and o-$Mg_2Si_5N_8$, calculated within the GGA. Each symbol represents a calculation.

6.4.3 Decomposition Under Pressure

To determine, if and and if so, up to what pressures hypothetic $Mg_2Si_5N_8$ is stable against other compounds in the Mg-Si-N system, the two before discussed decomposition pathways of $M_2Si_5N_8$ were examined:
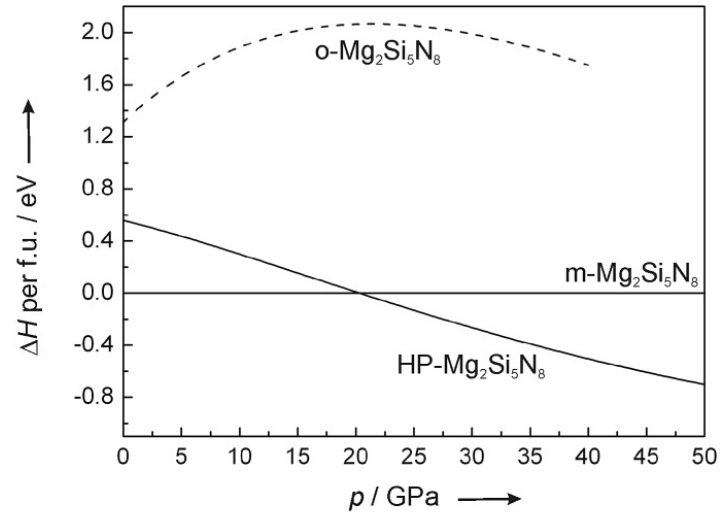
Figure 6.14: Enthalpy-pressure (H-p) diagram for the transition of m-$Mg_2Si_5N_8$ into HP-$Mg_2Si_5N_8$ ($p_t = 20\,GPa$) and into o-$Mg_2Si_5N_8$ (derived from the evaluation of the E-V data by the Murnaghan EOS).
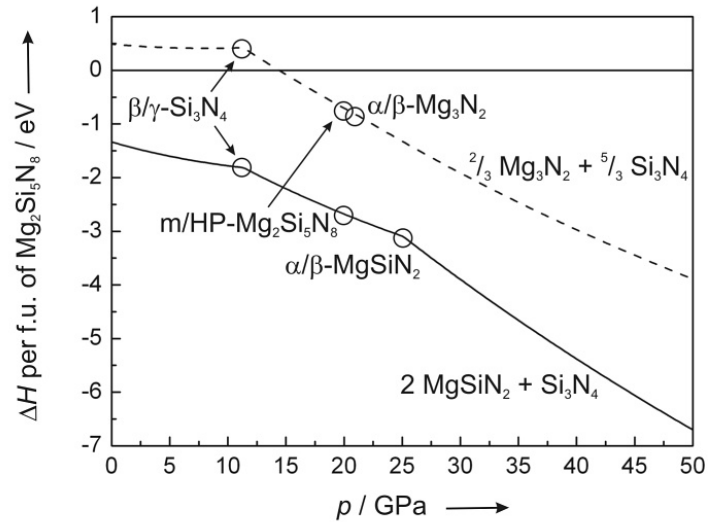
Figure 6.15: Enthalpy-pressure diagram for the decomposition reactions of hypothetic $Mg_2Si_5N_8$ into $MgSiN_2$ and Si_3N_4 and into Mg_3N_2 and Si_3N_4 (Murnaghan EOS evaluation).

$$3 \text{ M}_2\text{Si}_5\text{N}_8 \rightarrow 2 \text{ M}_3\text{N}_2 + 5 \text{ Si}_3\text{N}_4 \qquad\qquad (6.5)$$

$$\text{M}_2\text{Si}_5\text{N}_8 \rightarrow 2 \text{ MSiN}_2 + \text{Si}_3\text{N}_4. \qquad\qquad (6.6)$$
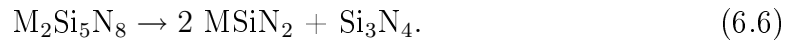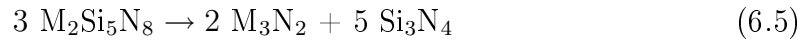
As becomes obvious from the reaction enthalpy of the two decomposition reactions as depicted in Figure 6.15, $\text{Mg}_2\text{Si}_5\text{N}_8$ would be stable against a phase agglomerate of 2/3 Mg_3N_2 and 5/3 Si_3N_4 up to 16 GPa, but it is always higher in enthalpy than a phase agglomerate of 2 MgSiN_2 and Si_3N_4. These findings explain at least from a thermodynamic point of view, why $\text{Mg}_2\text{Si}_5\text{N}_8$ could not be synthesized until now (allowing for the limitations presented by the three known structure types for $\text{A}_2\text{B}_5\text{X}_8$ compounds). Apparently, a phase agglomerate of 2 MgSiN_2 and Si_3N_4 constitutes a thermodynamical sink, which becomes even "deeper" under pressure.

7 Beryllium Nitridophosphate BeP$_2$N$_4$

P-N compounds often exhibit striking similarities to Si-O compounds. This can be traced back to the fact, that PN$_2^-$ is isoelectronic to SiO$_2$. HPN$_2$ exhibits a β-cristobalite type structure [280] and LiPN$_2$ and NaPN$_2$ [281, 282] are D1-type distortions of the filled β-cristobalite structure (isotypic to chalcopyrite). Besides the diverse substance class of the zeolites, also clathrates are known for SiO$_2$ frameworks. Clathrates are usually uncharged SiO$_2$ frameworks built up by corner-sharing SiO$_4$ tetrahedra, which host neutral molecules or nothing in their cage like pores. With [P$_4$N$_4$(NH)$_4$](NH$_3$) the first nitridic clathrate has been realized [283]. [P$_4$N$_4$(NH)$_4$](NH$_3$) exhibits an unprecedented HPN$_2$ framework structure of corner-sharing PN$_4$ tetrahedra.

However, P-N compounds also profit from the extended structural possibilities of N compared to O. Oxygen is limited to being terminal or bridging two tetrahedron centers, whereas N can connect up to four tetrahedron centers.

Phosphorus(V)nitride P$_3$N$_5$, which has been mentioned as early as 1862 [92] and whose synthesis was first reported in 1903 [284], but whose structure could not be solved until 1997 [285], already evinces edge-sharing PN$_4$ tetrahedra in its ambient-pressure modification. This finding is in contrast to the ambient-pressure modifications of Si$_3$N$_4$ (α- and β-Si$_3$N$_4$) as well as cubic BN, which are solely built up of corner-sharing TN$_4$ tetrahedra [2, 3, 286]. For P$_3$N$_5$ as well as Si$_3$N$_4$ increased coordination numbers for P (and Si, respectively) could be realized under pressure [4, 5, 22, 23]. At 11 GPa γ-P$_3$N$_5$ can be synthesized, which exhibits not only PN$_4$ tetrahedra, but also PN$_5$ quadratic pyramids. Layers of edge- and corner-sharing PN$_5$ quadratic pyramids are interconnected by chains of corner-sharing PN$_4$ tetrahedra. Further high-pressure phases have been predicted by Kroll and Schnick [24]

and by Dong et al. [287]. Kroll and Schnick propose a kyanite structure for δ-P$_3$N$_5$, comprising PN$_6$ octahedra and PN$_4$ tetrahedra, which may distort upon quenching to ambient conditions along a shear distortion path, resulting in monoclinic δ'-P$_3$N$_5$ built up of PN$_6$ octahedra, PN$_5$ trigonal bipyramids and PN$_4$ tetrahedra. Dong et al. propose a V$_3$O$_5$-type structure, composed solely of PN$_6$ octahedra, as a second high-pressure phase of P$_3$N$_5$.

Hardness measurements by Vickers indentation method revealed a hardness (H$_V$) of 5.1(7) GPa for partly crystalline ambient-pressure P$_3$N$_5$ and of 9.7(21) GPa for γ-P$_3$N$_5$ [23]. The respective bulk moduli for α- and γ-P$_3$N$_5$ were calculated to 87 to 99 GPa and 103 to 116 GPa [24]. Hypothetic δ'-P$_3$N$_5$ might even be harder. Its bulk modulus has been calculated to 240 GPa [24].

The nitridophosphate BeP$_2$N$_4$ crystallizes in the phenakite(Be$_2$SiO$_4$)-type structure [25]. It is the only MP$_2$N$_4$ compound of the group II elements exhibiting this structure type. MgP$_2$N$_4$, CaP$_2$N$_4$ and SrP$_2$N$_4$ crystallize in the megakalsilite(KAlSiO$_4$)-type structure, whereas BaP$_2$N$_4$ is isotypic to high-pressure CaB$_2$O$_4$-IV [25–29]. All mentioned structures of MP$_2$N$_4$ are built up by corner-sharing PN$_4$ tetrahedra.

Since BeP$_2$N$_4$ exhibits the phenakite structure like β-Si$_3$N$_4$ [3], which transforms into a spinel-type structure under pressure (γ-Si$_3$N$_4$) [4, 5], a spinel-type high-pressure phase of BeP$_2$N$_4$ seems to be likely. This is even mores so, as Si$_3$N$_4$ and BeP$_2$N$_4$ are iso(valence)electronic (32 valence electrons per formula unit) and the ionic radii of Be^{2+} and P^{5+} are comparable to that of Si^{4+} [183]. In analogy to γ-Si$_3$N$_4$, which exhibits a significantly higher hardness than α- and β-Si$_3$N$_4$ [7], spinel-type BeP$_2$N$_4$ can be expected to be harder than phenakite-type BeP$_2$N$_4$ and – due to its makeup of small atoms, its short bonds and high covalency in addition to a partly increased coordination number from 4 to 6 – to be a quite hard material [288, 289]. Therefore, spinel-type BeP$_2$N$_4$ was calculated within LDA and GGA and the transition pressure of phenakite-type BeP$_2$N$_4$ into spinel-type BeP$_2$N$_4$ was derived from energy-volume calculations.

7.1 BeP$_2$N$_4$

BeP$_2$N$_4$ crystallizes in the trigonal space group $R\bar{3}$ (no. 148), isotypic to phenakite Be$_2$SiO$_4$ [290, 291]. The structure is built up of all-side corner sharing BeN$_4$ and PN$_4$ tetrahedra, giving a coordination description Be$^{[4]}$P$_2^{[4]}$N$_4^{[3]}$. The connectivity of the tetrahedra is identical to that in phenakite and β-Si$_3$N$_4$, with a prominent characteristic of the structure being *sechser* ring channels along [001] (compare Figure 7.1).

BeP$_2$N$_4$ - experimental   BeP$_2$N$_4$ - calculated

β-Si$_3$N$_4$ BeP$_2$N$_4$ - calculated
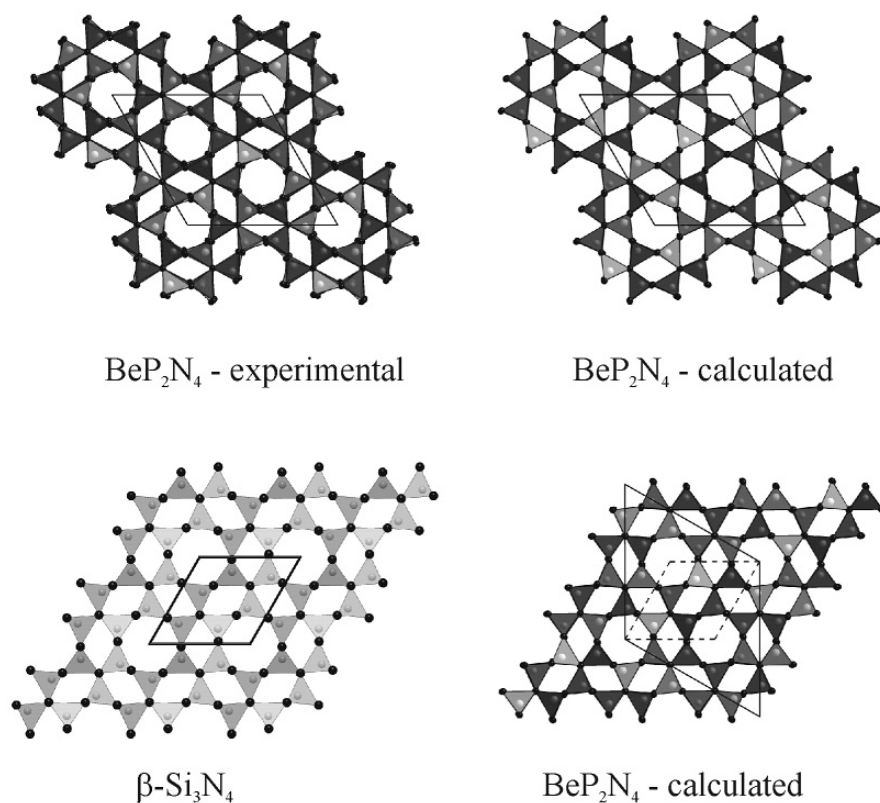
Figure 7.1: Structures of BeP$_2$N$_4$ (annealed) compared to calculated structure and β-Si$_3$N$_4$ (viewed along [001]).

In contrast to β-Si$_3$N$_4$ and phenakite, the structure of BeP$_2$N$_4$ is somewhat more distorted, which becomes obvious when examining the x and y fractional coordinates of atoms placed above each other viewed along [001]. In β-Si$_3$N$_4$ they are

identical, due to the higher symmetry, and in phenakite, they are almost identical with only very small deviations. In BeP$_2$N$_4$ larger deviations are found (compare Table 7.1). However, when comparing these deviations for raw product BeP$_2$N$_4$ and an annealed sample, they are smaller for the annealed sample, suggesting, that annealing leads towards higher crystallinity. The deviations are even smaller within structure optimized BeP$_2$N$_4$ from LDA and GGA calculations.

Table 7.1: Deviations in the fractional x- and y-coordinates of cations and anions in BeP$_2$N$_4$ and phenakite Be$_2$SiO$_2$ placed above each other viewd along [001]

structure	$\Delta_{(x/y)}$ (anions)	$\Delta_{(x/y)}$ (cations)
BeP$_2$N$_4$ (raw product) [25]	$0.0147 - 0.0423$	$0.0171 - 0.0165$
BeP$_2$N$_4$ (annealed) [25]	$0.0057 - 0.0339$	$0.0147 - 0.0212$
BeP$_2$N$_4$ (LDA)	$0.0051 - 0.0125$	$0.0027 - 0.0042$
BeP$_2$N$_4$ (GGA)	$0.0054 - 0.0135$	$0.0026 - 0.0051$
Be$_2$SiO$_4$ [291]	$0.0006 - 0.0020$	$0.0013 - 0.0015$

A similar tendency is reflected in the tetrahedra angles N-P-N and N-Be-N compared to those in phenakite (O-Be-O and O-Si-O) and β-Si$_3$N$_4$ (N-Si-N) (Table 7.2). They are scattered over a larger range in raw product BeP$_2$N$_4$, which becomes significantly reduced in annealed BeP$_2$N$_4$ but is still larger than that found in phenakite and β-Si$_3$N$_4$. Again the values obtained from the optimized structures are still closer to those found in phenakite and β-Si$_3$N$_4$.

With regard to the (Be/P)-N-(Be/P) angles (Table 7.2), the spread found for these angles in raw product BeP$_2$N$_4$ is larger than that in all other structures. The values in annealed BeP$_2$N$_4$ as well as in the calculated structures are similar to those in phenakite and β-Si$_3$N$_4$.

The calculated bond lengths P-N and Be-N in comparison to the experimental values are given in Table 7.3. The spread of the calculated bond lengths is smaller than that for the experimentally determined structure. However all values adopt values similar to those found in α-P$_3$N$_5$ [292] and α-Be$_3$N$_2$ [179] with P-N bonds in raw product BeP$_2$N$_4$ and Be-N bonds in annealed BeP$_2$N$_4$ exhibiting the largest spread in bond lengths.

Table 7.2: Tetrahedra angles and cation-anion-cation angles in BeP_2N_4 (experimental [25] and calculated) as well as in phenakite [291] and β-Si_3N_4 [3].

	N-P-N (O-Be-O)	N-Be-N (O-Si-O)
BeP_2N_4 (raw product)	$93.82 - 133.04$	$81.94 - 131.47$
BeP_2N_4 (annealed)	$98.73 - 118.43$	$101.42 - 117.95$
BeP_2N_4 (LDA)	$108.70 - 112.50$	$107.11 - 109.38$
BeP_2N_4 (GGA)	$107.22 - 112.78$	$106.72 - 109.26$
Be_2SiO_4	$107.56 - 114.29$	$107.80 - 113.01$
β-Si_3N_4	$108.69 - 115.64$	
	A-X-B (A, B = Be, P, Si; X = N, O)	
BeP_2N_4 (raw product)	$102.47 - 127.18$	
BeP_2N_4 (annealed)	$110.69 - 125.88$	
BeP_2N_4 (LDA)	$110.48 - 127.98$	
BeP_2N_4 (GGA)	$112.28 - 128.15$	
Be_2SiO_4	$113.08 - 123.69$	
β-Si_3N_4	$115.64 - 121.91$	

Table 7.3: Bond lengths in BeP_2N_4 (experimental [25] and calculated), compared to values in α-P_3N_5 [292] and α-Be_3N_2 [179].

	$Be^{[4]}$-N	$P^{[4]}$-N
BeP_2N_4 (raw product)	$159.77 - 179.41$	$157.18 - 186.77$
BeP_2N_4 (annealed)	$148.20 - 181.08$	$160.35 - 172.96$
BeP_2N_4 (LDA)	$170.52 - 173.10$	$161.86 - 163.73$
BeP_2N_4 (GGA)	$172.58 - 175.99$	$163.58 - 165.47$
α-P_3N_5 (Cc)	/	$150.72 - 174.46$
α-P_3N_5 ($C2/c$)	/	$153.66 - 172.59$
α-Be_3N_2	$172.45 - 181.55$	/
Ionic Radii (Shannon [183])	171	163
Ionic Radii (Baur [184])	175	158

7.2 Spinel Structures

Spinels are compounds of composition AB_2X_4. The anions X form a cubic close packing (ccp) and the cations occupy $^1/_8{}^{th}$ of the tetrahedral voids and half of the octahedral voids. In the normal spinel structure the A atoms occupy the tetrahedral voids, whereas the B atoms are located in the octahedral voids (Figure 7.2). In inverse spinels, half of the B atoms occupy tetrahedral sites and half occupy octahedral sites, whereas the A atoms occupy the remaining octahedral sites (Figure

7.2). In between these two types of spinel structures countless partly inverse spinel structures can be envisaged [293].
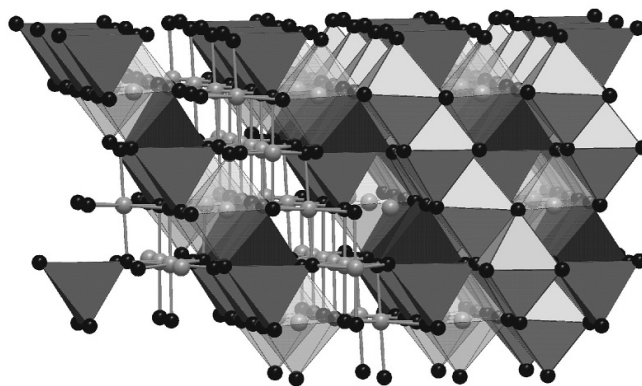
BeP$_2$N$_4$ - normal spinel
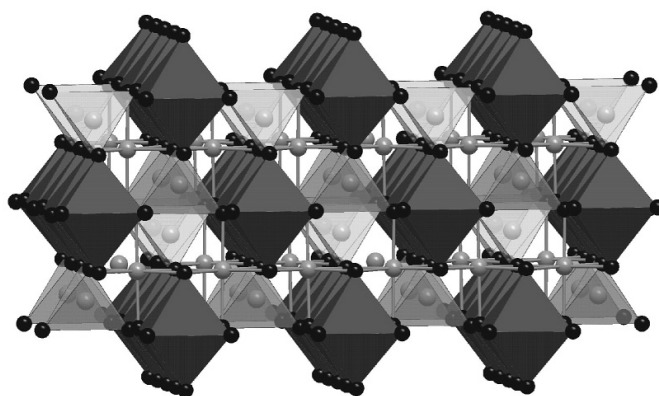
BeP$_2$N$_4$ - inverse spinel

Figure 7.2: Spinel and inverse spinel structure (Be polyhedra are depicted in black).

BeP$_2$N$_4$ was calculated in the normal as well as the inverse spinel structure. Normal spinel crystallizes in space group $Fd\bar{3}m$ (no. 227, cubic). The Be atoms were located on the tetrahedral sites, the P atoms on the octahedral sites. Therefore, in normal spinel BeP$_2$N$_4$ (sp-BeP$_2$N$_4$) the coordination number of P would be increased from four to six for all P atoms compared to ambient-pressure BeP$_2$N$_4$. The coordination of Be remains unchanged.

To construct the inverse spinel structure, the primitive unit cell of normal spinel was used as a starting point. This cell contains two formula units, resulting in two tetrahedral and four octahedral positions. The tetrahedral positions were solely occupied by P. For the distribution of the remaining P and Be atoms on the octahedral positions, from a combinatorial point of view six patterns were possible. However, all combinations resulted in the same structure (Figure 7.3). The resulting structure for inverse spinel exhibits the orthorhombic space group *Imma* (no. 74). An inverse spinel high-pressure phase of BeP_2N_4 (isp-BeP_2N_4) would result in a partially increased coordination number for P, as only half of the P atoms are occupying octahedral sites, whereas the coordination number for all Be would be increased from four to six, which, to the best knowledge of the author, is not yet known except for central Be in Zr_6 clusters [294–298].

normal spinel   inverse spinel
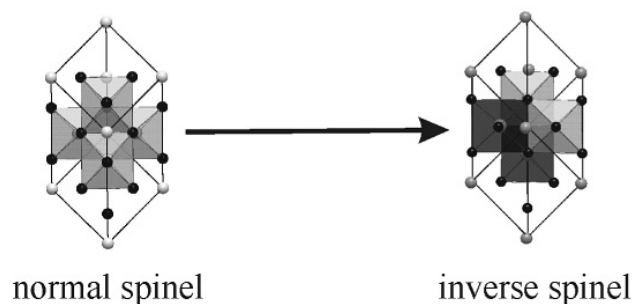
Figure 7.3: Construction of inverse spinel from the normal spinel structure (Be atoms drawn light gray, P atoms dark gray, N atoms black; Be/PN_6 octahedra are drawn, PN_6 octahedra light gray, BeN_6 octahedra black.

The calculated P-N and Be-N distances for sp-BeP_2N_4 and inverse sp-BeP_2N_4 are listed in Table 7.4. They are all in the range of such bonds found in Be_3N_2 and P_3N_5 compounds. $Be^{[6]}$-N distances are longer than $Be^{[4]}$-N distances, as are bond lengths $P^{[6]}$-N in comparison to bond lengths $P^{[4]}$-N.

Table 7.4: Bond lengths in normal and inverse spinel BeP$_2$N$_4$, compared to values in γ-P$_3$N$_5$ [22, 23] and α-Be$_3$N$_2$ [179] as well as the theoretically predicted P$_3$N$_5$ phases δ-P$_3$N$_5$ [24] and δ'-P$_3$N$_5$ [24] .

	Be[4]-N	Be[6]-N	P[4]-N	P[5]-N	P[6]-N
sp-BeP$_2$N$_4$ (LDA)	173.76	/	/	/	176.19
sp-BeP$_2$N$_4$ (GGA)	179.91	/	/	/	182.24
isp-BeP$_2$N$_4$ (LDA)	/	181.49, 184.53	162.37, 172.23	/	176.72, 181.39
isp-BeP$_2$N$_4$ (GGA)	/	183.39, 187.22	164.05, 175.36	/	178.93, 183.99
γ-P$_3$N$_5$	/	/	158.65, 169.76	165.71 − 177.54	/
δ-P$_3$N$_5$	/	/	156.3 − 159.9	/	164.9 − 186.9
δ'-P$_3$N$_5$	/	/	153.9 − 165.7	159.2 − 187.1	174.3 − 185.1
α-Be$_3$N$_2$	172.45 − 181.55	/	/	/	/
γ-Be$_3$N$_2$ (LDA)	167.18 − 181.91	198.33	/	/	/
γ-Be$_3$N$_2$ (GGA)	168.86 − 185.35	201.08	/	/	/
Ionic Radii (Shannon [183])	171	191	163	175	184
Ionic Radii (Baur [184])	177	/	160	/	/

7.3 Ground State Properties of BeP$_2$N$_4$ Polymorphs

Phenakite-type BeP$_2$N$_4$ exhibits both within LDA and GGA the lowest ground state energy (LDA: -58.817 eV; GGA: -52.840 eV) and density. The calculated density (LDA: 3.31 g cm⁻³; GGA: 3.20 g cm⁻³) matches quite well the experimental value (3.26 g cm⁻³ [25]). Spinel-type BeP$_2$N$_4$ is about 22 % denser than phenakite-type BeP$_2$N$_4$ and 1.105 eV (LDA) and 1.611 eV (GGA), respectively, higher in energy. Inverse spinel-type BeP$_2$N$_4$ is the densest phase of the three considered (about 24 - 25 % denser than phenakite-type BeP$_2$N$_4$ and about 2% denser than spinel-type BeP$_2$N$_4$). It comes out 2.428 eV (LDA) and 2.979 eV higher in energy than phenakite-type BeP$_2$N$_4$ and 1.323 eV (LDA) and 1.368 eV (GGA) higher than spinel-type BeP$_2$N$_4$.

Phenakite-type BeP_2N_4 exhibits the lowest bulk modulus (220 GPa (GGA)). Spinel-type BeP_2N_4 has a zero-pressure bulk modulus of 291 GPa within LDA and of 263 GPa within GGA. The highest bulk modulus was found for inverse spinel-type BeP_2N_4, which amounts to 316 GPa within LDA and to 278 GPa within GGA. All calculated values are listed in Table 7.5.

Table 7.5: E_0, V_0, B_0 and ρ_0 of phenakite-type, spinel-type (sp) and inverse spinel-type (isp) BeP_2N_4 within LDA and GGA (E_0 and V_0 given per formula unit).

	E_0 / eV	V_0 / 10^6 pm^3	B_0 / GPa	ρ_0 / g cm^{-1}
BeP_2N_4 (LDA)	-58.817	63.66	/	3.31
sp-BeP_2N_4	-57.721	52.01	291	4.05
isp-BeP_2N_4	-56.389	50.97	316	4.14
BeP_2N_4 (GGA)	-52.840	65.99	220	3.20
sp-BeP_2N_4	-51.229	54.11	263	3.90
isp-BeP_2N_4	-49.861	53.11	278	3.97

A high bulk modulus is an indicator for hardness, but not a sufficient precondition for hardness, since the hardness of a material is determined by various factors. It is widely accepted, that small atoms, short bonds, a high degree of covalency, a high bond density and a high packing efficiency are required for hard materials [288, 289]. An increase of the coordination number alone will not necessarily effect a higher hardness, since it indeed increases the packing efficiency but also bond length and ionicity. This results in opposed effects on the hardness and it remains to be seen which factor is dominant [289]. For spinel-type γ-Si_3N_4 an increase in hardness as compared to β-Si_3N_4 is paralleled by an increase in bulk modulus. As BeP_2N_4 is iso(valence)electronic to Si_3N_4, the ionic radii for Be^{2+} and P^{5+} are similar to that of Si^{4+} [183], the phase transformation from phenakite-type to spinel-type BeP_2N_4 is also accompanied by an increase of the bulk modulus and the bulk modulus of spinel-type BeP_2N_4 adopts a value between that of corundum ($B_0 = 252$ GPa, $H_V = 20$ GPa [203]) and γ-Si_3N_4 (B_0 exp. = 290 - 317 GPa [7, 8], B_0 calculated = 292 - 319 GPa [4, 6], $H_V = 30$-43 GPa [7]), spinel-type BeP_2N_4 is likely to exhibit a hardness similar to these compounds and higher than that of phenakite-type BeP_2N_4, which would render it a quite hard material.

7.4 Energy-Volume Calculations for BeP$_2$N$_4$

In Figure 7.4 the energy-volume curves calculated within GGA is depicted. From this, the enthalpy-pressure phase diagram, as depicted in Figure 7.5 was derived. Accordingly, the transition pressure of phenakite-type BeP$_2$N$_4$ into spinel-type BeP$_2$N$_4$ was calculated to 24 GPa within GGA. Inverse spinel-type BeP$_2$N$_4$ was found to be always higher in enthalpy than either phenakite-type or spinel-type BeP$_2$N$_4$ up to 100 GPa (compare also Figure 7.6). Therefore, only spinel-type BeP$_2$N$_4$ seems to be a candidate for a high-pressure phase of BeP$_2$N$_4$.

As the calculated transition pressure for phenakite-type BeP$_2$N$_4$ into spinel-type BeP$_2$N$_4$ is quite low with 24 GPa, this phase transition might well be already observable in multi-anvil setups and should be easily detectable in diamond anvil cell setups, even if - due to kinetic effects - the experimental transition pressure is somewhat higher than the calculated value.
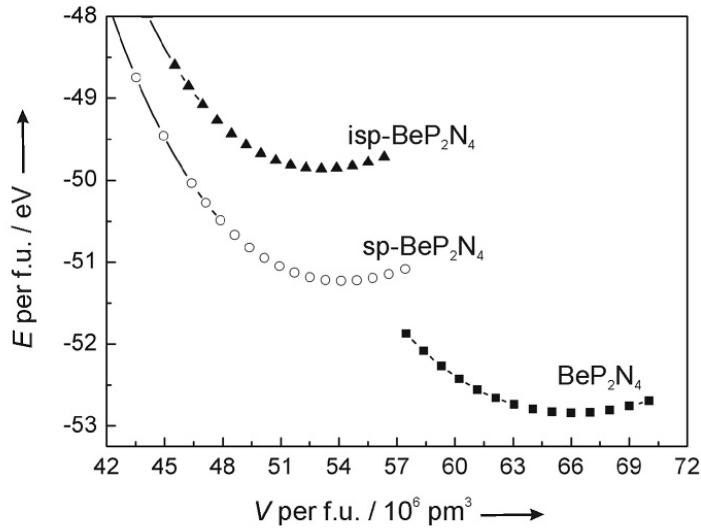
Figure 7.4: Energy-volume (E-V) phase diagram of phenakite-type, spinel-type (sp) and inverse spinel-type (isp) BeP$_2$N$_4$, calculated within the GGA. Each symbol represents a calculation.
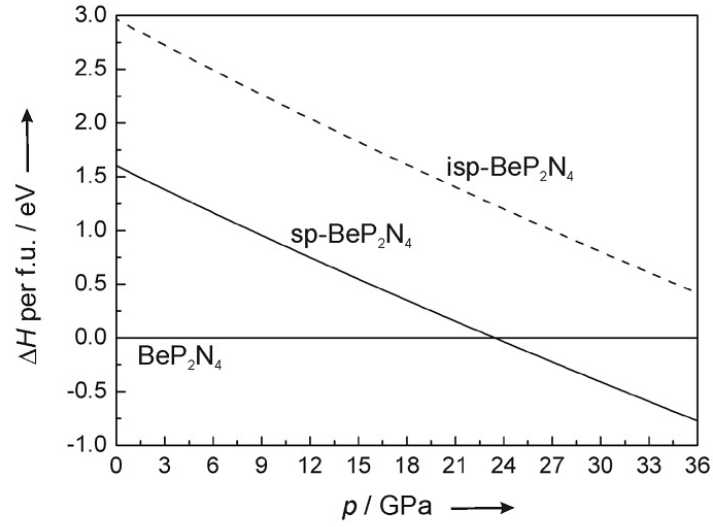
Figure 7.5: Enthalpy-pressure (*H-p*) diagram for the transition of phenakite-type BeP$_2$N$_4$ into spinel-type (sp) BeP$_2$N$_4$ (p$_t$ = 24 GPa). Inverse spinel-type (isp) BeP$_2$N$_4$ remains always higher in enthalpy than either other polymorph (GGA, derived from the evaluation of the *E-V* data by the Murnaghan EOS).
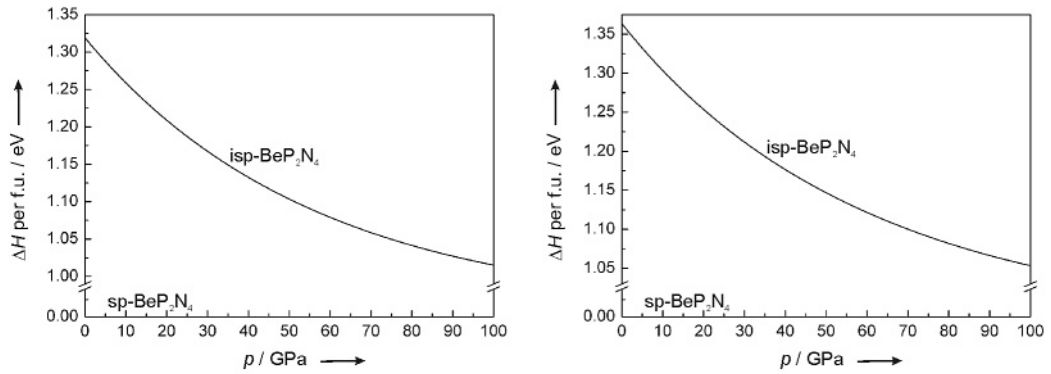
Figure 7.6: Enthalpy-pressure (*H-p*) diagrams for the transition of spinel-type (sp) BeP$_2$N$_4$ into inverse spinel-type (isp) BeP$_2$N$_4$ (left: LDA, right: GGA, derived from the evaluation of the *E-V* data by the Murnaghan EOS).

8 Conclusion and Prospects

Binary Group II Nitrides

Binary oxides and nitrides are usually regarded as simple and well characterized compounds, which do not preserve further mysteries and promise no further discoveries. However, this is not true, which is vividly illustrated by the binary group II nitrides. Only for Be_3N_2, Mg_3N_2 and Ca_3N_2 ambient-pressure structures are known, while the binary nitrides of formula Sr_3N_2 and Ba_3N_2 have eluded all efforts to discover their secrets. It is even unknown, if these compounds do exist or if the multitude of known other binary strontium-nitrogen and barium-nitrogen compounds constitute a thermodynamic and kinetic sink, which prevents the formation of the binary nitrides M_3N_2.

Calculations for Be_3N_2, Mg_3N_2 and Ca_3N_2 revealed a wide range of promising high-pressure phases. Especially the high-pressure chemistry of Ca_3N_2 is a very rich one, revealing four high-pressure phases bellow 40 GPa. Subsequent high-pressure high-temperature experiments hopefully will confirm these findings.

For Sr_3N_2 and Ba_3N_2 ground-state structures have been proposed. But, even if these compounds are not synthesizeable at ambient pressure, they or their high-pressure polymorphs may well be synthesizeable under high pressure. Subsequent calculations are needed to clarify the thermodynamical stability of the proposed structures against phase agglomerates of other binary Sr- and Ba-nitrogen compounds and N_2 or Sr and Ba, respectively. Examples of such equilibria, that have to be accounted for, are given in Figure 8.1.

$$4\,M_3N_2 \;\rightleftharpoons\; 6\,M_2N + N_2 \qquad \text{(a)}$$

$$M_3N_2 \;\rightleftharpoons\; MN_2 + 2\,M \qquad \text{(b)}$$

$$3\,M_3N_2 \;\rightleftharpoons\; 2\,M_4N_3 + M \qquad \text{(c)}$$
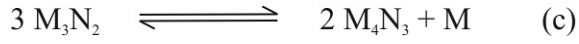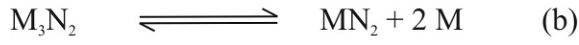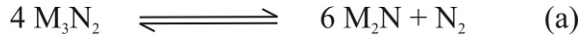
Figure 8.1: Different reactions to be investigated for M_3N_2.

Künzel [146] proposed a disordered NaCl-type structure for Ba_3N_2. Preliminary calculations with a triple NaCl unit cell, however, revealed, that this structure is higher in enthalpy than most calculated structure types and becomes even more so under pressure. Still, it has to be considered, that a triple unit cell leaves only limited possibilities to simulate a disordered structure. Therefore, calculations with larger supercells have to be conducted to further clarify this matter.

Nitridosilicates

Nitridosilicates have been extensively investigated at ambient pressure and a wide range of ambient-pressure nitridosilicates are known. All 14 known group II element nitridosilicates are listed in Table 8.1. However, no investigations into the high-pressure chemistry, besides one density functional study on $MgSiN_2$ [245], had been conducted so far.

Table 8.1: Nitridosilicates of group II elements. Compounds covered in this thesis are highlighted gray. Compounds with experimentally realized high-pressure phase are marked with an asterisk *.

Be	Mg	Ca	Sr	Ba
$BeSiN_2$ [13]	$MgSiN_2$[234, 235]	$CaSiN_2$ [14]	$SrSiN_2$ [14]	$BaSiN_2$ [14]
/	/	$Ca_2Si_5N_8$* [15, 204]	$Sr_2Si_5N_8$ [16]	$Ba_2Si_5N_8$ [16]
/	/	$Ca_5Si_2N_6$ [299]	/	$Ba_5Si_2N_6$ [300]
/	/	/	$SrSi_7N_{10}$ [301]	$BaSi_7N_{10}$ [302]
/	/	/	$SrSi_6N_8$ [17]	$BaSi_6N_8$ [303]

Calculations for all $MSiN_2$ nitridosilicates of group II elements revealed various high-pressure polymorphs of these compounds. Even coordinations of five and six for Si

should be within experimental reach. Six-fold coordinated Si (SiN_6 octahedra) so far have only been realized in $Ce_{16}Si_{15}O_6N_{32}$ [243] at ambient pressure and in γ-Si_3N_4 [4] at high pressure.

First calculations for pressure-induced decomposition reactions for ambient-pressure $Ca_2Si_5N_8$ revealed a quite low decomposition pressure (11 GPa), indicating low phase transformation pressures for potential high-pressure phases, if any do exist, as they had to appear before decomposition. Subsequent experiments actually revealed a novel high-pressure phase, HP-$Ca_2Si_5N_8$ (see chapter 6.1, page 118 and reference [204]), which in turn could be calculated by density functional theory. Preliminary experiments at higher pressure indicate the predicted decomposition into $CaSiN_2$ and Si_3N_4 [304]. However, further experiments are needed to corroborate this findings.

The discovery of HP-$Ca_2Si_5N_8$ strongly motivates the search for further high-pressure polymorphs of nitridosilicates, in particular as the calculated decomposition pressures of $Sr_2Si_5N_8$ and $Ba_2Si_5N_8$ are quite low as well (19 and 24 GPa, respectively). No experiments to ellucidate their high-pressure behavior have been conducted so far.

Besides the eight examined group II element nitridosilicates there remain a further six to be thoroughly investigated (c.f. Table 8.1), among them the two reduced nitridosilicates $SrSi_6N_8$ and $BaSi_6N_8$ [17, 303], which open up a pathway to novel structural features and material properties. Further investigations into the high-pressure chemistry of other nitridosilicates as well as oxonitridosilicates, which further broaden the scope of structural and material properties, seem worthwhile.

Nitridophosphates

BeP_2N_4, which exhibits the phenakite structure at ambient pressure, has an already quite high bulk modulus of 220 GPa within GGA. In accordance to phenakite-type β-Si_3N_4 transforming into spinel-type γ-Si_3N_4, a pressure-induced phase transformation of BeP_2N_4 into a spinel-type high-pressure phase is anticipated. The calculated transition pressure amounts to 24 GPa and lays at the upper boundary of pressure attainable in multianvil setups, but is well within the routine pressure range of diamond anvil cell setups. With a calculated bulk modulus of 263 (LDA) to 291 GPa

(GGA), which is comparable to that of γ-Si_3N_4, interesting material properties are anticipated for this polymorph of BeP_2N_4. The comparatively low calculated transition pressure as well as the predicted high bulk modulus warrant experiments aiming at the synthesis of spinel-type BeP_2N_4.

As a possible competitive high-pressure phase to the spinel-type structure a mega-kalsilite-type structure has to be considered. This high-pressure phase would be consistent with the pressure-homologues rule, since MgP_2N_4, CaP_2N_4 and SrP_2N_4 adopt this structure type at ambient pressure. As a further high-pressure phase the CaB_2O_4-IV structure, adopted by BaP_2N_4, has to be considered. Further density functional calculations should allow a deeper insight into this issue.

As experimental and theoretical phases of P_3N_5, the binary mother compound of nitridophosphates, exhibits very interesting structural properties, this trend is most likely to be continued in high-pressure nitridophosphates. Therefore, theoretical and experimental investigations of high-pressure nitridophosphates are most likely to be a profitable and interesting endeavor. The quite low calculated transition pressure for phenakite- to spinel-type BeP_2N_5 and the even low transition pressure for α- to γ-P_3N_5 indicate that these high-pressure phases are not unlikely to appear in a reasonable pressure range, viable in multianvil and diamond anvil high-pressure experiments.

9 Summary

The aim of this work was to investigate the high-pressure behavior of different nitride compounds by means of *Density Functional Theory* (DFT). The *Vienna ab-initio Simulation Package* (VASP) was used, which combines the total energy pseudopotential method with a plane-wave basis set. Calculations were performed using both the *Local Density Approximation* (LDA) as well as the *Generalized Gradient Approximation* (GGA) for the exchange correlation potential and the *Projector-Augmented-Wave* (PAW) method was employed.

The group II element nitrides M_3N_2, nitridosilicates $MSiN_2$ and $M_2Si_5N_8$ and the nitridophosphate BeP_2N_4 were examined with regard to the prediction of novel high-pressure phases, aiming especially at coordination numbers for Si and P higher than four. Due to their makeup of small atoms, short bonds, high covalency and probably (partly) increased coordination number for Si and P, they can be expected to be quite hard material, the more so as their parent compounds α-/β/γ-Si_3N_4 and α-/γ-P_3N_5 are already evincing considerable hardness.

1. Nitrides M_3N_2 of group II elements

Be_3N_2: The high-pressure behavior of Be_3N_2 was studied up 300 GPa. Evaluating many hypothetical polymorph of composition A_3X_2 leads to proposing one high-pressure polymorph for both α- and β-Be_3N_2, an anti-A-sesquioxide structure. Energy-volume calculations revealed, that α-Be_3N_2 will transform into γ-Be_3N_2 at 125 GPa and β-Be_3N_2 at 82 GPa. No transformation from α- into β-Be_3N_2 or vice versa will take place under pressure.

Mg_3N_2: For α-Mg_3N_2 two high-pressure phases were found. The transformation into β-Mg_3N_2 (anti-B-sesquioxide-type structure) was calculated to 21 GPa and

the transformation to γ-Mg_3N_2 (anti-A-sesquioxide-type structure) to 65 GPa. The group-subgroup relation between β-Mg_3N_2 and γ-Mg_3N_2 (B- and A-sesquioxide) are discussed as well as the thereof resulting analogy to the displacive phase transformation of B- to A-sesquioxide-type rare earth oxides M_2O_3.
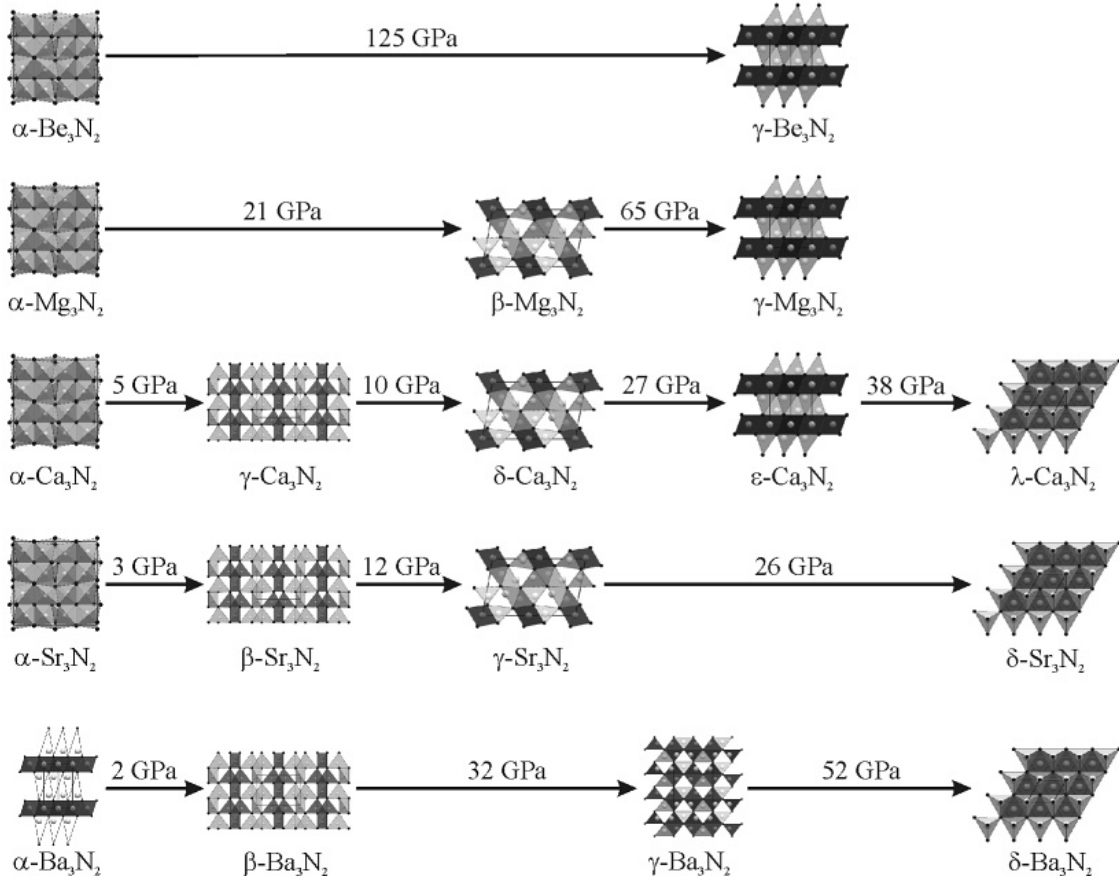
Figure 9.1: Phase sequences of M_3N_2 (M = Be, Mg, Ca, Sr, Ba) under pressure.

Ca_3N_2: The high-pressure behavior of Ca_3N_2 was studied up 100 GPa. Four high-pressure polymorphs for both α- and β-Ca_3N_2 are proposed: (1) an anti-Rh_2O_3-II structure at 5 GPa, (2) an anti-B-sesquioxide structure at 10 GPa, (3) and anti-A-sesquioxide structure at 27 GPa and (4) an hitherto unknown hexagonal structure ($P6_3/mmc$) at 38 GPa, derived from the post-perovskite structure of $CaIrO_3$ and exhibiting octahedrally as well as trigonal bipyramidally coordinated Ca.

Sr_3N_2: The structure and true nature of Sr_3N_2 and Ba_3N_2 are yet unknown. Among

all tested structures of type A_3X_2 the anti-bixbyite structure turned out as the one with the lowest energy (α-Sr_3N_2). A high-pressure phase sequence very similar to that of Ca_3N_2 was found, excepting the anti-A-sesquioxide structure: (1) an anti-Rh_2O_3-II structure at 3 GPa, (2) an anti-B-sesquioxide structure at 12 GPa and (3) the hexagonal $P6_3/mmc$ structure at 26 GPa.

Ba_3N_2: For Ba_3N_2 the structure with the lowest energy was not the anti-bixbyite structure, but a variant of the anti-A-sesquioxide-type structure with a significantly increased c/a-ratio. The development of the c/a-ratio of this structure under pressure was examined, revealing a gradual reduction under pressure. Three high-pressure polymorphs are proposed for hypothetic α-Ba_3N_2: (1) an anti-Rh_2O_3-II structure at 2 GPa, (2) an anti-$CaIrO_3$ structure at 32 GPa and (3) the hexagonal $P6_3/mmc$ structure at 52 GPa.

The development of the density for Ca_3N_2 and Ba_3N_2 and the zero-pressure bulk moduli of the various high-pressure phases for all group II element nitrides M_3N_2 have been examined as well.

2. Nitridosilicates $MSiN_2$ of group II elements

$BeSiN_2$, $MgSiN_2$ and $CaSiN_2$: $BeSiN_2$ and $MgSiN_2$ exhibit the same ambient-pressure structure, which is an ordered wurtzite variant and can be derived from idealized filled β-cristobalite by a C1-type distortion. The structure of ambient-pressure $CaSiN_2$ can also be derived from idealized filled β-cristobalite but by a different type of distortion (D1-type). For all three compounds energy-volume calculations revealed a NaCl superstructure under pressure, achieving six-fold coordination for Si: for $BeSiN_2$ a s-$LiFeO_2$ structure (76 GPa) and for $MgSiN_2$ and $CaSiN_2$ a m-$LiFeO_2$ structure (24 and 60 GPa, respectively). For $BeSiN_2$ and $CaSiN_2$ an intermediate phase appears, for $BeSiN_2$ a chalcopyrite-type structure and for $CaSiN_2$ a $CaGeN_2$-type structure. These two tetragonal structures are closely related, as their main difference is a significantly different c/a-ratio, which results for chalcopyrite-type structures in having a tetrahedral coordination for both cations, whereas in $CaGeN_2$-type structures one cation is tetrahedrally and one bisdisphenoidally coordinated. Both structures can also be derived from idealized filled β-cristobalite.

They are obtained through a B1-type distortion. The group-subgroup relation of the BeSiN$_2$/MgSiN$_2$, the CaSiN$_2$, the chalcopyrite and CaGeN$_2$ and the idealized filled β-cristobalite structure and the resultant displacive phase transformation pathways are discussed.
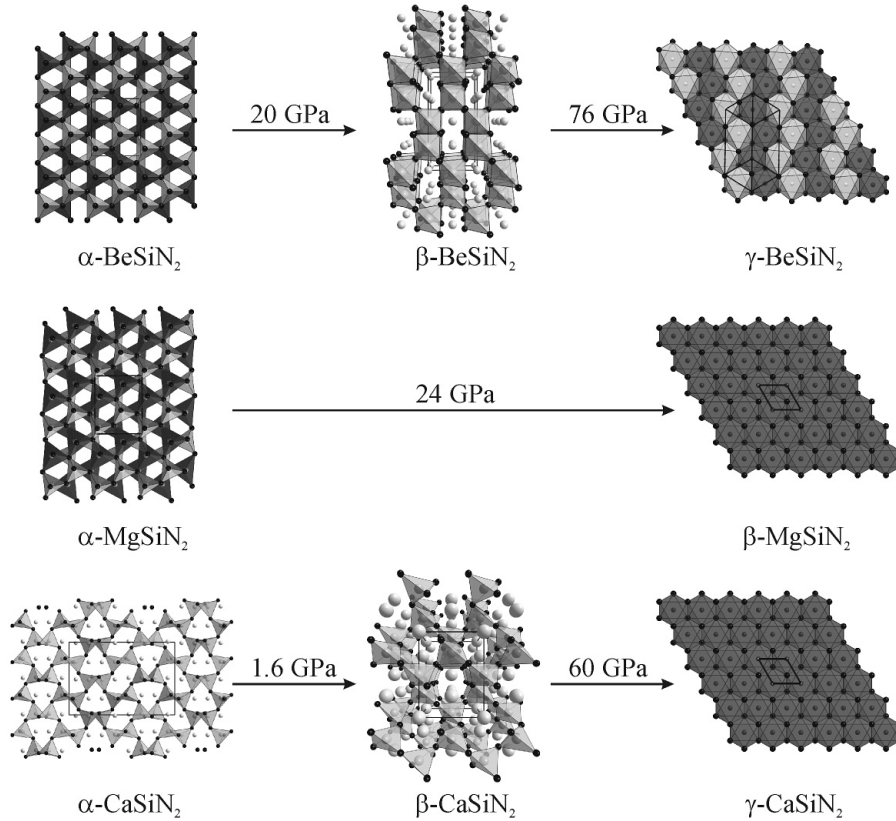
Figure 9.2: Phase sequences of MSiN$_2$ (M = Be, Mg, Ca) under pressure.

SrSiN$_2$ and BaSiN$_2$: The SrSiN$_2$ and the BaSiN$_2$ ambient-pressure structures are not three-dimensional tetrahedra networks, but layered structures. Both structures are related by a group-subgroup relation, which is discussed. Both compounds exhibit a similar high-pressure behavior. According to calculations, monoclinic SrSiN$_2$ first transforms into the orthorhombic BaSiN$_2$ structure at 2 GPa, most likely via a displacive phase transformation pathway. For both SrSiN$_2$ and BaSiN$_2$, following the orthorhombic BaSiN$_2$ structure, a transformation into the CaSiN$_2$ structure (14 and 43 GPa, respectively), followed by transformation into a hitherto unknown *Pbcm* structure (84 and 102 GPa, respectively), derived from the CaSiN$_2$ structure,

is found. The *Pbcm* structure is related to the $CaSiN_2$ structure by a group-subgroup relation and represents the first link of the $CaSiN_2$ structure on its way towards the ideal filled β-cristobalite structure. However, in the *Pbcm* structure the coordination for Si is increased from tetrahedral to trigonal bipyramidal. For $SrSiN_2$ as a final high-pressure polymorph the m-$LiFeO_2$ structure is found (130 GPa), resulting in octahedrally coordinated Si.
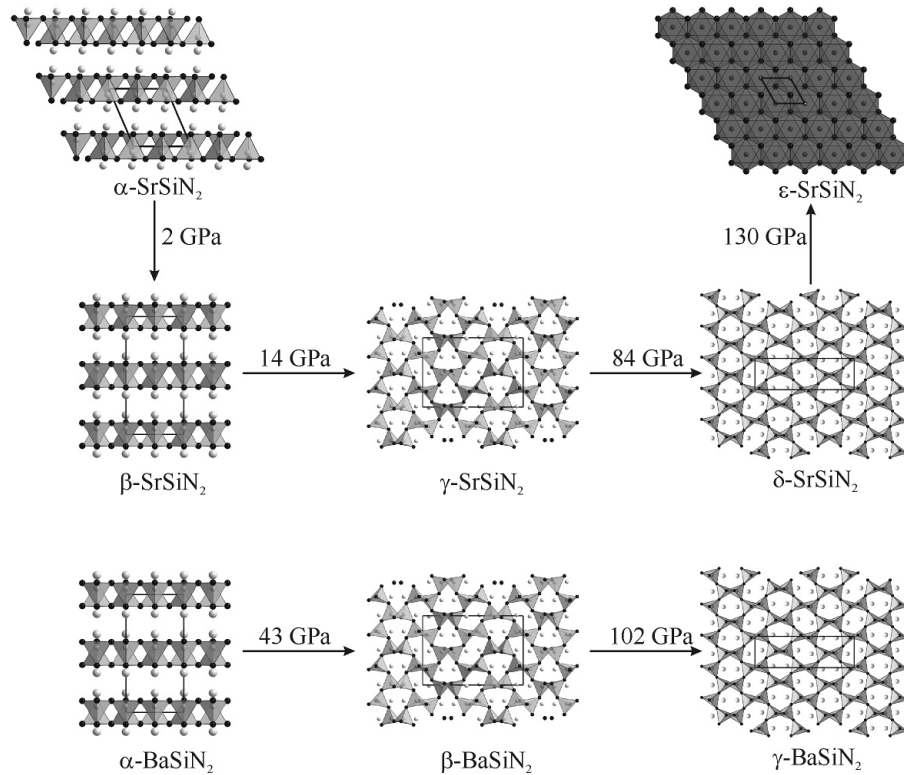
Figure 9.3: Phase sequences of $MSiN_2$ (M = Sr, Ba) under pressure.

Decomposition: For all group II element nitridosilicates $MSiN_2$ the decomposition into binary nitrides M_3N_2 and Si_3N_4 under pressure was examined. For all except $BeSiN_2$ it is found, that $MSiN_2$ always is lower in enthalpy than a phase agglomerate of M_3N_2 and Si_3N_4, taking all predicted high-pressure phases of M_3N_2 and β- as well as γ-Si_3N_4 into account. $BeSiN_2$ is thermodynamically stable against decomposition only up to 66 GPa, at which pressure a phase agglomerate of Be_3N_2 and Si_3N_4 is more favorable. However, above 83 GPa $BeSiN_2$ should reappear adopting the γ-$BeSiN_2$ structure.

3. Nitridosilicates $M_2Si_5N_8$ of group II elements

Ca$_2$Si$_5$N$_8$: Experimental HP-Ca$_2$Si$_5$N$_8$ as well as hypothetical o-Ca$_2$Si$_5$N$_8$ (isostructural to the ambient pressure modifications of Sr$_2$Si$_5$N$_8$ and Ba$_2$Si$_5$N$_8$) were studied as high-pressure phases of Ca$_2$Si$_5$N$_8$ up to 100 GPa. The transition pressure into HP-Ca$_2$Si$_5$N$_8$ was calculated to 1.7 GPa, whereas o-Ca$_2$Si$_5$N$_8$ will not be adopted as a high-pressure phase. Two different decomposition pathways of Ca$_2$Si$_5$N$_8$ (into Ca$_3$N$_2$ and Si$_3$N$_4$ or into CaSiN$_2$ and Si$_3$N$_4$) and their pressure dependence were examined. It was found that a pressure induced decomposition of Ca$_2$Si$_5$N$_8$ into CaSiN$_2$ and Si$_3$N$_4$ is preferred and that Ca$_2$Si$_5$N$_8$ is no longer thermodynamically stable under pressures exceeding 15 GPa.

Ca$_2$Si$_5$N$_8$ HP-Ca$_2$Si$_5$N$_8$ M$_2$Si$_5$N$_8$ (M = Sr, Ba)
o-Ca$_2$Si$_5$N$_8$
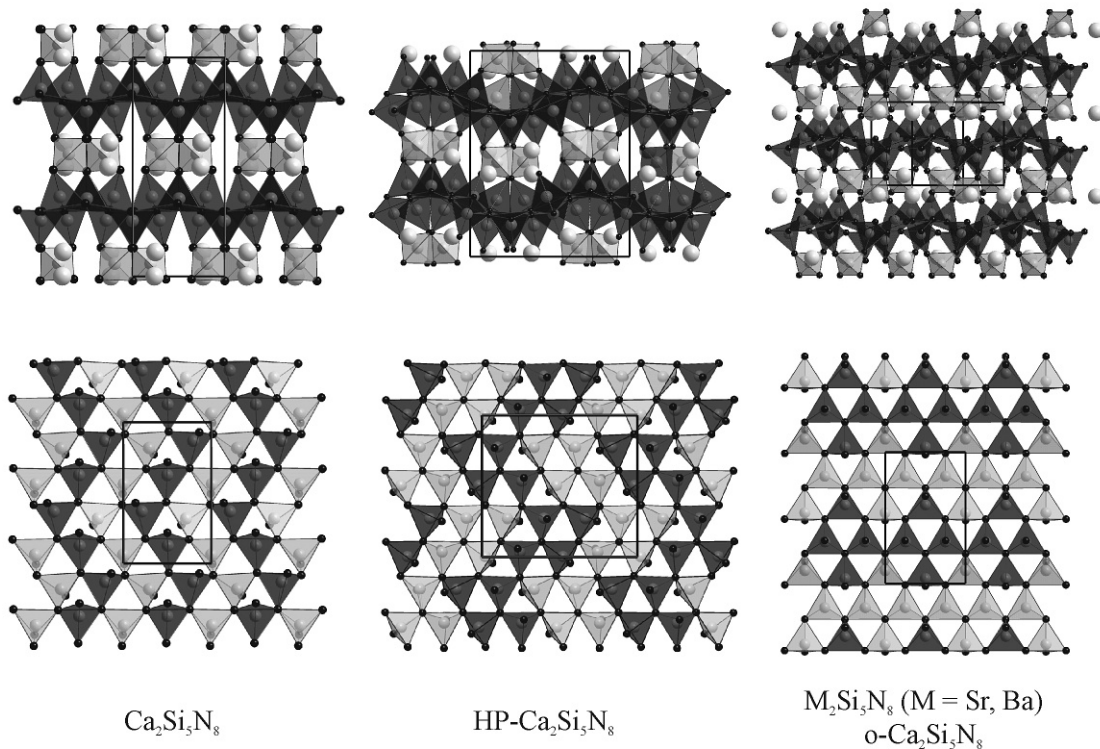
Figure 9.4: Structures of Ca$_2$Si$_5$N$_8$, HP-Ca$_2$Si$_5$N$_8$ and Sr$_2$Si$_5$N$_8$/Ba$_2$Si$_5$N$_8$.

Sr$_2$Si$_5$N$_8$ and Ba$_2$Si$_5$N$_8$: The structure of the high-pressure phase of Ca$_2$Si$_5$N$_8$,

HP-$Ca_2Si_5N_8$, was tested for both $Sr_2Si_5N_8$ and $Ba_2Si_5N_8$ as a potential high-pressure phase. For $Sr_2Si_5N_8$ structure optimization resulted in a higher density than for orthorhombic $Sr_2Si_5N_8$, whereas "HP-$Ba_2Si_5N_8$" turned out to be less dense than the ambient-pressure phase. However, when examining the decomposition of $Sr_2Si_5N_8$, it became obvious, that $Sr_2Si_5N_8$ will decompose into a phase agglomerate of 2 $SrSiN_2$ and Si_3N_4 before it transforms into HP-$Sr_2Si_5N_8$.

For both $Sr_2Si_5N_8$ and $Ba_2Si_5N_8$ it was found, that a decomposition into $MSiN_2$ and Si_3N_4 is preferred over a decomposition into M_3N_2 and Si_3N_4. The decomposition pressure for $Sr_2Si_5N_8$ was calculated to 19 GPa and the decomposition pressure of $Ba_2Si_5N_8$ to 24 GPa.

$Mg_2Si_5N_8$: For hypothetic $Mg_2Si_5N_8$ the structures of $Ca_2Si_5N_8$ (m-$Mg_2Si_5N_8$), HP-$Ca_2Si_5N_8$ (HP-$Mg_2Si_5N_8$) and $Sr_2Si_5N_8$/$Ba_2Si_5N_8$ (o-$Mg_2Si_5N_8$) were calculated. m-$Mg_2Si_5N_8$ turned out as the polymorph with the lowest energy, transforming into HP-$Mg_2Si_5N_8$ at 20 GPa. However, examining the decomposition into Mg_3N_2 and Si_3N_4 and into $MgSiN_2$ and Si_3N_4, it was revealed, that $Mg_2Si_5N_8$ would be thermodynamically stable against Mg_3N_2 and Si_3N_4 up to 16 GPa, but a phase agglomerate of 2 $MgSiN_2$ and Si_3N_4 is always lower in enthalpy than any considered $Mg_2Si_5N_8$ structure.

4. Beryllium Nitridophosphate BeP$_2$N$_4$

The nitridophosphate BeP_2N_4, like β-Si_3N_4, crystallizes in the phenakite(Be_2SiO_4)-type structure. As β-Si_3N_4 transforms into a spinel-type structure under pressure (γ-Si_3N_4), a spinel-type high-pressure phase of BeP_2N_4 seems to be likely. Normal spinel BeP_2N_4 (an unprecedented octahedral coordination for P and tetrahedrally coordinated Be) as well as ideal inverse spinel BeP_2N_4 (an unprecedented octahedral coordination for Be and half of P tetrahedrally and half octahedrally coordinated) were calculated. Inverse spinel BeP_2N_4 comes out denser than spinel BeP_2N_4. However energy-volume calculations revealed, that, up to 100 GPa, only spinel BeP_2N_4 becomes lower in enthalpy than phenakite BeP_2N_4, inverse spinel BeP_2N_4 being always higher in enthalpy than spinel BeP_2N_4. The transition pressure of phenakite to spinel BeP_2N_4 was calculated to 24 GPa within GGA. It is widely accepted, that small atoms, short bonds, a high degree of covalency, a high bond density and a high

packing efficiency are required for hard materials, which applies to both phenakite and spinel BeP_2N_4. In combination with the fact, that the calculated bulk moduli for both phases are comparable to those of corundum and γ-Si_3N_4 and that P_3N_5 itself exhibits a Vickers hardness of 5.1(7) GPa for partly crystalline ambient-pressure P_3N_5 and of 9.7(21) GPa for γ-P_3N_5, this suggests, that phenakite and spinel BeP_2N_4 are likely to be rather hard materials.

BeP₂N₄ - normal spinel

BeP₂N₄ - phenakite

BeP₂N₄ - inverse spinel
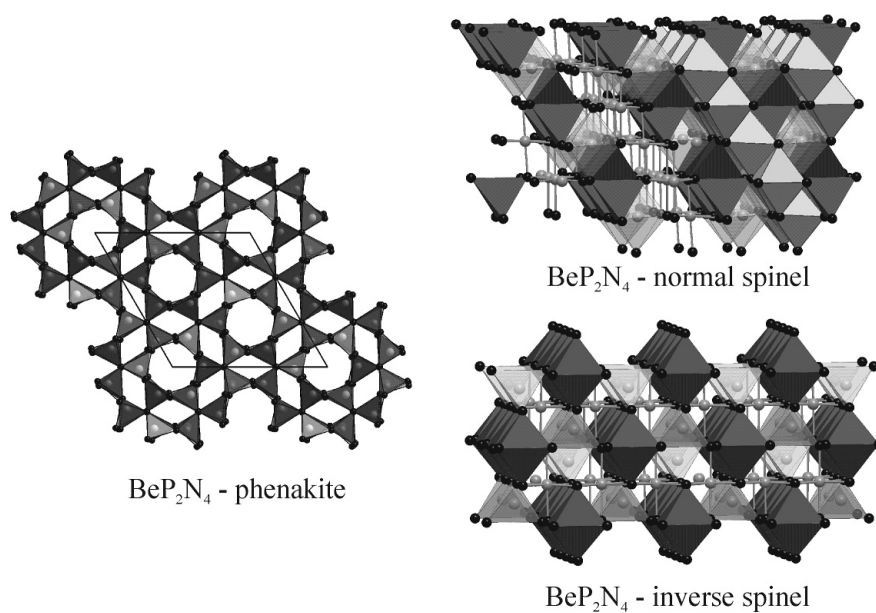
Figure 9.5: Structures of BeP_2N_4, experimental (phenakite-type) and hypothetic (normal and inverse spinel-type.

Appendix A – Crystallographic Data

Silicon Nitride Si_3N_4

Table A1: Crystallographic data of β-Si_3N_4 [3] compared to calculated values (atomic parameters: (1) experimental coordinates, (2) coordinates from LDA calculation, (3) coordinates from GGA calculation).

		experimental	LDA	GGA
space group		$P6_3/m$ (no. 176, hexagonal)		
a / pm		760.80	757.65	765.63
c / pm		291.07(5)	289.14	292.38
V / 10^6 pm ^{3}		145.90(3)	143.74	148.43
ρ / g cm^{-3}		3.19	3.24	3.14
atom	Wyckoff position	x	y	z
Si1	6h	0.17200	0.76900	1/4
	6h	0.17377	0.76733	1/4
	6h	0.17499	0.76892	1/4
N1	6h	0.33333	0.03300	1/4
	6h	0.33008	0.02936	1/4
	6h	0.32996	0.03082	1/4
N2	2c	1/3	2/3	1/4
	2c	1/3	2/3	1/4
	2c	1/3	2/3	1/4

Table A2: Crystallographic data of γ-Si$_3$N$_4$ [4, 5] compared to calculated values (atomic parameters: (1) experimental coordinates, (2) coordinates from LDA calculation, (3) coordinates from GGA calculation).

		experimental	LDA	GGA
space group		$Fd\bar{3}m$ (no. 227, cubic)		
a / pm		773.81(2)	769.50	778.62
V / 10^6 pm^3		463.34	455.64	472.04
ρ / g cm^{-3}		4.02	4.09	3.95
atom	Wyckoff position	x	y	z
Si1	8a	0	0	0
	8a	0	0	0
	8a	0	0	0
Si2	16d	5/8	5/8	5/8
	16d	5/8	5/8	5/8
	16d	5/8	5/8	5/8
N1	32e	0.38468(1)	0.38468(1)	0.38468(1)
	32e	0.38245	0.38245	0.38245
	32e	0.38245	0.38245	0.38245

Nitrides M₃N₂ of Group II Elements

Table A3: Crystallographic data of α-Be$_3$N$_2$ [179] compared to calculated values (atomic parameters: (1) experimental coordinates, (2) coordinates from LDA calculation, (3) coordinates from GGA calculation).

		experimental	LDA	GGA
space group		$Ia\bar{3}$ (no. 206, cubic)		
a / pm		814.52	805.16	814.56
V / 10^6 pm^3		540.39(1)	521.98	540.46
ρ / g cm^{-3}		2.71	2.80	2.71
atom	Wyckoff-Position	x	y	z
Be1	48e	0.3865(11)	0.1465(10)	0.3758(15)
		0.38593	0.14563	0.38023
		0.38629	0.14575	0.38005
N1	24d	0.9785(4)	0	1/4
		0.97876	0	1/4
		0.97919	0	1/4
N2	8b	1/4	1/4	1/4
		1/4	1/4	1/4
		1/4	1/4	1/4

Table A4: Crystallographic data of γ-Be$_3$N$_2$ (anti-A-sesquioxide-type [180, 181]) (atomic parameters: (1) coordinates from LDA calculation, (2) coordinates from GGA calculation).

		LDA	GGA
space group		$P\bar{3}m1$ (no. 164, trigonal)	
Z		1	
a / pm		278.66	281.72
c / pm		459.33	467.16
V / 10^6 pm^3		30.89	32.11
ρ / g cm^{-3}		2.96	2.85
atom	Wyckoff position	x	y	z
Be1	2d	1/3	2/3	0.74750
		1/3	2/3	0.74694
Be2	1a	0	0	0
		0	0	0
N1	2d	1/3	2/3	0.35147
		1/3	2/3	0.35019

Table A5: Crystallographic data of β-Be$_3$N$_2$ [139] compared to calculated values (atomic parameters: (1) experimental coordinates, (2) coordinates from LDA calculation, (3) coordinates from GGA calculation).

		experimental	LDA	GGA
space group		$P6_3/mmc$ (no. 194, hexagonal)		
Z		2		
a / pm		284.1	281.77	284.80
c / pm		969.3	963.41	976.26
V / 10^6 pm ^{3}		67.75	66.24	68.58
ρ / g cm^{-3}		2.70	2.76	2.67
atom	Wyckoff-Position	x	y	z
Be1	4f	1/3	2/3	0.075
		1/3	2/3	0.07802
		1/3	2/3	0.07833
Be2	2b	0	0	1/4
		0	0	1/4
		0	0	1/4
N1	2a	0	0	0
		0	0	0
		0	0	0
N2	2c	1/3	2/3	1/4
		1/3	2/3	1/4
		1/3	2/3	1/4

Table A6: Crystallographic data of α-$\mathrm{Mg_3N_2}$ [144] compared to calculated values (atomic parameters: (1) experimental coordinates, (2) coordinates from LDA calculation, (3) coordinates from GGA calculation).

		experimental	LDA	GGA
space group		$Ia\bar{3}$ (no. 206, cubic)		
Z		16		
a / pm		996.76(4)	984.03	1001.50
V / 10^6 pm^3		990.31(7)	952.86	1004.50
ρ / g cm^{-3}		2.71	2.81	2.67
atom	Wyckoff position	x	y	z
Mg1	48e	0.3893(1)	0.1522(1)	0.3822(1)
		0.38928	0.15253	0.38222
		0.38910	0.15264	0.38240
N1	24d	0.9690(2)	0	1/4
		0.96863	0	1/4
		0.96893	0	1/4
N2	8b	1/4	1/4	1/4
		1/4	1/4	1/4
		1/4	1/4	1/4

Table A7: Crystallographic data of β-Mg$_3$N$_2$ (anti-B-sesquioxide-type [191]) (atomic parameters: (1) coordinates from LDA calculation, (2) coordinates from GGA calculation).

		LDA		GGA
space group		$C2/m$ (no. 12, monoclinic)		
Z		6		
a / pm		1313.02		1342.44
b / pm		324.93		330.41
c / pm		800.18		814.43
β / pm		100.59		100.76
V / 10^6 pm^3		335.58		354.89
ρ / g cm^{-3}		3.00		2.83

atom	Wyckoff position	x	y	z
Mg1	4i	0.12317	0	0.28107
		0.12250	0	0.28111
Mg2	4i	0.32770	1/2	0.03116
		0.32776	1/2	0.03094
Mg3	4i	0.29010	1/2	0.37810
		0.28967	1/2	0.37809
Mg4	4i	0.46478	0	0.33560
		0.46368	0	0.33487
Mg5	2b	0	1/2	0
		0	1/2	0
N1	4i	0.13562	1/2	0.48614
		0.13562	1/2	0.48725
N2	4i	0.18964	1/2	0.13759
		0.19012	1/2	0.13765
N3	4i	0.46790	1/2	0.18128
		0.49790	1/2	0.18104

Table A8: Crystallographic data of γ-Mg_3N_2 (anti-A-sesquioxide-type [180, 181]) (atomic parameters: (1) coordinates from LDA calculation, (2) coordinates from GGA calculation).

		LDA	GGA	
space group		$P\bar{3}m1$ (no. 164, trigonal)		
Z		1		
a / pm		339.09	344.26	
c / pm		557.66	573.16	
V / 10^6 pm^3		55.53	58.83	
ρ / g cm^{-3}		3.02	2.85	
atom	Wyckoff position	x	y	z
Mg1	2d	1/3	2/3	0.65763
		1/3	2/3	0.65814
Mg2	1a	0	0	0
		0	0	0
N1	2d	1/3	2/3	0.24349
		1/3	2/3	0.24401

Table A9: Crystallographic data of α-Ca_3N_2 [192] compared to calculated values (atomic parameters: (1) experimental coordinates, (2) coordinates from LDA calculation, (3) coordinates from GGA calculation).

		experimental	LDA	GGA
space group		$Ia\bar{3}$ (no. 206, cubic)		
Z		16		
a / pm		1147.3(1)	1119.87	1145.36
V / 10^6 pm^3		1510.2(3)	1404.44	1502.55
ρ / g cm^{-3}		2.61	2.80	2.62
atom	Wyckoff position	x	y	z
Ca1	48e	0.389(1)	0.153(1)	0.382(1)
		0.39008	0.15448	0.38253
		0.38965	0.15424	0.38269
N1	8b	1/4	1/4	1/4
		1/4	1/4	1/4
		1/4	1/4	1/4
N2	24d	0.960(2)	0	1/4
		0.95959	0	1/4
		0.96059	0	1/4

Table A10: Crystallographic data of β-Ca_3N_2 [145] compared to calculated values (atomic parameters: (1) experimental coordinates, (2) coordinates from LDA calculation, (3) coordinates from GGA calculation).

		experimental	LDA	GGA
space group		$R\bar{3}c$ (no. 167, trigonal)		
Z		6		
a / pm		618.94	605.24	618.48
c / pm		1661.15	1622.65	1662.13
V / 10^6 pm ^{3}		551.11	514.77	550.61
ρ / g cm^{-3}		2.69	2.87	2.68
atom	Wyckoff position	x	y	z
Ca1	18e	0.30005	0	1/4
		0.29904	0	1/4
		0.30000	0	1/4
N1	12c	0	0	0.35254
		0	0	0.35358
		0	0	0.35349

Table A11: Crystallographic data of γ-Ca_3N_2 (anti-Rh_2O_3-II-type structure [168]) (atomic parameters: (1) coordinates from LDA calculation, (2) coordinates from GGA calculation).

		LDA	GGA	
space group		$Pbna$ (no. 60, orthorhombic)		
Z		4		
a / pm		607.34	620.30	
b / pm		621.32	635.20	
c / pm		872.08	895.97	
V / 10^6 pm ^{3}		329.08	353.03	
ρ / g cm^{-3}		2.99	2.79	
atom	Wyckoff position	x	y	z
Ca1	8d	0.60687	0.10538	0.84741
		0.60627	0.10513	0.84712
Ca2	4c	0.04474	1/4	0
		0.04498	1/4	0
N1	8d	0.75250	0.03232	0.11230
		0.75278	0.03142	0.11210

Table A12: Crystallographic data of λ-Ca_3N_2 (hexagonal $P6_3/mmc$-type structure, see chapter 4.1.3) (atomic parameters: (1) coordinates from LDA calculation, (2) coordinates from GGA calculation).

		LDA		GGA
space group		$P6_3/mmc$ (no. 194, hexagonal)		
Z		2		
a / pm		382.90		389.11
c / pm		1230.07		1318.63
V / 10^6 pm ^{3}		156.18		172.90
ρ / g cm^{-3}		3.15		2.85

atom	Wyckoff position	x	y	z
Ca1	4f	1/3	2/3	0.8851
		1/3	2/3	0.08620
Ca2	2b	0	0	1/4
		0	0	1/4
N1	2a	0	0	0
		0	0	0
N2	2d	2/3	1/3	1/4
		2/3	1/3	1/4

Table A13: Crystallographic data of δ-Ca$_3$N$_2$ (anti-B-sesquioxide-type structure [191]) (atomic parameters: (1) coordinates from LDA calculation, (2) coordinates from GGA calculation).

		LDA		GGA
space group		$C2/m$ (no. 12, monoclinic)		
Z		6		
a / pm		1458.82		1504.98
b / pm		370.47		378.30
c / pm		913.27		934.90
β / pm		100.38		100.54
V / 10^6 pm^3		485.50		523.30
ρ / g cm^{-3}		3.04		2.82
atom	Wyckoff position	x	y	z
Ca1	4i	0.12762	0	0.27897
		0.12567	0	0.27775
Ca2	4i	0.32764	1/2	0.03494
		0.32800	1/2	0.03518
Ca3	4i	0.29041	1/2	0.37822
		0.28073	1/2	0.37949
Ca4	4i	0.47058	0	0.34129
		0.46826	0	0.33945
Ca5	2b	0	1/2	0
		0	1/2	0
N1	4i	0.14105	1/2	0.48721
		0.14105	1/2	0.48828
N2	4i	0.18231	1/2	0.13116
		0.18256	1/2	0.13023
N3	4i	0.46954	1/2	0.18805
		0.46936	1/2	0.18775

Table A14: Crystallographic data of ϵ-Ca$_3$N$_2$ (anti-A-sesquioxide-type structure (Ni$_2$Al$_3$-type) [181]) (atomic parameters: (1) coordinates from LDA calculation, (2) coordinates from GGA calculation).

		LDA		GGA
space group		$P\bar{3}m1$ (no. 164, trigonal)		
Z		1		
a / pm		408.62		419.71
c / pm		525.57		539.83
V / 10^6 pm^3		76.00		82.35
ρ / g cm^{-3}		3.24		2.99

atom	Wyckoff position	x	y	z
Ca1	2d	1/3	2/3	0.68694
		1/3	2/3	0.68311
Ca2	1a	0	0	0
		0	0	0
N1	2d	1/3	2/3	0.22734
		1/3	2/3	0.23052

Table A15: Crystallographic data of ϵ'-Ca$_3$N$_2$ (anti-A-sesquioxide-type structure [180]) (atomic parameters: (1) coordinates from LDA calculation, (2) coordinates from GGA calculation).

		LDA		GGA
space group		$P\bar{3}m1$ (no. 164, trigonal)		
Z		1		
a / pm		381.79		385.72
c / pm		639.80		685.20
V / 10^6 pm^3		80.77		88.29
ρ / g cm^{-3}		3.05		2.79

atom	Wyckoff position	x	y	z
Ca1	2d	1/3	2/3	0.65933
		1/3	2/3	0.66459
Ca2	1a	0	0	0
		0	0	0
N1	2d	1/3	2/3	0.23589
		1/3	2/3	0.23087

Table A16: Crystallographic data of α-Sr_3N_2 (anti-bixbyite-type [179]) (atomic parameters: (1) coordinates from LDA calculation, (2) coordinates from GGA calculation).

		LDA		GGA
space group		$Ia\bar{3}$ (no. 206, cubic)		
Z		16		
a / pm		1231.95		1202.10
V / 10^6 pm^3		1869.73		1737.08
ρ / g cm^{-3}		4.13		4.45
atom	Wyckoff position	x	y	z
Sr1	48e	0.38940	0.15546	0.38346
		0.39001	0.15576	0.38324
N1	24d	0.95624	0	1/4
		0.95526	0	1/4
N2	8b	1/4	1/4	1/4
		1/4	1/4	1/4

Table A17: Crystallographic data of β-Sr_3N_2 (anti-Rh_2O_3-II-type [168]) (atomic parameters: (1) coordinates from LDA calculation, (2) coordinates from GGA calculation).

		LDA		GGA
space group		$Pbna$ (no. 60, orthorhombic)		
Z		4		
a / pm		651.69		666.29
b / pm		665.80		682.23
c / pm		935.05		963.71
V / 10^6 pm^3		405.71		438.07
ρ / g cm^{-3}		4.76		4.41
atom	Wyckoff position	x	y	z
Sr1	8d	0.60760	0.10501	0.84717
		0.60663	0.10413	0.84674
Sr2	4c	0.04413	1/4	0
		0.04462	1/4	0
N1	8d	0.75238	0.03258	0.11279
		0.75275	0.03171	0.11237

Table A 18: Crystallographic data of γ-Sr_3N_2 (anti-B-sesquioxide-type [191]) (atomic parameters: (1) coordinates from LDA calculation, (2) coordinates from GGA calculation).

		LDA		GGA
space group		$C2/m$ (no. 12, monoclinic)		
Z		6		
a / pm		1562.35		1614.75
b / pm		396.99		406.03
c / pm		985.14		1011.35
β / pm		100.56		100.66
V / 10^6 pm^3		600.67		651.63
ρ / g cm^{-3}		4.82		4.45

atom	Wyckoff position	x	y	z
Sr1	4i	0.12768	0	0.27613
		0.12634	0	0.27377
Sr2	4i	0.32717	1/2	0.03755
		0.32794	1/2	0.03882
Sr3	4i	0.28994	1/2	0.37915
		0.28998	1/2	0.38142
Sr4	4i	0.47156	0	0.34306
		0.46985	0	0.34085
Sr5	2b	0	1/2	0
		0	1/2	0
N1	4i	0.14199	1/2	0.48738
		0.14218	1/2	0.48849
N2	4i	0.17969	1/2	0.12956
		0.17973	1/2	0.12735
N3	4i	0.46975	1/2	0.18905
		0.47016	1/2	0.18897

Table A19: Crystallographic data of γ'-Sr_3N_2 (anti-B-sesquioxide-type [191]) (atomic parameters: (1) coordinates from LDA calculation, (2) coordinates from GGA calculation).

		LDA		GGA
space group		$C2/m$ (no. 12, monoclinic)		
Z		6		
a / pm		1617.95		1665.54
b / pm		378.59		389.72
c / pm		1168.86		1203.24
β / pm		105.72		105.72
V / 10^6 pm^3		689.20		751.81
ρ / g cm^{-3}		4.20		3.85

atom	Wyckoff position	x	y	z
Sr1	4i	0.15930	0	0.22071
		0.15912	0	0.21794
Sr2	4i	0.33453	1/2	0.07096
		0.33472	1/2	0.07036
Sr3	4i	0.32434	1/2	0.46091
		0.32428	1/2	0.46583
Sr4	4i	0.50836	0	0.30691
		0.50995	0	0.30369
Sr5	2b	0	1/2	0
		0	1/2	0
N1	4i	0.16565	1/2	0.40437
		0.16595	1/2	0.40233
N2	4i	0.17480	1/2	0.07577
		0.17487	1/2	0.07437
N3	4i	0.49597	1/2	0.17244
		0.49591	1/2	0.17124

Table A20: Crystallographic data of δ-Sr_3N_2 (hexagonal $P6_3/mmc$-type structure, see chapter 4.1.3) (atomic parameters: (1) coordinates from LDA calculation, (2) coordinates from GGA calculation).

		LDA	GGA	
space group		$P6_3/mmc$ (no. 194, hexagonal)		
Z		2		
a / pm		411.52	418.36	
c / pm		1324.48	1430.78	
V / 10^6 pm^3		194.25	216.87	
ρ / g cm^{-3}		4.97	4.45	

atom	Wyckoff position	x	y	z
Sr1	4f	1/3	2/3	0.08889
		1/3	2/3	0.08648
Sr2	2b	0	0	1/4
		0	0	1/4
N1	2a	0	0	0
		0	0	0
N2	2d	2/3	1/3	1/4
		2/3	1/3	1/4

Table A21: Crystallographic data of α-Ba_3N_2 (anti-"A-sesquioxide"-type [180, 181]) (atomic parameters: (1) coordinates from LDA calculation, (2) coordinates from GGA calculation).

		LDA	GGA	
space group		$P\bar{3}m1$ (no. 164, trigonal)		
Z		1		
a / pm		392.14	404.17	
c / pm		1045.02	1102.95	
V / 10^6 pm^3		139.17	156.03	
ρ / g cm^{-3}		5.25	4.68	

atom	Wyckoff position	x	y	z
Ba1	2d	1/3	2/3	0.70459
		1/3	2/3	0.71689
Ba2	1a	0	0	0
		0	0	0
N1	2d	1/3	2/3	0.17460
		1/3	2/3	0.16903

Table A 22: Crystallographic data of β-Ba_3N_2 (anti-Rh_2O_3-II-type [168]) (atomic parameters: (1) coordinates from LDA calculation, (2) coordinates from GGA calculation).

		LDA	GGA	
space group		*Pbna* (no. 60, orthorhombic)		
Z		4		
a / pm		695.57	709.54	
b / pm		700.78	722.22	
c / pm		991.06	1026.84	
V / 10^6 pm^3		483.08	526.20	
ρ / g cm^{-3}		6.05	5.55	
atom	Wyckoff position	x	y	z
Ba1	8d	0.84741	0.10299	0.84741
		0.60675	0.10293	0.84625
Ba2	4c	0.04224	1/4	0
		0.04218	1/4	0
N1	8d	0.75482	0.03399	0.11731
		0.75397	0.03079	0.11597

Table A 23: Crystallographic data of γ-Ba_3N_2 (anti-$CaIrO_3$-type structure [193]) (atomic parameters: (1) coordinates from LDA calculation, (2) coordinates from GGA calculation).

		LDA	GGA	
space group		*Cmcm* (no. 63, orthorhombic)		
Z		4		
a / pm		380.29	389.95	
b / pm		1257.24	1295.85	
c / pm		983.09	1032.04	
V / 10^6 pm^3		470.03	521.51	
ρ / g cm^{-3}		6.22	5.60	
atom	Wyckoff position	x	y	z
Ba1	4c	1/2	0.39532	1/4
		1/2	0.39154	1/4
Ba2	8f	1/2	0.14124	0.06922
		1/2	0.13641	0.07233
N1	4c	0	0.25037	1/4
		0	0.25067	1/4
N2	4a	0	0	0
		0	0	0

Table A24: Crystallographic data of δ-Ba$_3$N$_2$ (hexagonal $P6_3/mmc$-type structure, see chapter 4.1.3) (atomic parameters: (1) coordinates from LDA calculation, (2) coordinates from GGA calculation).

		LDA	GGA	
space group		$P6_3/mmc$ (no. 194, hexagonal)		
Z		2		
a / pm		438.80	445.60	
c / pm		1429.11	1544.45	
V / 10^6 pm ^{3}		238.30	265.58	
ρ / g cm^{-3}		6.13	5.50	
atom	Wyckoff position	x	y	z
Ba1	4f	1/3	2/3	0.08992
		1/3	2/3	0.08778
Ba2	2b	0	0	1/4
		0	0	1/4
N1	2a	0	0	0
		0	0	0
N2	2d	2/3	1/3	1/4
		2/3	1/3	1/4

Nitridosilicates MSiN$_2$ of Group II Elements

Table A 25: Crystallographic data of α-BeSiN$_2$ [13] compared to calculated values (atomic parameters: (1) experimental coordinates, (2) coordinates from LDA calculation, (3) coordinates from GGA calculation).

		experimental	LDA	GGA
space group		*Pna*2$_1$ (no. 33, orthorhombic)		
Z		4		
a / pm		497.7(5)	494.03	499.73
b / pm		574.7(6)	569.89	577.02
c / pm		467.4(3)	464.15	469.89
V / 10^6 pm^3		133.7(3)	130.68	135.49
ρ / g cm^{-3}		3.24	3.31	3.19
atom	Wyckoff position	x	y	z
Be1	4a	0.08300	0.62500	0.00000
		0.08295	0.62518	0.00452
		0.08325	0.62524	0.00443
Si1	4a	0.08300	0.12500	0.00000
		0.08600	0.12500	0.00368
		0.08539	0.12506	0.00379
N1	4a	0.08300	0.12500	0.375(4)
		0.08020	0.12317	0.37948
		0.07935	0.12268	0.37875
N1	4a	0.08300	0.62500	0.375(9)
		0.08325	0.62689	0.38232
		0.08405	0.62750	0.38303

Table A26: Crystallographic data of β-BeSiN$_2$ (chalcopyrite-type structure [239]) (atomic parameters: (1) coordinates from LDA calculation, (2) coordinates from GGA calculation).

		LDA		GGA
space group		$I\bar{4}2d$ (no. 122, tetragonal)		
Z		4		
a / pm		401.94		407.06
c / pm		807.66		816.31
c/a-ratio		2.01		2.01
V / 10^6 pm^3		130.48		135.26
ρ / g cm^{-3}		3.31		3.20
atom	Wyckoff position	x	y	z
Be1	4b	0	0	1/2
		0	0	1/2
Si1	4a	0	0	0
		0	0	0
N1	8d	0.24658	1/4	1/8
		0.24536	1/4	1/8

Table A27: Crystallographic data of γ-BeSiN$_2$ (s-LiFeO$_2$-type structure [240]) (atomic parameters: (1) coordinates from LDA calculation, (2) coordinates from GGA calculation).

		LDA		GGA
space group		$I4_1/amd$ (no. 144, tetragonal)		
Z		4		
a / pm		373.22		377.13
c / pm		778.38		795.48
V / 10^6 pm^3		108.42		113.14
ρ / g cm^{-3}		3.99		3.82
atom	Wyckoff position	x	y	z
Be1	4b	0	0	1/2
		0	0	1/2
Si1	4a	0	0	0
		0	0	0
N1	8e	0	0	0.23751
		0	0	0.23533

Table A28: Crystallographic data of α-MgSiN$_2$ [235] compared to calculated values (atomic parameters: (1) experimental coordinates, (2) coordinates from LDA calculation, (3) coordinates from GGA calculation).

		experimental	LDA	GGA
space group		$Pna2_1$ (no. 33, orthorhombic)		
Z		4		
a / pm		527.9	523.77	530.69
b / pm		647.6	641.75	649.89
c / pm		499.2	499.55	502.75
V / 10^6 pm^3		170.66	166.57	173.39
ρ / g cm^{-3}		3.13	3.21	3.08
atom	Wyckoff position	x	y	z
Mg1	4a	0.076(2)	0.625(5)	0.00(5)
		0.08368	0.62280	0.99444
		0.08459	0.62274	0.99455
Si1	4a	0.072(2)	0.131(5)	0.000
		0.07074	0.12549	0.00589
		0.06989	0.12543	0.00607
N1	4a	0.049(2)	0.095(2)	0.356(3)
		0.04907	0.09583	0.35379
		0.04810	0.09515	0.35261
N2	4a	0.110(1)	0.652(4)	0.414(2)
		0.10834	0.65514	0.41588
		0.10968	0.65582	0.41677

Table A29: Crystallographic data of β-MgSiN$_2$ (m-LiFeO$_2$-type structure [244]) (atomic parameters: (1) coordinates from LDA calculation, (2) coordinates from GGA calculation).

		LDA	GGA	
space group		$R\bar{3}m$ (no. 166, trigonal)		
Z		3		
a / pm		280.91	285.01	
c / pm		1445.26	1467.99	
V / 10^6 pm^3		98.77	103.27	
ρ / g cm^{-3}		4.06	3.88	
atom	Wyckoff position	x	y	z
Mg1	3a	0	0	0
		0	0	0
Si1	3b	0	0	1/2
		0	0	1/2
N1	6c	0	0	0.23690
		0	0	0.23660

Table A30: Crystallographic data of β-CaSiN$_2$ (CaGeN$_2$-type structure [250]) (atomic parameters: (1) coordinates from LDA calculation, (2) coordinates from GGA calculation).

		LDA	GGA	
space group		$I\bar{4}2d$ (no. 122, tetragonal)		
Z		4		
a / pm		519.83	524.60	
c / pm		685.66	711.65	
c/a-ratio		1.32	1.36	
V / 10^6 pm^3		185.28	195.85	
ρ / g cm^{-3}		3.45	3.26	
atom	Wyckoff position	x	y	z
Ca1	4b	0	0	1/2
		0	0	1/2
Si1	4a	0	0	0
		0	0	0
N1	8d	0.34930	1/4	1/8
		0.35278	1/4	1/8

Table A31: Crystallographic data of α-CaSiN$_2$ [14] compared to calculated values (atomic parameters: (1) experimental coordinates, (2) coordinates from LDA calculation, (3) coordinates from GGA calculation).

		experimental	LDA	GGA
space group		*Pbca* (no. 61, orthorhombic)		
Z		16		
a / pm		512.29(3)	505.61	516.32
b / pm		1020.74(6)	1006.25	1027.50
c / pm		1482.33(9)	1470.26	1485.69
V / 10^6 pm^3		775.13(8)	748.07	788.19
ρ / g cm^{-3}		3.30	3.42	3.24
atom	Wyckoff position	x	y	z
Ca1	8c	0.2414(1)	0.0097(1)	0.06500
		0.24103	0.01001	0.06520
		0.23993	0.00702	0.06505
Ca2	8c	0.3462(1)	0.2741(1)	0.18765
		0.34937	0.27478	0.18738
		0.34674	0.27362	0.18789
Si1	8c	0.2265(2)	0.0166(1)	0.3121(1)
		0.22791	0.01642	0.31188
		0.22516	0.01648	0.31202
Si2	8c	0.3172(2)	0.2700(1)	0.4372(1)
		0.31891	0.27032	0.43722
		0.31525	0.27002	0.43741
N1	8c	0.0949(6)	0.4774(3)	0.2155(2)
		0.09711	0.47571	0.21463
		0.09662	0.47687	0.21555
N2	8c	0.1495(6)	0.2761(3)	0.0354(2)
		0.15387	0.27795	0.03605
		0.14813	0.27539	0.03621
N3	8c	0.1972(5)	0.4268(3)	0.4090(2)
		0.19312	0.42804	0.40984
		0.19684	0.42725	0.40939
N4	8c	0.2762(6)	0.1798(3)	0.3382(2)
		0.28046	0.18152	0.33701
		0.27203	0.18018	0.33813

Table A32: Crystallographic data of γ-CaSiN$_2$ (m-LiFeO$_2$-type structure [244]) (atomic parameters: (1) coordinates from LDA calculation, (2) coordinates from GGA calculation).

		LDA	GGA	
space group		$R\bar{3}m$ (no. 166, trigonal)		
Z		3		
a / pm		294.26	299.35	
c / pm		1571.19	1596.83	
V / 10^6 pm^3		117.82	123.92	
ρ / g cm^{-3}		4.07	3.87	
atom	Wyckoff position	x	y	z
Ca1	3a	0	0	0
		0	0	0
Si1	3b	0	0	1/2
		0	0	1/2
N1	6c	0	0	0.22961
		0	0	0.22942

Table A33: Crystallographic data of CaSiN$_2$ in the α-BeSiN$_2$- and α-MgSiN$_2$-type structure [13, 235]) (atomic parameters: (1) coordinates from LDA calculation, (2) coordinates from GGA calculation).

		LDA	GGA	
space group		$Pna2_1$ (no. 33, orthorhombic)		
Z		4		
a / pm		519.51	533.98	
b / pm		726.00	727.40	
c / pm		509.85	521.45	
V / 10^6 pm^3		192.30	202.54	
ρ / g cm^{-3}		3.32	3.15	
atom	Wyckoff position	x	y	z
Ca1	4a	0.06165	0.62152	0.97971
		0.07227	0.52067	0.98195
Si1	4a	0.05737	0.12567	0.00785
		0.05743	0.12579	0.00814
N1	4a	0.01447	0.07477	0.33864
		0.01428	0.07324	0.33444
N2	4a	0.11987	0.67596	0.44380
		0.12427	0.67682	0.44547

Table A34: Crystallographic data of α-SrSiN$_2$ [14] compared to calculated values (atomic parameters: (1) experimental coordinates, (2) coordinates from LDA calculation, (3) coordinates from GGA calculation).

		experimental	LDA	GGA
space group		$P2_1/c$ (no. 14, monoclinic)		
Z		4		
a / pm		597.50(5)	590.19	598.28
b / pm		728.26(7)	717.19	736.70
c / pm		549.69(4)	546.17	554.10
β / pm		113.496(4)	113.34	112.66
V / 10^6 pm^3		219.36(3)	212.22	225.37
ρ / g cm^{-3}		4.35	4.50	4.24
atom	Wyckoff position	x	y	z
Sr1	4e	0.3393(1)	0.5724(1)	0.1756(1)
		0.34222	0.57068	0.17836
		0.33771	0.57513	0.17602
Si1	4e	0.1078(4)	0.1419(3)	0.0671(4)
		0.10999	0.14191	0.06636
		0.10516	0.14142	0.07085
N1	4e	0.210(2)	0.5905(8)	0.585(2)
		0.20764	0.59253	0.58276
		0.20941	0.58673	0.57891
N2	4e	0.219(2)	0.2252(8)	0.385(2)
		0.22699	0.22736	0.38368
		0.21021	0.21692	0.39061

Table A35: Crystallographic data of β-SrSiN$_2$ (BaSiN$_2$-type structure [14]) (atomic parameters: (1) coordinates from LDA calculation, (2) coordinates from GGA calculation).

		LDA	GGA	
space group		$Cmca$ (no. 64, orthorhombic)		
Z		8		
a / pm		544.35	552.93	
b / pm		1088.55	1115.51	
c / pm		713.74	726.33	
V / 10^6 pm^3		422.93	448.00	
ρ / g cm^{-3}		4.51	4.26	
atom	Wyckoff position	x	y	z
Sr1	8f	0	0.32843	0.06795
		0	0.33044	0.06850
Si1	8f	0	0.05603	0.14188
		0	0.05524	0.14139
N1	8f	0	0.39752	0.40481
		0	0.39850	0.40636
N1	8e	1/4	0.11737	1/4
		1/4	0.11383	1/4

Table A 36: Crystallographic data of γ-SrSiN$_2$ (CaSiN$_2$-type structure [14]) (atomic parameters: (1) coordinates from LDA calculation, (2) coordinates from GGA calculation).

		LDA		GGA
space group		*Pbca* (no. 61, orthorhombic)		
Z		16		
a / pm		516.09		526.57
b / pm		1034.37		1055.17
c / pm		1519.12		1538.14
V / 10^6 pm^3		810.95		854.62
ρ / g cm^{-3}		4.71		4.47
atom	Wyckoff position	x	y	z
Sr1	8c	0.25574	0.02069	0.06517
		0.25391	0.01776	0.06476
Sr2	8c	0.33234	0.26880	0.18461
		0.33032	0.26868	0.18502
Si1	8c	0.25543	0.00989	0.31166
		0.25366	0.01031	0.31164
Si2	8c	0.30310	0.26477	0.43640
		0.29974	0.26465	0.43649
N1	8c	0.06281	0.47638	0.21831
		0.06207	0.47809	0.21898
N2	8c	0.11090	0.29309	0.02194
		0.10577	0.29095	0.02177
N3	8c	0.17218	0.41296	0.40228
		0.17456	0.41235	0.40145
N4	8c	0.31842	0.16840	0.34290
		0.31232	0.16760	0.34371

Table A37: Crystallographic data of δ-SrSiN$_2$ (*Pbcm*-type structure, see chapter 5.1.4) (atomic parameters: (1) coordinates from LDA calculation, (2) coordinates from GGA calculation).

		LDA		GGA
space group		*Pbcm* (no. 57, orthorhombic)		
Z		8		
a / pm		537.98		532.84
b / pm		1715.17		1644.41
c / pm		410.04		485.27
V / 10^6 pm^3		378.36		425.20
ρ / g cm^{-3}		5.05		4.49

atom	Wyckoff position	x	y	z
Sr1	4d	0.44253	0.06844	3/4
		0.48151	0.06494	3/4
Sr2	4d	0.94997	0.18029	3/4
		0.98499	0.18512	3/4
Si1	4d	0.46212	0.18905	1/4
		0.46289	0.18573	1/4
Si2	4d	0.96842	0.06097	1/4
		0.96484	0.06396	1/4
N1	4d	0.47535	0.29059	1/4
		0.49884	0.28912	1/4
N2	4d	0.68804	0.11313	1/4
		0.65631	0.09955	1/4
N3	4d	0.18634	0.13656	1/4
		0.15540	0.15033	1/4
N4	4d	0.95889	0.03852	3/4
		0.97211	0.03815	3/4

Table A38: Crystallographic data of ϵ-SrSiN$_2$ (m-LiFeO$_2$-type structure [244]) (atomic parameters: (1) coordinates from LDA calculation, (2) coordinates from GGA calculation).

		LDA		GGA
space group		$R\bar{3}m$ (no. 166, trigonal)		
Z		3		
a / pm		302.20		308.31
c / pm		1663.63		1686.62
V / 10^6 pm^3		131.58		138.84
ρ / g cm^{-3}		5.44		5.16
atom	Wyckoff position	x	y	z
Sr1	3a	0	0	0
		0	0	0
Si1	3b	0	0	1/2
		0	0	1/2
N1	6c	0	0	0.22511
		0	0	0.22518

Table A39: Crystallographic data of α-BaSiN$_2$ [14] compared to calculated values (atomic parameters: (1) experimental coordinates, (2) coordinates from LDA calculation, (3) coordinates from GGA calculation).

		experimental	LDA	GGA
space group		*Cmca* (no. 64, orthorhombic)		
Z		8		
a / pm		560.09(2)	557.37	565.22
b / pm		1134.90(4)	1126.19	1157.68
c / pm		758.44(3)	752.53	764.12
V / 10^6 pm^3		482.10(3)	472.37	500.00
ρ / g cm^{-3}		5.34	5.44	5.14
atom	Wyckoff position	x	y	z
Ba1	8f	0	0.3356(1)	0.06523(2)
		0	0.33459	0.06473
		0	0.33557	0.06445
Si1	8f	0	0.04941(6)	0.14045(9)
		0	0.04968	0.14066
		0	0.04883	0.14042
N1	8f	0	0.3981(2)	0.4192(3)
		0	0.39795	0.41865
		0	0.39935	0.41986
N2	8e	1/4	0.0978(2)	1/4
		1/4	0.09875	1/4
		1/4	0.09607	1/4

Table A40: Crystallographic data of β-BaSiN$_2$ (CaSiN$_2$-type structure [14]) (atomic parameters: (1) coordinates from LDA calculation, (2) coordinates from GGA calculation).

		LDA		GGA
space group		*Pbca* (no. 61, orthorhombic)		
Z		16		
a / pm		538.66		547.91
b / pm		1082.46		1100.70
c / pm		1545.24		1568.55
V / 10^6 pm^3		900.90		945.97
ρ / g cm^{-3}		5.70		5.43
atom	Wyckoff position	x	y	z
Ba1	8c	0.25073	0.01300	0.06646
		0.25024	0.01306	0 06648
Ba2	8c	0.33496	0.26007	0.18740
		0.33539	0.26105	0.18738
Si1	8c	0.25665	0.00464	0.31280
		0.25482	0.00525	0.31275
Si2	8c	0.30389	0.25854	0.43829
		0.30176	0.25861	0.43822
N1	8c	0.03833	0.48212	0.22824
		0.03851	0.48340	0.22897
N2	8c	0.10309	0.27954	0.02242
		0.09949	0.277795	0.02192
N3	8c	0.19775	0.39795	0.39520
		0.20074	0.39825	0.39468
N4	8c	0.30688	0.15051	0.35557
		0.30188	0.15057	0.35592

Table A41: Crystallographic data of γ-BaSiN$_2$ at 105 GPa (*Pbcm*-type structure, see section 5.1.5) (atomic parameters: coordinates from GGA calculation).

		GGA		
space group		*Pbcm* (no. 57, orthorhombic)		
Z		8		
a / pm		501.01		
b / pm		1594.55		
c / pm		388.05		
V / 10^6 pm^3		310.01		
ρ / g cm^{-3}		8.29		
atom	Wyckoff position	x	y	z
Ba1	4d	0.41827	0.06061	3/4
Ba2	4d	0.93317	0.18658	3/4
Si1	4d	0.44409	0.19073	1/4
Si2	4d	0.95136	0.05981	1/4
N1	4d	0.44379	0.29327	1/4
N2	4d	0.67902	0.11816	1/4
N3	4d	0.17285	0.13458	1/4
N4	4d	0.90961	0.03497	3/4

Table A42: Crystallographic data of γ'-BaSiN$_2$ (*Imma*-type structure, see section 5.1.5) (atomic parameters: (1) coordinates from LDA calculation, (2) coordinates from GGA calculation).

		LDA		GGA	
space group		*Imma* (no. 74, orthorhombic)			
Z		4			
a / pm		428.96		437.14	
b / pm		553.83		564.39	
c / pm		881.32		898.13	
V / 10^6 pm^3		209.38		221.58	
ρ / g cm^{-3}		6.14		5.80	
atom	Wyckoff position	x	y	z
Ba1	4e	1/2	1/4	0.11636
		1/2	1/4	0.11505
Si1	4e	0	3/4	0.12735
		0	3/4	0.12711
N1	4e	0	3/4	0.32560
		0	3/4	0.32394
N2	4a	0	1/2	0
		0	1/2	0

Table A43: Crystallographic data of γ'-BaSiN$_2$-II (*Imma*-type structure, see chapter 5.1.5) (atomic parameters: (1) coordinates from LDA calculation, (2) coordinates from GGA calculation).

		LDA	GGA	
space group		*Imma* (no. 74, orthorhombic)		
Z		4		
a / pm		494.46	503.27	
b / pm		548.91	558.69	
c / pm		830.13	844.92	
V / 10^6 pm^3		225.31	237.57	
ρ / g cm^{-3}		5.70	5.41	
atom	Wyckoff position	x	y	z
Ba1	4e	1/2	1/4	0.12189
		1/2	1/4	0.12032
Si1	4e	0	3/4	0.12212
		0	3/4	0.12126
N1	4e	0	3/4	0.32489
		0	3/4	0.32273
N2	4a	0	1/2	0
		0	1/2	0

Table A44: Crystallographic data of γ'-BaSiN$_2$-III (*Imma*-type structure, see section 5.1.5) (atomic parameters: (1) coordinates from LDA calculation, (2) coordinates from GGA calculation).

		LDA	GGA	
space group		*Imma* (no. 74, orthorhombic)		
Z		4		
a / pm		555.89	564.35	
b / pm		706.41	717.17	
c / pm		769.64	781.38	
V / 10^6 pm^3		302.23	316.25	
ρ / g cm^{-3}		4.25	4.06	
atom	Wyckoff position	x	y	z
Ba1	4e	1/2	1/4	0.16071
		1/2	1/4	0.15857
Si1	4e	0	3/4	0.11836
		0	3/4	0.11693
N1	4e	0	3/4	0.33085
		0	3/4	0.32799
N2	4a	0	1/2	0
		0	1/2	0

Nitridosilicates $M_2Si_5N_8$ of Group II Elements

Table A45: Crystallographic data of $Ca_2Si_5N_8$ [15] compared to calculated values (atomic parameters: (1) experimental coordinates, (2) coordinates from LDA calculation, (3) coordinates from GGA calculation).

		experimental	LDA	GGA
space group		Cc (no. 9, monoclinic)		
Z		4		
a / pm		1435.2(3)	1426.7	1442.1
b / pm		561.0(1)	555.8	563.4
c / pm		968.9	960.5	974.9
β / pm		112.06(3)	112.03	111.92
V / 10^6 pm^3		723.00	705.98	734.73
ρ / g cm^{-3}		3.06	3.13	3.01
atom	Wyckoff position	x	y	z
Ca1	4a	0.0000	0.7637(3)	0.0000
		0.00073	0.76575	0.00316
		0.00158	0.76405	0.00324
Ca2	4a	0.6112(1)	0.7457(2)	0.2000(8)
		0.60956	0.74567	0.19761
		0.60850	0.74792	0.19591
Si1	4a	0.0581(2)	0.8055(2)	0.3539(2)
		0.05780	0.80322	0.35375
		0.05768	0.80494	0.35325
Si2	4a	0.7557(1)	0.2097(3)	0.3182(2)
		0.75531	0.20837	0.31704
		0.75568	0.20942	0.31803
Si3	4a	0.7545(1)	0.4966(4)	0.0631(2)
		0.75397	0.49719	0.06290
		0.75416	0.49665	0.06306
Si4	4a	0.3627(1)	0.2078(4)	0.3681(2)
		0.36261	0.20709	0.36838
		0.36240	0.20769	0.36808
Si5	4a	0.8552(4)	0.0027(4)	0.1264(2)
		0.85596	0.00250	0.12604
		0.85565	0.00199	0.12629
N1	4a	0.9866(5)	0.638(1)	0.4289(6)
		0.98712	0.63623	0.43149
		0.98672	0.63781	0.42980
N2	4a	0.1286(4)	0.009(1)	0.9959(5)
		0.12817	0.01129	0.99825
		0.12861	0.01179	0.99722
N3	4a	0.7959(2)	0.2424(6)	0.1702(3)
		0.79565	0.24213	0.16920

atom	Wyckoff position	x	y	z
		0.79506	0.24145	0.16931
N4	4a	0.8027(3)	0.7484(6)	0.1752(3)
		0.80353	0.74817	0.17554
		0.80358	0.74716	0.17600
N5	4a	0.9798(3)	0.999(1)	0.2178(6)
		0.98175	0.99628	0.21777
		0.98126	0.99641	0.21768
N6	4a	0.8335(2)	0.0145(5)	0.9349(4)
		0.83472	0.01337	0.93468
		0.83425	0.01358	0.93527
N7	4a	0.6309(5)	0.157(1)	0.2732(7)
		0.63049	0.15344	0.27188
		0.63105	0.15482	0.27305
N8	4a	0.7960(3)	0.4826(6)	0.4161(3)
		0.79401	0.48334	0.41423
		0.79519	0.48317	0.41572

Table A46: Crystallographic data of HP-$Ca_2Si_5N_8$ [204] compared to calculated values (atomic parameters: (1) experimental coordinates, (2) coordinates from LDA calculation, (3) coordinates from GGA calculation).

		experimental	LDA	GGA
space group		$Pbca$ (no. 61, orthorhombic)		
Z		8		
a / pm		1058(2)	1048.3	1065.9
b / pm		965.2(4)	957.3	970.8
c / pm		1366(2)	1352.3	1368.2
V / 10^6 pm^3		1395(2)	1357.01	1415.79
ρ / g cm^{-3}		3.17	3.26	3.12

atom	Wyckoff position	x	y	z
Ca1	8c	0.61524	0.15710	0.51597
		0.61487	0.15479	0.51497
		0.61304	0.15479	0.51485
Ca2	8c	0.88767	0.05759	0.40161
		0.88794	0.05981	0.40223
		0.88538	0.05951	0.40299
Si1	8c	0.89866	0.22495	0.65032
		0.89935	0.22418	0.65015
		0.89899	0.22461	0.65064
Si2	8c	0.66428	0.22806	0.77397
		0.66449	0.22845	0.77370

atom	Wyckoff position	x	y	z
		0.66437	0.22821	0.77439
Si3	8c	0.75652	0.96480	0.65560
		0.75745	0.96478	0.65474
		0.75598	0.96527	0.65579
Si4	8c	0.47940	0.99552	0.70824
		0.48047	0.99530	0.70902
		0.47925	0.99597	0.70897
Si5	8c	0.33029	0.15186	0.54115
		0.33032	0.15173	0.54147
		0.32983	0.15155	0.54078
N1	8c	0.41920	0.26874	0.47060
		0.42181	0.27020	0.47332
		0.42053	0.26990	0.47270
N2	8c	0.43205	0.04136	0.59668
		0.43336	0.04082	0.59719
		0.43235	0.04254	0.59772
N3	8c	0.24113	0.24800	0.61904
		0.24011	0.25317	0.61874
		0.23883	0.25110	0.61787
N4	8c	0.77000	0.94119	0.53427
		0.77130	0.94397	0.53186
		0.76965	0.94434	0.53319
N5	8c	0.52322	0.13369	0.79036
		0.52262	0.13151	0.79078
		0.52215	0.13207	0.79066
N6	8c	0.87773	0.88921	0.72220
		0.88806	0.88806	0.72066
		0.87860	0.88873	0.72217
N7	8c	0.75599	0.14245	0.68291
		0.75369	0.14292	0.68207
		0.75413	0.14327	0.68315
N8	8c	0.61705	0.89253	0.70096
		0.61761	0.89166	0.70220
		0.61609	0.89258	0.70219

Table A47: Crystallographic data of o-$Ca_2Si_5N_8$ ($Sr_2Si_5N_8$-type structure [16]) (atomic parameters: (1) coordinates from LDA calculation, (2) coordinates from GGA calculation).

		LDA		GGA
space group		$Pmn2_1$ (no. 31, orthorhombic)		
Z		2		
a / pm		562.2		570.4
b / pm		665.0		675.3
c / pm		926.2		937.9
V / 10^6 pm ^{3}		346.26		361.24
ρ / g cm^{-3}		3.19		3.06

atom	Wyckoff position	x	y	z
Ca1	2a	0	0.89886	0.00075
		0	0.90088	0.00174
Ca2	2a	0	0.90283	0.35505
		0	0.90741	0.35599
Si1	4b	0.25323	0.66895	0.68501
		0.25238	0.66870	0.68434
Si2	2a	0	0.05658	0.67503
		0	0.05682	0.67586
Si3	2a	0	0.42072	0.46001
		0	0.42096	0.46008
Si4	2a	0	0.40479	0.90617
		0	0.40454	0.90529
N1	2a	0	0.18048	0.51245
		0	0.18317	0.51499
N2	4b	0.25824	0.92102	0.67252
		0.25525	0.91956	0.67269
N3	4b	0.25085	0.44385	0.01437
		0.25061	0.44342	0.01352
N4	2a	0	0.59619	0.77954
		0	0.59387	0.77791
N5	2a	0	0.17242	0.83960
		0	0.17303	0.83950
N6	2a	0	0.43250	0.27201
		0	0.42853	0.27194

Table A48: Crystallographic data of $Sr_2Si_5N_8$ [16] compared to calculated values (atomic parameters: (1) experimental coordinates, (2) coordinates from LDA calculation, (3) coordinates from GGA calculation).

		experimental	LDA	GGA
space group		$Pmn2_1$ (no. 31, orthorhombic)		
Z		2		
a / pm		571.0(1)	566.06	574.51
b / pm		682.2(1)	678.34	687.41
c / pm		934.1(2)	927.30	939.96
V / 10^6 pm^3		363.87	356.07	371.21
ρ / g cm^{-3}		3.90	3.99	3.83
atom	Wyckoff position	x	y	z
Sr1	2a	0	0.86945(16)	0
		0	0.87187	0.00004
		0	0.87329	0.99998
Sr2	2a	0	0.88164(15)	0.36863(9)
		0	0.88281	0.36814
		0	0.88477	0.36790
Si1	4b	0.25180(18)	0.66693(14)	0.68358(33)
		0.25238	0.66736	0.68292
		0.25171	0.66760	0.68282
Si2	2a	0	0.05493(23)	0.67711(46)
		0	0.05469	0.67730
		0	0.05487	0.67749
Si3	2a	0	0.41958(47)	0.46192(38)
		0	0.42010	0.46071
		0	0.41986	0.46099
Si4	2a	0	0.40135(47)	0.90228(36)
		0	0.40155	0.90228
		0	0.40167	0.90189
N1	2a	0	0.1909(13)	0.5204(12)
		0	0.18903	0.52051
		0	0.19037	0.52193
N2	4b	0.24781(66)	0.91217(48)	0.67282(91)
		0.25006	0.91418	0.67149
		0.24774	0.91351	0.67173
N3	4b	0.24888(68)	0.44434(52)	0.01051(46)
		0.24963	0.44391	0.01105
		0.24945	0.44379	0.01089
N4	2a	0	0.58719(85)	0.77345(59)
		0	0.58685	0.77369
		0	0.58618	0.77317
N5	2a	0	0.1715(15)	0.8355(12)
		0	0.17267	0.83931
		0	0.17401	0.83844
N6	2a	0	0.4270(87)	0.27224(56)
		0	0.42798	0.27149
		0	0.42480	0.27173

Table A49: Crystallographic data of HP-$Sr_2Si_5N_8$ (HP-$Ca_2Si_5N_8$-type structure [204]) (atomic parameters: (1) coordinates from LDA calculation, (2) coordinates from GGA calculation).

		LDA		GGA
space group		*Pbca* (no. 61, orthorhombic)		
Z		8		
a / pm		1063.11		1080.46
b / pm		964.79		979.12
c / pm		1379.38		1395.26
V / 10^6 pm ^{3}		1414.80		1476.05
ρ / g cm^{-3}		4.02		3.85

atom	Wyckoff position	x	y	z
Sr1	8c	0.61670	0.16669	0.52434
		0.61536	0.16669	0.52418
Sr2	8c	0.88300	0.05292	0.39907
		0.88239	0.05365	0.39955
Si1	8c	0.89685	0.22632	0.65347
		0.89642	0.22742	0.65387
Si2	8c	0.66254	0.22595	0.77548
		0.66254	0.22620	0.77617
Si3	8c	0.75568	0.96552	0.65972
		0.75458	0.96649	0.66041
Si4	8c	0.47498	0.99670	0.70554
		0.47388	0.99780	0.70548
Si5	8c	0.32758	0.14838	0.53678
		0.32690	0.14783	0.53627
N1	8c	0.41241	0.27032	0.46898
		0.41119	0.26923	0.46836
N2	8c	0.42501	0.03774	0.59548
		0.42447	0.03967	0.59593
N3	8c	0.23376	0.23676	0.61721
		0.23279	0.23529	0.61646
N4	8c	0.77258	0.93884	0.54025
		0.77155	0.93988	0.54111
N5	8c	0.51672	0.13584	0.78430
		0.51633	0.13683	0.78440
N6	8c	0.87524	0.88910	0.72698
		0.87329	0.89001	0.72825
N7	8c	0.75440	0.14310	0.68692
		0.75453	0.14387	0.68765
N8	8c	0.61383	0.89581	0.70203
		0.61267	0.89709	0.70200

Table A 50: Crystallographic data of $Ba_2Si_5N_8$ [16] compared to calculated values (atomic parameters: (1) experimental coordinates, (2) coordinates from LDA calculation, (3) coordinates from GGA calculation).

		experimental	LDA	GGA
space group		$Pmn2_1$ (no. 31, orthorhombic)		
Z		2		
a / pm		578.3(1)	574.01	582.55
b / pm		695.9(1)	693.09	701.95
c / pm		939.1(2)	932.41	945.66
V / 10^6 pm^3		377.93(12)	370.95	38.70
ρ / g cm^{-3}		4.63	4.72	4.53
atom	Wyckoff position	x	y	z
Ba1	2a	0	0.85443(7)	0
		0	0.85333	0.00268
		0	0.85529	0.00165
Ba2	2a	0	0.87878(6)	0.36749(6)
		0	0.87915	0.37067
		0	0.87878	0.37063
Si1	4b	0.25085(24)	0.66376(16)	0.67931(31)
		0.25134	0.66357	0.68107
		0.25067	0.66443	0.68121
Si2	2a	0	0.05225	0.6772(4)
		0	0.05219	0.67967
		0	0.05255	0.67961
Si3	2a	0	0.41852(40)	0.46117(30)
		0	0.41998	0.46263
		0	0.41931	0.46280
Si4	2a	0	0.39960(36)	0.89643(29)
		0	0.39929	0.89867
		0	0.39978	0.89850
N1	2a	0	0.19678(100)	0.52791(84)
		0	0.19824	0.53099
		0	0.19849	0.53130
N2	4b	0.23920(91)	0.90631(61)	0.66940(77)
		0.23987	0.90558	0.67135
		0.23822	0.90558	0.67169
N3	4b	0.24683(84)	0.44763(55)	0.00702(51)
		0.24670	0.44611	0.00859
		0.24677	0.44592	0.00884
N4	2a	0	0.57654(86)	0.76541(61)
		0	0.57581	0.76638
		0	0.57642	0.76666
N5	2a	0	0.17358(120)	0.83538(86)
		0	0.17395	0.83825
		0	0.17572	0.83711
N6	2a	0	0.42230(96)	0.27051(66)
		0	0.42053	0.27247
		0	0.41772	0.27265

Table A51: Crystallographic data of HP-$Ba_2Si_5N_8$ (HP-$Ca_2Si_5N_8$-type structure) (atomic parameters: (1) coordinates from LDA calculation, (2) coordinates from GGA calculation).

		LDA		GGA
space group		*Pbca* (no. 61, orthorhombic)		
Z		8		
a / pm		1079.79		1096.69
b / pm		979.72		994.75
c / pm		1407.38		1423.23
V / 10^6 pm^3		1488.86		1552.64
ρ / g cm^{-3}		4.70		4.51

atom	Wyckoff position	x	y	z
Ba1	8c	0.61310	0.17279	0.53455
		0.61249	0.17224	0.53337
Ba2	8c	0.88745	0.05573	0.39860
		0.88702	0.05640	0.39872
Si1	8c	0.89429	0.23169	0.65834
		0.89374	0.23254	0.65818
Si2	8c	0.66071	0.22473	0.77928
		0.66077	0.22485	0.77948
Si3	8c	0.75452	0.96948	0.66561
		0.75354	0.96991	0.66557
Si4	8c	0.46802	0.99982	0.70202
		0.46729	0.00061	0.70212
Si5	8c	0.31970	0.14227	0.53076
		0.31952	0.14221	0.53086
N1	8c	0.39978	0.26355	0.46229
		0.39917	0.26282	0.46225
N2	8c	0.41229	0.03580	0.59437
		0.41260	0.03781	0.59488
N3	8c	0.22351	0.22229	0.61239
		0.22345	0.22144	0.61253
N4	8c	0.77570	0.94269	0.54864
		0.77466	0.94299	0.54877
N5	8c	0.51151	0.14148	0.77746
		0.51115	0.14329	0.77799
N6	8c	0.86829	0.89050	0.73443
		0.86682	0.89124	0.73509
N7	8c	0.75767	0.14469	0.69571
		0.75727	0.14517	0.69545
N8	8c	0.60925	0.90369	0.70029
		0.60852	0.90436	0.70017

Table A52: Crystallographic data of monoclinic $Mg_2Si_5N_8$ ($Ca_2Si_5N_8$-type structure [15]) (atomic parameters: (1) coordinates from LDA calculation, (2) coordinates from GGA calculation).

		LDA		GGA
space group		Cc (no. 9, monoclinic)		
Z		4		
a / pm		1406.15		1421.61
b / pm		531.76		538.78
c / pm		948.43		961.22
β / pm		111.00		110.97
V / 10^6 pm ^{3}		662.07		687.47
ρ / g cm^{-3}		3.02		2.91
atom	Wyckoff position	x	y	z
Mg1	4a	0.02917	0.76379	0.04283
		0.02960	0.76282	0.04197
Mg2	4a	0.58057	0.75928	0.17233
		0.58008	0.75970	0.17081
Si1	4a	0.05774	0.77338	0.36111
		0.05774	0.77502	0.35998
Si2	4a	0.75360	0.18658	0.31246
		0.75409	0.18732	0.31328
Si3	4a	0.74786	0.49432	0.05865
		0.74841	0.49518	0.05950
Si4	4a	0.36145	0.18408	0.36525
		0.36127	0.18481	0.36563
Si5	4a	0.86438	0.99353	0.12318
		0.86371	0.99341	0.12357
N1	4a	0.98560	0.58661	0.43969
		0.98547	0.58875	0.43813
N2	4a	0.12258	0.04674	0.01822
		0.12289	0.04604	0.01659
N3	4a	0.78607	0.21844	0.15457
		0.78674	0.22052	0.15604
N4	4a	0.82092	0.72217	0.17359
		0.81958	0.72443	0.17469
N5	4a	0.99243	0.98230	0.21680
		0.99176	0.98193	0.21572
N6	4a	0.84607	0.01453	0.93247
		0.84509	0.01550	0.93332
N7	4a	0.62915	0.10233	0.27555
		0.62933	0.10388	0.27501
N8	4a	0.77393	0.48523	0.3518
		0.77563	0.48364	0.39766

Table A53: Crystallographic data of HP-$Mg_2Si_5N_8$ (HP-$Ca_2Si_5N_8$-type structure) (atomic parameters: (1) coordinates from LDA calculation, (2) coordinates from GGA calculation).

		LDA		GGA
space group		*Pbca* (no. 61, orthorhombic)		
Z		8		
a / pm		1030.07		1047.92
b / pm		945.29		958.95
c / pm		1323.38		1338.35
V / 10^6 pm ^{3}		1288.59		1344.91
ρ / g cm^{-3}		3.10		2.97
atom	Wyckoff position	x	y	z
Mg1	8c	0.60077	0.12671	0.49319
		0.59888	0.12744	0.49332
Mg2	8c	0.87720	0.06104	0.41979
		0.87445	0.06390	0.42159
Si1	8c	0.90747	0.21265	0.64571
		0.90588	0.21606	0.64723
Si2	8c	0.67206	0.22626	0.77532
		0.67072	0.22797	0.77600
Si3	8c	0.75574	0.95825	0.65019
		0.75476	0.96179	0.65181
Si4	8c	0.48688	0.98761	0.71693
		0.48572	0.99036	0.71625
Si5	8c	0.33710	0.15961	0.54662
		0.33563	0.15784	0.54519
N1	8c	0.43732	0.27441	0.47925
		0.43469	0.27240	0.47777
N2	8c	0.44693	0.05071	0.60359
		0.44537	0.05099	0.60274
N3	8c	0.24115	0.27460	0.61332
		0.23999	0.27167	0.61212
N4	8c	0.75586	0.95728	0.52275
		0.75562	0.95886	0.52448
N5	8c	0.53904	0.11429	0.80516
		0.53642	0.11845	0.80333
N6	8c	0.88300	0.87830	0.71480
		0.88068	0.88196	0.71682
N7	8c	0.76379	0.13352	0.68686
		0.76281	0.13701	0.68746
N8	8c	0.61749	0.87817	0.69818
		0.61676	0.88214	0.69920

Table A54: Crystallographic data of o-Mg$_2$Si$_5$N$_8$ (Sr$_2$Si$_5$N$_8$-type structure [16]) (atomic parameters: (1) coordinates from LDA calculation, (2) coordinates from GGA calculation).

		LDA		GGA
space group		$Pmn2_1$ (no. 31, orthorhombic)		
Z		2		
a / pm		565.29		572.08
b / pm		679.22		688.13
c / pm		926.64		936.40
V / 10^6 pm^3		355.79		368.63
ρ / g cm^{-3}		2.81		2.71

atom	Wyckoff position	x	y	z
Mg1	2a	0	0.99817	0.02369
		0	0.00061	0.02353
Mg2	2a	0	0.03546	0.33271
		0	0.03802	0.33287
Si1	4b	0.24945	0.65808	0.68127
		0.24890	0.65851	0.68112
Si2	2a	0	0.05371	0.67898
		0	0.05426	0.67910
Si3	2a	0	0.42334	0.46319
		0	0.42310	0.46331
Si4	2a	0	0.40338	0.90301
		0	0.40393	0.90270
N1	2a	0	0.18500	0.52032
		0	0.18591	0.52103
N2	4b	0.25232	0.90997	0.67428
		0.25116	0.90985	0.67444
N3	4b	0.24713	0.44684	0.01186
		0.24731	0.44678	0.01181
N4	2a	0	0.57684	0.76822
		0	0.57758	0.76833
N5	2a	0	0.16724	0.84420
		0	0.16888	0.84360
N6	2a	0	0.41193	0.27528
		0	0.41003	0.27517

Beryllium Nitridophosphate BeP$_2$N$_4$

Table A55: Crystallographic data of BeP$_2$N$_4$ [25] compared to calculated values (atomic parameters: (1) experimental coordinates, (2) coordinates from LDA calculation, (3) coordinates from GGA calculation).

		experimental	LDA	GGA
space group		$R\bar{3}$ (no. 148, trigonal)		
Z		18		
a / pm		1269.45(2)	1263.42	1278.22
c / pm		834.86(2)	828.95	839.45
V / 10^6 pm^3		1165.13(4)	1145.92	1187.78
ρ / g cm^{-3}		3.26	3.31	3.20
atom	Wyckoff position	x	y	z
Be1	18f	0.2080(20)	0.2223(20)	0.249(4)
		0.19309	0.21189	0.24998
		0.19345	0.21169	0.24974
P1	18f	0.217(5)	0.0208(4)	0.4165(7)
		0.21310	0.01874	0.41729
		0.21281	0.01858	0.41721
P2	18f	0.2011(5)	0.0061(5)	0.0770(7)
		0.21044	0.01462	0.08270
		0.20959	0.01352	0.08278
N1	18f	0.1936(10)	0.0730(8)	0.2486(15)
		0.20516	0.08195	0.24871
		0.20417	0.08074	0.24851
N2	18f	0.3318(11)	0.3297(11)	0.2611(16)
		0.33691	0.33618	0.24929
		0.33744	0.33667	0.24924
N3	18f	0.1293(10)	0.2158(10)	0.0805(15)
		0.12149	0.21184	0.07558
		0.12201	0.21138	0.07514
N4	18f	0.1297(13)	0.2275(10)	0.4192(15)
		0.11811	0.21251	0.42444
		0.11805	0.21229	0.42485

Table A56: Crystallographic data of sp-BeP$_2$N$_4$ (spinel-type structure [305]) (atomic parameters: (1) coordinates from LDA calculation, (2) coordinates from GGA calculation).

		LDA	GGA	
space group		$Fd\bar{3}m$ (no. 227, cubic)		
Z		8		
a / pm		746.54	756.48	
V / 10^6 pm ^{3}		416.06	432.90	
ρ / g cm^{-3}		4.05	3.90	
atom	Wyckoff position	x	y	z
Be1	8a	1/8	1/8	1/8
		1/8	1/8	1/8
P1	16d	1/2	0	0
		1/2	0	0
N1	32e	0.50938	0.24062	0.00938
		0.50947	0.24053	0.00947

Table A57: Crystallographic data of isp-BeP$_2$N$_4$ (ideal inverse spinel) (atomic parameters: (1) coordinates from LDA calculation, (2) coordinates from GGA calculation).

		LDA	GGA	
space group		$Imma$ (no. 74, orthorhombic)		
Z		4		
a / pm		532.38	539.86	
b / pm		520.69	527.97	
c / pm		735.46	745.27	
V / 10^6 pm ^{3}		203.87	212.42	
ρ / g cm^{-3}		4.14	3.97	
atom	Wyckoff position	x	y	z
Be1	4b	0	1/2	1/2
		0	1/2	1/2
P1	4c	1/4	1/4	1/4
		1/4	1/4	1/4
P2	4e	0	3/4	0.11169
		0	3/4	0.11047
N1	8h	0	0.48664	0.25341
		0	0.48682	0.25409
N2	8i	0.25469	3/4	0.99026
		0.25439	3/4	0.99009

Appendix B – Calculational Details

Table B1: K-point mesh, atoms per cell and type of cell used for calculations.

structure	k-point mesh	atoms/cell	type of cell
β-Si$_3$N$_4$	3x3x8	14	primitive
γ-Si$_3$N$_4$	4x4x4	14	primitive
α-Be$_3$N$_2$	2x2x2	80	conventional
β-Be$_3$N$_2$	8x8x4	10	primitive
γ-Be$_3$N$_2$	6x6x4	5	primitive
α-Mg$_3$N$_2$	2x2x2	80	conventional
β-Mg$_3$N$_2$	2x6x4	30	conventional
γ-Mg$_3$N$_2$	6x6x4	5	primitive
α-Ca$_3$N$_2$	2x2x2	80	conventional
β-Ca$_3$N$_2$	6x6x2	30	conventional
γ-Ca$_3$N$_2$	8x8x4	20	primitive
δ-Ca$_3$N$_2$	2x6x4	30	conventional
ϵ-Ca$_3$N$_2$	6x6x4	5	primitive
λ-Ca$_3$N$_2$	8x8x4	10	primitive
α-Sr$_3$N$_2$	2x2x2	80	conventional
β-Sr$_3$N$_2$	8x8x4	20	primitive
γ-Sr$_3$N$_2$	2x6x4	30	conventional
δ-Sr$_3$N$_2$	8x8x4	10	primitive
α-Ba$_3$N$_2$	6x6x4	5	primitive
β-Ba$_3$N$_2$	8x8x4	20	primitive
γ-Ba$_3$N$_2$	8x2x4	20	conventional
δ-Ba$_3$N$_2$	8x8x4	10	primitive
Ba$_3$N$_2$ (anti-bixbyite)	2x2x2	80	conventional
α-BeSiN$_2$	4x4x4	16	primitive
β-BeSiN$_2$	5x5x5	16	conventional
γ-BeSiN$_2$	5x5x4	16	conventional
α-MgSiN$_2$	4x4x4	16	primitive
β-MgSiN$_2$	7x7x2	12	conventional

structure	k-point mesh	atoms/cell	type of cell
α-CaSiN$_2$	4x2x2	64	primitive
β-CaSiN$_2$	5x5x5	16	conventional
γ-CaSiN$_2$	7x7x2	12	conventional
α-SrSiN$_2$	4x4x4	16	conventional
β-SrSiN$_2$	6x4x6	32	conventional
γ-SrSiN$_2$	6x4x4	64	primitive
δ-SrSiN$_2$	6x4x6	32	primitive
ϵ-SrSiN$_2$	7x7x2	12	conventional
α-BaSiN$_2$	4x2x4	32	conventional
β-BaSiN$_2$	6x4x4	64	primitive
γ-BaSiN$_2$	6x4x6	32	primitive
γ'-BaSiN$_2$	4x4x2	16	conventional
γ'-BaSiN$_2$-II	4x4x2	16	conventional
γ'-BaSiN$_2$-III	4x4x2	16	conventional
Ca$_2$Si$_5$N$_8$	3x3x2	30	primitive
HP-Ca$_2$Si$_5$N$_8$	2x2x2	120	primitive
o-Ca$_2$Si$_5$N$_8$	4x4x2	30	primitive
Sr$_2$Si$_5$N$_8$	4x4x2	30	primitive
HP-Sr$_2$Si$_5$N$_8$	2x2x2	120	primitive
Ba$_2$Si$_5$N$_8$	4x4x2	30	primitive
HP-Ba$_2$Si$_5$N$_8$	2x2x2	120	primitive
m-Mg$_2$Si$_5$N$_8$	2x2x2	30	primitive
HP-Mg$_2$Si$_5$N$_8$	2x2x2	120	primitive
o-Mg$_2$Si$_5$N$_8$	4x4x2	30	primitive
BeP$_2$N$_4$	6x6x6	42	primitive
sp-BeP$_2$N$_4$	6x6x6	14	primitive
isp-BeP$_2$N$_4$	6x6x6	14	primitive

Appendix C – Simulated Powder Patterns

Binary Nitrides M_3N_2 of the Group II Elements
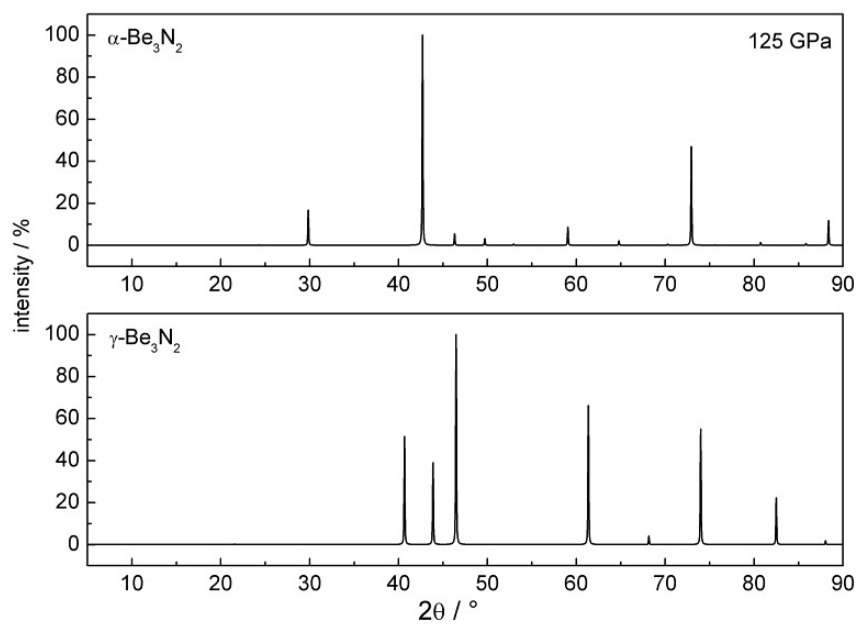
Figure C1: Powder diffraction patterns of α-Be$_3$N$_2$ (top) and γ-Be$_3$N$_2$ (bottom) at $125\,$GPa (Cu-K$_{\alpha 1}$ radiation, Deby-Scherrer-Geometry).
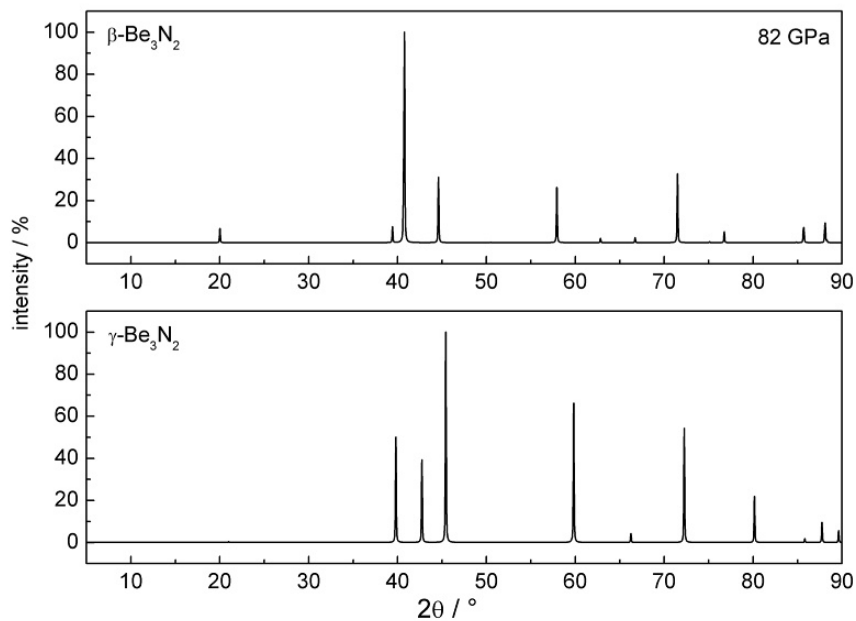
Figure C2: Powder diffraction patterns of β-Be$_3$N$_2$ (top) and γ-Be$_3$N$_2$ (bottom) at 82 GPa (Cu-K$_{\alpha 1}$ radiation, Deby-Scherrer-Geometry).
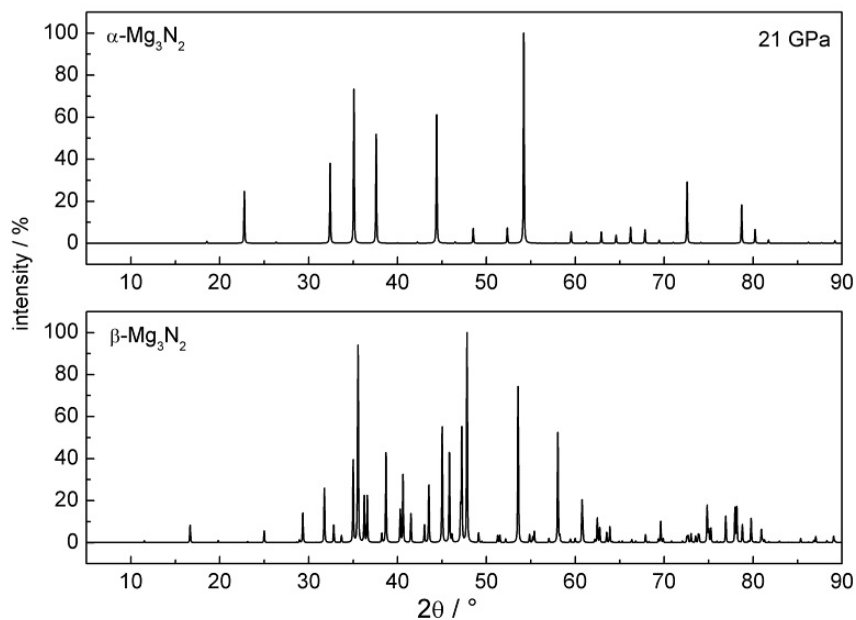
Figure C3: Powder diffraction patterns of α-Mg$_3$N$_2$ (top) and β-Mg$_3$N$_2$ (bottom) at 21 GPa (Cu-K$_{\alpha 1}$ radiation, Deby-Scherrer-Geometry).
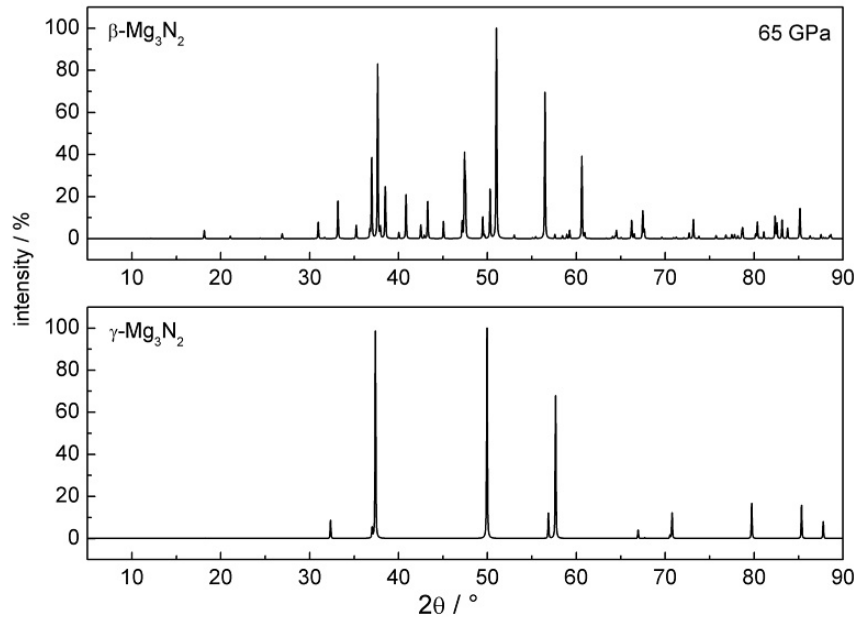
Figure C4: Powder diffraction patterns of β-Mg$_3$N$_2$ (top) and γ-Mg$_3$N$_2$ (bottom) at 65 GPa (Cu-K$_{\alpha 1}$ radiation, Deby-Scherrer-Geometry).
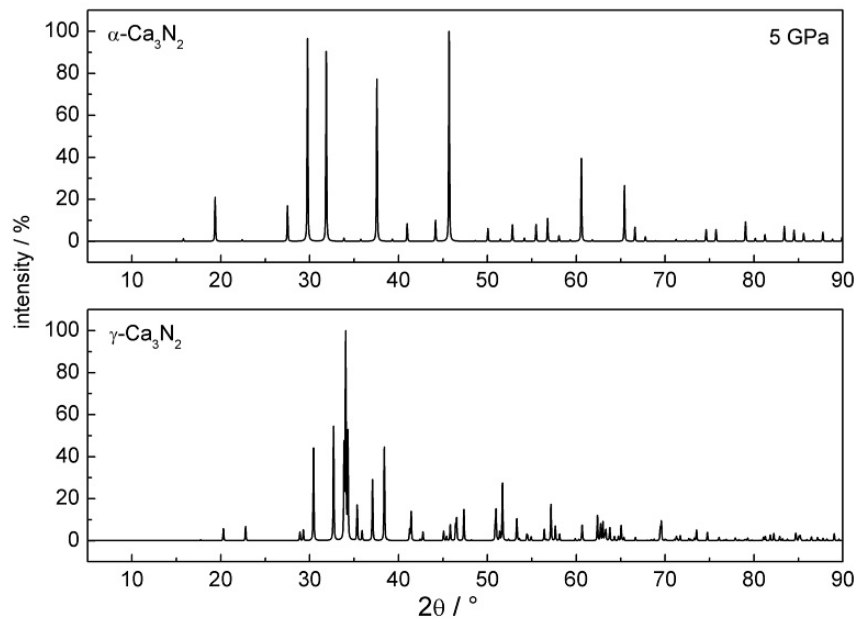
Figure C5: Powder diffraction patterns of α-Ca$_3$N$_2$ (top) and γ-Ca$_3$N$_2$ (bottom) at 5 GPa (Cu-K$_{\alpha 1}$ radiation, Deby-Scherrer-Geometry).
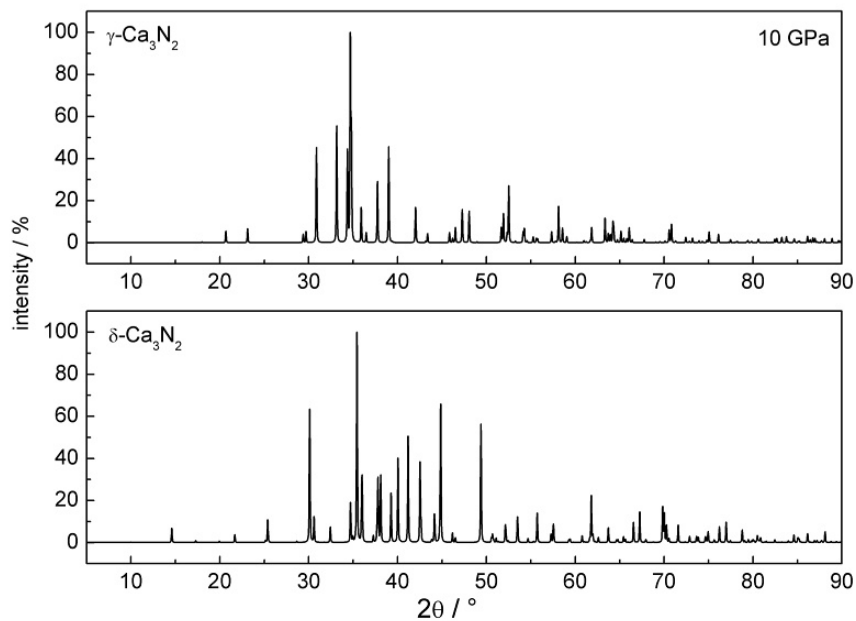
Figure C6: Powder diffraction patterns of γ-Ca_3N_2 (top) and δ-Ca_3N_2 (bottom) at $10\,GPa$ (Cu-$K_{\alpha 1}$ radiation, Deby-Scherrer-Geometry).
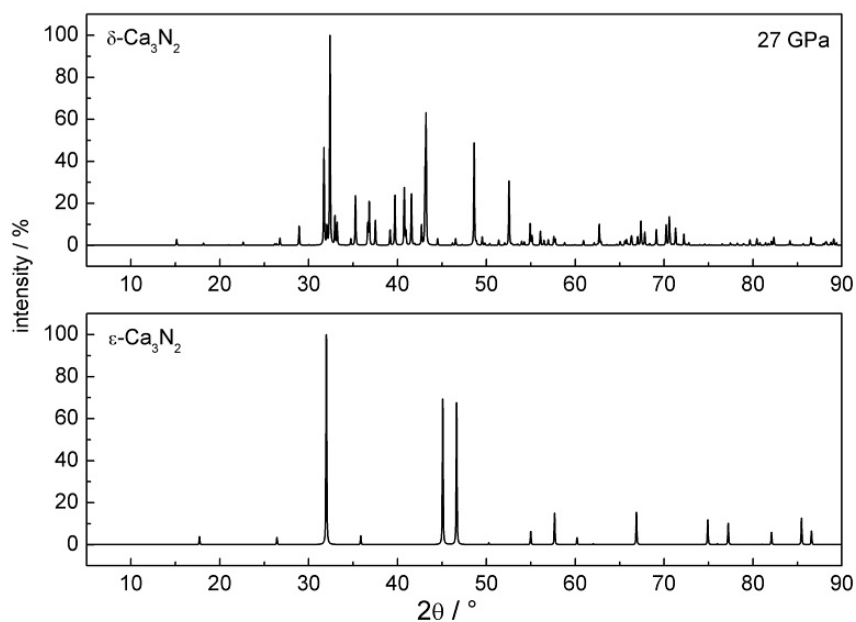
Figure C7: Powder diffraction patterns of δ-Ca_3N_2 (top) and ϵ-Ca_3N_2 (bottom) at $27\,GPa$ (Cu-$K_{\alpha 1}$ radiation, Deby-Scherrer-Geometry).
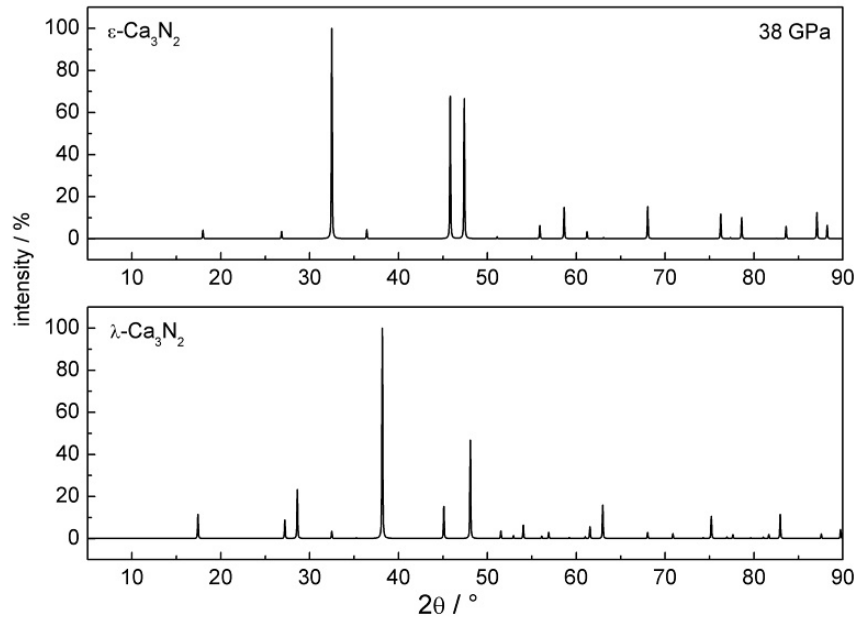
Figure C8: Powder diffraction patterns of ϵ-Ca_3N_2 (top) and λ-Ca_3N_2 (bottom) at 38 GPa (Cu-$K_{\alpha 1}$ radiation, Deby-Scherrer-Geometry).
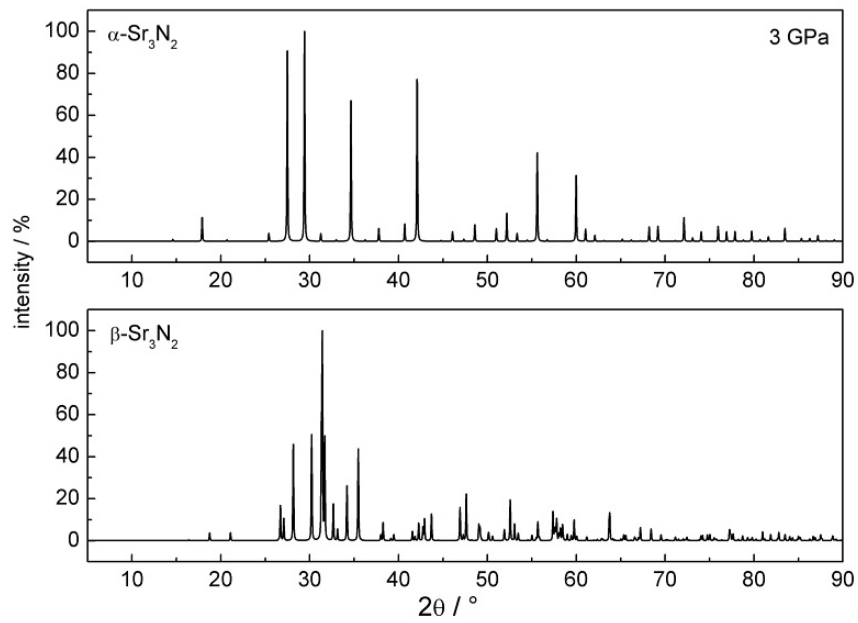
Figure C9: Powder diffraction patterns of α-Sr_3N_2 (top) and β-Sr_3N_2 (bottom) at 3 GPa (Cu-$K_{\alpha 1}$ radiation, Deby-Scherrer-Geometry).
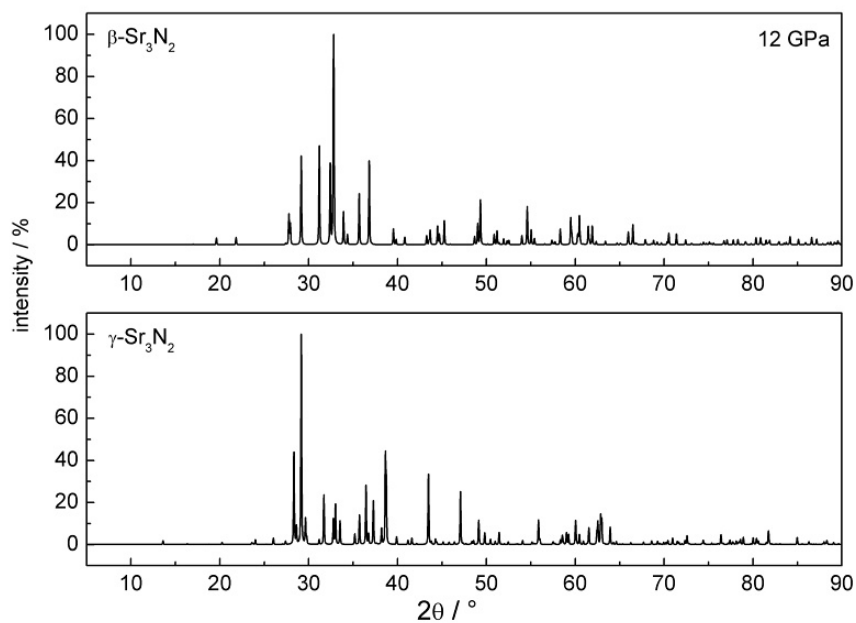
Figure C10: Powder diffraction patterns of β-Sr$_3$N$_2$ (top) and γ-Sr$_3$N$_2$ (bottom) at 12 GPa (Cu-K$_{\alpha 1}$ radiation, Deby-Scherrer-Geometry).
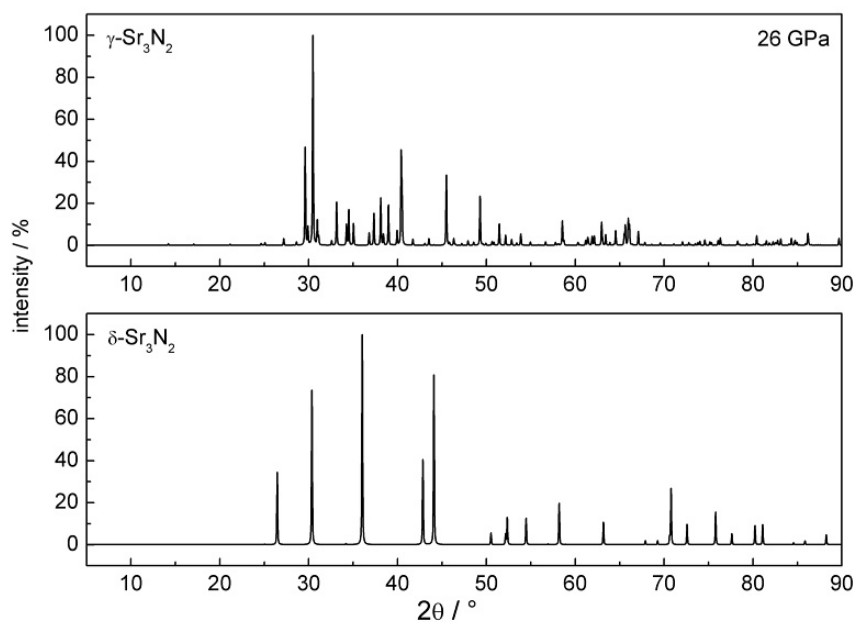
Figure C11: Powder diffraction patterns of γ-Sr$_3$N$_2$ (top) and δ-Sr$_3$N$_2$ (bottom) at 26 GPa (Cu-K$_{\alpha 1}$ radiation, Deby-Scherrer-Geometry).
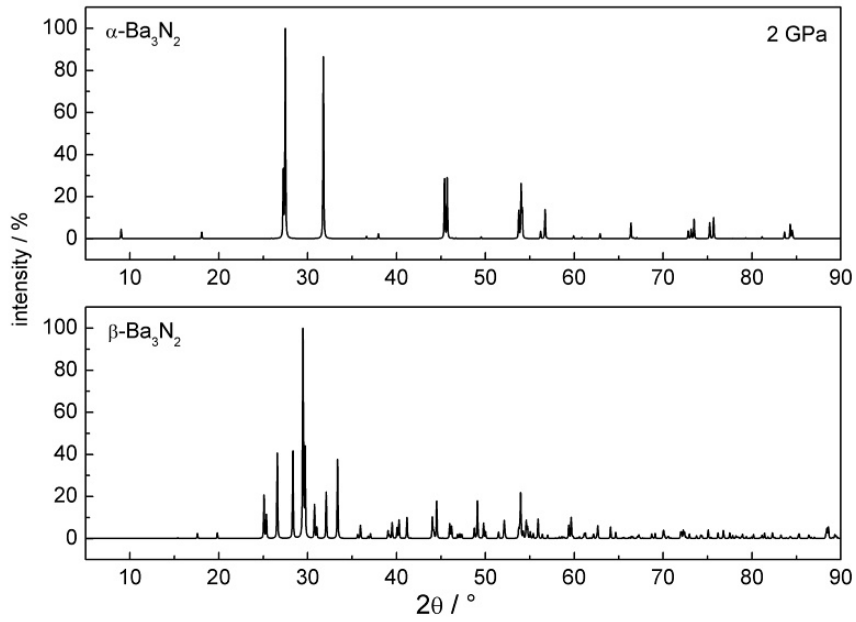
Figure C12: Powder diffraction patterns of α-Ba$_3$N$_2$ (top) and β-Ba$_3$N$_2$ (bottom) at 2 GPa (Cu-K$_{\alpha1}$ radiation, Deby-Scherrer-Geometry).
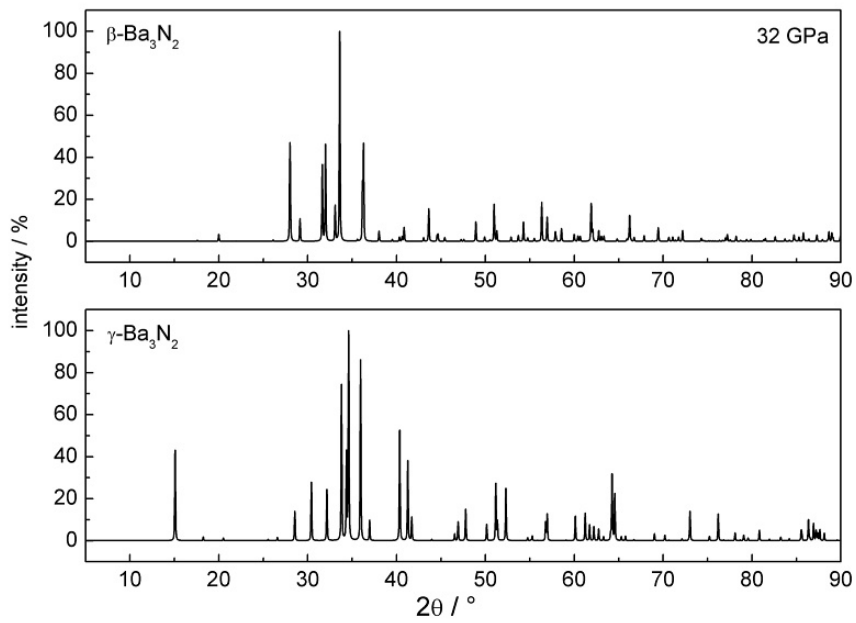
Figure C13: Powder diffraction patterns of β-Ba$_3$N$_2$ (top) and γ-Ba$_3$N$_2$ (bottom) at 32 GPa (Cu-K$_{\alpha1}$ radiation, Deby-Scherrer-Geometry).
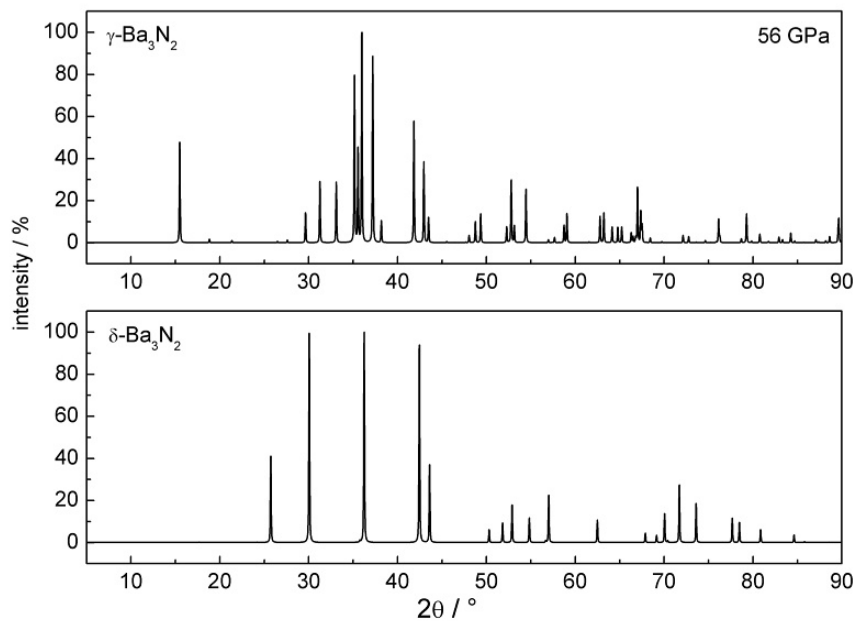
Figure C14: Powder diffraction patterns of γ-Ba$_3$N$_2$ (top) and δ-Ba$_3$N$_2$ (bottom) at 56 GPa (Cu-K$_{\alpha 1}$ radiation, Deby-Scherrer-Geometry).

Nitridosilicates MSiN$_2$ of the Group II Elements
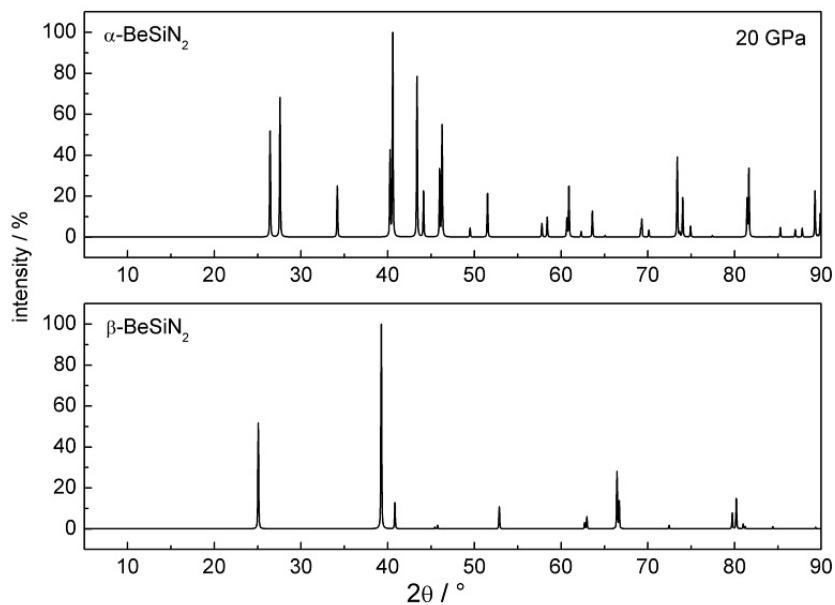
Figure C15: Powder diffraction patterns of α-BeSiN$_2$ (top) and β-BeSiN$_2$ (bottom) at 20 GPa (Cu-K$_{\alpha 1}$ radiation, Deby-Scherrer-Geometry).
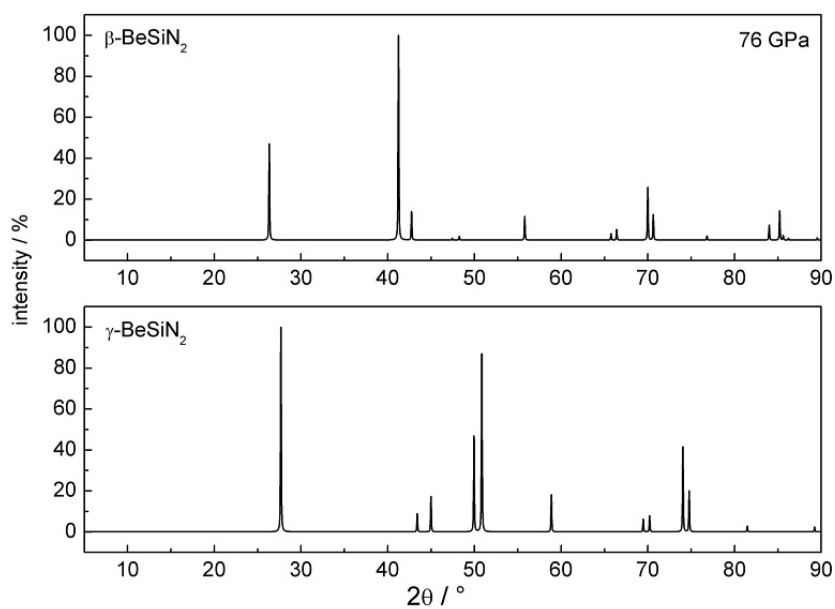
Figure C16: Powder diffraction patterns of β-BeSiN$_2$ (top) and γ-BeSiN$_2$ (bottom) at 76 GPa (Cu-K$_{\alpha 1}$ radiation, Deby-Scherrer-Geometry).
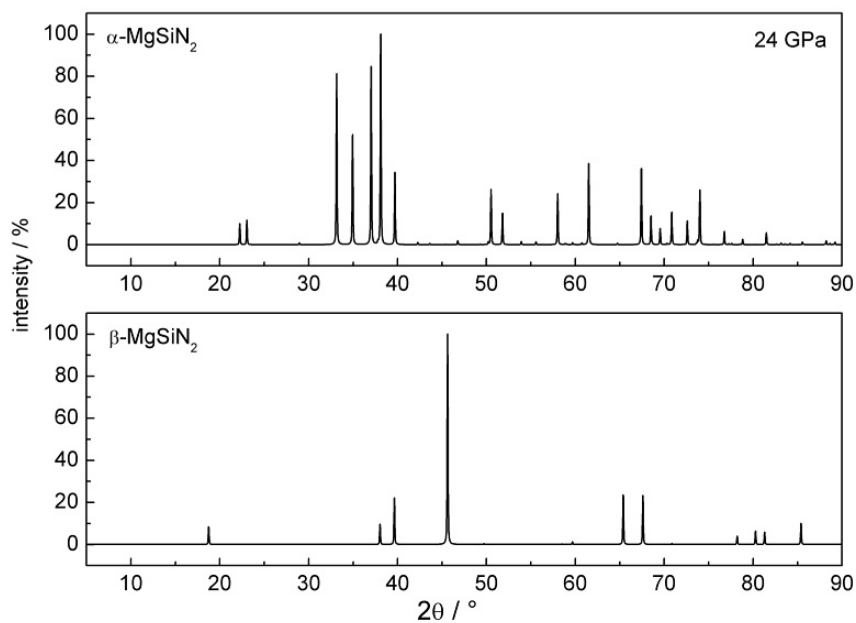
Figure C17: Powder diffraction patterns of α-MgSiN$_2$ (top) and β-MgSiN$_2$ (bottom) at 24 GPa (Cu-K$_{\alpha 1}$ radiation, Deby-Scherrer-Geometry).
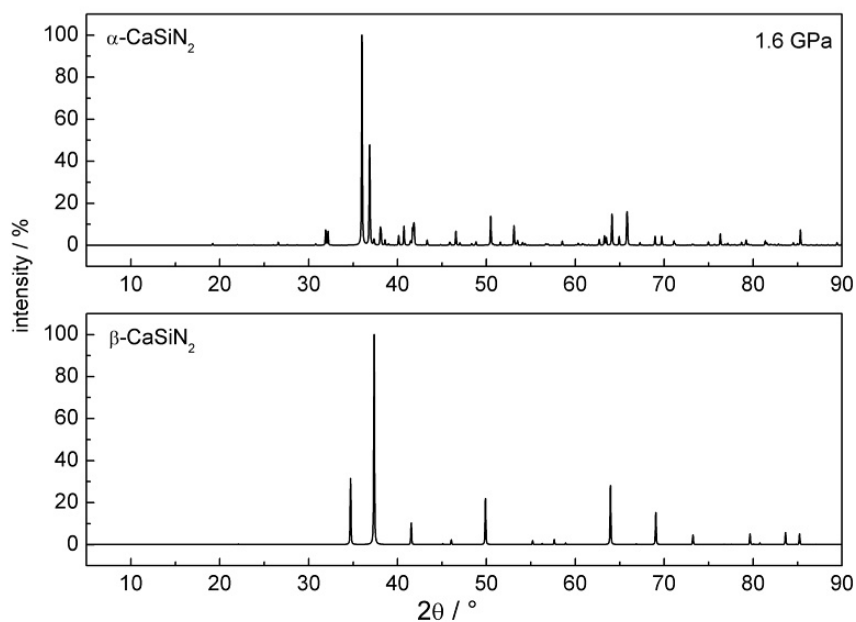
Figure C18: Powder diffraction patterns of α-CaSiN$_2$ (top) and β-CaSiN$_2$ (bottom) at 1.6 GPa (Cu-K$_{\alpha 1}$ radiation, Deby-Scherrer-Geometry).
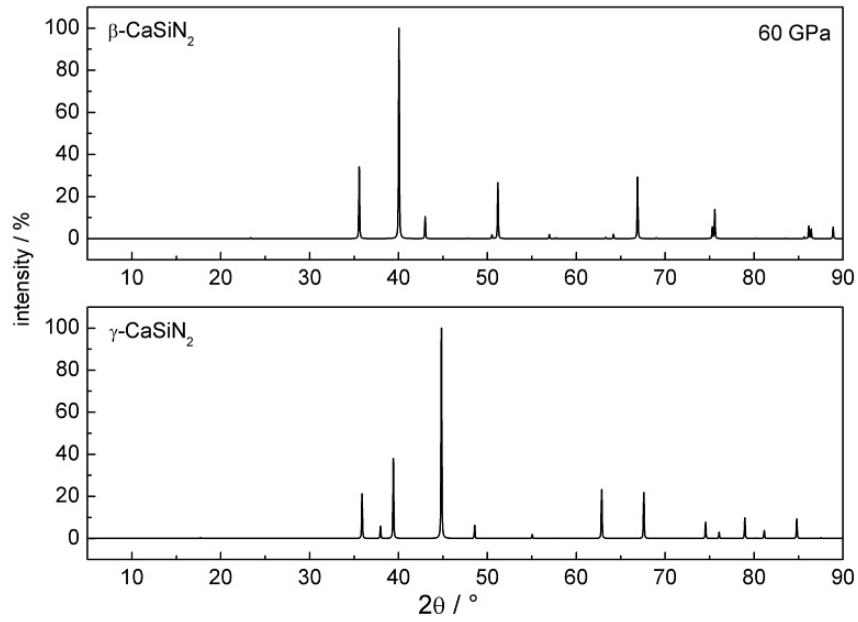
Figure C19: Powder diffraction patterns of β-CaSiN$_2$ (top) and γ-CaSiN$_2$ (bottom) at 60 GPa (Cu-K$_{\alpha 1}$ radiation, Deby-Scherrer-Geometry).
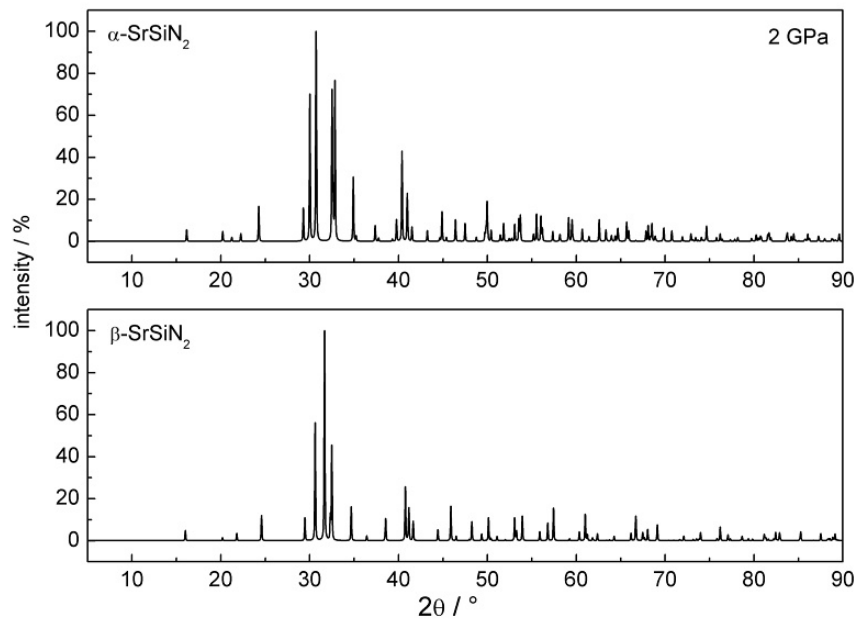
Figure C20: Powder diffraction patterns of α-SrSiN$_2$ (top) and β-SrSiN$_2$ (bottom) at 2 GPa (Cu-K$_{\alpha 1}$ radiation, Deby-Scherrer-Geometry).
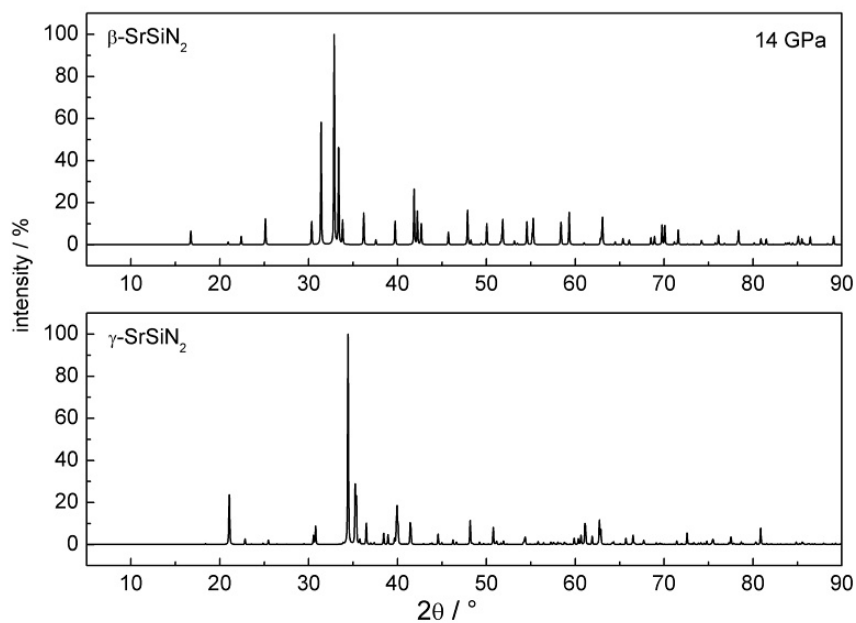
Figure C21: Powder diffraction patterns of β-SrSiN$_2$ (top) and γ-SrSiN$_2$ (bottom) at 14 GPa (Cu-K$_{\alpha1}$ radiation, Deby-Scherrer-Geometry).
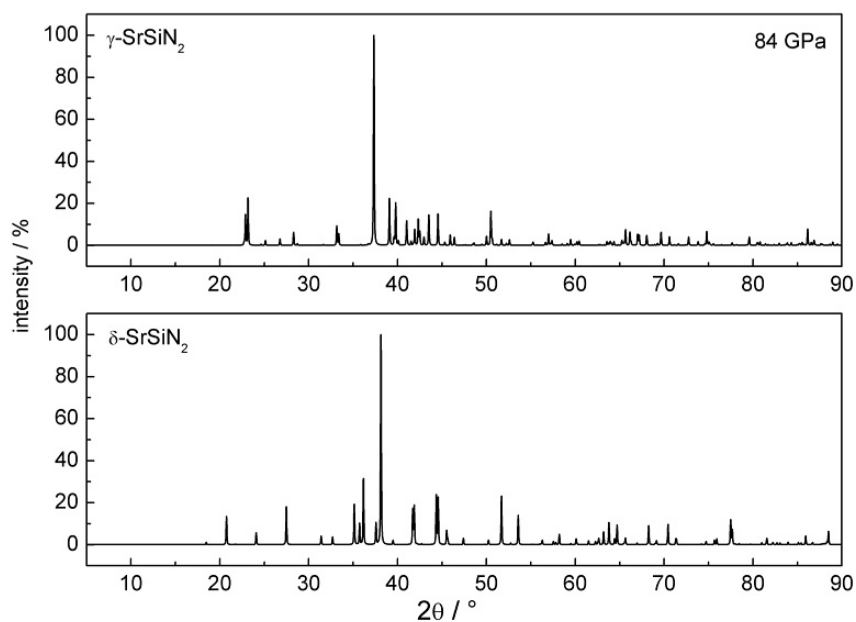
Figure C22: Powder diffraction patterns of γ-SrSiN$_2$ (top) and δ-SrSiN$_2$ (bottom) at 84 GPa (Cu-K$_{\alpha1}$ radiation, Deby-Scherrer-Geometry).
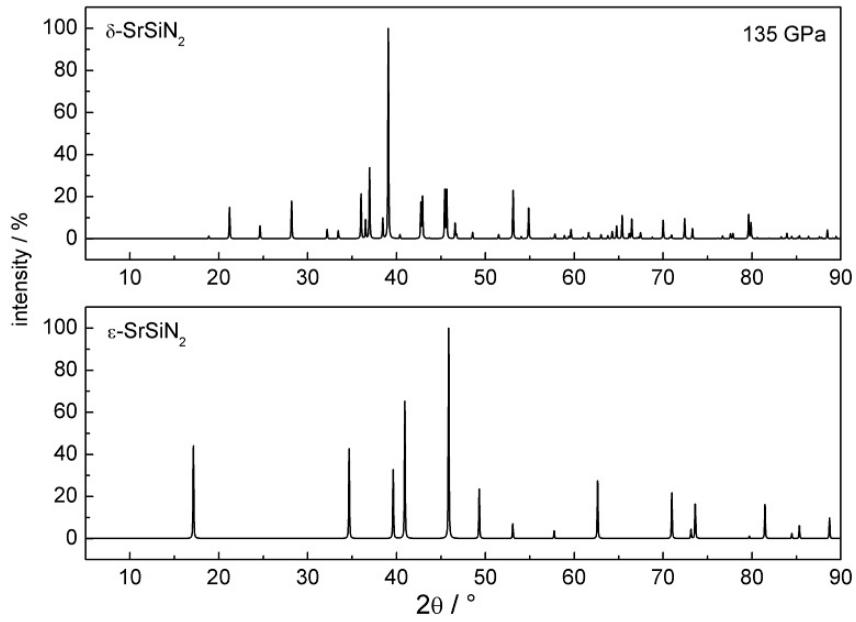
Figure C23: Powder diffraction patterns of δ-SrSiN$_2$ (top) and ϵ-SrSiN$_2$ (bottom) at 130 GPa (Cu-K$_{\alpha1}$ radiation, Deby-Scherrer-Geometry).
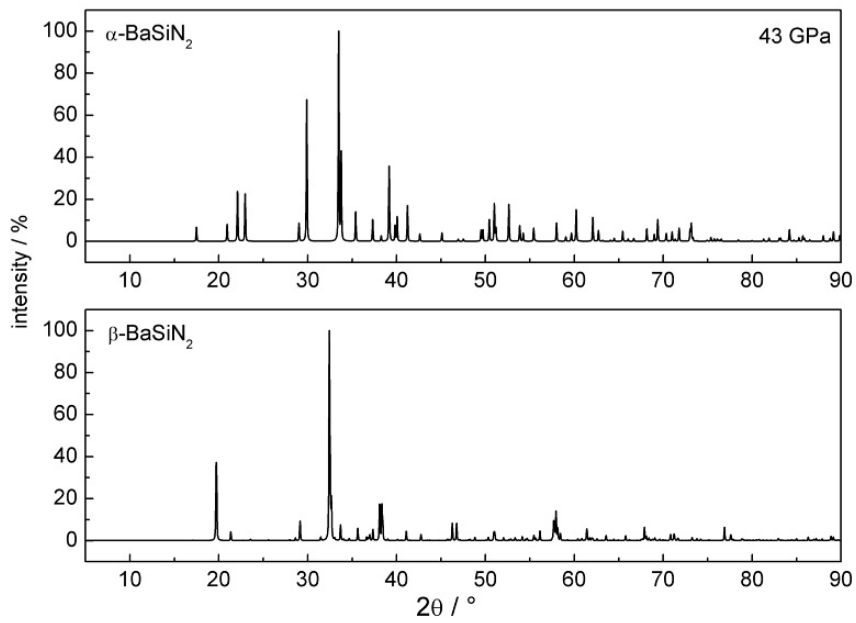
Figure C24: Powder diffraction patterns of α-BaSiN$_2$ (top) and β-BaSiN$_2$ (bottom) at 43 GPa (Cu-K$_{\alpha1}$ radiation, Deby-Scherrer-Geometry).
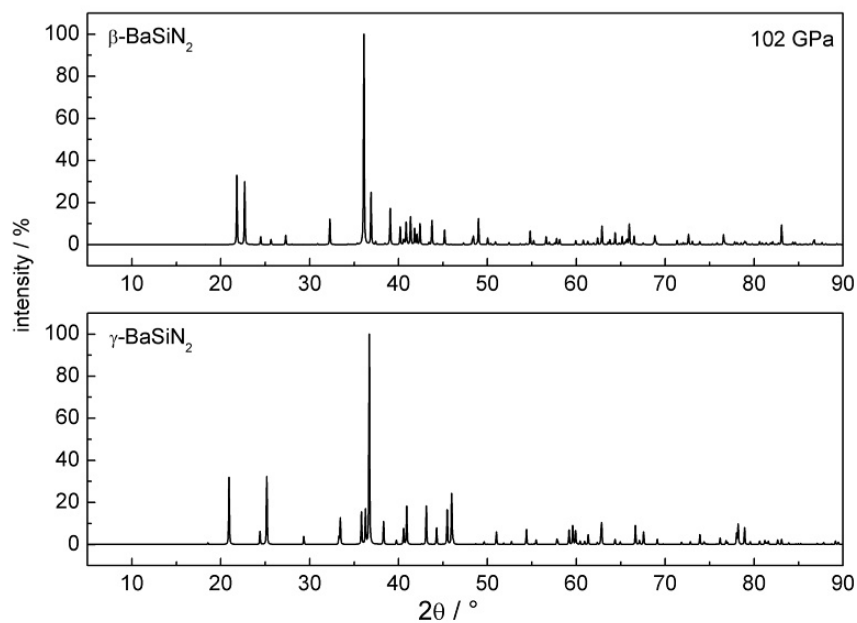
Figure C25: Powder diffraction patterns of β-BaSiN$_2$ (top) and γ-BaSiN$_2$ (bottom) at 102 GPa (Cu-K$_{\alpha 1}$ radiation, Deby-Scherrer-Geometry).

Appendix D – Equations of State fitted to Ba$_3$N$_2$

While fitting the Murnaghan, the Birch and the Vinet equation of state (EOS) to the calculated data points for the different calculated polymorphs of Ba$_3$N$_2$ it became obvious, that, when using all data points significant errors where introduced in V_0 and E_0. Therefore, only 15 data points where used to obtain accurate values for V_0 and E_0, which where subsequently used to fit all calculated data points.

The difference between the two possible fitting procedures are illustrated by way of example of anti-A-sesquioxide type Ba$_3$N$_2$ in Figure D1 to D3. First all data points (black squares, connected by a spline fit (solid line)) where all fitted by one EOS without any fixed parameters (**(1)** dashed-dotted line) and by the same EOS with predetermined V_0 and E_0 (**(2)** dashed line). It can be clearly seen, that curve **(1)** always has a minimum shifted significantly to lower volumina and is not able to describe the true curve progression at volumes around V_0, whereas for curve **(2)** this area is fitted quite well. Both fitting procedures result in almost equal variations from the true curve progression for smaller volumes.

It becomes also obvious that the Birch and Vinet equation of state are better suited to fit the calculated energy-volume data than the Murnaghan equation of state. For the Murnaghan equation of state the difference in V_0 amounts to 6.73 10^6 pm^3 and the difference on E_0 to 0.012 eV. For the Birch and Vinet equation of states the deviations are smaller, but still significant (Birch EOS: $\Delta V_0 = 5.07\ 10^6$ pm^3, $\Delta E_0 = 0.003$ eV; Vinet EOS: $\Delta V_0 = 5.94\ 10^6$ pm^3, $\Delta E_0 = 0.002$ eV).
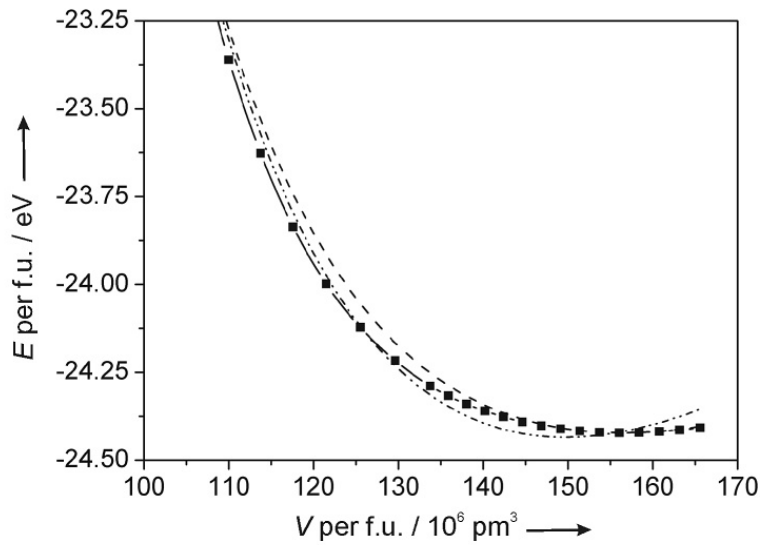
Figure D1: Murnaghan equation of state fit to the calculated data points for anti-A-sesquioxide-type Ba$_3$N$_2$ (black squares: calculated data points, solid line: spline fit, dashed-dotted line: Murnaghan equation of state fit, dashed line: Murnaghan equation of state fit with predetermined V_0 and E_0).
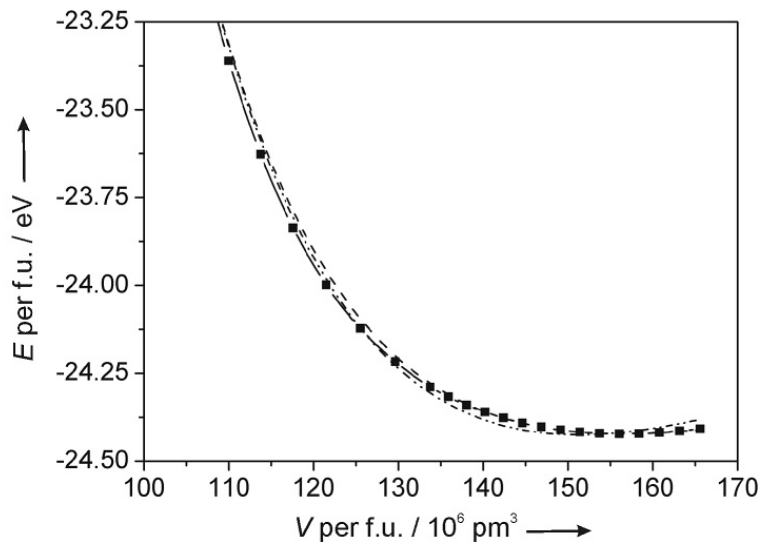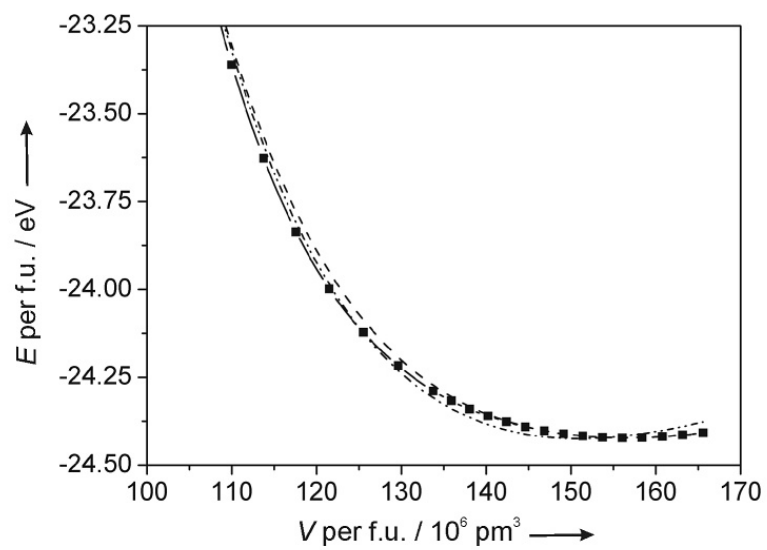

Figure D2: Birch equation of state fit to the calculated data points for anti-A-sesquioxide-type Ba$_3$N$_2$ (black squares: calculated data points, solid line: spline fit, dashed-dotted line: Birch equation of state fit, dashed line: Birch equation of state fit with predetermined V_0 and E_0).

Figure D3: Vinet equation of state fit to the calculated data points for anti-A-sesquioxide-type Ba_3N_2 (black squares: calculated data points, solid line: spline fit, dashed-dotted line: Vinet equation of state fit, dashed line: Vinet equation of state fit with predetermined V_0 and E_0).

Appendix E – Details on Selected Group-Subgroup Relations

Several structures occurring during the search for high-pressure polymorphs of $MSiN_2$ compounds are related to the idealized filled β-cristobalite structure (filled C9 structure). The experimentally found structures of α-$BeSiN_2$ [13], α-$MgSiN_2$ [234, 235] and α-$CaSiN_2$ [14] as well as theoretical β-$BeSiN_2$ ($CuFeS_2$-type [239]) and β-$CaSiN_2$ ($CaGeN_2$-type [250]) can be derived from filled β-cristobalite by concerted rotation of tetrahedra. For illustrations of these rotation patterns see Figure E1 and the works of Thompson et al. [237] and O'Keeffe and Hyde [238].

Certain intermediate structures of the group-subgroup scheme (Figure 5.23, page 106) were obtained upon compressing $SrSiN_2$ and $BaSiN_2$ in the $MgSiN_2$-type and $CaSiN_2$-type structure, as they distorted towards a higher symmetry. Calculating $BaSiN_2$ in the $MgSiN_2$-type structure resulted in an immediate distortion towards *Pnma* (no. 62), which further distorted towards *Imma* (no. 74) upon compression. Compressing $BaSiN_2$ in the $CaSiN_2$-type structure gives a distortion towards *Pbcm* (no. 57). Not all of the thus obtained structures are relevant for the enthalpy-pressure phase diagrams of the examined $MSiN_2$ compounds (c.f. chapter 5.2). However, δ-$SrSiN_2$ and γ-$BaSiN_2$ were identified with the *Pbcm* structure. For neither the *Imma*, *Pnma* or *Pbcm* structure corresponding compounds could be found either in *Pearson's Crystal Structure Database of Inorganic Compounds* [306] or the *Inorganic Crystal Structure Database* (ICSD) [307].
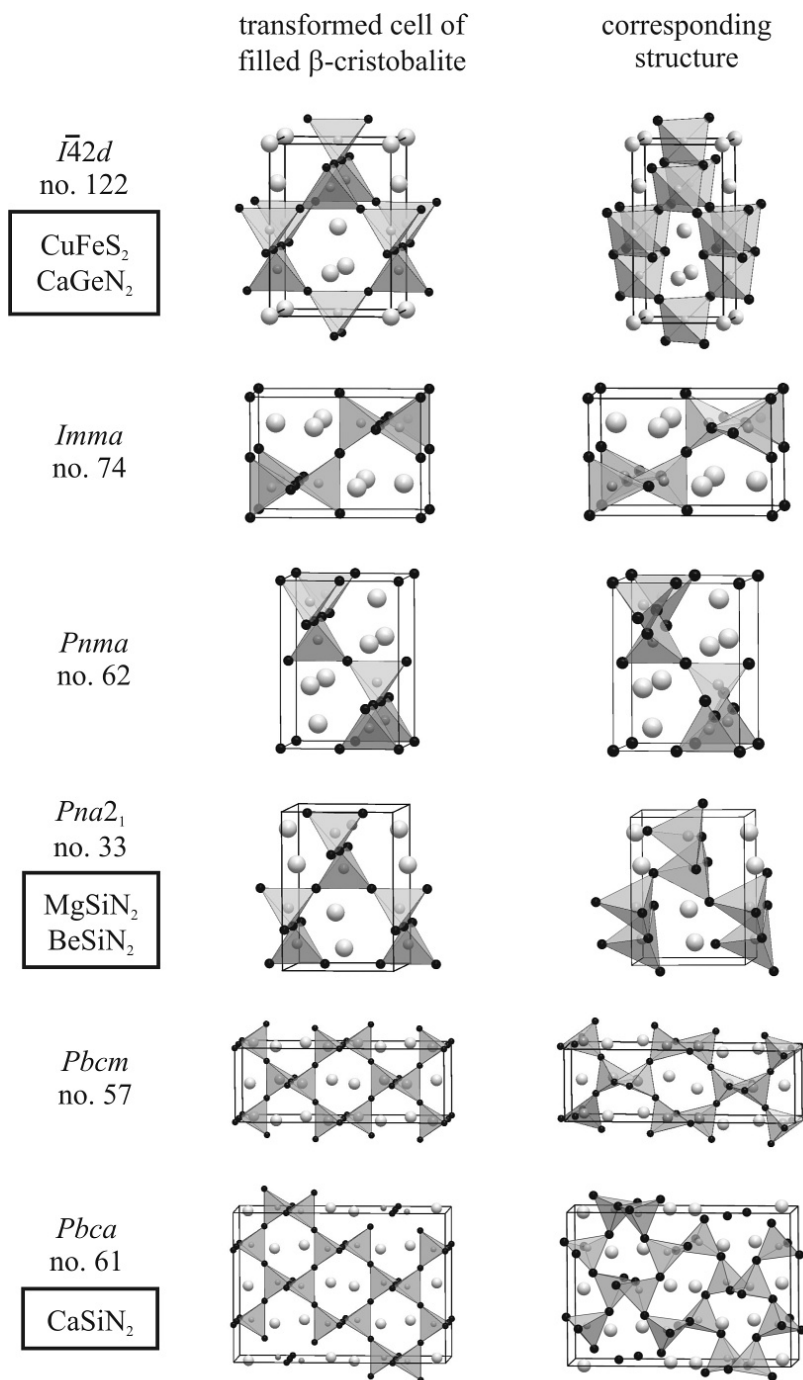
Figure E1: Comparison of the symmetry-reduced unit cell of the idealized filled β-cristobalite structure to the structures found in $MSiN_2$ compounds (experimental and calculated).

Appendix F – AWK-Script to Convert CONTCAR- and POSCAR-files to INS-files

The AWK-script CONTCAR2INS is used in combination with a simple bash-script to convert CONTCAR or POSCAR-files of VASP into INS-files as used by SHELX.

Bash-Scrip

```
#!/bin/bash
echo "CONTCAR to INS"
echo "Name of Input-file?"
read INPUT
echo "Type in atom types in order as in CONTCAR/POSCAR!"
read ATOMS_1
echo $ATOMS_1 > ATOMS_1
echo "Title for ins-file?"
read TITLE
echo "TITL" $TITLE > TITLE
cat ATOMS_1 $INPUT > AWK-INPUT
LC_ALL=C ./contcar2ins.awk AWK-INPUT > $INPUT.1
cat TITLE $INPUT.1 > $INPUT.ins
```

CONTCAR2INS

```
#!/usr/bin/awk -f
# Copyright (C) 2007 Rebecca Roemer http://fantasia-fuoco.de
# This program is free software:  you can redistribute it and/or
# modify it under the terms of the GNU General Public License as
# published by the Free Software Foundation, either version 3 of
# the License, or (at your option) any later version.

# This program is distributed in the hope that it will be useful,
# but WITHOUT ANY WARRANTY; without even the implied warranty of
# MERCHANTABILITY or FITNESS FOR A PARTICULAR PURPOSE.  See the
# GNU General Public License for more details.

# You should have received a copy of the GNU General Public License
# along with this program.  If not, see http://www.gnu.org/licenses/.

# Authors:
# * Rebecca Roemer (rr) http://fantasia-fuoco.de
# * Michael Decker (mad) http://Inspire-Mind.de

# Version:
# * 0.0.0.4:  2008-04-17 - remove bug for angle of unit cell
# calculation for scaling factors other than 1.000000
# * 0.0.0.3:  2008-03-23 - generalization for variable number of
# atom sorts (mad)
# * 0.0.0.2:  2008-03-18 - include scaling factor in calculation of
# unit cell lattice (rr)
# * 0.0.0.1:  2007-11-11 - Only working for CONTCARs containing one,
# two and three atom sorts and scaling factor 1.000000 for matrix (rr)

# Tested:
# * 2008-03-23:  Kubuntu 7.10 with
```

```
# - GNU Awk 3.1.5
# * 2008-03-21:  Suse 10.2


BEGIN {
#setting different variables
myLineCounter = 0;
maxLineCounter = 0;

# cell parameters
axis[1] = 0 ; # a-axis
axis[2] = 0 ; # b-axis
axis[3] = 0 ; # c-axis

#norm (ger.  Betrag) for a-, b, und c-vector
betrag[1] = 0 ; # norm a-vector
betrag[2] = 0 ; # norm b-vector
betrag[3] = 0 ; # norm c-vector

# values needed for calculation of cell parameters
cosin[1] = 0 ; # cos(alpha)
cosin[2] = 0 ; # cos(beta)
cosin[3] = 0 ; # cos(gamma)

# Scalierung der Matrixelemente
scale[1] = 0

# Matrix describing unit cell
# a1 a2 a3 (line 3 of input)
# b1 b2 b3 (line 4 of input)
# c1 c2 c3 (line 5 of input)
a[1] = 0 ; # a1
a[2] = 0 ; # a2
```

```
a[3] = 0 ; # a3
b[1] = 0 ; # b1
b[2] = 0 ; # b2
b[3] = 0 ; # b3
c[1] = 0 ; # c1
c[2] = 0 ; # c2
c[3] = 0 ; # c3

# Unit cell angles
alpha[1] = 0 ;
beta[1] = 0 ;
gamma[1] = 0 ;

# number of atoms of different atom sorts
atom[1] = 0 ;
atom[2] = 0 ;
atom[3] = 0 ;

# total number of atoms in unit cell
number_atoms[1] = 0;

# atom sorts
atom_sort[1] = 0;

sumOfPreviousAtoms = 0;
currentAtomCount = 0;
}

# Functions from:  http://www.gladir.com/CODER/AWK/acos.htm
function abs(a) {
if(a<0) a=-a;
return a;
}
```

```
function acos(a) {
pi=3.141592653589793 ;
if(abs(a)==1) {
return (1-a)*pi/2  ;
} else {
return atan2(-a,sqrt(1-a*a))+2*atan2(0.5,0.5) ;
}
}


{ myLineCounter++;
}


myLineCounter == 1 {
for (i=1 ; i <= NF ; i++)
{ atom_sort[i] = $i ;
}
}


myLineCounter == 3 {
cale[1] = $1;
}


myLineCounter == 4 {
axis[1] = (((scale[1]*$1)^2 + (scale[1]*$2)^2 +
(scale[1]*$3)^2)^(1/2)) ;
}


myLineCounter == 4 {
betrag[1] = ((($1)^2 + ($2)^2 + ($3)^2)^(1/2)) ;
}


# Choose according to your awk (** or ^ for "to the power of")
```

```
# myLineCounter == 4 {
# axis[1] = (((scale[1]*$1)**2 + (scale[1]*$2)**2 +
# (scale[1]*$3)**2)**(1/2)) ;
# }


myLineCounter == 4 {
a[1] = $1 ;
a[2] = $2 ;
a[3] = $3 ;
}


# Choose according to your awk (** or ^ for "to the power of")
# myLineCounter == 5 {
# axis[2] = (((scale[1]*$1)**2 + (scale[1]*$2)**2 +
# (scale[1]*$3)**2)**(1/2)) ;
# }


myLineCounter == 5 {
axis[2] = (((scale[1]*$1)^2 + (scale[1]*$2)^2 +
(scale[1]*$3)^2)^(1/2));
}


myLineCounter == 5 {
betrag[2] = ((($1)^2 + ($2)^2 + ($3)^2)^(1/2)) ;
}


myLineCounter == 5 {
b[1] = $1 ;
b[2] = $2 ;
b[3] = $3 ;
}


# Choose according to your awk (** or ^ for "to the power of")
```

```
# myLineCounter == 6 {
# axis[3] = (((scale[1]*$1)**2 + (scale[1]*$2)**2 +
# (scale[1]*$3)**2)**(1/2)) ;
#}

myLineCounter == 6 {
axis[3] =(((scale[1]*$1)^2 + (scale[1]*$2)^2 +
(scale[1]*$3)^2)^(1/2)) ;
}
myLineCounter == 6 {
betrag[3] = ((($1)^2 +($2)^2 + ($3)^2)^(1/2)) ;
}

myLineCounter == 6 {
c[1] = $1 ;
c[2] = $2 ;
c[3] = $3 ;
}

myLineCounter == 6 {
cosin[1] = ((b[1] * c[1] + b[2] * c[2] + b[3] * c[3]) /
(betrag[2] * betrag[3]));
cosin[2] = ((a[1] * c[1] + a[2] * c[2] + a[3] * c[3]) /
(betrag[1] * betrag[3]));
cosin[3] = ((b[1] * a[1] + b[2] * a[2] + b[3] * a[3]) /
(betrag[2] * betrag[1]));
}

myLineCounter == 6 {
alpha[1] = ( acos(cosin[1]) * (180 / 3.141592653589793)) ;
beta[1] = ( acos(cosin[2]) * (180 / 3.141592653589793)) ;
gamma[1] = ( acos(cosin[3]) * (180 / 3.141592653589793)) ;
}
```

```
myLineCounter == 7 {
printf "%s%.8f %.8f %.8f %.8f %.8f %.8f\n",
"CELL 0.71073 ", axis[1] , axis[2] ,axis[3] , alpha[1] , beta[1] ,
gamma[1] ;
}


myLineCounter == 7 {
print "LATT-1";
printf "%s", "SFAC ";
}


myLineCounter == 7 {
for (i=1 ; i <NF ; i++)
{ printf "%s %s" , atom_sort[i],"" ;
}
for (i=NF ; i == NF ; i++)
{ printf "%s\n", atom_sort[i] ;
}
for (i=1 ; i <= NF; i++)
{ atom[i] = $i ;
}
max_line[0] = 8;
max_line[1] = ( atom[1] + 8) ;
for (i=2 ; i <= NF; i++)
{ max_line[i] = max_line[(i-1)] + atom[i] ;
}
}


(myLineCounter > max_line[maxLineCounter]) &&
(myLineCounter <= max_line[maxLineCounter+1]) {
currentAtomCount++;
printf "%s %s %s %s %s\n",
```

```
atom_sort[maxLineCounter+1] currentAtomCount, maxLineCounter+1 ,
$1,  $2,  $3 ;
# if we are on the last line of current atom, we have to move to the
# next atom
(myLineCounter == max_line[maxLineCounter+1]) {
maxLineCounter++;
currentAtomCount= 0;
}

END { print "END" }
}
```

Bibliography

[1] W. Schnick, *Angew. Chem.* **1993**, *105*, 846-858; *Angew. Chem. Int. Ed. Engl.* **1993**, *32*, 806-818.

[2] S. N. Ruddlesden, P. Popper, *Acta Crystallogr.* **1958**, *11*, 465–468.

[3] D. Hardie, K. H. Jack, *Nature* **1957**, *180*, 332–333.

[4] A. Zerr, G. Miehe, G. Serghiou, M. Schwarz, E. Kroke, R. Riedel, H. Fueß, P. Kroll, R. Boehler, *Nature* **1999**, *400*, 340–342.

[5] M. Schwarz, G. Miehe, A. Zerr, E. Kroke, B. T. Poe, H. Fuess, R. Riedel, *Adv. Mater.* **2000**, *12*, 883–887.

[6] P. Kroll, M. Milko, *Z. Anorg. Allg. Chem.* **2003**, *629*, 1737–1750.

[7] A. Zerr, M. Kempf, M. Schwarz, E. Kroke, M. Göken, R. Riedel, *J. Am. Ceram. Soc.* **2002**, *85*, 86–90.

[8] J. Z. Jiang, H. Lindelov, L. Gerward, K. Stahl, J. M. Recio, P. Mori-Sanchez, S. Carlson, M. Mezouar, E. Dooryhee, A. Fitch, D. J. Frost, *Phys. Rev. B* **2002**, *65*, 161202/1–4.

[9] W. Y. Ching, L. Ouyang, *Phys. Rev. B* **2000**, *61*, 8692–8700.

[10] P. Kroll, J. van Appen, *Phys. Status Solidi B* **2001**, *226*, R6–R7.

[11] T. Sekine, Talk presented at the 2nd International Workshop on Spinel Nitrides and Related Materials, Rüdesheim **2004**.

[12] P. Kroll, *J. Solid State Chem.* **2003**, *176*, 530–537.

[13] P. Eckerlin, *Z. Anorg. Allg. Chem.* **1967**, *353*, 225–235.

[14] Z. A. Gál, P. M. Mallinson, H. J. Orchard, S. J. Clarke, *Inorg. Chem.* **2004**, *43*, 3998–4006.

[15] T. Schlieper, W. Schnick, *Z. Anorg. Allg. Chem.* **1995**, *621*, 1037–1041.

[16] T. Schlieper, W. Milius, W. Schnick, *Z. Anorg. Allg. Chem.* **1995**, *621*, 1380–1384.

[17] F. Stadler, O. Oeckler, J. Senker, H. A. Höppe, P. Kroll, W. Schnick, *Angew. Chem.* **2005**, *117*, 573-576; *Angew. Chem. Int. Ed.* **2005**, *44*, 567-570.

[18] H. A. Höppe, H. Lutz, P-Morys, W. Schnick, A. Seilmeier, *J. Phys. Chem. Solids* **2000**, *61*, 2001–2006.

[19] R. Mueller-Mach, G. Mueller, M. R. Kramers, H. A. Höppe, F. Stadler, W. Schnick, T. Juestel, P. Schmidt, *Phys. Status Solidi A* **2005**, *202*, 1727–1732.

[20] H. Lutz, S. Joosten, J. Hoffmann, P. Lehmeier, A. Seilmeier, H. A. Höppe, W. Schnick, *J. Phys. Chem. Solids* **2004**, *65*, 1285–1290.

[21] W. Schnick, R. Bettenhausen, B. Götze, H. A. Höppe, H. Huppertz, E. Irran, K. Köllisch, R. Lauterbach, M. Orth, S. Rannabauer, T. Schlieper, B. Schwarze, F. Wester, *Z. Anorg. Allg. Chem.* **2003**, *629*, 902–912.

[22] K. Landskron, H. Huppertz, J. Senker, W. Schnick, *Angew. Chem.* **2001**, *113*, 2713-2716; *Angew. Chem. Int. Ed.* **2001**, *40*, 2643-2645.

[23] K. Landskron, H. Huppertz, J. Senker, W. Schnick, *Z. Anorg. Allg. Chem.* **2002**, *628*, 1465–1471.

[24] P. Kroll, W. Schnick, *Chem. Eur. J.* **2002**, *8*, 3530–3537.

[25] F. Karau, Dissertation, Ludwig-Maximilians Universität, **2007**.

[26] F. Pucher, personal communication, **2008**.

[27] F. W. Karau, L. Seyfart, O. Oeckler, J. Senker, K. Landskron, W. Schnick, *Chem. Eur. J.* **2007**, *13*, 6841–6852.

[28] F. Karau, W. Schnick, *Z. Anorg. Allg. Chem.* **2006**, *632*, 231–237.

[29] F. Karau, W. Schnick, *J. Solid State Chem.* **2005**, *178*, 135–141.

[30] I. N. Levine, *Quantum Chemistry*, Prentice Hall, Upper Saddle River, New Jersey, 5th ed., **2000**.

[31] A. Szabo, N. S. Ostlund, *Modern Quantum Chemistry*, Dover Publications, Mineola, New York, **1996**.

[32] M. Born, J. R. Oppenheimer, *Annalen der Physik* **1927**, *84*, 457–484.

[33] L. H. Thomas, *Proc. Camb. Phil. Soc.* **1927**, *23*, 542–153.

[34] E. Fermi, *Rend. Accad. Lincei* **1927**, *6*, 602–607.

[35] E. Fermi, *Z. Phys.* **1928**, *48*, 73–79.

[36] E. Fermi, *Rend. Accad. Lincei* **1928**, *7*, 342–246.

[37] P. Hohenberg, W. Kohn, *Phys. Rev.* **1964**, *136*, B864–B871.

[38] W. Kohn, L. J. Sham, *Phys. Rev.* **1965**, *140*, A1133–A1138.

[39] R. G. Parr, W. Yang, *Density-Functional Theory of Atoms and Molecules*, Oxford University Press, New York, **1989**.

[40] D. M. Ceperley, B. J. Alder, *Phys. Rev. Lett.* **1980**, *45*, 566–569.

[41] S. J. Vosko, L. Wilk, M. Nusair, *Can. J. Phys.* **1980**, *58*, 1200–1211.

[42] F. Jensen, *Introduction to Computational Chemistry*, Wiley, Chichester, **1999**.

[43] U. von Barth, L. Hedin, *J. Phys. C* **1972**, *5*, 1629–1642.

[44] J. D. Perdew, Y. Wang, *Phys. Rev. B* **1986**, *33*, 8800–8802.

[45] C. Lee, W. Yang, R. G. Parr, *Phys. Rev. B* **1988**, *37*, 785–789.

[46] A. D. Becke, *Phys. Rev. A* **1988**, *38*, 3098–3100.

[47] J. P. Perdew, *Phys. Rev. B* **1986**, *33*, 8822–8824.

[48] J. P. Perdew, *Phys. Rev. B* **1986**, *34*, 7406–7406.

[49] A. D. Becke, M. R. Roussel, *Phys. Rev. A* **1989**, *39*, 3761–3767.

[50] J. P. Perdew, J. A. Chevary, S. H. Vosko, K. A. Jackson, M. R. Pederson, D. J. Singh, C. Fiolhais, *Phys. Rev. B* **1992**, *46*, 6671–6687.

[51] A. D. Becke, *J. Chem. Phys.* **1996**, *104*, 1040–1046.

[52] M. Fuchs, J. L. F. D. Silva, C. Stampfl, J. Neugebauer, M. Scheffer, *Phys. Rev. B* **2002**, *65*, 245212/1–13.

[53] G. Ortiz, *Phys. Rev. B* **1992**, *45*, 11328–11331.

[54] F. Bloch, *Z. Phys.* **1928**, *52*, 555–600.

[55] S. Elliott, *The Physics and Chemistry of Solids*, Wiley, Chichester, **1998**.

[56] E. Schachinger, H. Sormann, *Theoretische Festkörperphysik I und II*, Lecture at TU Gratz, published online, `http://itp.tugraz.at/LV/ewald/TFKP`, visited 28th May 2008.

[57] B. Meyer, *Computational Nanoscience: Do It Yourself! - The Pseudopotential Plane Wave Approach, NIC Series, Vol. 31*, John von Neumann Institute for Computing, Jülich, **2006**, pp. 71–83.

[58] H. J. Monkhorst, J. D. Pack, *Phys. Rev. B* **1976**, *13*, 5188–5192.

[59] G. Kresse, J. Hafner, *Phys. Rev. B* **1993**, *47*, 558–561.

[60] G. Kresse, Dissertation, Technische Universität Wien, **1993**.

[61] G. Kresse, J. Furthmüller, *Comput. Mater. Sci.* **1996**, *6*, 15–50.

[62] G. Kresse, J. Furthmüller, *Phys. Rev. B* **1996**, *54*, 11169–11186.

[63] G. Kresse, J. Furthmüller, VASP the GUIDE, Institut für Materialphysik, Universität Wien, Sensengasse 8, A-1130 Wien, Austria, **2007**.

[64] P. E. Blöchl, *Phys. Rev. B* **1994**, *50*, 17953–17979.

[65] G. Kresse, D. Joubert, *Phys. Rev. B* **1999**, *59*, 1758–1775.

[66] F. D. Murnaghan, *Proc. Nat. Acad. Sci.* **1944**, *30*, 244–247.

[67] F. Birch, *J. Geophys. Res.* **1952**, *57*, 227–286.

[68] P. Vinet, J. Ferrante, J. R. Smith, J. H. Rose, *Phys. Rev. B* **1887**, *35*, 1945–1953.

[69] P. Vinet, J. H. Rose, J. Ferrante, J. R. Smith, *J. Phys.: Condens. Matter* **1989**, *1*, 1941–1963.

[70] F. Guinea, J. H. Rose, J. R. Smith, J. Ferrante, *Appl. Phys. Lett.* **1984**, *44*, 53–55.

[71] J. H. Rose, J. R. Smith, F. Guinea, J. Ferrante, *Phys. Rev. B* **1984**, *29*, 2963–2969.

[72] J. Hama, K. Suito, *J. Phys.: Condens. Matter* **1996**, *8*, 67–81.

[73] L. M. Thomas, J. Shanker, *Phys. Status Solidi B* **1995**, *189*, 363–369.

[74] J. Hama, K. Suito, N. Kawakami, *Phys. Rev. B* **1989**, *39*, 3351–3360.

[75] N. N. Kalitkin, L. V. Kuz'mina, *Sov. Phys.-Solid State* **1972**, *13*, 1938–1943.

[76] G. Kresse, J. Hafner, *Phys. Rev. B* **1994**, *49*, 14251–14269.

[77] J. P. Perdew, A. Zunger, *Phys. Rev. B* **1981**, *23*, 5048–5079.

[78] J. P. Perdew in *Electronic Structures of Solids '91* (Eds.: P. Ziesche, H. Eschrig), Akademie Verlag, Berlin, **1991**.

[79] J. P. Perdew, K. Burke, M. Ernzerhof, *Phys. Rev. Lett.* **1996**, *77*, 3865–3868.

[80] T. Demuth, Y. Jeanvoine, J. Hafner, J. G. Ángyán, *J. Phys.: Condens. Matter* **1999**, *11*, 3833–3874.

[81] A. Zupan, P. Blaha, K. Schwartz, J. P. Perdew, *Phys. Rev. B* **1998**, *58*, 11266–11272.

[82] H. Lange, G. Wötting, G. Winter, *Angew. Chem.* **1991**, *103*, 1606-1625; *Angew. Chem. Int. Ed. Engl.* **1991**, *30*, 1579-1597.

[83] A. F. Holleman, E. Wiberg, *Lehrbuch der Anorganischen Chemie*, de Gruyter, Berlin, 101st ed., **1995**.

[84] A. Reyes-Serrato, D. Galvan, I. L. Garzon, *Phys. Rev. B* **1995**, *52*, 6293–6300.

[85] Y. Cai, L. Zhang, Q. Zeng, L. Cheng, Y. Xu, *Phys. Rev. B* **2006**, *74*, 174301/1–4.

[86] S. R. Srinivasa, L. Cartz, J. D. Jorgensen, T. G. Worlton, R. Beyerlein, M. Billy, *J. Appl. Crystallogr.* **1977**, *10*, 167–171.

[87] L. Cartz, J. D. Jorgensen, *J. Appl. Phys.* **1981**, *52*, 236–244.

[88] Y. M. Li, M. B. Kruger, J. H. Nyuyen, W. A. Caldwell, R. Jeanloz, *Solid State Commun.* **1997**, *103*, 107–112.

[89] R. Vogelsang, M. Grimsditch, *Appl. Phys. Lett.* **2000**, *76*, 982–984.

[90] A. Y. Liu, M. L. Cohen, *Phys. Rev. B* **1990**, *41*, 10727–10734.

[91] A. C. Vournasos, *Z. Anorg. Chem.* **1912**, *77*, 191–196.

[92] F. Briegleb, A. Geuther, *Ann. Chem. Pharm.* **1862**, *123*, 228–241.

[93] H. Moissan, *C. R. Hebd. Séanc. Acad. Sci.* **1898**, *127*, 497–501.

[94] M. Maquenne, *C. R. Hebd. Séanc. Acad. Sci.* **1892**, *114*, 220–221.

[95] J. Jian, G. Wang, C. Wang, W. X. Yuan, X. L. Chen, *J. Cryst. Growth* **2006**, *291*, 72–76.

[96] S. Hampshire, H. K. Park, D. P. Thompson, K. H. Jack, *Nature* **1978**, *274*, 880–882.

[97] W. Schnick, V. Schultz-Coulon, *Angew. Chem.* **1993**, *105*, 308-309; *Angew. Chem. Int. Ed. Engl.* **1993**, *32*, 280-281.

[98] F. E. Rohrer, R. Nesper, *J. Solid State Chem.* **1998**, *135*, 194–200.

[99] P. F. Henry, M. T. Weller, *Angew. Chem.* **1998**, *110*, 3040-3041; *Angew. Chem. Int. Ed.* **1998**, *37*, 2855-2857.

[100] G. Demazeau, L. Boutinaud-vel, V. Gonnet, *Proc. Int. Conf. Adv. Hard Mater. Prod.* **1992**, 38/1–6.

[101] H. Q. Bao, H. Li, G. Wang, B. Song, W. J. Wang, X. L. Chen, *J. Cryst. Growth* **2008**, *310*, 2955–2959.

[102] P. Eckerlin, A. Rabenau, H. Hortmann, *Z. Anorg. Allg. Chem.* **1967**, *353*, 113–121.

[103] S. Leoni, R. Niewa, L. Akselrud, Y. Prots, W. Schnelle, T. Goesku, M. Cetinkol, M. Somer, R. Kniep, *Z. Anorg. Allg. Chem.* **2005**, *631*, 1818–1824.

[104] R. Marchand, Y. Laurent, *Mater. Res. Bull.* **1982**, *17*, 399–403.

[105] F. Stadler, W. Schnick, *Z. Anorg. Allg. Chem.* **2007**, *633*, 589–592.

[106] H. D. Gregory, M. G. Barker, J. Daniel, P. P. Edwards, M. Slaski, *Materials Research Society Symposium Proceedings* **1999**, *547*, 401–406.

[107] S. Oshio, (Mtushita Electric Industrial Co., Ltd.), WO-A1 2005103199, **2005**.

[108] F. E. Rohrer, R. Nesper, *J. Solid State Chem.* **1998**, *135*, 194–200.

[109] N. E. Brese, F. J. DiSalvo, *J. Solid State Chem.* **1995**, *120*, 372–377.

[110] V. Schultz-Coulon, W. Schnick, *Z. Anorg. Allg. Chem.* **1997**, *623*, 69–74.

[111] V. Schultz-Coulon, W. Schnick, *Z. Naturforsch. B: Chem. Sci.* **1995**, *50*, 619–622.

[112] G. Matoba, JP-B 50010804, **1975**.

[113] G. Matoba, JP-B 50010803, **1975**.

[114] H. Kobayashi, (Nippon Kokan K. K.), JP-A 03006314, **1991**.

[115] Taguchi Chokei, JP 55094432, **1980**.

[116] H. Willners, SE 115621, **1946**.

[117] T. M. Shaw, O. L. Krivanek, G. Thomas, *J. Am. Ceram. Soc.* **1979**, *62*, 305–306.

[118] O. Abe, *Ceram. Int.* **1990**, *16*, 53–60.

[119] N. Uchida, M. Koizumi, M. Shimeda, *J. Am. Ceram. Soc.* **1985**, *68*, C38–C40.

[120] R. Becker, *CIF - Ceramic Forum International* **1981**, *58*, 271–277.

[121] H. Imagawa, K. Anazai, T. Takano, M. Kasori, K. Shinozaki, A. Tsuge, (Toshiba Corp.), JP-A 60186478, **1985**.

[122] J. C. Hwang, S. M. Fuller, (Dow Chemicals Co.), WO-A1 9748659, **1997**.

[123] Y. Kurokawa, K. Uchiumi, (NEC Corp.), JP-A 61232273, **1986**.

[124] R. H. Wentdorf, Jr., *J. Chem. Phys.* **1962**, *36*, 1990–1991.

[125] T. Kuratomi, JP-A 52039599, **1977**.

[126] H. Lorenz, I. Orgzall, E. Hinze, *Diamond Relat. Mater.* **1995**, *4*, 1050–1055.

[127] G. Bocquillon, C. Loriers-Susse, J. Loriers, *C. R. Hebd. Séanc. Acad. Sci. Series II: Mechaniques Physique Chimie Sciences de la Terre et de l'Univers* **1992**, *315*, 1069–1072.

[128] J. Degawa, K. Tsuji, (Sumitomo Electric Industries, Ltd.), JP-A 01018436, **1989**.

[129] Showa Denki KK, JP-A 59073410, **1984**; JP-B 03047132, **1991**.

[130] G. Bocquillon, C. Loriers-Susse, J. Loriers, *J. Mater. Sci.* **1993**, *28*, 3547–3556.

[131] T. Kuratomi, JP-A 52024199, **1977**.

[132] K. Bradley, P. G. Collins, J.-C. P. Gabriel, Y. Kwon, S. Jhi, G. Gruner, (Nanomix Inc.), WO-A1 2003050447, **2003**.

[133] Y. Kwon, S. Jhi, K. Bradley, P. G. Collins, J.-C. P. Gabriel, G. Gruner, M. Cohen, S. Marvin, A. Zettle, (Nanomix Inc.), WO-A1 2003050036, **2003**.

[134] Y. Nakamori, G. Kitahara, K. Miwa, S. Towata, S. Orimo, *Appl. Phys. A: Mater. Sci. Process.* **2004**, *80*, 1–3.

[135] H. Leng, T. Ichikawa, S. Hino, T. Nakagawa, H. Fujii, *J. Phys. Chem. B* **2005**, *109*, 10744–10748.

[136] T. Ichikawa, H. Y. Leng, S. Isobe, N. Hanada, H. Fujii, *J. Power Sources* **2006**, *159*, 126–131.

[137] Y. Kojima, Y. Kawai, N. Ohba, *J. Power Sources* **2006**, *159*, 81–87.

[138] M. von Stackelberg, R. Paulus, *Z. Phys. Chem. B* **1933**, *22*, 305–322.

[139] P. Eckerlin, A. Rabenau, *Z. Anorg. Allg. Chem.* **1960**, *304*, 218–229.

[140] I. S. Gladkaya, G. N. Kremkova, N. A. Bendeliani, *J. Mater. Sci. Lett.* **1993**, *12*, 1547–1548.

[141] H. H. Franck, M. A. Beredig, G. Hoffmann, *Naturwissenschaften* **1933**, *21*, 330–331.

[142] H. Hartmann, H. J. Fröhlich, *Z. Anorg. Allg. Chem.* **1934**, *218*, 190–192.

[143] R. S. Bradley, D. C. Munro, M. Whitfield, *J. Inorg. Nucl. Chem.* **1966**, *28*, 1803–1812.

[144] O. Reckeweg, F. J. DiSalvo, *Z. Anorg. Allg. Chem.* **2001**, *627*, 371–377.

[145] P. Höhn, personal communication.

[146] H. T. Künzel, Dissertation, Universität Stuttgart, **1980**.

[147] J. Gaudé, P. L'Haridon, Y. Laurent, J. Lang, *Bull. Soc. Fr. Mineral. Cristal-logr.* **1972**, *95*, 56–60.

[148] G. Auffermann, Y. Prots, R. Kniep, *Angew. Chem.* **2001**, *113*, 565-567; *Angew. Chem. Int. Ed.* **2001**, *40*, 547-549.

[149] Y. Prots, G. Auffermann, M. Tovar, R. Kniep, *Angew. Chem.* **2002**, *114*, 2398-2394; *Angew. Chem. Int. Ed.* **2002**, *41*, 2288-2290.

[150] F. J. Llewellyn, F. E. Whitmore, *J. Chem. Soc.* **1957**, *1947*, 881–884.

[151] U. Steinbrenner, A. Simon, *Z. Anorg. Allg. Chem.* **1998**, *624*, 228–232.

[152] O. Reckeweg, F. DiSalvo, *Solid State Sci.* **2002**, *4*, 575–584.

[153] Y. Okamoto, J. C. Goswami, *Inorg. Chem.* **1966**, *5*, 1281–1283.

[154] G. V. Vajenine, G. Auffermann, Y. Prots, W. Schelle, R. K. Kremer, A. Simon, R. Kniep, *Inorg. Chem.* **2001**, *40*, 4866–4870.

[155] C. S. Choi, *Acta Crystallogr. Sect. B: Struct. Sci.* **1969**, *25*, 2638–2644.

[156] J. Santillan, S.-H. Shim, G. Shen, V. B. Prakapenka, *Geophys. Res. Lett.* **2006**, *33*, L15307/1–5.

[157] J. Tsuchiya, T. Tsuchiya, R. M. Wentzcovitch, *Phys. Rev. B* **2005**, *72*, 020103/1–4.

[158] W. Duan, R. M. Wentzcovitch, K. T. Thomson, *Phys. Rev. B* **1998**, *57*, 10363–10369.

[159] J.-F. Lin, O. Degtyareva, C. T. Prewitt, P. Dera, N. Sata, E. Gregoryanz, H.-K. Mao, R. J. Hemley, *Nat. Mater.* **2004**, *3*, 389–392.

[160] N. Funamori, R. Jeanloz, *Science* **1997**, *278*, 1109–1111.

[161] T. Mashimo, K. Tsumoto, K. Nakamura, Y. Noguchi, K. Fukuoka, Y. Syono, *Geophys. Res. Lett.* **2000**, *27*, 2021–2024.

[162] H. Cynn, D. G. Isaak, R. E. Cohen, M. F. Nicol, O. L. Anderson, *Am. Mineral.* **1990**, *75*, 439–442.

[163] F. C. Morton, R. E. Cohen, *Am. Mineral.* **1994**, *79*, 789–792.

[164] K. T. Thomson, R. M. Wentzcovitch, M. S. T. Bukowinski, *Science* **1996**, *274*, 1880–1882.

[165] A. R. Oganov, S. Ono, *Proc. Nat. Acad. Sci. USA* **2005**, *102*, 10828–10831.

[166] R. Caracas, R. E. Cohen, *Phys. Rev. B* **2007**, *76*, 184101/1–8.

[167] S. Ono, A. R. Oganov, T. Koyama, H. Shimizu, *Earth Planet. Sci. Lett.* **2006**, *246*, 326–335.

[168] R. D. Shannon, C. T. Prewitt, *J. Solid State Chem.* **1970**, *2*, 134–136.

[169] G. K. Rozenberg, L. S. Dubrovinsky, M. P. Pasternak, O. Naaman, T. L. Bihan, R. Ahuja, *Phys. Rev. B* **2002**, *65*, 064112/1–8.

[170] S.-H. Shim, T. S. Duffy, *Am. Mineral.* **2002**, *87*, 318–326.

[171] S. Ono, Y. Ohishi, *J. Phys. Chem. Solids* **2005**, *66*, 1714–1720.

[172] A. Gurlo, P. Kroll, R. Riedel, *Chem. Eur. J.* **2008**, *14*, 3306–3310.

[173] H. Yusa, T. Tsuchiya, N. Sata, Y. Ohishi, *Phys. Rev. B* **2008**, *77*, 064107/1–9.

[174] R. Hoppe, *Angew. Chem.* **1970**, *82*, 7-16; *Angew. Chem. Int. Ed. Engl.* **1970**, *9*, 25-34.

[175] R. Hoppe, *Angew. Chem.* **1966**, *78*, 52-63; *Angew. Chem. Int. Ed. Engl.* **1966**, *5*, 95-106.

[176] R. Hoppe, *Z. Naturforsch. A: Phys. Sci.* **1995**, *50*, 555–567.

[177] C. Weiß, R. Hoppe, *Z. Anorg. Allg. Chem.* **1996**, *622*, 1019–1026.

[178] R. Hübenthal, MAPLE, Programm for the calculation of the Madlung Part of Lattice Energy, Vers. 4, University of Gießen, Gießen (Germany), **1993**.

[179] O. Reckeweg, C. Lind, A. Simon, F. J. DiSalvo, *Z. Naturforsch. B: Chem. Sci.* **2003**, *58*, 159–162.

[180] S. Barbezat, J. Loriers, *C. R. Hebd. Séanc. Acad. Sci.* **1952**, *234*, 1978–1980.

[181] A. J. Bradley, A. Taylor, *Philos. Mag.* **1937**, *23*, 1049–1067.

[182] D. Hall, G. E. Gurr, G. A. Jeffrey, *Z. Anorg. Allg. Chem.* **1969**, *369*, 108–112.

[183] R. D. Shannon, *Acta Crystallogr. Sect. A: Found. Crystallogr.* **1976**, *32*, 751–767.

[184] W. H. Baur, *Crystallogr. Rev.* **1987**, *1*, 59–83.

[185] M. G. M. Armenta, A. Reyes-Serrato, *Comput. Mater. Sci.* **2001**, *21*, 95–100.

[186] A. Reyes-Serrato, G. Soto, A. Gamietea, M. H. Farias, *J. Phys. Chem. Solids* **1998**, *59*, 743–746.

[187] A. Mokhtari, H. Akbarzadeh, *Phys. B* **2002**, *324*, 305–311.

[188] M. G. M. Armenta, A. Reyes-Serrato, M. A. Borja, *Phys. Rev. B* **2000**, *62*, 4890–4898.

[189] E. Orhan, S. Jobic, R. Brec, R. Marchand, J.-Y. Saillard, *J. Mater. Chem.* **2002**, *12*, 2475–2479.

[190] A. Mokhtari, H. Akbarzadeh, *Phys. B* **2003**, *337*, 122–129.

[191] D. T. Cromer, *J. Phys. Chem.* **1957**, *61*, 753–755.

[192] Y. Laurent, J. Lang, M. T. LeBihan, *Acta Crystallogr. Sect. B: Struct. Sci.* **1968**, *24*, 494–499.

[193] F. Rodi, D. Babel, *Z. Anorg. Allg. Chem.* **1965**, *336*, 17–23.

[194] E. Schweda, Z. C. Kang, *Binary Rare Earth Oxides*, Springer Verlag, New York, 1st ed., **2004**.

[195] Q. Guo, Y. Zhao, C. Jiang, W. L. Mao, Z. Wang, *Solid State Commun.* **2008**, *145*, 250–254.

[196] H. R. Hoekstra, *Inorg. Chem.* **1966**, *5*, 754–757.

[197] H. R. Hoekstra, K. A. Gingerich, *Science* **1964**, *146*, 1163–1164.

[198] E. Husson, C. Proust, P. Gillet, J. P. Itie, *Mater. Res. Bull.* **1999**, *34*, 2085–2092.

[199] T. Hongo, K.-I. Kondo, K. G. Kazutaka, T. Atou, *J. Mater. Sci.* **2007**, *42*, 2582–2585.

[200] M. B. Kruger, J. H. Nguyen, Y. M. Li, W. A. Caldwell, M. H. Manghnani, R. Jeanloz, *Phys. Rev. B* **1997**, *55*, 3456–3460.

[201] O. Yeheskel, Y. Gefen, *Mater. Sci. Eng.* **1985**, *71*, 95–99.

[202] H. He, T. Sekine, T. Kobayashi, H. Hirosaki, *Phys. Rev. B* **2000**, *62*, 11412–11417.

[203] R. Ahuja, L. S. Dubrovinsky, *J. Phys.: Condens. Matter* **2002**, *14*, 10995–10999.

[204] S. R. Römer, C. Braun, O. Oeckler, P. Schmidt, P. Kroll, W. Schnick, *Chem. Eur. J.* **2008**, *14*, 7892–7902.

[205] Z. Lences, K. Hirao, P. Sajgalik, M. J. Hoffmann, *Key Eng. Mater.* **2006**, *317-318*, 857–860.

[206] G. Peng, G. Jiang, W. Li, B. Zhang, L. Chen, *J. Am. Ceram. Soc.* **2006**, *89*, 3824–3826.

[207] G. Peng, G. Jiang, H. Zhuang, W. Li, S. Xu, *Mater. Res. Bull.* **2005**, *40*, 2139–2143.

[208] H. Hayashi, K. Hirao, M. Toriyama, S. Shuzo, K. Itatani, *J. Am. Ceram. Soc.* **2001**, *84*, 3060–3062.

[209] X. Zhu, H. Hayashi, Y. Zhou, K. Hrao, *J. Mater. Res.* **2004**, *19*, 3270–3278.

[210] G. Peng, G. Jiang, W. Li, B. Zhang, L. L. Chen, *J. Am. Ceram. Soc.* **2006**, *89*, 3824–3826.

[211] C. Greskovich, *J. Mater. Sci.* **1979**, *14*, 2427–2438.

[212] C. Greskovich, *Commun. Am. Ceram. Soc.* **1981**, *64*, C31–C31.

[213] C. Greskovich, *NATO ASI Series Series E: Applied Sciences* **1983**, *65*, 283–292.

[214] W. D. Pasco, *Gov. Rep. Announce. Index (U. S.)* **1984**, *84*, 121.

[215] Y. Oyama, O. Kamigaito, *Yogyo Kyokaishi* **1973**, *81*, 209–203.

[216] Y. Inomata, K. Yukino, T. Matsuyama, T. Wada, *Yogyo Kyokaishi* **1976**, *84*, 534–539.

[217] W. Braue, H. J. Dudek, G. Ziegler, *J. Non-Cryst. Solids* **1983**, *56*, 185–189.

[218] J. T. Li, Y. L. Xia, C. C. Ge, *5th International Symposium on Ceramic Materials and Components for Engines 1994*, **1995**.

[219] W. A. Groen, M. J. Kraan, G. de With, *J. Eur. Ceram. Soc.* **1993**, *12*, 413–420.

[220] H. T. Hintzen, P. Swaanen, R. Metselaar, W. A. Groen, M. J. Kraan, *J. Mater. Sci. Lett.* **1994**, *13*, 1314–1316.

[221] S. Tanaka, K. Itatani, H. Uchida, M. Aizawa, I. J. Davies, H. Suemasu, A. Nozue, I. Okada, *J. Eur. Ceram. Soc.* **2002**, *22*, 777–783.

[222] R. J. Bruls, A. A. Kudyba-Jansen, P. Gerharts, H. T. Hintzen, R. Metselaar, *J. Mater. Sci.: Mater. Electron.* **2002**, *13*, 63–75.

[223] R. J. Bruls, H. T. Hintzen, R. Metselaarr, J. C. V. Miltenburg, *J. Phys. Chem. B* **1998**, *102*, 7871–7876.

[224] R. J. Bruls, H. T. Hintzen, R. Metselaar, *J. Eur. Ceram. Soc.* **2005**, *25*, 767–779.

[225] S. Tanaka, K. Itatani, H. T. Hintzen, A. C. A. Delsing, I. Okada, *J. Eur. Ceram. Soc.* **2004**, *24*, 2163–2168.

[226] R. J. Bruls, H. T. Hintzen, R. Metselaar, *Therm. Conductivity* **1999**, *24*, 3–14.

[227] L. Peng, L. Xu, J. Zhicheng, J. Zhang, J. Yang, Y. Qian, *Commun. Am. Ceram. Soc.* **2008**, *91*, 333–336.

[228] W. A. Groen, M. J. Kraan, G. de With, *J. Mater. Sci.* **1994**, *29*, 3161–3166.

[229] S. S. Lee, S. Lim, S. S. Sun, J. F. Wager, *Proceedings of SPIE - The International Society for Optical Engineering* **1997**, *3241*, 75–83.

[230] R. L. Toquin, A. K. Cheetham, *Chem. Phys. Lett.* **2006**, *423*, 352–356.

[231] G. K. Gaido, G. P. Dubrovskii, *Izvestiya Akademii Nauk SSSR Neorganicheskie Materialy* **1974**, *10*, 564–566.

[232] A. M. Zykov, G. K. Gaido, *Mater. Soveshch. Lyumin. (Kristallofosfory), 21st,* **1973**.

[233] C. J. Duan, X. J. Wang, W. M. Otten, A. C. A. Delsing, J. T. Zhao, H. T. Hintzen, *Chem. Mater.* **2008**, *20*, 1597–1605.

[234] J. David, Y. Laurent, J. Lang, *Bull. Soc. Fr. Mineral. Cristallogr.* **1970**, *93*, 153–159.

[235] M. Wintenberger, F. Tcheou, J. David, J. Lang, *Z. Naturforsch. B: Chem. Sci.* **1980**, *35*, 604–606.

[236] R. G. Blair, R. B. Kaner, *229th ACS National Meeting, San Diego, CA, United States,* **2005**.

[237] J. G. Thompson, R. L. Withers, S. R. Palethorpe, A. Melnitchenko, *J. Solid State Chem.* **1998**, *141*, 29–49.

[238] M. O´Keeffe, B. G. Hyde, *Acta Crystallogr. Sect. B: Struct. Sci.* **1976**, *32*, 2923–2936.

[239] L. Pauling, L. O. Brockway, *Z. Kristallographie Kristallgeometrie Kristallphysik Kristallchemie* **1932**, *82*, 188–194.

[240] D. E. Cox, W. J. Takei, G. Shirane, *Am. Crystallogr. Assoc.* **1962**, *1962P*, 6–6.

[241] V. L. Shaposhnikov, A. V. Krivosheeva, F. A. D'Avitaya, J.-L. Lazzari, V. E. Borisenko, *Phys. Status Solidi B* **2008**, *245*, 142–148.

[242] A. G. Petukhov, W. R. L. Lambrecht, B. Segall, *Phys. Rev. B* **1994**, *49*, 4549–4558.

[243] K. Köllisch, W. Schnick, *Angew. Chem.* **1999**, *111*, 368-370; *Angew. Chem. Int. Ed.* **1999**, *38*, 357-359.

[244] N. Douakha, M. Holzapfel, E. Chappel, G. Chouteau, L. Croguennec, A. Ott, B. Ouladdiaf, *J. Solid State Chem.* **2002**, *163*, 406–411.

[245] C. M. Fang, H. T. Hintzen, G. de With, *Appl. Phys. A: Mater. Sci. Process.* **2004**, *78*, 717–719.

[246] J. Y. Huang, L.-C. Tang, M. H. Lee, *J. Phys.: Condens. Matter* **2001**, *13*, 10417–10431.

[247] W. A. Groen, M. J. Kaan, G. de With, *J. Eur. Ceram. Soc.* **1993**, *12*, 413–420.

[248] R. J. Bruls, Dissertation, University of Eindhoven, **2000**.

[249] C. M. Fang, R. A. de Groot, R. J. Bruls, H. T. Hintzen, G. de With, *J. Phys.: Condens. Matter* **1999**, *11*, 4833–4842.

[250] M. Maunaye, J. Guyader, Y. Laurent, J. Lang, *Bull. Soc. Fr. Mineral. Cristallogr.* **1971**, *94*, 347–352.

[251] B. Manoun, S. K. Saxena, H. P. Liermann, R. P. Gulve, E. Hoffman, M. W. Asrsoum, G. Hug, C. S. Zha, *Appl. Phys. Lett.* **2004**, *85*, 1514–1516.

[252] V. L. Solozhenko, O. O. Kurakevych, *Solid State Commun.* **2005**, *133*, 385–388.

[253] C. D. Martin, K. W. Chapman, P. J. Chupas, V. Prakapenka, P. L. Lee, S. D. Shastri, J. B. Parise, *Am. Mineral.* **2007**, *92*, 1048–1053.

[254] A. Neuhaus, *Chimia* **1964**, *18*, 93–103.

[255] L. Pauling, *The nature of the chemical bond*, Cornell University Press, Ithaca, New York, **1960**.

[256] I. D. Brown, D. Altermatt, *Acta Crystallogr. Sect. B: Struct. Sci.* **1985**, *41*, 244–247.

[257] N. E. Brese, M. M. O'Keeffe, *Acta Crystallogr. Sect. B: Struct. Sci.* **1991**, *47*, 192–197.

[258] N. E. Brese, M. O'Keeffe in *Structure and Bonding 79*, Springer, Berlin, **1992**, Chapter Crystal Chemistry of Inorganic Nitrides, pp. 307–378.

[259] Y. Fei, *Am. Mineral.* **1999**, *84*, 272–272.

[260] H. Baltache, R. Khenata, M. Sahnoun, M. Driz, B. Abbar, B. Bouhafs, *Phys. B* **2004**, *344*, 334–342.

[261] P. Cortona, A. V. Monteleone, *J. Phys.: Condens. Matter* **1996**, *8*, 8983–8994.

[262] S. Desgreniers, *Phys. Rev. B* **1998**, *58*, 14102–14105.

[263] S. M. Sharma, Y. M. Gupta, *Phys. Rev. B* **1998**, *58*, 5964–5971.

[264] P. Perlin, C. Jauberthie-Carillon, J. P. Itie, A. S. Miguel, I. Grzegory, A. Polian, *Phys. Rev. B* **1992**, *45*, 83–89.

[265] H. Xia, Q. Xia, A. L. Ruoff, *Phys. Rev. B* **1993**, *47*, 12925–12928.

[266] M. Ueno, M. Yoshida, A. Onodera, O. Shimomura, K. Takemura, *Phys. Rev. B* **1994**, *49*, 14–21.

[267] M. Ueno, A. Onodera, O. Shimomura, K. Takemura, *Phys. Rev. B* **1992**, *45*, 10123–10130.

[268] P. Perlin, C. Jauberthie-Carillon, J. P. Itie, A. S. Miguel, I. Grzegory, A. Polian, *High Press. Res.* **1991**, *7*, 96–98.

[269] P. Perlin, I. Gorczyca, S. Porowski, T. Suski, N. E. Christensen, A. Polian, *Jpn. J. Appl. Phys. Suppl.* **1993**, *32*, 135–137.

[270] S. Uehara, T. Masamoto, A. Onodera, M. Ueno, O. Shimomura, K. Takemura, *J. Phys. Chem. Solids* **1997**, *58*, 2093–2099.

[271] R.-J. Xie, N. Hirosaki, *Sci. Technol. Adv. Mater.* **2007**, *8*, 588–600.

[272] R.-J. Xie, N. Hirosaki, N. Kimuara, K. Sakuma, M. Mitomo, *Appl. Phys. Lett.* **2007**, *90*, 191101/1–3.

[273] X. Piao, T. Horikawa, H. Hanzawa, K. Machida, *Appl. Phys. Lett.* **2006**, *88*, 161908/1–3.

[274] Y. Q. Li, G. deWith, H. T. Hintzen, *J. Solid State Chem.* **2008**, *181*, 515–524.

[275] M. Yamada, T. Naitou, K. Izuno, H. Tamaki, Y. Murazaki, M. Kameshima, T. Mukai, *Jpn. J. Appl. Phys.* **2003**, *42*, L20–L23.

[276] I. Idrestedt, C. Brosset, *Nature* **1964**, *201*, 1211–1211.

[277] A. Bischoff, T. Grund, T. Jording, B. Heying, R. D. Hoffmann, U. C. Rodewald, R. Pöttgen, *Z. Naturforsch. B: Chem. Sci.* **2005**, *60*, 1231–1234.

[278] C. M. Fang, H. T. Hintzen, G. D. With, R. A. D. Groot, *J. Phys.: Condens. Matter* **2001**, *13*, 67–76.

[279] A. Togo, P. Kroll, personal communication.

[280] S. Horstmann, E. Irran, W. Schnick, *Angew. Chem.* **1997**, *109*, 2085-2087; *Angew. Chem. Int. Ed. Engl.* **1997**, *36*, 1992-1994.

[281] W. Schnick, J. Lücke, *Z. Anorg. Allg. Chem.* **1990**, *588*, 19–25.

[282] K. Landskron, S. Schmid, W. Schnick, *Z. Anorg. Allg. Chem.* **2001**, *627*, 2469–2472.

[283] F. Karau, W. Schnick, *Angew. Chem.* **2006**, *118*, 4617-4620; *Angew. Chem. Int. Ed.* **2006**, *45*, 4505-4508.

[284] A. Stock, B. Hoffmann, *Berichte d. D. Chem. Gesellschaft* **1903**, *36*, 814–819.

[285] S. Horstmann, E. Irran, W. Schnick, *Angew. Chem.* **1997**, *109*, 1938-1940; *Angew. Chem. Int. Ed. Engl.* **1997**, *36*, 1873-1875.

[286] H. R. Wentorf, *J. Chem. Phys.* **1957**, *26*, 956–956.

[287] J. Dong, A. A. Kinkhabwala, P. F. McMillan, *Phys. Status Solidi B* **2004**, *241*, 2319–2325.

[288] C.-M. Sung, M. Sung, *Mater. Chem. Phys.* **1996**, *43*, 1–18.

[289] F. Gao, R. Xu, K. Liu, *Phys. Rev. B* **2005**, *71*, 052103/1–4.

[290] L. W. Bragg, *Proc. Royal Soc. London Ser. A: Math. Phys. Sci.* **1927**, *113*, 642–657.

[291] P. Hartmann, *Z. Kristallogr.* **1989**, *187*, 139–143.

[292] S. Horstmann, E. Irran, W. Schnick, *Z. Anorg. Allg. Chem.* **1998**, *624*, 620–628.

[293] U. Müller, *Anorganische Strukturchemie*, B. G. Teubner, Stuttgart, 3rd ed., **1996**.

[294] R. P. Ziebarth, J. D. Corbett, *J. Am. Chem. Soc.* **1988**, *110*, 1132–1139.

[295] R. P. Zierbarth, J. D. Corbett, *Inorg. Chem.* **1989**, *28*, 626–631.

[296] M. Köckerling, R. Y. Qi, J. D. Corbett, *Inorg. Chem.* **1996**, *35*, 1437–1443.

[297] R. Y. Qi, J. D. Corbett, *Inorg. Chem.* **1995**, *34*, 1646–1651.

[298] J. Zhang, J. D. Corbett, *Z. Anorg. Allg. Chem.* **1991**, *598/599*, 363–370.

[299] F. Ottinger, R. Nesper, *Z. Anorg. Allg. Chem.* **2005**, *631*, 1597–1602.

[300] H. Yamane, F. J. DiSalvo, *J. Alloys Compd.* **1996**, *240*, 33–36.

[301] G. Pilet, J. A. Hoeppe, W. Schnick, S. Esmaeilzadeh, *Solid State Sci.* **2005**, *7*, 391–396.

[302] H. Huppertz, W. Schnick, *Chem. Eur. J.* **1997**, *3*, 249–252.

[303] F. Stadler, W. Schnick, *Z. Anorg. Allg. Chem.* **2007**, *633*, 589–592.

[304] C. Braun, personal communication.

[305] G. Bacon, *Acta Crystallogr.* **1952**, *5*, 684–686.

[306] ASM International, Pearson's Crystal Data, Crystal Structure Database for Inorganic Compounds, Materials Park (USA), **2007-2008**.

[307] Fachinformationszentrum Karlsruhe, Inorganic Crystal Structure Database, Karlsruhe (Germany), **2008**.

Publications

Major results of this thesis were published or are to be published in scientific journals by way of the following publications. References of of previously published work, as well as oral and poster presentations are included separately below.

I Published or to be Published as Part of this Thesis

"BeP_2N_4 – Synthesis, Characterization and First Principal Calculations of Spinel-Type High-Pressure Phases"
S. R. Römer, F. Pucher, F. Karau, W. Schnick, (in preparation).

"Theoretical Investigations of High-Pressure Phase Transitions of the Layered Alkaline Earth Nitridosilicates $SrSiN_2$ and $BaSiN_2$"
S. R. Römer, P. Kroll, W. Schnick, (in preparation).

"Group II Element Nitrides M_3N_2 under pressure: A Comparative Density Functional Study"
S. R. Römer, T. Dörfler, P. Kroll, W. Schnick, (submitted).

"A Density Functional Study of the High-Pressure Chemistry of $MSiN_2$ (M = Be, Mg, Ca): Prediction of High-Pressure Phases and Examination of Pressure-Induced Decomposition"
S. R. Römer, P. Kroll, W. Schnick, (submitted).

"*A Density Functional Study of Calcium Nitride Ca_3N_2: Refined Geometries and Prediction of High Pressure Phases*"
S. R. Römer, W. Schnick, P. Kroll, *J. Phys. Chem. C* **2009**, DOI: 10.1021/jp8077002.

"*High-Pressure Synthesis and Characterization of the Alkaline Earth Borate β-BaB_4O_7*"
J. S. Knyrim, S. R. Römer, W. Schnick, H. Huppertz, *Solid State Sci.* **2009**, *2009, 11*, 336-342.

"*HP-$Ca_2Si_5N_8$ - A New High-Pressure Nitridosilicate: Synthesis, Structure, Luminescence and DFT-Calculations*"
S. R. Römer, C. Braun, O. Oeckler, P. J. Schmidt, P. Kroll, W. Schnick, *Chem. Eur. J.* **2008**, *14*, 7892-7902.

II Other Publications (2005-2009)

"*Synthesis, Single Crystal Structure Determination and Rietveld Refinement of Cadmium Tetrametaphosphimate Octahydrate $Cd_2(PO_2NH)_4 \cdot 8\,H_2O$*"
S. R. Römer, W. Schnick, *Z. Anorg. Allg. Chem.* **2009**, *635*, (in press).

"*Synthesis and Crystal Structure of Sodium Copper Tetrametaphosphimate Heptahydrate $Na_2Cu(PO_2NH)_4 \cdot 7\,H_2O$ and Sodium Potassium Copper Tetrametaphosphimate Heptahydrate $K_xNa_{2-x}Cu(PO_2NH)_4 \cdot 7\,H_2O$*"
S. R. Römer, W. Schnick, *Solid State Sci.* **2007**, *9*, 644-652.

"*Synthesis and Crystal Structure of Lithium Tetrametaphosphimate Tetrahydrate $Li_4(PO_2NH)_4 \cdot 4\,H_2O$*"
S. R. Römer, W. Schnick, *Z. Anorg. Allg. Chem.* **2006**, *632*, 59-63.

"*Synthesis and Crystal-Structure Determination by X-ray Powder Diffraction of Nickel Tetrametaphosphimate-octahydrate $Ni_2(PO_2NH)_4 \cdot 8\,H_2O$*"
S. R. Römer, W. Schnick, *Z. Anorg. Allg. Chem.* **2005**, *631*, 1749-1750.

"Syntheses, Crystal Structures and Properties of the Tetrametaphosphimates $M_2^{II}(PO_2NH)_4 \cdot 8\,H_2O$ with M^{II} = Mg, Mn, Co, and Zn"
S. R. Römer, W. Schnick, *Z. Anorg Allg. Chem.* **2005**, *631*, 31-37.

III Presentations

Oral Presentations

"A Density Functional Study on Pressure Induced Decomposition and Phase Transformation Reactions in M-Si-N-Systems (M = Mg, Ca, Sr)"
S. R. Römer, P. Kroll, W. Schnick, Workshop DFT-CMS-07, 6th November 2007, Munich, Germany.

"Synthesen, Eigenschaften und theoretische Untersuchungen von Hochdruckmodifikationen der Nitrido- und Oxonitridosilicate - Part 2"
S. R. Römer, P. Kroll, W. Schnick, I. Workshop of the SPP 1236 of the DFG, 31st Octboer to 1st November 2006, Hünfeld, Germany.

"Pressure Induced Decomposition and Phase Transformation Reactions in M-Si-N-Systems (M = Be, Mg, Ca, Sr, Ba) - A DFT Study"
S. R. Römer, P. Kroll, W. Schnick, I. Berichtskolloquium of the SPP 1236 of the DFG, 1st to 3rd October 2007, Hünfeld, Germany.

"Part 2 - DFT Calculations: The System $Ca_2Si_5N_8$-$CaSiN_2$-Ca_3N_2-Si_3N_4 under High Pressure"
S. R. Römer, P. Kroll, W. Schnick, II. Berichtskolloquium of the SPP 1236 of the DFG, 16th to 18th June 2008, Freiberg, Germany.

Poster Presentations

"*HP-Ca$_2$Si$_5$N$_8$: A New High Pressure Phase - DFT calculations*"
S. R. Römer, C. Braun, P. Kroll, W. Schnick, I. Berichtskolloquium of the SPP 1236
of the DFG, 1st to 3rd October 2007, Hünfeld, Germany.

"*A Density Functional Study of the Alkaline Earth Nitride Ca$_3$N$_2$: Refined Geometries and High-Pressure Phases*"
S. R. Römer, P. Kroll, W. Schnick, II. Berichtskolloquium of the SPP 1236 of the
DFG, 16th to 18th June 2008, Freiberg, Germany.

"*HP-Ca$_2$Si$_5$N$_8$ - A New High-Pressure Nitridosilicate: Synthesis, Structure, Luminescence and DFT-Calculations*"
C. Braun, S. R. Römer, O. Oeckler, P. J. Schmidt, P. Kroll, W. Schnick, The 46th
European High Pressure Research Group Conference, 7th to 12th September 2008,
Valencia, Spain.

"*HP-Ca$_2$Si$_5$N$_8$: A New High Pressure Phase - DFT calculations*"
S. R. Römer, P. Kroll, W. Schnick, 14. Vortragstagung der FG Festkörperchemie
und Materialforschung, 24th to 26th September 2008, Bayreuth, Germany.

"*High-pressure phases of Alkaline Earth Nitrides M$_3$N$_2$ - A DFT Study*"
S. R. Römer, T. Dörfler, P. Kroll, W. Schnick, 14. Vortragstagung der FG Festkörperchemie und Materialforschung, 24th to 26th September 2008, Bayreuth, Germany.

IV CSD Reference Numbers

$Cd_2(PO_2NH)_4 \cdot 8\,H_2O$ CSD-420259

$Na_2Cu(PO_2NH)_4 \cdot 7\,H_2O$ CSD-417834

$K_{0.47}Na_{1.53}CuPO_2NH)_4 \cdot 7\,H_2O$ CSD-417833

$\text{Li}_4(\text{PO}_2\text{NH})_4 \cdot 4\,\text{H}_2\text{O}$ CSD-415548

$\text{Ni}_2(\text{PO}_2\text{NH})_4 \cdot 8\,\text{H}_2\text{O}$ CSD-415283

$\text{Mg}_2(\text{PO}_2\text{NH})_4 \cdot 8\,\text{H}_2\text{O}$ CSD-414086

$\text{Mn}_2(\text{PO}_2\text{NH})_4 \cdot 8\,\text{H}_2\text{O}$ CSD-414088

$\text{Co}_2(\text{PO}_2\text{NH})_4 \cdot 8\,\text{H}_2\text{O}$ CSD-414087

$\text{Zn}_2(\text{PO}_2\text{NH})_4 \cdot 8\,\text{H}_2\text{O}$ CSD-414085

Curriculum Vitae

PERSONAL INFORMATION

Name: Susanne Rebecca Römer

Date of Birth: 25/09/1979

Place of Birth: München

SCHOOL EDUCATION

09/1986 - 07/1990	Gerhardinger Grundschule (primary school), Pfaffenhofen/Ilm
09/1990 - 06/1999	Schyrengymnasium (secondary school), Pfaffenhofen/Ilm Abitur (A-Levels): 1.1 focus on biology and english

UNIVERSITY EDUCATION

11/1999 - 10/2001	Grundstudium "Diplom Chemie" (Undergraduate Studies in Chemistry), Ludwig-Maximilians-Universität München Preliminary Diploma Exams: 1.4
10/2001 - 11/2003	Hauptstudium "Diplom Chemie" (Graduate Studies in Chemistry) , Ludwig-Maximilians-Universität München Diploma Exams: 1.0
09/2002 - 10/2002	Internship in Organic Chemistry, Université René Descartes, Paris V, France

01/2004 - 07/2004	Diploma Thesis with Professor Dr. W. Schnick, Chair for Inorganic Solid State Chemistry, Ludwig-Maximilians-Universität München (1.0) Titel: "*Synthese, Charakterisierung und Eigenschaften neuer Tetrametaphosphimate*" ("Syntheses, Characterization and Properties of Novel Tetrametaphosphimates")
09/2004 - today	PhD Thesis with Professor Dr. W. Schnick, Chair for Inorganic Solid State Chemistry, Ludwig-Maximilians-Universität München Titel: "*Density Functional Calculations of pressure-induced Phase Transformations of Nitridosilicates and Nitridophosphates*"

WORK EXPERIENCE

09/2004 - today	Research assistant (research and teaching), Chair for Inorganic Solid State Chemistry, Ludwig-Maximilians-Universität München
11/2006 - 05/2008	Freelance secondary employment as fire artist (acrobatics and performance)

AWARDS

Abitur: Award for excellence (1999)

Scholarship of the Bavarian State (*Stipendium für besonders Begabte nach dem Bayerischen Begabtenförderungsgesetz*) (1999 to 2004)

Oral Diploma Exams: Award for excellence (2003)

Römer Scholarship of the Dr. Klaus Römer Foundation (2008)